U.PORTO

FEUP FACULDADE DE ENGENHARIA
UNIVERSIDADE DO PORTO

Low Computational Cost Gear Mesh Stiffness Modeling: Application to gear dynamics and design optimization

João Duarte Marques Marafona

A thesis submitted to:
Faculty of Engineering of the University of Porto

Doctoral Program in Mechanical Engineering

Supervisor: Doctor Pedro Miguel Teixeira Marques

Co-supervisor: Professor Ramiro Carneiro Martins

Porto, 2023

The present work was performed at
INEGI - Institute of Science and Innovation in Mechanical and Industrial Engineering
Unit of Tribology, Vibrations and Industrial Maintenance
Campus of the Faculty of Engineering of the University of Porto
Rua Dr. Roberto Frias, 400
4200-465 Porto
Portugal.

João Duarte Marques Marafona
E-mail (FEUP): up201306219@up.pt
E-mail (INEGI): jmarafona@inegi.up.pt

INEGI - Instituto de Ciência e Inovação em Engenharia Mecânica e Engenharia Industrial
Unidade de Tribologia, Vibrações e Manutenção Industrial
Campus da Faculdade de Engenharia da Universidade do Porto
Rua Dr. Roberto Frias, 400
4200-465 Porto
Portugal.

Abstract

Evolution is inevitable and part of it is overcoming problems by looking at them as opportunities for innovation. This is an era of sustainability where the application of different sources of energy is in development and there are significant energy concerns causing drastic changes in drive technology. Gears, as the main tribological element used to transmit motion and power, will play a prominent role in energy generation and mobility trends. It is up for gear engineers to step up and turn into value all their knowledge in order to find the necessary gear designs. The purpose of this work is to develop a gear mesh stiffness model capable of keeping up with current and forthcoming needs so a low computational cost approach is taken as it allows to easily explore different gear design solutions.

A study on the different types of gear mesh stiffness models in the literature is performed, establishing four types of models: analytical, finite element, hybrid and approximate. Their implementation procedures as well as positive and negative features are analyzed, showing that approximate gear mesh stiffness models have the lowest computational cost. The developed gear mesh stiffness model, which is of the approximate type, comprises two instances, the definition of the single tooth pair slice mesh stiffness and the gear mesh stiffness modeling algorithm for both spur and helical gears. The gear modeling also includes the implementation of a gear-shaft-bearing dynamic model. This results in a set of tools for gear quasi-static and dynamic evaluation that is applied for a parametric study of a modeling stiffness variable, which is mostly neglected in the literature; an analysis of the overlap ratio influence on gear behavior as a preliminary approach to experimental testing on the concept of integer overlap ratio gear design and a research on gear design optimization aiming at improved dynamic behavior without computing the dynamic response.

The developed work gives an approximate definition of the single tooth pair slice mesh stiffness which when applied to approximate analytical models improves the accuracy of their mesh stiffness estimations due to the asymmetrical shape considered and the removal of free/user-defined parameters. The developed approximate gear mesh stiffness model is simple to implement and gives fast mesh stiffness estimations that can consider extension of contact, profile modifications, border weakening effect and any type of manufacturing/assembly error that can be modeled as a change in the separation distance - it is sound and flexible as it can attend current needs and be adapted for future investigations.

Keywords: Gear modeling, Gear mesh stiffness, Gear dynamics, Gear design, Gear optimization.

Resumo

A evolução é inevitável e parte dela consiste em superar os problemas encarando-os como oportunidades de inovação. Esta é uma era de sustentabilidade onde a aplicação de diferentes fontes de energia está em desenvolvimento e existe uma grande preocupação energética que leva a alterações drásticas no projeto de transmissões mecânicas. As engrenagens, como principal elemento tribológico usado para transmitir movimento e potência, têm um papel preponderante nas novas tendências de geração de energia e mobilidade. Cabe aos engenheiros transformar o seu conhecimento em valor para definir engrenagens que satisfaçam os requisitos impostos. O objetivo deste trabalho é desenvolver um modelo da rigidez de engrenamento capaz de acompanhar as necessidades atuais e emergentes. Para isso, uma modelação de baixo custo computacional é estudada pois permite explorar facilmente diversas geometrias de engrenagens.

Os diferentes modelos de rigidez de engrenamento são estudados, de onde são definidos quatro tipos diferentes: analíticos, elementos finitos, híbridos e aproximados. Os seus processos de implementação assim como as suas principais vantagens e desvantagens são analisados, revelando que os modelos de rigidez de engrenamento aproximados são os que possuem o custo computacional mais baixo. O modelo de rigidez de engrenamento desenvolvido, que é do tipo aproximado, inclui duas componentes, a definição da rigidez de um par de dentes de largura infinitesimal e do algoritmo de modelação da rigidez de engrenamento para engrenagens de dentado reto e helicoidal. A modelação de engrenagens também inclui a implementação de um modelo dinâmico de engrenagens, veios e rolamentos. Isto resulta numa ferramenta para avaliação do comportamento quase-estático e dinâmico de engrenagens que é utilizado para um estudo paramétrico de uma variável de modelação da rigidez, que é tipicamente desprezada na literatura; uma análise da influência da razão de condução suplementar no comportamento de engrenagens como uma abordagem preliminar aos testes experimentais ao conceito de projeto de engrenagens com razão de condução suplementar com valor inteiro e uma pesquisa sobre otimização do projeto de engrenagem para melhorar o comportamento dinâmico sem necessidade de calcular a resposta dinâmica.

O trabalho desenvolvido proporciona uma definição para a rigidez de um par de dentes de largura infinitesimal que, quando aplicada a modelos aproximados, melhora a exatidão das estimativas de rigidez de engrenamento devido à forma assimétrica considerada e à remoção de parâmetros livres. O modelo aproximado da rigidez de engrenamento desenvolvido é simples de implementar e fornece estimativas rápidas da rigidez que podem considerar extensão de contato, modificações de perfil, efeito de enfraquecimento da borda e qualquer tipo de erro de fabrico/montagem que pode ser modelado como uma mudança na distância de separação - é um modelo robusto e flexível, pois pode atender às necessidades atuais e ser adaptado para investigações futuras.

Palavras-chave: Modelação de engrenagens; Rigidez de engrenamento; Dinâmica de engrenagens; Projeto de engrenagens; Otimização de engrenagens.

"Live as if you were to die tomorrow. Learn as if you were to live forever."

Mahatma Gandhi

Acknowledgments

List of the people who I am thankful for, alphabetically ordered. Personal thanks was given to every person on this list.

Ângela Martins	João Amorim	Justino Cruz
Beatriz Graça	João Marafona	Maria Marques
Carlos Fernandes	João Tavares	Marta Marafona
Carlos António	Jorge Seabra	Pedro Marques
Daniel Camões	José Almacinha	Pedro Romio
David Gonçalves	José Marafona	Ramiro Martins
Gonçalo Carneiro	José Rodrigues	Stephane Portron

I gratefully acknowledge the funding of Fundação para a Ciência e a Tecnologia (FCT) through the grant SFRH/BD/147889/2019 and the support given by my supervisors Doctor Pedro Marques and Professor Ramiro Martins whom without the *philosophiae doctor* would not have been possible.

I am also thankful to INEGI Institute of Science and Innovation in Mechanical and Industrial Engineering for being the host institution as well as the directors of the Unit of Tribology, Vibrations and Industrial Maintenance Professor Jorge Seabra and Professor Carlos Fernandes.

Contents

Abstract i

Resumo iii

Acknowledgments vii

Contents ix

List of figures xiii

List of tables xvii

Nomenclature xix

1. Introduction 1

1.1. Background and motivation 1

1.2. Objective and research approach 2

1.3. Scientific contributions 2

1.4. Outline 4

2. Mesh stiffness models 5

2.1. A look into mesh stiffness 5

2.2. Analytical models 10

2.2.1. Potential energy method 10

2.2.2. Literature review on analytical models 16

2.3. Finite element models 30

2.3.1. Details of finite element method 30

2.3.2. Literature review on finite element models 32

2.4. Hybrid models . . . 37
2.5. Approximate analytical models . . . 42
2.5.1. Models for the estimation of the single tooth pair mesh stiffness . . . 42
2.5.2. Models based on the analytical description of the contact lines' length . . . 45
2.6. Polymer gears . . . 52
2.7. New trends and the gear mesh stiffness . . . 55
2.8. Closure . . . 56

3. Single tooth pair slice mesh stiffness 61
3.1. Background . . . 61
3.2. Potential energy method . . . 64
3.3. Shape parameters . . . 65
3.3.1. Asymmetry parameter, λ . . . 66
3.3.2. Amplitude parameter, α_k . . . 69
3.4. Maximum stiffness . . . 71
3.4.1. Number of teeth . . . 72
3.4.2. Helix angle . . . 72
3.4.3. Module and facewidth . . . 73
3.4.4. Profile shift coefficients . . . 73
3.4.5. Young's modulus . . . 74
3.5. Assessment process . . . 74
3.5.1. Shape parameters . . . 75
3.5.2. Maximum stiffness . . . 77
3.6. Single tooth pair slice mesh stiffness . . . 80
3.7. Closure . . . 81

4. Gear modeling 83
4.1. Background . . . 83
4.2. Gear mesh stiffness model . . . 86
4.2.1. Slice transmission error . . . 86
4.2.2. Extension of contact . . . 89
4.2.3. Mesh stiffness and transmission error . . . 92
4.2.4. Assessment process . . . 93
4.3. Dynamic model . . . 94

4.3.1. Gear components 94
4.3.2. Shaft components 97
4.3.3. Bearing components 97
4.3.4. Equations of motion 97
4.3.5. Algorithm 98
4.3.6. Dynamic parameters 99
4.3.7. Assessment process 99
4.4. Effect of asymmetry 100
4.4.1. Gear mesh stiffness 101
4.4.2. Dynamic transmission error 103
4.4.3. Load distribution 107
4.5. Closure 110

5. Integer overlap ratio gears: preliminary study 113
5.1. Background 113
5.2. Gear design 114
5.3. Gear mesh stiffness 119
5.4. Gear dynamics 121
5.5. Gear noise level 124
5.6. Closure 125

6. Gear design optimization 127
6.1. Background 127
6.2. Gear design optimization problem 130
6.2.1. Problem statement 131
6.2.2. Gear mesh stiffness 133
6.2.3. Gear dynamics 134
6.2.4. Genetic algorithm 135
6.3. Gear optimization: relaxed problem 138
6.3.1. Stiffness *versus* Dynamics 140
6.3.2. Noise level 142
6.4. Gear optimization: full problem 143
6.4.1. Stiffness *versus* Dynamics 145
6.4.2. Noise level 146

6.5. Closure 147

7. Conclusion **149**

7.1. Conclusions 149

7.2. Future work 152

References **153**

List of figures

2.1. Geometrical parameters of involute tooth. 11

2.2. Trend of the peak-to-peak mesh stiffness variation with the center distance variation. 18

2.3. Spring schematic of traditional analytical method and improved analytical method. 19

2.4. Tooth slice coupling model. 20

2.5. Schematic of the helical tooth slice division. 22

2.6. Illustration of tooth with tip chipping. 26

2.7. Example of gear tooth profiles with different wear cycles. 27

2.8. Sliced tooth with spalling. 28

2.9. Finite element calculation of the force-deflection curve with representation of different stiffness approaches. 33

2.10. Finite element model of a spur gear pair with bore surfaces highlighted. 34

2.11. Global and partial FE models. 39

2.12. Full and partial FE models. 40

2.13. Finite element model and tooth contact model. 41

2.14. Web structure for the proposed finite element model and the three-dimensional finite element model. 41

2.15. Normalized single tooth pair stiffness according to Cai and Hayashi. 43

2.16. Definition of coordinates ξ and η for a gear with an arbitrary overlap ratio. . . . 48

3.1. Example of the effect of the shape parameters on the tooth pair structural stiffness. 66

3.2. Stiffness ratio between the PEM and the ISO* maximum stiffness for each z_1. . . 72

3.3. Histogram of the R-squared values for the tooth pair structural stiffness shape. . 75

3.4. Comparison between the potential energy method and the model curves for the tooth pair structural stiffness shape. 76

3.5. Influence of independent variables in the tooth pair structural stiffness shape. . . 78

3.6. Histogram of the maximum tooth pair structural stiffness relative error comparing to PEM. 79

3.7. Influence of independent variables in the maximum tooth pair structural stiffness value. 79

3.8. Comparison between the potential energy method, the developed model and the literature model curves for the single tooth pair slice mesh stiffness. 81

4.1. Flowchart of the gear mesh stiffness model. 87

4.2. Definition of the coordinate system. 88

4.3. Theoretical transmission error and separation distances in recess and approach for teeth. 91

4.4. Gear mesh stiffness assessment: comparison between the developed model and FEM. 94

4.5. Schematic of the dynamic system. 95

4.6. Schematic of the gear subsystem. 95

4.7. Dynamic assessment: comparison between the implemented model and Raclot and Velex 100

4.8. Example of Campbell's diagram for selection of the speed range. 102

4.9. Effect of asymmetry on the gear mesh stiffness: spur gears. 103

4.10. Effect of asymmetry on the gear mesh stiffness: helical gears. 103

4.11. Effect of asymmetry on gear dynamics: spur gears. 104

4.12. Effect of asymmetry on gear dynamics: helical gears. 104

4.13. Dynamic analysis for the worst spur gear: with and without asymmetry. 105

4.14. Stiffness analysis for the worst spur gear: with and without asymmetry. 105

4.15. Dynamic analysis for the worst helical gear: with and without asymmetry. 106

4.16. Stiffness analysis for the worst helical gear: with and without asymmetry. 106

4.17. Effect of asymmetry on load sharing ratio: spur gears. 107

4.18. Effect of asymmetry on load sharing ratio: helical gears. 108

4.19. Effect of asymmetry on dynamic mesh force: spur gears. 109

4.20. Effect of asymmetry on dynamic mesh force: helical gears. 109

5.1. IOR map for $\varepsilon_\beta = 1$. 117

5.2. IOR map for $\varepsilon_\beta = 2$. 118

5.3. Gear mesh stiffness. 120

5.4. Gear mesh stiffness fluctuation around its average. 120

5.5. Peak-to-peak amplitude of the gear mesh stiffness amplitude. 121

5.6. RMS of the gear mesh stiffness fluctuation around its average. 121
5.7. RMS of the normalized gear mesh stiffness fluctuation around its average. 121
5.8. Schematic of the dynamic system. 122
5.9. Peak-to-peak amplitude of the DTE. 123
5.10. Variation of the first three harmonic amplitudes of DTE_{osc}. 123
5.11. Average DTE peak-to-peak amplitude. 124
5.12. Average A_{RMS} of the DTE oscillating component. 124
5.13. Overall noise level at different rotating speeds. 125

6.1. Schematic of the single-stage transmission system. 130
6.2. Schematic of the dynamic system. 135
6.3. Pseudo-code of the genetic algorithm. 137
6.4. Comparison between the optimum solutions with stiffness and dynamic objective functions. 139
6.5. Comparison between the high-end individuals in a contact/overlap ratios map. . 140
6.6. Evolution of the best solution along the generations: relaxed problem. 141
6.7. Correlation for gear mesh stiffness - relaxed problem. 142
6.8. Correlation for gear dynamics - relaxed problem. 142
6.9. Correlation for noise level - relaxed problem. 143
6.10. Correlation for normalized dynamic amplitude - relaxed problem. 143
6.11. Comparison between the optimum solutions with stiffness and dynamic objective functions. 144
6.12. Comparison between the high-end individuals in a contact/overlap ratios map. . 145
6.13. Evolution of the best solution along the generations: full problem. 146
6.14. Correlation for gear mesh stiffness - full problem. 146
6.15. Correlation for gear dynamics - full problem. 146
6.16. Correlation for noise level - full problem. 147
6.17. Correlation for normalized dynamic amplitude - full problem. 147

List of tables

2.1. Coefficients of the polynomial curve fitting 15
2.2. Summary of spur gear analytical models. 22
2.3. Summary of helical gear analytical models. 25
2.4. Summary of damaged gears analytical models. 29
2.5. Softwares used to perform finite element analysis of the gear mesh stiffness. . . . 31
2.6. Modeling of gears for finite element analysis of the gear mesh stiffness. 31
2.7. Types of elements for finite element analysis of the gear mesh stiffness. 31
2.8. Comparison between the different types of gear mesh stiffness models. 58

3.1. Gear parameters for the number of teeth evaluation. 67
3.2. Gear parameters for the profile shift coefficients evaluation. 68
3.3. Gear parameters for the helix angle evaluation. 70
3.4. Gear parameters for the module/facewidth evaluation. 73
3.5. Interval of gear parameters for the assessment. 75
3.6. Gear parameters for the best and worst cases. 76
3.7. Gear parameters for the example gears. 80

4.1. Gear parameters for the assessment gears. 93
4.2. Inputs for gearbox dynamic model. 98
4.3. Interval of gear parameters for the evaluation of the asymmetry effect. 101
4.4. Bearing stiffnesses for each shaft. 101

5.1. Geometrical parameters of the H501 and H951 gears. 114
5.2. Parameters imposed for the development of the IOR gears. 115
5.3. Parameters for the IOR gears developed. 116
5.4. Parameters for the IOR100 variants. 118

5.5. Experimental tests safety factors for the IOR100 variants. 119
5.6. Gears' material properties. 119
5.7. Shaft data. 122
5.8. Bearing data. 122

6.1. Parameters from the single-stage gear system. 131
6.2. Bearing data. 134
6.3. Genetic algorithm parameters. 138
6.4. Nominal working conditions for the relaxed problem. 139
6.5. Design variables of the optimum individuals: relaxed problem. 139
6.6. Nominal working conditions for the full problem. 144
6.7. Design variables of the optimum individuals: full problem. 144

Nomenclature

Quantities

α	pressure angle	rad
α_{C}	load angle	rad
$\alpha_{\mathrm{Fourier}}$	relative variation in mesh stiffness amplitude	-
α_k	relative amplitude of the single tooth pair (slice) mesh stiffness	-
α_{T}	angle given by the inverse cosine of the ratio base radius and load point radius	rad
α_{t}	transverse pressure angle	rad
β	helix angle	rad
β_{b}	base helix angle	rad
χ	displacement	m
$\overline{\Delta\mathrm{DMF}}$	average dynamic mesh force relative difference	-
ΔK	gear mesh stiffness fluctuation component	$\mathrm{N\,m^{-1}}$
$\overline{\Delta\mathcal{L}}$	average load sharing ratio relative difference	-
δ	transmission error	m
$\delta^{\mathrm{s},i}$	slice transmission error of tooth pair i	m
δ^{s}	slice transmission error	m
δ_θ	rotational form of the transmission error	rad
Δ_{s}	separation distance	m
$\Delta_{\mathrm{s}}^{\mathrm{s},i}$	slice separation distance of tooth pair i	m
ε_{L}	normalized maximum contact line length	-
η	normalized coordinate along a contact line	-
$\gamma(y)$	tooth angular thickness at section y	rad
γ_{b}	tooth angular thickness at base radius	rad
γ_{C}	tooth angular thickness at load radius	rad

γ_{p}	tooth angular thickness at root radius	rad
λ	asymmetry of the single tooth pair slice mesh stiffness	-
λ^{PEM}	asymmetry of the single tooth pair slice mesh stiffness by PEM	-
$\mathcal{L}$	load sharing ratio	-
$\mathcal{L}^{\mathrm{s}}$	slice load sharing ratio	-
$\nu(y)$	profile polar angle	rad
ν	Poisson's ratio	-
ϕ_i	normalized path of contact coordinate shift	-
ϕ_i^{L}	normalized contact line coordinate shift	-
ψ	parameter related to the c_{f}^h factor	-
ρ	density of the material	$\mathrm{kg\,m^{-3}}$
ρ_{fP}^*	fillet radius of basic rack profile normalized by the normal module	-
τ	time normalized to the meshing period	-
θ	rotation angle	rad
θ_{p}	angle between the tooth centerline and the juncion with the root circle	rad
$\tilde{X}$	peak-to-peak amplitude of the DTE normalized by δ	–
ε	total contact ratio	-
ε_α	contact ratio	-
$\varepsilon_\alpha^{\mathrm{w}}$	contact ratio under load	-
ε_β	overlap ratio	-
φ_M	functions representing the time variations of the mesh stiffness per unit contact length	-
ξ	normalized coordinate along the path of contact	-
ξ_{C}	normalized coordinate of the tooth load point	-
ξ_{inn}	normalized coordinate for the start point of meshing	-
a	center distance	m
A_{c}	cross section area	$\mathrm{m^2}$
A_{RMS}	equivalent root-mean-square	m
b	gear facewidth	m
b_{s}	coordinate along the gear facewidth	m
b_{avg}	effective gear facewidth for stiffness calculation	mm
b_{H}	half Hertz contact width	m
C	amount of tip/root relief	m

C_f	shear correction factor	-
$c_\mathrm{f}^{s,h}$	stiffness correction factor	-
d	reference diameter	m
$e(y)$	tooth chordal thickness at section y	m
$\overline{E}$	average relative difference	-
E_i	modulus of elasticity	Pa
$f(\boldsymbol{X})$	objective function	-
F	involute profile normal load	N
F^s	load applied on a slice	N
F_c	compressive load	N
F_bt	nominal transverse load in the plane fo action (base tangent plane)	N
G	transverse modulus of elasticity	Pa
$g_j(\boldsymbol{X})$	constraint functions for the gear design optimization problem	-
$H(X)$	Heaviside function	-
h	ratio between the tooth root radius and hub radius	-
H_t	total tooth depth	mm
$\bar{h}_\mathrm{i}$	distance along the line of action between the contact point and the tooth centerline	m
$h_j(\boldsymbol{X})$	constraint functions for the gear evaluation model	-
H_V	gear meshing loss factor	-
h_aP^*	addendum of basic rack profile normalized by the normal module	-
h_fP^*	dedendum of basic rack profile normalized by the normal module	-
I	mass moment of inertia (x and y axis)	$\mathrm{kg\,m^2}$
i	refering to a tooth pair, tooth pair i ($i \in \mathbb{Z}$)	-
I_s	second moment of area	$\mathrm{m^4}$
$\mathrm{inv}(X)$	involute function	-
J	mass moment of inertia (z axis)	$\mathrm{kg\,m^2}$
K	gear mesh stiffness	$\mathrm{N\,m^{-1}}$
k	stiffness	$\mathrm{N\,m^{-1}}$
k^l	linear stiffness	$\mathrm{N\,m^{-1}}$
K^M	gear mesh stiffness per unit of contact length	$\mathrm{N\,m^{-2}}$
K^p	gear mesh stiffness at the pitch point	$\mathrm{N\,m^{-1}}$
$k^{\mathrm{s},i}$	single tooth pair slice mesh stiffness	$\mathrm{N\,m^{-1}}$

k^{str}	tooth pair structural stiffness	-
k^{st}	single tooth stiffness	$\mathrm{N\,m^{-1}}$
K^{s}	slice gear mesh stiffness	$\mathrm{N\,m^{-1}}$
$k^{\mathrm{tp,s}}$	independent single tooth pair slice mesh stiffness	$\mathrm{N\,m^{-1}}$
k^{tp}	single tooth pair mesh stiffness	-
k^{t}	torsional stiffness	$\mathrm{N\,m\,rad^{-1}}$
k_0	average mesh stiffness per unit contact length	$\mathrm{N\,m^{-2}}$
k_{ad}	addendum shortening normalized by the normal module	-
K_{avg}	average gear mesh stiffness	$\mathrm{N\,m^{-1}}$
K_{A}	application factor	-
k_{a}	axial compressive stiffness of a single tooth	$\mathrm{N\,m^{-1}}$
k_{b}	bending stiffness of a single tooth	$\mathrm{N\,m^{-1}}$
k_{f}	fillet-foundation stiffness	$\mathrm{N\,m^{-1}}$
k_{H}	contact or Hertzian stiffness	$\mathrm{N\,m^{-1}}$
k_{L}	line stiffness distribution	-
$K_{\mathrm{max}}^{\mathrm{ISO}}$	maximum single tooth pair mesh stiffness from ISO	$\mathrm{N\,m^{-1}}$
$K_{\mathrm{max}}^{\mathrm{PEM}}$	maximum tooth pair structural stiffness from PEM	$\mathrm{N\,m^{-1}}$
$K_{\mathrm{max}}^{\mathrm{STR}}$	maximum tooth pair structural stiffness	$\mathrm{N\,m^{-1}}$
$K_{\mathrm{max}}^{\mathrm{tp}}$	maximum single tooth pair mesh stiffness	$\mathrm{N\,m^{-1}}$
K_{N}	time-varying mesh stiffness in the normal direction	$\mathrm{N\,m^{-1}}$
k_{s}	shear stiffness of a single tooth	$\mathrm{N\,m^{-1}}$
L	load	N
L^C	length of the tip/root relief normalized by the transverse base pitch	-
$L^{1\ \mathrm{m}}$	overall noise level	dB(A)
$L_{\mathrm{gm}}(\tau)$	time-varying gear contact length	m
M	bending moment	N m
m	mass	kg
m_{n}	normal module	m
m_{t}	transverse module	m
n	rotating speed	rpm
n^C	type of relief, linear ($n^C = 1$) or parabolic ($n^C = 2$)	-
p_{b}	circular base pitch	m
p_{bt}	transverse circular base pitch	m

P_{VZP}	gear power loss	W
$r(y)$	radius at section y	m
R	buttressing correction factor	-
R^K	ratio between the PEM and ISO* maximum tooth pair structural stiffness	-
R_{a}	average roughness value	µm
R_{z}	mean peak-to-valley roughness value	µm
r_{bi}	base radius of gear i	m
r_{C}	load point radius	m
r_{hub}	gear hub radius	m
r_{p}	tooth root radius	m
R_{X}	equivalent radius in the roling direction	m
s	tooth thickness at the pitch radius	m
S_{F}	tooth bending safety factor	-
S_{H}	surface durability safety factor	-
s_{p}	tooth root thickness	m
s^*_{ai}	tooth crest width normalized by the normal module	-
$\mathrm{Sinc}(X)$	sine cardinal function	-
T	applied torque	N m
t	meshing time of tooth pairs	s
t_{z}	meshing period time of tooth pairs	s
$\overline{\mathrm{TC}}$	curvature radius of the load point	m
$Tl^{s,h}$	trim function	-
U	energy	J
u	gear ratio	-
U_{a}	axial compressive energy	J
U_{b}	bending energy	J
u_{p}	distance along the tooth centerline measured from the tooth root to the loading tooth section	m
U_{s}	shear energy	J
U_{t}	total potential energy of a gear tooth	J
u_{t}	specific total tooth potential energy	$\mathrm{J\,N^{-2}}$
Ul_i^{∞}	normalized complementary contact line length	-
$Ul_i^{s,h}$	unbounded contact line length ratio	-

V	shear load	N
v	pitch line velocity	$\mathrm{m\,s^{-1}}$
W	transmitted power	kW
x	profile shift coefficient	-
$\boldsymbol{X}$	design variables	-
y	coordinate along the tooth centerline with origin at the gear rotation center	m
y_{C}	coordinate at load section	m
y_{p}	coordinate at tooth root section	m
y_{f}	fillet-foundation compliance	m
y_{H}	contact compliance	m
z	number of teeth	-
z_{v}	virtual number of teeth	-
A	theoretical start point of meshing	-
C	pitch point	-
DMF	dynamic mesh force	N
$\mathrm{DMF_{osc}}$	dynamic mesh force oscillating component	N
DTE	dynamic transmission error	m
$\mathrm{DTE_{osc}}$	dynamic transmission error oscillating component	m
E	theoretical end point of meshing	-
$\mathrm{RMS_D}$	average A_{RMS} of the $\mathrm{DTE_{osc}}$	m
$\mathrm{RMS_K}$	root-mean-square of the gear mesh stiffness fluctuation	$\mathrm{N\,m^{-1}}$
T	point of tangency at base circle	-

Superscripts

$\hat{}$	normalized stiffness component	-

Subscripts

g	wheel (for the degrees-of-freedom)	-
p	pinion (for the degrees-of-freedom)	-
1	pinion	-
2	wheel	-

Acronyms

CAD	Computer-Aided Design	-
EVs	Electric Vehicles	-

FE	Finite Element	-
FEA	Finite Element Analysis	-
FEM	Finite Element Method	-
FFT	Fast Fourier Transform	-
IOR	Integer Overlap Ratio	-
ISO	International Organization for Standardization	-
PEM	Potential Energy Method	-
PPA	Peak-to-Peak Amplitude	-
QSA	Quasi-Static Algorithm	-
QSTE	Quasi-Static Transmission Error	-
RMS	Root-Mean-Square	-
TE	Transmission Error	-

Chapter 1

Introduction

1.1. Background and motivation

Evolution is inevitable and part of it is overcoming problems by looking at them as opportunities for innovation. Drive technology is facing drastic changes due to the current global challenges such as descarbonization, circular economy and green pressure, representing opportunities for the fields of energy generation and mobility [1]. This era of sustainability means, for mobility, that powertrains will be subjected to changes due to the different sources of energy [2]. Moreover, there are renewable energy targets for the reduction of greenhouse gas emissions that must be met, revealing the necessity of increasing the capacity for renewable energies, with great focus on wind energy [3].

Focusing on tribological contacts, and according to Holmberg and Erdemir [4], these stand for around 23% of the world's total energy consumption. It is also stated that transportation and power generation sectors are expected to have the largest short term energy savings [4]. This shows how influential tribology is and will be in future times because of how it aligns with the discussed needs. Gears, as the main tribological element used to transmit motion and power, will play a prominent role in energy generation and mobility trends. It is up to gear engineers to step up and turn into value all their knowledge in order to find the required gear designs. Given the energy concerns, improvements in gear efficiency are of significant contribution. On another perspective, investigation on gear manufacturing can originate more ecological processes with higher productivity while repairing methods can extend the gears' lifespan. Noise, vibration and harshness are three key parameters for gear transmissions which besides affecting their performance and reliability also have their share on health and comfort [5–7].

Gears, as sources of failure, noise and vibration of gear transmission systems, need to have their behavior improved and modified to tackle their flaws and adjust it to desired requisites. In order to do so, it is necessary to characterize them and, therefore, gear modeling becomes of the utmost importance. Within gear modeling, gear mesh stiffness takes a critical function. Gear mesh stiffness modeling allows for the estimation of the load sharing ratio and transmission error which can be associated with gear meshing efficiency and its performance, affecting noise, vibration and durability. Due to the broad information that can be extracted from the gear mesh stiffness, it has applicability in several gear research topics such as design, optimization, dynamics and reliability. Consequently, as long as gears need to be adapted to the world's evolution, gear mesh stiffness is not going to leave their side.

1.2. Objective and research approach

This work takes on gear mesh stiffness modeling as the central topic of research given its importance and wide applicability in gear engineering. The purpose of this investigation is to develop a low computational cost gear mesh stiffness model to explore gear design solutions so that gears can keep up with current and upcoming needs. A low computational cost approach is taken as it allows for multiple and consecutive calculations to be performed in feasible time which is essential when it is necessary to explore different gear design solutions. The steps taken to fulfill this objective and prove its applicability are:

- look at the current state of gear mesh stiffness models by performing an extensive literature review on the different modeling approaches. Then, considering the intended outcome, the most suitable type gear mesh stiffness model is selected;
- develop the gear mesh stiffness model considering the main shortcomings of existing models as well as including the indispensable phenomena for an accurate gear mesh stiffness estimation. With the successful development of the gear mesh stiffness model, an extensive range of possibilities opens up;
- implement a gear-shaft-bearing dynamic model and perform large-scale parametric studies at both quasi-static and dynamic levels;
- perform numerical testing of a previously developed gear design concept (integer overlap ratio helical gears [8]) by evaluating how the modification of the overlap ratio influences the gear mesh stiffness, dynamic behavior and emitted noise level. Part of having a fast and accurate gear mesh stiffness model and an implementation of a dynamic model is being capable of performing numerical studies prior to experimental tests. Thus, giving an estimation of the expected behavior and allowing for the selection of the most appropriate equipment;
- study gear optimization approaches to find a dynamically optimized design in a straightforward manner, without computational demanding procedures.

The outcome of this work is a tool capable of exploring and studying gear transmissions for current and unforeseen issues. Whatever the problems/opportunities that arise, the developed gear mesh stiffness model and its unfolding gear analysis models will be useful.

1.3. Scientific contributions

The scientific publications originated from the work performed during the *philosophiae doctor* are presented in two sets. The first set is for papers that are reproduced in this document: contents are reproduced with permission of their respective publishers.

Paper A. João D.M. Marafona, Pedro M.T. Marques, Ramiro C. Martins, and Jorge H.O. Seabra. Mesh stiffness models for cylindrical gears: A detailed review. *Mechanism and Machine Theory*, 166:104472, 2021.

Paper B. João D.M. Marafona, Pedro M.T. Marques, Ramiro C. Martins, and Jorge H.O. Seabra. Approximate expression for the single tooth pair slice mesh stiffness. *Mechanism and Machine Theory*, 187:105367, 2023.

Paper C. João D.M. Marafona, Pedro M.T. Marques, Stephane Portron, Ramiro C. Martins, and Jorge H.O. Seabra. Gear mesh stiffness and dynamics: Influence of tooth pair structural stiffness asymmetry. *Mechanism and Machine Theory*, 190:105447, 2023.

Paper D. João D.M. Marafona, Pedro M.T. Marques, Ramiro C. Martins, and Jorge H.O. Seabra. Effect of overlap ratio on gear dynamic behavior and noise level. In VDI Wissensforum GmbH, editor, *International Conference on Gears 2023*, volume 2422 of *VDI-Berichte*. VDI Verlag, Düsseldorf, 2023. doi: doi.org/10.51202/9783181024225.

Paper E. João D.M. Marafona, Gonçalo N. Carneiro, Pedro M.T. Marques, Ramiro C. Martins, Carlos C. António, and Jorge H.O. Seabra. Gear design optimization: stiffness *versus* dynamics. *Mechanism and Machine Theory*, 191:105503, 2024.

Investigations/collaborations conducted during the *philosophiae doctor* resulted in further manuscripts/presentations/posters (second set) that are published or under review on scientific journals or conference proceedings.

1. Pedro M.T. Marques, João D.M. Marafona, and Jorge H.O. Seabra. Crowned Spur Gears for Constant Mesh Stiffness: A Conceptual Approach. *Mechanism and Machine Theory*, 189:105426, 2023.

2. Pedro M.T. Marques, João D.M. Marafona, Ramiro C. Martins, and Jorge H.O. Seabra. A continuous analytical solution for the load sharing and friction torque of involute spur and helical gears considering a non-uniform line stiffness and line load. *Mechanism and Machine Theory*, 161:104320, 2021.

3. João D.M. Marafona, Pedro M.T. Marques, Ramiro C. Martins, and Jorge H.O. Seabra. Influence of single tooth mesh stiffness asymmetry on gear mesh stiffness and dynamic response. *2nd Portuguese Conference on Multibody System Dynamics*, 2022. ISBN: 978-989-33-4087-5.

4. João D.M. Marafona, Pedro M.T. Marques, Ramiro C. Martins, and Jorge H.O. Seabra. Gear Mesh Stiffness: Comparative review and modeling. *5th Meeting of the Young Researchers of LAETA: Book of Abstracts*, 2022.

5. João D.M. Marafona, Pedro M.T. Marques, Ramiro C. Martins, and Jorge H.O. Seabra. A Look into Gear Mesh Stiffness. *Porto-Lyon Seminar 2021: Book of Abstracts*, 2022. DOI: 10.24840/978-972-752-293-4.

6. João D.M. Marafona, Pedro M.T. Marques, Ramiro C. Martins, and Jorge H.O. Seabra. The Shooting Method: Discontinuous Stiffness Systems. *Symposium on Mechanical Engineering: Book of Abstracts and Invited Lectures*, 2021. ISBN: 978-972-752-286-6.

7. João D.M. Marafona, Pedro M.T. Marques, Ramiro C. Martins, and Jorge H.O. Seabra. Analysis of the dynamic loads on integer overlap ratio helical gears. *Doctoral Congress in Engineering 2019*, Porto, Portugal, june 2019. ISBN-13: 978-972-752-252-1.

1.4. Outline

The document comprises seven chapters, being each one briefly described as follows.

Chapter 1: Introduction - contextualization of the *philosophiae doctor* research while also providing insight on its organization and presented contents.

Chapter 2 (Paper A): Mesh stiffness models - review on the different types of gear mesh stiffness models including implementation guidelines and comparative discussion.

Chapter 3 (Paper B): Single tooth pair slice mesh stiffness - development of an approximate expression for the single tooth pair slice mesh stiffness; necessary component for improved accuracy in gear mesh stiffness modeling.

Chapter 4 (Paper C): Gear modeling - presentation of the developed approximate gear mesh stiffness model and of the implemented gear-shaft-bearing dynamic model; large-scale gear exploratory study on the influence of a stiffness modeling parameter on gear quasi-static and dynamic behaviors.

Chapter 5 (Paper D): Integer overlap ratio gears: preliminary study - design of integer overlap ratio gears and research on how overlap ratio affects their gear mesh stiffness, dynamic response and noise level.

Chapter 6 (Paper E): Gear design optimization - optimization study to compare the design of gears with two approaches, gear mesh stiffness and dynamic behavior.

Chapter 7: Conclusion - highlight of relevant topics and main conclusions of this work; suggestions for future research.

Chapter 2

Mesh stiffness models

Gear transmissions have always been a subject of study for many different reasons which change due to the constant evolution of technology. Consequently, new topics must be addressed and different ways to solve the upcoming problems must be discovered. Gear mesh stiffness is a central topic for both gear design and gear dynamic modeling due to its ability to represent the gears' behavior, making it a subject of high interest in the field of gear transmissions. Different types of models are used to establish the gear mesh stiffness, namely, analytical, finite element, hybrid and approximate analytical models. In this chapter, implementation guidelines for each class of model are presented along with relevant literature, providing a broad range of information in great detail. Lastly, the main conclusions for each type of model are discussed and an overview of the future evolution of gear mesh stiffness is given.

2.1. A look into mesh stiffness

Gears, the most common machine element used to transmit motion and power, are constantly adapting to today's requirements. Whatever the shifts in demands that are awaiting, gears will prevail and find their way. The mesh stiffness of gears characterizes their behavior, which is crucial for their development. Whether the topic is design, optimization, dynamics or noise, the gear mesh stiffness plays one of the leading roles. So, in order for gears to keep adjusting throughout time, a proper definition of the gear mesh stiffness must exist.

Gear mesh stiffness is a central topic of research since it is the core element of a gear pair. In dynamics, it is the main responsible for the noise, vibration and dynamic loads, thus, the usage of an appropriate gear mesh stiffness representation largely affects the results of dynamic models [9–20]. In the design stage or for optimization purposes, gear mesh stiffness can be utilized as a tool to establish both the macro- and micro-geometry while considering the dynamic performance of gears due to its clear dynamic influence [8; 21–23].

Stiffness is the resistance of a body to the deflection induced by an applied load. In its simplest form (linear single degree of freedom system such as a spring), stiffness (k) is defined as the ratio of an applied load (L) over the corresponding generated displacement (χ), equation (2.1).

Contents in Chapter 2: Mesh stiffness models are reproduced with permission of the respective publisher from João D.M. Marafona, Pedro M.T. Marques, Ramiro C. Martins, and Jorge H.O. Seabra. Mesh stiffness models for cylindrical gears: A detailed review. *Mechanism and Machine Theory*, 166:104472, 2021.

$$k = \frac{L}{\chi} \tag{2.1}$$

For a linear system with n degrees of freedom, the stiffness is defined by a $n \times n$ matrix. Each element of the matrix (k_{ij}) is obtained according to equation (2.2), this is, the coefficient between the load applied in the degree of freedom i and the displacement produced by that load in the degree of freedom j.

$$k_{ij} = \frac{L_i}{\chi_j} \tag{2.2}$$

When the issue is the gear mesh stiffness, a similar description is usually applied, so the gear mesh stiffness represents the load on the gear mesh required for a given displacement. The deformations occurring during the loading process of a gear tooth are described by Attia [24], enlightening the complexity and multiple phenomena affecting the gear mesh stiffness. According to Attia [24], first the Hertzian deformation takes place at the contact point on the profile. Then, the load is transmitted to the tooth's body which causes bending, shear and compression deformations. The combination of these deformations at every cross-section defines their magnitude and direction. The load then reaches the tooth root and is also transferred to its adjacent parts. Finally, the load gets to the gear body and, if it is strained, there can be angular tooth deformation with respect to the gear center [24].

When discussing the stiffness of gears, it is important to leave a note on the transmission error (TE). Transmission error represents the difference between the perfect position (unmodified, geometrically perfect and infinitely rigid gears) and the actual position of a gear, in other words, it is the relative displacement of the output gear with respect to the input gear - mathematically expressed in its angular form by equation (2.3).

$$\delta_\theta = \theta_2 - \frac{r_{\mathrm{b}1}}{r_{\mathrm{b}2}}\theta_1 \tag{2.3}$$

where θ_i is the rotational angle of gear i and $r_{\mathrm{b}i}$ is the base radius of gear i. Notice that the transmission error is negative when the output gear (gear 2) lags behind its conjugate position. The transmission error in equation (2.3) can be modified to its linear form by multiplying it by $r_{\mathrm{b}2}$, becoming a displacement along the line of action.

Depending on the working conditions of the gear pair, two types of transmission error are commonly established, the static transmission error and the dynamic transmission error. The transmission error can be related to the gear mesh stiffness since it can be viewed as the displacement caused by an applied load, which, in this scenario, is referred to as static or loaded-static transmission error.

Gear mesh stiffness can be evaluated by means of torsional stiffness or linear stiffness, which can be related to each other. The torsional mesh stiffness, defined in equation (2.4), is given by the ratio of the applied torque (T) and the transmission error. Notice that the concept of stiffness is related to the elastic deflections and, therefore, the no-load transmission error (associated to the manufacturing errors) should, by definition, be removed from the transmission error when calculating the gear mesh stiffness since it does not translate as elastic deflections but as rigid-body displacement. Although, contributions of the no-load transmission error should not be disregarded when modeling a gear pair as they can remarkably modify its behavior.

$$k^{\mathrm{t}} = \frac{T}{\delta_\theta} \tag{2.4}$$

The linear mesh stiffness, established in equation (2.5), is the ratio of the applied load (L) and the displacement (δ) in the load's direction, usually along the line of action. In this situation δ is the linear transmission error.

$$k^{\mathrm{l}} = \frac{L}{\delta} \tag{2.5}$$

Either way, the relation between torsional and linear gear mesh stiffness is established according to equation (2.6).

$$k^{\mathrm{t}} = \frac{T_2}{\delta_\theta} = \frac{L\, r_{\mathrm{b}2}}{\delta_\theta} = \frac{L\, r_{\mathrm{b}2}^2}{\delta_\theta\, r_{\mathrm{b}2}} = \frac{L\, r_{\mathrm{b}2}^2}{\delta} = k^{\mathrm{l}}\, r_{\mathrm{b}2}^2 \tag{2.6}$$

The determination of stiffness requires an exact description of the load and displacement [25], which makes the computation of gear mesh stiffness a complex task. The complexity of the gear mesh stiffness arises from the many variables that affect the gear geometry and the contact conditions that change the description of the load and displacement.

The gear mesh stiffness can be obtained numerically or experimentally, although, experimental methods are mostly used for empirical studies, validation of numerical models or as monitoring techniques. So, experimental methods are not addressed in this chapter since the main concern is the gear mesh stiffness modeling. Regardless, some investigations on the measurement of stiffness and transmission error in gears are presented. For instance, [26–34] perform experimental measurements of the transmission error and [35–41] measure the stiffness of a single tooth, teeth pairs and of damaged teeth. Encoder error on the measurement of gear transmission error is studied in [42] and different methods for the measurement of angular speed and gear transmission error are reviewed and discussed in [43] and [44], respectively.

The literature research conducted on numerical methods for gear mesh stiffness modeling divided the different models into four classes: analytical, finite element, hybrid and approximate analytical. In short, every model resorts to different techniques to describe the gear mesh stiffness: analytical models use analytical expressions; finite element models employ the finite element method; hybrid models apply both analytical expressions and the finite element method and the approximate analytical models make use of simple and computational inexpensive approximate analytical expressions. All of the mentioned models have their advantages/disadvantages and are usually developed with a specific purpose, which may vary, for example, from the study of gear dynamics, profile modifications, teeth deflections, cracked teeth and the effects of gear geometrical parameters/errors on the mesh stiffness.

Early gear investigations were not directly concerned with gear mesh stiffness but rather with the strength of gear teeth. The question to answer was: "What is the breaking load of gear teeth?". Lewis' bending strength equations [45] answered that question and unified the around forty-eight "rules" for calculating the bending strength in existence at that time. None of those rules took into account the actual tooth form (unlike Lewis' equations) and they could present differences up to 500%. The Lewis' formula is based on the fact that a parabola enclosed on the gear tooth defines a beam of uniform strength. Later, it was found by empirical evidence (photoelastic technique) that Lewis' equations were wrong, as expected since it violated the

Saint Venant's principle, as stated by Wellauer and Seireg [46]. Many authors then improved Lewis' equations to be in agreement with the results from the photoelastic technique while others developed completely new approaches [46]. The works of Baud and Peterson [47] and Walker et al. [48] both presented equations for the gear teeth deflections. However, to deduce those formulae, Baud and Peterson [47] considered the tooth as a non-uniform cantilever beam while Walker et al. [48] resorted to experimental measurements taken on a fixed single tooth.

Constantin Weber and Kurt Banaschek [49; 50] presented a series of studies on the deflection of gears where it is established that the total deformation of meshing gear pairs emerges from three sources: tooth bending, gear body deformation and Hertzian contact. The developed expressions became a reference for the calculation of gear deflections and the foundation for future investigations which are currently employed in several different types of models [49; 50]. The works of Timoshenko and Goodier [51] and Timoshenko and Woinowsky-Krieger [52] give essential information of the theory of elasticity and the theory of plates and shells. These books [51; 52] present solutions to engineering problems of practical importance which are the basis for many engineering investigation, where gears are no exception.

The modeling of a gear tooth as a cantilever plate was first accomplished, according to [46], by C. W. MacGregor in 1935 [53] where the deflections and moments on a thin plate with infinite length under a concentrated load on the free edge were calculated. The investigations of Holl [54] and Jaramillo [55] on cantilever plates were fundamental for the development of many other studies including the semiempirical solution presented by Wellauer and Seireg [46]. This semiempirical solution relies on the superposition principle and the moment-image method (developed procedure) to obtain the bending moment distribution on a finite cantilever-plate under any transverse loads. The results were in agreement with experimental tests conducted on thin plates and tooth-shaped thick plates [46]. Attia [24] investigated the deflections of gear teeth with thin rims resorting to strain-energy theories. The gear teeth deflection accounted for the bending, shear and compression deformations of the gear tooth and adjacent part of the gear body, circumferential deformations of the gear body as well as the impact of deflections in the neighboring teeth [24]. Umezawa et al. [56] obtained a numerical solution by the finite difference method for the deflections due to a concentrated load of a finite length cantilever thick plate. New boundary conditions were applied which produced results in consonance with experimental deflections on a cantilever thick plate [56]. Then, Umezawa [57] expanded the previous work ([56]) for a rack-shaped cantilever plate with finite width, meaning that the deflections and moments were determined for a variable thickness cantilever plate under transverse loads applied at any location on the surface [57]. Seager [58] developed a set of equations describing the loading and deflections of a pair of involute helical gear teeth with the purpose of analyzing the static/quasi-static behavior of gear pairs and selecting the most adequate profile modifications. This work [58], based on Seager's dissertation, discusses several topics such as convective effects, separation distance, contact stiffness, profile modification and load distribution [58].

Terauchi and Nagamura [59] used two dimensional elastic theory and conformal mapping functions to determine the tooth deflections. The normal tooth load is approximated by a set of concentrated loads and the mapping functions are used to establish the tooth profile to finally reach the tooth deflections. The method was compared with well-known tooth deflection formulas to prove its validity. A discussion on the Hertzian contact deformation is also presented [59]. In a subsequent work Terauchi and Nagamura [60] employed the previously developed calculation method ([59]) to compute the deflections of several spur gear teeth. From these results simple and approximate expressions for the tooth deflections and contact Hertzian deformations were proposed [60]. Cardou and Tordion [61] seek the solution to the two difficulties found when calculating the gear tooth flexibility by the complex potential method: (i) the indeterminacy of the displacements

and (ii) the singularity at the point of interest (teeth contact point). While the first problem was solved by selecting a proper reference point for the calculations, the second was dealt with by calculating the displacements at a certain depth under the surface. Flexibility curves were compared with other works and found to be in agreement [61]. Steward [62; 63] presents a 3D elastic model for the meshing of spur gears. A 3D finite element analysis was applied to establish the influence coefficients that allow to determine the tooth centerline deflections curves for different tooth geometries. Concerning the contact compliance, it is included by 2D Hertzian contact theory with semiempirical correction coefficients for the regions close to the tooth tip. Deflections results agreed with experimental measurements [62; 63]. Yau et al. [64] use the Rayleigh-Ritz energy method to compute the deflections of tapered plates under concentrated loads, which are implemented to simulate gear teeth. When comparing the determined deflections with theoretical and experimental results, the differences found were assigned to the neglected shear deformations in the theoretical models and base distortion in the experimental tooth models [64].

Stegemiller and Houser [65] developed a model to determine the base deflections of wide facewidth gear teeth. This model is based on several finite element analysis and applies the moment image method presented in [46]. The base rotations and translations obtained with the model are in agreement with the acquired finite element results [65]. Kim et al. [66] adopted the finite prism method to calculate the load sharing, pressure distribution, mesh stiffness and tooth fillet stresses on webbed spur gears. The conducted analysis allowed the development of simple formula that can estimate with reliability the tooth root stress accounting for the effects of thin rims and webs [66]. Litvin et al. [67] resorted to the finite element method and tooth contact analysis to consider a distributed contact force in the calculation of transmission error, loaded tooth deflections, load sharing ratio, real contact ratio and tooth bending stress [67]. Guilbault et al. [68] integrate the finite strip method with a pseudo 3D model of the tooth base to compute the tooth bending stiffness and fillet stresses. The procedure is intended to be a fast and precise gear design tool. These facts were proved by the acceptable precision of the results and the reduced time required in processing the model when compared to 3D finite element analysis [68].

Smith [69] presented a comprehensive explanation and analysis to the design, development, metrology and troubleshooting of noise and vibration of gear. Among the several elucidated topics it stands out the transmission error measurement and modeling of spur and helical gears, including the thin slice assumption, as well as practical guidelines for a complete setup of experimental procedures [69]. Linke et al. [70] conduct a complete analysis to cylindrical gears covering every gear topic from the fundamental principles of gearing to the manufacturing. The load capacity and running performance of gears is thoroughly presented, incorporating the meshing characteristics and stiffness description/modeling [70].

The aforementioned investigations shed light on the developments of gear stiffness related studies throughout time. Some non-gear researches are mentioned due to their contributions in the development of gear investigations. The contents presented in those works contain useful information for any gear study as they explain gear phenomena in a direct and clear way. Besides that, a lot of experimental results are also shown. All the classes of gear mesh stiffness models currently employed can be found is these investigations.

This review is divided into seven sections, beginning with an introduction that defines the gear mesh stiffness, highlights its importance and presents some of the first developments on the deflections, stress and load sharing of gears. Then, a specific section for each class of gear mesh stiffness model is presented where not only the existing works are analyzed but also a description of the models' implementation procedures is performed. That being said, analytical models are

the first ones to be studied (Section 2.2) with emphasis to the potential energy method (complete description on how to obtain the gear mesh stiffness for spur gears) followed by the literature review. Section 2.3 is dedicated to the finite element models where guidelines for the key aspects are given together with the presentation of some works. The next section explores hybrid models (Section 2.4) and the approximate analytical models are detailed in Section 2.5. Section 2.6 analysis polymer gears and describes works related to their mesh stiffness. Throughout these sections there are discussions focusing critical aspects of the models. This chapter ends with an analysis of the different models studied, stating their advantages, disadvantages and purposes, as well as an overview of the gear mesh stiffness trends.

2.2. Analytical models

Analytical models express the gear mesh stiffness through the usage of analytical expressions acquired from mechanics of materials. The most common analytical method found in the literature is the potential energy method (PEM). There are also some references to the Ishikawa method, which is very similar to the potential energy method but the gear teeth are simplified as the combination of a rectangle and a trapezoid [71]. For these reasons, the potential energy method is going to be described.

2.2.1. Potential energy method

In the potential energy method, the gear tooth is modeled as a nonuniform cantilever beam fixed at the root (dedendum) circle. The total potential energy of a gear tooth (U_t) due to the external work done in deforming it can be divided into bending energy (U_b), shear energy (U_s) and axial compressive energy (U_a), as shown in equation (2.7). Equations (2.8) to (2.10) define the strain energy of the individual components [72]. The coordinate y is given by the axis defined along the tooth centerline with origin at the gear rotation center, as it can be seen in Figure 2.1.

$$U_\mathrm{t} = U_\mathrm{b} + U_\mathrm{s} + U_\mathrm{a} \tag{2.7}$$

$$U_\mathrm{b} = \int \frac{M^2}{2EI_\mathrm{s}}\,\mathrm{d}y \tag{2.8}$$

$$U_\mathrm{s} = \int \frac{C_\mathrm{f}V^2}{2A_\mathrm{c}G}\,\mathrm{d}y \tag{2.9}$$

$$U_\mathrm{a} = \int \frac{F_\mathrm{c}^2}{2A_\mathrm{c}E}\,\mathrm{d}y \tag{2.10}$$

In equations (2.8) to (2.10), M is the bending moment, E is the modulus of elasticity of the material, I_s is the second moment of area of the cross-section, C_f is the shear correction factor ($C_\mathrm{f} = 1.2$ for rectangular cross-section), V is the shear load, A_c is the area of the cross-section, G is the transverse modulus of elasticity of the material and F_c is the compressive load [72].

Considering the geometrical parameters of the involute tooth as described by Figure 2.1, the previously mentioned parameters can be defined from equations (2.11) to (2.15). The work of Pedrero et al. [73] is taken as a reference in the following description.

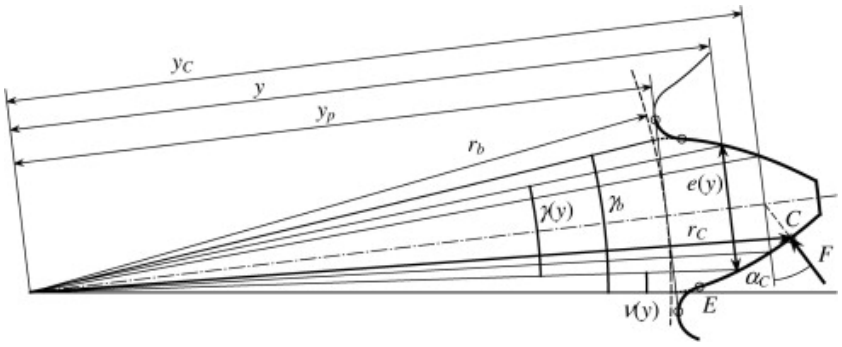

Figure 2.1: Geometrical parameters of involute tooth. Reprinted from [73].

$$M = F\cos(\alpha_{\mathrm{C}})(y_{\mathrm{C}} - y) \tag{2.11}$$

$$I_{\mathrm{s}} = \frac{b\, e^3(y)}{12} \tag{2.12}$$

$$V = F\cos(\alpha_{\mathrm{C}}) \tag{2.13}$$

$$A_{\mathrm{c}} = b\, e(y) \tag{2.14}$$

$$F_{\mathrm{c}} = F\sin(\alpha_{\mathrm{C}}) \tag{2.15}$$

where F is the involute profile normal load, α_{C} is the load angle, b is the facewidth, $e(y)$ is the tooth chordal thickness at section y and y_{C} is the coordinate of the load section.

Replacing the terms defined in equations (2.11) to (2.15) into equations (2.8) to (2.10), equations (2.16) to (2.18) are obtained.

$$U_{\mathrm{b}} = 6\frac{F^2\cos^2(\alpha_{\mathrm{C}})}{Eb}\int_{y_{\mathrm{p}}}^{y_{\mathrm{C}}} \frac{(y_{\mathrm{C}} - y)^2}{e^3(y)}\,\mathrm{d}y \tag{2.16}$$

$$U_{\mathrm{s}} = 0.6\frac{F^2\cos^2(\alpha_{\mathrm{C}})}{Gb}\int_{y_{\mathrm{p}}}^{y_{\mathrm{C}}} \frac{\mathrm{d}y}{e(y)} \tag{2.17}$$

$$U_{\mathrm{a}} = \frac{F^2\sin^2(\alpha_{\mathrm{C}})}{2Eb}\int_{y_{\mathrm{p}}}^{y_{\mathrm{C}}} \frac{\mathrm{d}y}{e(y)} \tag{2.18}$$

The integration limits, y_{p} and y_{C}, are the values of y corresponding to the fixed boundary of the tooth and the load section. The fixed boundary is given by the chordal tooth root line while the load section is defined by the intersection of the line of action and the tooth centerline. Attend on Figure 2.1 for a visual interpretation of the previous geometrical parameters.

The next step consists on defining the geometrical parameters as a function of the load point.

For that purpose, a normalized coordinate (ξ_C), which is the ratio between the curvature radius at the load point C ($\overline{TC}$) and the circular base pitch (p_b), is defined in equation (2.19).

$$\xi_C = \frac{\overline{TC}}{p_b} = \frac{\sqrt{r_C^2 - r_b^2}}{m_n \pi \cos(\alpha)} \tag{2.19}$$

The parameters/coordinates that remain undefined are the load angle (α_C), radius of the load point (r_C), tooth chordal thickness ($e(y)$) and the integration limits (y_p and y_C) which are all established in equations (2.20) to (2.27).

First, the load angle is defined by equations (2.20) to (2.22).

$$\alpha_C = \alpha_T - 0.5\gamma_C \tag{2.20}$$

$$\alpha_T = \arccos\left(\frac{r_b}{r_C}\right) \tag{2.21}$$

$$\gamma_C = 2\left(\frac{s}{d} + \text{inv}(\alpha_t) - \text{inv}(\alpha_T)\right) \tag{2.22}$$

where s is the tooth thickness at the pitch radius, d is the pitch diameter, inv is the involute of an angle and α_t is the transverse pressure angle. After some mathematical work on equation (2.20), the load angle can be written as a function of the coordinate ξ_C, as presented in equation (2.23).

$$\alpha_C = \frac{2\pi}{z}\xi_C - \frac{\pi}{2z} - \frac{2x\tan(\alpha)}{z} - \text{inv}(\alpha_t) \tag{2.23}$$

In equation (2.23) x is the profile shift coefficient.

The tooth chordal thickness $e(y)$ is presented on equation (2.24) as a function of the angular thickness of the tooth ($\gamma(y)$, defined on equation (2.25)).

$$e(y) = 2r(y)\sin\left(\frac{\gamma(y)}{2}\right) \tag{2.24}$$

$$\gamma(y) = \gamma_b - 2\nu(y) \tag{2.25}$$

$\nu(y)$ is the polar angle of the profile which is measured from the radius of the involute start point at the base circle, see Figure 2.1. This angle is defined for both the involute profile and the root trochoid in [74].

Finally, the integration limits y_p and y_C are defined in equations (2.26) and (2.27), respectively.

$$y_p = r_p\cos(\gamma_p) \tag{2.26}$$

$$y_C = \frac{r_b}{\cos(\alpha_C)} \tag{2.27}$$

where γ_p is the angular thickness of the tooth at the root radius.

Considering that the load-deflection relationship is linear, the strain energy relates with the stiffness according to equation (2.28) [72].

$$U = \frac{L^2}{2k} \tag{2.28}$$

U is the total potential energy of the system, which in this scenario is the single tooth total potential energy, L is the total load applied in the system, meaning it is the involute profile normal load (F) and k is the system's stiffness (single tooth stiffness).

Equation (2.29) defines the total potential energy for a single tooth, U_t. Also, to easily work the expression, $F^2/2$ is taken out of each term, highlighting the specific total tooth potential energy - u_t.

$$U_t = U_b + U_s + U_a = \frac{F^2}{2} u_t \tag{2.29}$$

Substituting equation (2.29) into equation (2.28), the single tooth stiffness can be written in order to the specific total potential energy, see equation (2.30).

$$k^{st} = \frac{1}{u_t} \tag{2.30}$$

At this point, the stiffness of a single tooth is obtained. However, the entire system is not made of a single tooth. The gear mesh stiffness includes at least one pair of teeth, meaning that the contact stiffness must be taken into account. Moreover, the contribution of the gear body to the tooth deflections must not be disregarded, so the fillet-foundation stiffness must be included.

Concerning the contact stiffness, three main approaches were found to calculate the contact compliance (y_H) [75]: (1) an approximate Hertzian and compression approach originally used at Hamilton Standard [75]; (2) a semi-empirical approach developed by Palmgren [76] and (3) a closed form approach developed by Weber [49]. The approaches are presented as follows [75].

(1) Approximate Hertzian and compression approach originally used at Hamilton Standard [75]:

$$y_H \approx \frac{4F}{\pi b}\left[\left(\frac{1-\nu_1^2}{E_1}\right)+\left(\frac{1-\nu_2^2}{E_2}\right)\right]\left[1+\frac{\pi}{4}\right] \tag{2.31}$$

(2) Semi-empirical approach developed by Palmgren [76]:

$$y_H = \frac{1.275F^{0.9}}{E_{12}^{0.9}b^{0.8}} = \frac{4\left(1-\nu^2\right)F}{\pi E_{12} b}\left\{1.10\frac{b^2E_{12}}{F}\right\}^{0.1} \tag{2.32}$$

where $E_{12} = \frac{1}{2}\left(\frac{1}{E_1}+\frac{1}{E_2}\right)$.

(3) Closed form approach developed by Weber [49]:

$$y_{\mathrm{H}} = \frac{2F}{\pi b}\left[\left(\frac{1-\nu_1^2}{E_1}\right)\left\{\ln\frac{2\bar{h}_1}{b_{\mathrm{H}}} - \left(\frac{\nu_1}{2\left(1-\nu_1\right)}\right)\right\} + \left(\frac{1-\nu_2^2}{E_2}\right)\left\{\ln\frac{2\bar{h}_2}{b_{\mathrm{H}}} - \left(\frac{\nu_2}{2\left(1-\nu_2\right)}\right)\right\}\right] \tag{2.33}$$

$$b_{\mathrm{H}} = \left\{\frac{4F}{\pi b}\left[\left(\frac{1-\nu_1^2}{E_1}\right) + \left(\frac{1-\nu_2^2}{E_2}\right)\right] \Big/ \left[\frac{1}{R_{\mathrm{X1}}} + \frac{1}{R_{\mathrm{X2}}}\right]\right\}^{1/2} \tag{2.34}$$

where b_{H}, given in equation (2.34), is the half Hertz contact width, $\bar{h}_1$ and $\bar{h}_2$ are the distances on the pinion and on the wheel between the point of contact and the tooth centerline along the line of action and R_{X1} and R_{X2} are the curvature radii of the pinion and wheel, respectively.

The Hertzian contact stiffness can then be obtained through the Hertzian compliance according to the relationship presented in equation (2.35).

$$k_{\mathrm{H}} = \frac{F}{y_{\mathrm{H}}} \tag{2.35}$$

Still on the topic of gear contact stiffness, Sainsot and Velex [77] perform an in-depth analysis to several gear teeth contact deflection formulae in the literature, including the ones shown from equations (2.31) to (2.34). The comparison study revealed that some of the gear teeth contact expressions applied in mesh stiffness models are not adequate for such purpose. An expression for gear teeth contact deflections/stiffness, which corroborated with finite element simulations, is developed and presented by Sainsot and Velex [77], equation (2.36).

$$y_{\mathrm{H}} = \left[\ln\left(\left(1+\sqrt{1+\frac{1}{\overline{k}^2}}\right)\overline{k}\right) - \frac{0.429}{1+\sqrt{1+\frac{1}{\overline{k}^2}}}\right]\left[\frac{b_{\mathrm{H}}^2}{4}\left(\frac{1}{R_{\mathrm{X1}}}+\frac{1}{R_{\mathrm{X2}}}\right)\right] \tag{2.36}$$

where $\overline{k}$ is a datum depth in the normal direction normalized by the half Hertz contact [77].

The most common fillet-foundation compliance analysis is the one developed by Sainsot et al. [78] based on the theory of Muskhelishvili applied for circular elastic rings. The expression for the fillet-foundation compliance, equation (2.37), depends only on $h = r_{\mathrm{p}}/r_{\mathrm{hub}}$ and θ_{p}, which are the ratio between the tooth root radius and the hub radius and the angle between the tooth centerline and the junction with the root circle, respectively [78].

$$y_{\mathrm{f}} = \frac{F\cos^2\alpha_{\mathrm{C}}}{Eb}\left\{L^*\left(\frac{u_{\mathrm{p}}}{s_{\mathrm{p}}}\right)^2 + M^*\left(\frac{u_{\mathrm{p}}}{s_{\mathrm{p}}}\right) + P^*\left(1+Q^*\tan^2\alpha_{\mathrm{C}}\right)\right\} \tag{2.37}$$

with

L^*, M^*, P^* and Q^*: functions which depend on h and θ_{p};

α_{C}: load angle;

u_p: distance along the tooth centerline measured from the tooth root to the loading tooth section;

s_p: tooth root thickness.

Under the assumption of plain strain conditions, the functions L^*, M^*, P^* and Q^* were fitted to polynomial functions for a realistic range of h and θ_p, leading to equation (2.38) [78].

$$X_i\left(h,\theta_\mathrm{p}\right) = A_i/\theta_\mathrm{p}^2 + B_i h^2 + C_i h/\theta_\mathrm{p} + D_i/\theta_\mathrm{p} + E_i h + F_i \tag{2.38}$$

the coefficients A_i, B_i, C_i, D_i, E_i and F_i are shown in Table 2.1.

Table 2.1: Coefficients of the polynomial curve fitting. Reprinted from [78].

	$\boldsymbol{A_i \times 10^5}$	$\boldsymbol{B_i \times 10^3}$	$\boldsymbol{C_i \times 10^4}$	$\boldsymbol{D_i \times 10^3}$	$\boldsymbol{E_i}$	$\boldsymbol{F_i}$
$L^*\left(h,\theta_\mathrm{p}\right)$	−5.574	−1.9986	−2.3015	4.7702	0.0271	6.8045
$M^*\left(h,\theta_\mathrm{p}\right)$	60.111	28.100	−83.431	−9.9256	0.1624	0.9086
$P^*\left(h,\theta_\mathrm{p}\right)$	−50.952	185.50	0.0538	53.300	0.2895	0.9236
$Q^*\left(h,\theta_\mathrm{p}\right)$	−6.2042	9.0889	−4.0964	7.8297	−0.1472	0.6904

A more detailed explanation of the theory and calculation procedure behind the fillet-foundation compliance can be found in [78]. Equation (2.35) can also be used to obtain the fillet-foundation stiffness by replacing the Hertzian compliance by the fillet-foundation compliance, as presented in equation (2.39).

$$k_\mathrm{f} = \frac{F}{y_\mathrm{f}} \tag{2.39}$$

The fillet-foundation stiffness accounts for the effect of the gear body deflection on a single tooth, meaning that when two pairs of teeth are in mesh (each of the engaging gear bodies has two teeth in mesh), the fillet-foundation stiffness presented will lead to an overestimation of the gear mesh stiffness. Take one of the gear bodies as an example, where actually the contributions of two gear bodies, each one with a single tooth, are being added when, what should be included are the contributions of two teeth in a single body. In order to solve this issue, Ma et al. [17] developed a procedure to account for more than one teeth pair in mesh by calculating correction coefficients with the Finite Element Method (FEM). The fillet-foundation stiffness for two teeth pairs in contact is assumed to be proportional to the fillet-foundation stiffness of a single pair in contact with a constant ratio. This ratio, computed with the Finite Element Method, is the fillet-foundation correction coefficient. Later, Xie et al. [79] developed analytical expressions for the fillet-foundation deflections resorting to the elastic circular ring theory of Muskhelishvili that took into account the cross influence of simultaneously loaded gear teeth and hence analytically fixing the fillet-foundation stiffness overestimation. Consult the works of Ma et al. [17] and Xie et al. [79] for a more comprehensive description of these solutions.

Since this section is dedicated to analytical methods, namely the potential energy method, the gear mesh stiffness presented will not account for the fillet-foundation correction coefficients. The single tooth pair mesh stiffness is given by equation (2.40) as the previously established stiffness terms are in series.

$$k^{\mathrm{tp}} = \frac{1}{\frac{1}{k_1^{\mathrm{st}}} + \frac{1}{k_2^{\mathrm{st}}} + \frac{1}{k_{\mathrm{H}}} + \frac{1}{k_{\mathrm{f1}}} + \frac{1}{k_{\mathrm{f2}}}} \tag{2.40}$$

Equation (2.40) gives the stiffness for a single pair of teeth. If both the pinion and the wheel only had a single tooth, its gear mesh stiffness would be given by equation (2.40). The fillet-foundation stiffness is not, in this scenario, being overestimated. Although, when the entire gear mesh is considered and there is more than one pair of teeth engaged, there will be an overestimation of the gear mesh stiffness, as previously explained. Moreover, note that in case of nonlinear Hertzian contact stiffness (advised Hertzian contact stiffness formulation according to [77]) equation (2.40) is only valid for each discrete position and corresponding applied load (local slope/tangent stiffness), requiring an iterative process.

The gear mesh stiffness is obtained by adding the single tooth pair mesh stiffness of all gear teeth pairs in mesh according to their position, which is described by equation (2.41).

$$K = \sum_{i=1}^{N} k_i^{\mathrm{tp}} \tag{2.41}$$

being N the total number of teeth pairs in mesh.

The gear mesh stiffness established here is one of the ways to determine the gear mesh stiffness of spur gears and it is a solid basis for other implementations of the potential energy method. Besides the variety of procedures for spur gears, there are also different methods to calculate the gear mesh stiffness for helical gears which slightly diverge from the spur gear methodology. The different calculation approaches for helical and spur gears will not be presented here, although, along the next section those procedures will be briefly reported.

2.2.2. Literature review on analytical models

Several models with distinct purposes can be found in the literature. Some compare different approaches and others evaluate the effect of gear parameters and errors on the gear mesh stiffness. A wide variety of works is presented in order to get an overview of the researches on analytical methods for the calculation of gear mesh stiffness. As the following studies are summarized, for a complete description it is recommended to check the references.

Spur gears

Mahr and Kissling [80] from KISSsoft® performed a comparative study on the calculation of the tooth meshing stiffness with different tooth contact analysis software packages. KISSsoft®'s gear mesh stiffness model, for spur and helical gears, is a discretized toothing model (based on Petersen and Weber/Banaschek models) with torsional coupling, smoothing of the tooth form curvature for the Hertzian deformations (commonly applied at the tooth tip) and reduced bending stiffness on the side edges of helical gear teeth. The deformation components comprised in the model are the bending and shear deformations, the gear body deformations and the Hertzian deformations - more information can be found in KISSsoft®'s User Manual [81]. The bending, shear and gear body deformations are proportional to the external load but the Hertzian deformations are nonlinear. Two different types of tooth meshing stiffness are mentioned, the secant and tangent stiffnesses. The secant stiffness (absolute stiffness) is measured from the

unloaded tooth to the tooth in operation while the tangent stiffness (operating stiffness) describes the dynamic behavior of the mesh. The single tooth pair stiffness using KISSsoft®'s package was compared with a FEM analysis and they were in agreement [80].

Since gear design softwares were mentioned, the opportunity to talk about other softwares will be taken as there are distinct approaches amongst them. Mahr and Kissling [80] and Beinstingel et al. [82] compare and discuss stiffness results from various softwares. KISSsoft®'s approach [80], based on Petersen and Weber/Banaschek models, was already presented above. LVR®, according to [80], is based on the same spring-slice model of Petersen and Weber/Banaschek but, as opposed to KISSsoft®, the slices are in the normal section. Furthermore, LVR® considers coupling between the slices and the buttressing effect yet the influence of the neighboring teeth in mesh is neglected. Next, RIKOR® [80] uses a spring-slice model with slice coupling regarding tooth deformation, tooth tilting and Hertzian deformations and it does not take into account effect of buttressing. Although, RIKOR®'s stiffness model does include the influence between the teeth in mesh through the effect of torsion and shear deformations of the gear body. STIRAK® [80; 82] combines the work of Neupert with a finite element model to estimate the gear mesh stiffness. Even though STIRAK® models the gears' exact tooth geometry it does not take into consideration the extension of contact, evidence is found by the abrupt changes in the mesh stiffness from single to double contact regions in [82]. Simpack® and DPZ®, respectively based on the works of Weber/Banaschek and Schmidt, approximate the tooth root contour and in the presence of undercut teeth, suitably reduce the wheel's tip diameter which leads to different starting meshing points when compared to the other softwares [82].

Dai et al. [83] proposed an analytical model for the mesh stiffness calculation of spur gears. The engagement of external-external and external-internal spur gears is studied taking special attention to the effect of addendum modifications. Bending, shear, axial compressive, fillet-foundation and Hertzian contact stiffnesses are the components considered in the potential energy method for the estimation of the gear mesh stiffness. By taking advantage of this model, the influence of the addendum modification on the gear mesh stiffness is evaluated and an experimental verification of the gear tooth bending stiffness for several torques is performed. The experimental tooth bending stiffness, acquired resorting to strain gauges placed at the tooth root of an internal spur gear, is found to be enclosed by the analytical tooth bending stiffness curves obtained when the addendum modifications are and are not considered [83].

Luo et al. [18] investigated the effects of center distance variation on spur gears' mesh stiffness. In this study, both time-varying and constant center distance variations can be included, hence assembly errors, runout errors, shaft bending and bearing deformation can all be taken into account in this model. For the definition of the gear mesh stiffness, the potential energy method is used along with a new gear mesh kinematic model which can evaluate the actual contact positions of tooth engagement. The model was validated by comparing the results with others found in the literature. When studying the gear mesh stiffness with and without runout errors, it was concluded that the runout errors change the frequency content of the mesh stiffness. Besides that, the peak-to-peak mesh stiffness variation and the gear center distance variation have a linear relationship, as shown in Figure 2.2. Finally, when analyzing multiple faults simultaneously, it was discovered that the effects of multiple faults is not the same as the combination of the individual faults, so the faults merge in a nonlinear manner [18].

Xiong et al. [20] modified the potential energy method to include the influence of backlash on the gear mesh stiffness. The backlash is included by developing tooth profile equations as a function of the backlash. The components of the tooth pair energy are the Hertzian, bending, shear, axial compressive and fillet-foundation energies. The effect of backlash on the gear mesh stiffness

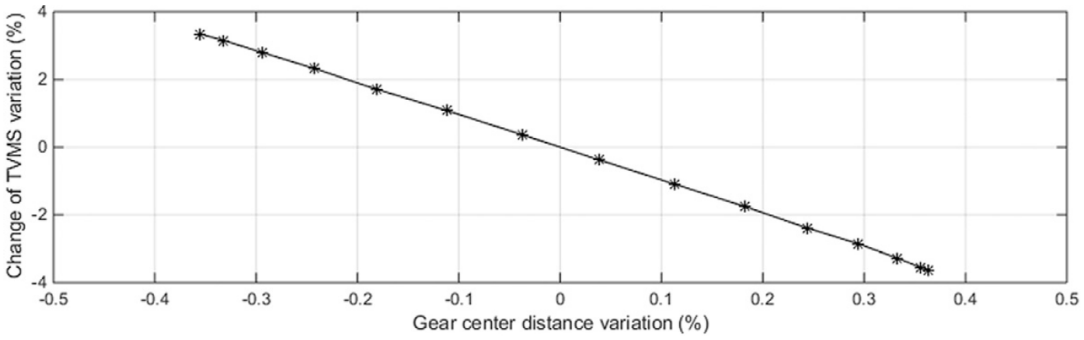

Figure 2.2: Trend of the peak-to-peak mesh stiffness variation with the center distance variation. Reprinted from [18].

was studied and it was concluded that increasing the backlash, reduces the mesh stiffness. The nonlinear dynamic behavior of spur gears with different backlash values was analyzed by fitting the mesh stiffness curves obtained with the previous model in a Fourier series [20].

A very similar gear mesh stiffness model was used by Yang et al. [84] to investigate the nonlinear dynamic response of a spur gear pair. The obtained analytical gear mesh stiffness is inserted in a single degree of freedom torsional model where the mesh damping, backlash and transmission error are also included. The calculation of the transmission error considers profile modifications and spacing errors. So, profile modifications and spacing errors are not included in the mesh stiffness model but are accounted for in the dynamic model [84].

Ma et al. [17] developed an analytical method for the calculation of the mesh stiffness of spur gears which takes into consideration tooth profile modifications, extended tooth contact, Hertzian stiffness and an improved fillet-foundation stiffness. This model solves the overestimate of double tooth contact engagement where an extra gear body stiffness was taken into account when more than one pair of teeth was in contact - issue present on some analytical methods. The calculation schematic starts with the definition of the tooth stiffness as a cantilever beam - bending, shear and compressive stiffnesses - and then the teeth pair stiffness is computed by adding the stiffness of each tooth with the Hertzian contact stiffness, which are all in series. The total mesh stiffness for all teeth pairs in mesh is the summation of their stiffnesses with the contribution of the gear body - where FEM calculated coefficients are used to correct the extra gear body. Figure 2.3 shows a spring schematic for the traditional (left) and improved (right) analytical methods. The left schematic on Figure 2.3 leads to an overestimation of the gear mesh stiffness as the fillet-foundation stiffness is included twice - there is only one gear body for two teeth, not two gear bodies each one with a tooth. Although, on the right side of Figure 2.3, the fillet-foundation is properly included due to the correction coefficients. In order to include the extended tooth contact on the gear mesh stiffness, the meshing position and separation distances are required to conclude if one, two or three pairs of teeth are in contact - the stiffness modifications are performed accordingly to obtain the final tooth mesh stiffness. The model is compared with FE (Finite Element) results, Chen's method [85] (traditional analytical method) and Fernandez del Rincon's method [86] (hybrid model). Ma et al. [17]'s model shows improved results compared to Chen's method considering the FE model as the reference. The FE model is coherent with Fernandez del Rincon's method but the improved analytical model had a slightly higher maximum mesh stiffness value when compared to the two previous models. The currently presented model was used to evaluate the effect of the length and magnitude of profile modifications on the gear mesh stiffness [17].

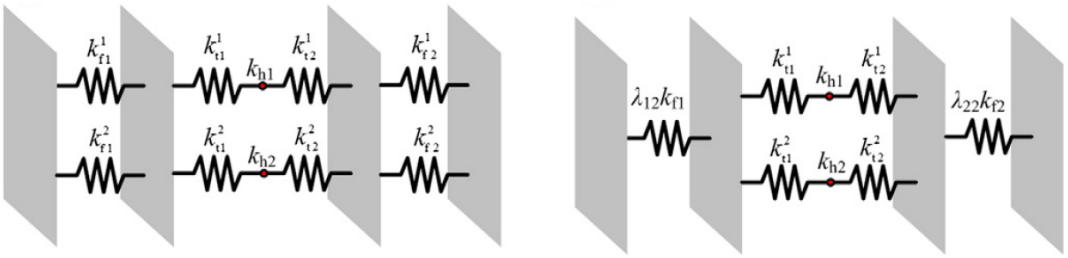

Figure 2.3: Spring schematic of traditional analytical method (left) and improved analytical method (right). Reprinted from [17].

Ma et al. [87] presented further developments on the previous work ([17]) by introducing the effects of tip-fillet and friction in their model. For the introduction of friction, a Coulomb friction model was considered with a constant coefficient of friction. Therefore, the gear radial and tangential meshing loads are modified, changing the gear bending, shear and axial compressive stiffnesses. The tip-fillet, a modification to the gear tooth profile, was included via the profile errors. The gear mesh stiffness under different coefficients of friction and tip-fillet radius is evaluated and validated with the finite element method. According to the results, the friction has an higher impact than the tip-fillet on the gear mesh stiffness [87].

Wang et al. [88] defined a gear mesh stiffness model for spur gears with two main characteristics, them being the tooth coupling stiffness and the errors along the tooth width direction. The gear tooth is sliced along its width direction (slicing method) and the stiffness of each sliced tooth pair is composed by bending, shear and axial compressive stiffnesses (potential energy method), the Hertzian contact stiffness as well as the fillet-foundation stiffness with correction coefficients for multi-tooth contact [17]. The coupling effect of teeth slices was simulated as springs, attend on Figure 2.4 for a schematic of the slice coupling model. In Figure 2.4, k_{ts} is the slice tooth stiffness, F_{s} is the force applied on a slice and k_{ij}^{c} is the coupling stiffness between tooth slice i and j. The tooth coupling stiffness (k_{ij}^{c}) depends on the stiffness of the adjacent tooth slices, gear module, tooth slice width and a slice coupling factor (C_{c}). The contact coupling effect between teeth slices is ignored. The misalignment errors and lead crown modifications are introduced in the gear mesh stiffness as spacing errors along the tooth width direction. The model is validated and the effect of the tooth coupling is studied by comparing three mesh stiffness models, a finite element model, the presented tooth coupling model ($C_{\mathrm{c}} = 2.75$) and a slice without coupling model (SWCM, $C_{\mathrm{c}} = 0$). The models were compared considering both misalignment and lead crown which led to the conclusion that the coupling effect is fundamental for the evaluation of the mesh stiffness with spacing errors in the tooth width direction. The maximum relative error for the misalignment and lead crown analysis was of 5.1% and 17.1% for the SWCM while for the proposed model was 2.0% and 1.3% when taking the FE model as the reference. The proposed model was in corroboration with the finite element analysis and hence was utilized to analyze the effect of different magnitudes of misalignment and lead crown relief on the gear mesh stiffness [88].

Xie et al. [79] established analytical expressions for gear body deflections induced by gear teeth through structure coupling effect. The formulas are developed based on the elastic circular ring theory of Muskhelishvili and assume a different stress distribution as it is found in [78]. While in [78] the normal and tangential stress distributions were assumed to be linear and constant, respectively, in [79] a cubic and parabolic stress distributions were correspondingly presupposed for the normal and tangential stress distributions. The new gear body-induced deflections were compared with a finite element analysis and Sainsot et al.'s [78] formulas. The proposed formula

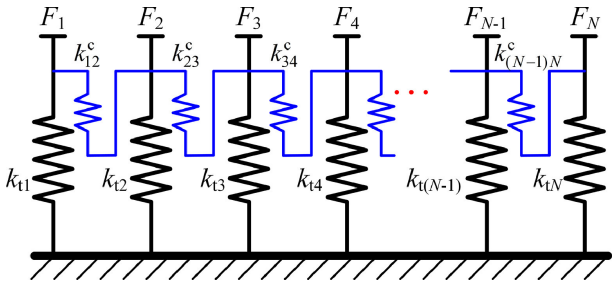

Figure 2.4: Tooth slice coupling model. Reprinted from [88].

presented closer results to the FE model than Sainsot et al.'s [78] formulas. Regarding the structure coupling gear body-induced tooth deflections, the maximum error found was of around 5%. Along with this findings, an enhanced gear mesh stiffness model was introduced which proved to be in agreement with a FE model [79]. In another work [89], the previously mentioned model was further improved.

Xie and Shu [89] presented four different spur gear mesh stiffness models which are successive improvements of each other. The first one discussed is the rigid gear body (RGB) model where the only flexibility comes from the gear teeth. The gear mesh stiffness is determined considering the bending, shear and axial compressive flexibilities of the gear tooth with the potential energy method and a linear Hertzian contact flexibility. Next, the flexible gear body (FGB) model employs the contributions of the gear body deflections through the expressions developed in [78] and the influence of tooth profile error (deformation compatibility conditions). The revised flexible gear body (RFGB) model does not contemplate tooth profile errors but it accounts for the coupling effect of adjacent teeth by finite element calculated correction coefficients. The proposed model, improved flexible gear body (IFGB) model, uses the formulas developed in [79] to analytically describe the gear body induced tooth flexibility with coupling effect, eliminating the need of the finite element method for correction coefficients. Moreover, this model updated the deformation compatibility conditions to include the effect of adjacent teeth, allowing both tooth profile modifications and coupling effects simultaneously. All the models were compared with the IFGB and FEM models. The improved flexible gear body model is the most complete model presented in [89] and it does not require the need for the finite element methods. When all four models were compared to the FEM results, the IFGB model showed the smallest error [89].

Chen et al. [90] calculated the gear mesh stiffness of spur gears with tooth profile deviations with an analytical model that includes the tooth deformation, contact deformation, fillet-foundation deformation and gear body structure coupling. The tooth deformation is determined with the potential energy method, the contact deformation with a nonlinear Hertzian contact expression and both the fillet-foundation and the gear body structure coupling are defined analytically with the expressions developed in [79]. With all the stiffness components defined and given the tooth deviations, the gear mesh can be computed. The validation procedure consists on the application of a finite element analysis to three distinct gear pairs each under three hub bore radius. Due to the flexibility of this model, the influence of several effects/parameters on the gear mesh stiffness can be studied, hence, tooth profile modifications, teeth linear and nonlinear contact, coupling methods and tooth profile errors were investigated [90].

Discussion Up until now, the described works were dedicated to the mesh stiffness of spur gears. There are a few topics that deserve a more extensive discussion, namely, the overestimation of the fillet-foundation stiffness under multi-tooth contact, to which Ma et al. [17] presented a

solution to. Although, this methodology resorts to the finite element method to define correction factors which makes the calculation process more time consuming and less flexible (a finite element model for each gear pair analyzed). This setback was solved and the gear body coupling effect can be analytically determined with the expressions developed by Xie et al. [79]. This is a substantial improvement for analytical gear mesh stiffness models since it eliminates the need of a finite element analysis, which an analytical model should not require.

A topic that differs among the works analyzed and will also vary in the upcoming investigations is what kind of Hertzian contact stiffness is implemented: linear and nonlinear expression for the Hertzian deformations were found in the literature. According to Chen et al. [90], linear Hertzian contact stiffness leads to an overestimation of the gear mesh stiffness against the nonlinear expression. From the aforementioned, the best approach is to consider the nonlinear Hertzian contact deformations as the results should be more accurate. This subject is also analyzed by Sainsot and Velex [77], where it is shown that Hertzian contact deflections are nonlinear.

The extension of tooth contact occurs when the teeth deflections due to the applied load are higher than the distance that separates them. This phenomenon, that takes place outside the normal path of contact, loads the teeth tip corner, which is undesirable and is one of the main reasons why profile modifications are applied in gears. To properly estimate the contact extension and include it in an analytical model, the separation distance needs to be defined. Several authors [35; 91–95] studied the separation distance and the impact of tooth contact extension on the transmission error. There can be significant changes in the quasi-static and dynamic behavior of spur gears when teeth contact extension is considered, showing its importance for gear mesh modeling.

In the determination of the mesh stiffness of spur gear, it is not very common to use the slicing method (division of the gear in thin slices along its width direction), although Wang et al. [88] employed it when analyzing spur gears with tooth width modifications along with a slice coupling model. If all slices were contributing equally for the gear mesh stiffness, the coupling between the slices would not affect the final results. For these situations, the coupling effect can be neglected, but that does not mean it does not exist since the load will always be transferred between each slice. However, when the slices are different from each other, their contributions are not the same so a weighting/distribution function is required for a proper gear mesh modeling.

A very complete analytical spur gear mesh stiffness model can be implemented considering all the studies shown so far. That model would include extension of contact, tooth profile errors, tooth width errors, analytical gear body coupling and slice coupling. A recap of the analyzed works on analytical models for spur gears can be found on Table 2.2.

Helical gears

Chung et al. [96] analytically studied the mesh stiffness and transmission error of helical gears. The geometry and contact positions of the helical gear are completely defined and the mesh stiffness is computed with the potential energy method by dividing the tooth into thin slices along its width. Each slice is viewed as an independent spur gear, see Figure 2.5 for a visual interpretation of the slicing procedure. The stiffness calculation of each slice comprises the tooth stiffness (bending, shear and axial compressive stiffnesses), the fillet-foundation stiffness (as in [78]) and the contact stiffness. The mesh stiffness is obtained by adding the stiffnesses according to the meshing position, slice tooth and number of contacting gear tooth pairs. Finite element analysis on three distinct gear geometries (one spur and two helical gears) validated the results obtained by this model. The impact of neglecting the trochoidal root profile on the mesh stiffness

Table 2.2: Summary of spur gear analytical models.

Analytical Model	Transverse and Contact Stiffnesses	Fillet-foundation Stiffness	FE corrected Fillet-foundation Stiffness	Analytical (corrected) Fillet-foundation Stiffness	Profile Errors	Tooth Width Errors	Tooth Friction	Slice Coupling Stiffness
Dai et al. [83]	✓	✓	-	-	-	-	-	-
Luo et al. [18]	✓	✓	-	-	-	-	-	-
Xiong et al. [20]	✓	✓	-	-	-	-	-	-
Yang et al. [84]	✓	✓	-	-	✓*	-	-	-
Ma et al. [17]	✓	-	✓	-	✓	-	-	-
Ma et al. [87]	✓	-	✓	-	✓	-	✓	-
Wang et al. [88]	✓	-	✓	-	-	✓	-	✓
Xie et al. [79]	✓	-	-	✓	-	-	-	-
Xie and Shu [89]	✓	-	-	✓	✓	-	-	-
Chen et al. [90]	✓	-	-	✓	✓	-	-	-

* not directly included in the mesh stiffness model.

and transmission error was investigated. It was discovered that the mistreatment of the root profile leads to less accurate results, mainly in the bending component due to the variations in the moment arm [96].

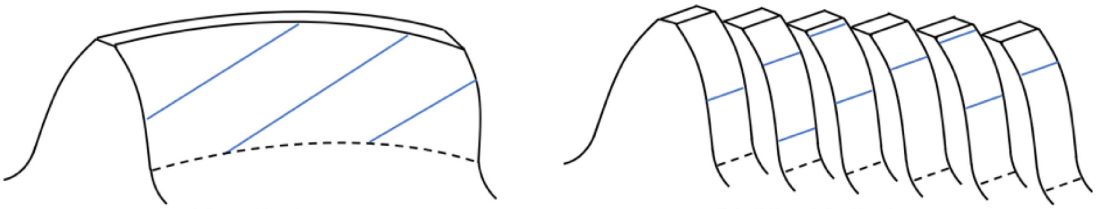

Figure 2.5: Schematic of the helical tooth slice division. Reprinted from [96].

Feng et al. [16] defined the time-varying mesh stiffness of helical gears analytically using the slicing and the potential energy methods. The mesh stiffness at a given position is equal to the sum of the slices' stiffness at that same position. Figure 2.5 shows the schematic of tooth slices. Each independent thin gear slice is viewed as a spur gear, hence its mesh stiffness is obtained with the potential energy method, which in this work considers the fillet-foundation stiffness with FE calculated coefficients, Hertzian stiffness, bending stiffness, shearing stiffness and axial compressive stiffness. The tooth-face friction affects the bending, shear and axial compressive stiffnesses according to the modifications it introduces in the tooth load. The model was validated by comparing the results with a FE model, Chang's method [12], Cai's method [97], Gu's method [13], Wang's method [98] and ISO 6336. For the gears analyzed, the model presented results very close to the FE model and in some conditions yields closer values to the FE model than other of the previously mentioned models. Upon validation, this analytical model was used to investigate the effect of the helix angle, gear width, modification coefficient and friction coefficient on helical gears' mesh stiffness [16].

Yu and Mechefske [14] created a new model for the determination of the single tooth pair stiffness of helical gears. This improved analytical model uses the slicing principle method where a parabola-like weighting factor distribution along the tooth facewidth is applied for the coupling effect. The "thin-slice" approach (slicing principle) divides a helical gear into slices of spur gears. The stiffness of each equivalent spur gear is calculated through analytical formulae

(potential energy method) and accounts for the bending, shearing, compressive, Hertzian and fillet-foundation stiffnesses. Since the helical gear was assumed as a series of staggered spur gears, the helical single tooth stiffness is given by the sum of the stiffness of each slice (spur gear). Although, by doing this, each slice is independent from each other. To include the coupling within each slice, a Gaussian curve is applied for each slice considering that the amplitude of the Gaussian curve is higher for the slices on the tooth edges. The non-uniform weighting distribution is obtained by the sum of Gaussian curves of each slice, originating a parabolic-like curve with the maximum at the middle and minimum at the edges. The final tooth stiffness is reached by including the weighting function in the tooth stiffness expression. Different kind of models are compared with the developed model - analytical model with no coupling, ISO standard and FE model - which revealed more accurate stiffness curves in terms of shape and values when compared to the analytical models without slice coupling [14].

Wang et al. [99] developed a model to establish the mesh stiffness of helical gears with profile modifications by slicing a helical gear teeth with planes normal to the gear rotation axis, as shown in Figure 2.5. In this model, each slice is viewed as a two-dimensional model and the calculation of the deformation of each slice takes into account the loads applied in other slices, meaning that each slice is not independent. The process of computing the mesh stiffness of helical gears with linear tip modification starts with the calculation of the time-varying contact line length for a perfect helical gear. Then, the gear is divided into slices and the deformation and modification amounts are defined for each slice. There are two possible situations, the amount of modification is larger than the deformation (meaning that the slices do not contact each other) or the contact line is on the modified flank. For the first case, the contact line length and stiffness are defined as zero whereas for the second case, the contact line length and stiffness for the slices are computed through the contact status of each slice (contact line length) and the division of the loads by the deformations (stiffness). The deformation of each slice is calculated considering the bending, shearing, contact and fillet-foundation deformations. The stiffness of each tooth is given by combining the stiffness of each slice. The single tooth pair stiffness is obtained combining the wheel's and the pinion's tooth stiffnesses. The resulting stiffness was compared with a finite element model and even tough the shape obtained is close, the stiffness values are slightly off. Regardless, the model was still considered approved and was used to study the influence of linear tip modification on the total contact length and mesh stiffness of helical gear pairs [99].

Tang et al. [100] established a mesh stiffness model for spur gears which was modified for helical gears to include the coupling effects. The spur gear mesh stiffness is obtained from the potential energy method with bending, shear and axial compressive energies, Hertzian contact stiffness and fillet-foundation stiffness ([78]). This spur gear model was the basis for the development of two different helical gear models, a single coupling model and a double coupling model. The helical gear is divided into slices along its width and each slice is connected by a single spring (single coupling model). In this model, the coupling stiffness relates both the gear body and tooth stiffness of each slice. Its value is given by the torsional stiffness of the gear body and the shear stiffness between the teeth slices. In the double coupling model, the gear body and gear tooth slices are connected separately. The gear body coupling stiffness consists on the torsional and shear stiffness of the slices while the tooth slices are connected by a shear stiffness and a scale factor to account for the different load locations in the tooth profile between slices along a line of contact. The spur and helical gear models were validated with a FEA and by other models found in the literature. The tooth and gear body coupling stiffnesses were analyzed for different helical gear pairs and it was found that the tooth coupling stiffness has more impact on the gear mesh stiffness than the gear body coupling stiffness [100].

Wang et al. [101] presented a gear mesh stiffness model for helical gears where the axial mesh

stiffness component is also introduced. The total mesh stiffness is composed by two components, transverse mesh stiffness and axial mesh stiffness. The transverse mesh stiffness is given by the sum of the stiffnesses of each tooth slice without tooth coupling. This mesh stiffness component includes the bending, shear and axial compressive stiffnesses by the potential energy energy, the Hertzian contact stiffness and the transverse gear foundation stiffness considering a FE correction factor. The axial mesh stiffness is comprised by the tooth axial stiffness and axial gear foundation stiffness, both determined by the potential energy method. However, while the first accounts for the bending and torsional energies, the second only considers the bending energy. The axial gear foundation stiffness model assumes a semicircular variable cross-section cantilever beam to determine the bending energy which, according to a finite element analysis, is a good approximation. The model is validated by the finite element method in three distinct studies. The first study evaluates the maximum single tooth stiffness, the second is the comparison of the gear mesh stiffness while considering or not the axial mesh stiffness component and the last one is equal to the second one but for a different gear geometry. Finally, the effect of the helix angle on the gear mesh stiffness was investigated and the main conclusion is that the axial stiffness component has a relevant role on the total gear mesh stiffness as the results showed that the maximum relative error found when ignoring it is around 10% for an helix angle equal to 10° and keeps increasing from that point forward [101].

Hou et al. [102] developed a robust gear mesh stiffness model for helical gears by considering slice coupling stiffnesses between the teeth and fillet-foundation as well as including the axial stiffness. The stiffness of each slice is composed by the tooth and the fillet-foundation stiffnesses. The tooth stiffness is determined by potential energy method for both the axial and transverse components. The axial component includes the bending, shear and torsional energies while the transverse component the bending, shear and axial compressive energies. Concerning the fillet-foundation stiffness, its axial component is established by the potential energy method assuming the body as a cantilever beam (bending energy) while its transverse component is computed resorting to the expressions developed in [79]. For the Hertzian contact stiffness a nonlinear equation is applied. The neighboring slices are connected by springs in both the tooth and fillet-foundation regions. The stiffness of these springs is calculated with the contributions of the torsional and shear stiffnesses. Two gear pairs are submitted to a finite element analysis to perform the validation of the developed gear mesh stiffness model. The maximum error found when evaluating the mean, maximum and minimum values of the gear mesh stiffness was lower than 5%. By taking advantage of the inclusion of the axial stiffness and coupling effects on the model, the influence of the helix angle on the gear mesh stiffness fluctuations and mean value was analyzed. Two configurations were investigated, one where the axial effects were neglected and another where they were not. It was concluded that the axial effects do not have a significant influence on the mesh stiffness fluctuations yet ignoring them leads to an overestimation of the average mesh stiffness value, specially for helix angle values above 20° [102].

Discussion The main differences found in the helical gear models are related to the gear body coupling, the slice coupling and the axial stiffness. The axial mesh stiffness is not considered in many works when evaluating the total gear mesh stiffness but Wang et al. [101] and Hou et al. [102] included and studied it with their models. Similar conclusions were obtained, the axial mesh stiffness plays a relevant role in the gear mesh stiffness. Naturally, for small helix angles, the effects are not that pronounced but as it increases they cannot be disregarded.

The gear coupling effect has to be considered for helical gears. The analytical expressions in [79] allow to include the gear body coupling effect without the FEM. As for the slice coupling effect, it is fundamental for helical gears since the contribution of each slice is different even without

modifications. For any meshing position, the contact line is not perpendicular to the path of contact and therefore each slice will have different contact points along the tooth profile. The helical gear slice coupling is sometimes neglected by considering narrow-faced helical gear with small helix angles, situation where the coupling effect is very small. Nevertheless, this is still an approximation.

It is recommended that the previously discussed effects are incorporated in any helical gear mesh stiffness model. Table 2.3 sums up the studies of analytical models for helical gears.

Table 2.3: Summary of helical gear analytical models.

Analytical Model	Transverse and Contact Stiffnesses	Axial Stiffness	Fillet-foundation Stiffness	FE corrected Fillet-foundation Stiffness	Analytical (corrected) Fillet-foundation Stiffness	Profile Errors	Tooth Width Errors	Tooth Friction	Slice Coupling Stiffness
Chung et al. [96]	✓	-	✓	-	-	-	-	-	
Feng et al. [16]	✓	-	-	✓	-	-	-	✓	-
Yu and Mechefske [14]	✓	-	✓	-	-	-	-	-	✓
Wang et al. [99]	✓	-	✓	-	-	✓	-	-	✓
Tang et al. [100]	✓	-	✓	-	-	-	-	-	✓
Wang et al. [101]	✓	✓	-	✓	-	-	-	-	-
Hou et al. [102]	✓	✓	-	-	✓	-	-	-	✓

Damaged gears

The mesh stiffness of damaged gears is also a highly investigated topic. Several types of gear tooth damaged are studied such as pitting, spalling, wear and tooth cracks. In this section, both spur and helical gears are investigated, being spur gears analyzed first. Analytical models might not be the most accurate type of model for this kind of evaluation, nevertheless many authors obtained satisfactory results, as shown next.

Chen and Shao [85] created an analytical mesh stiffness model for spur gears capable to account for gear tooth errors and cracked teeth. In this model, the pinion and wheel were assumed to have rigid bodies. Also, the wheel was considered fixed while the pinion could rotate freely. The geometric formulation of the contact positions considered tooth errors - tooth profile modifications can be incorporated as tooth profile errors. Then, the relationship between gear tooth errors and gear mesh stiffness, load sharing ratio and loaded static transmission error is defined. For the calculation of these parameters, the single tooth pair stiffness needs to be obtained, so the potential energy method was adopted. The single tooth pair stiffness is given by adding the stiffnesses of the single tooth, the fillet-foundation and the Hertzian contact. The single tooth stiffness is obtained by integrating the bending, shear and axial compression stiffnesses along the tooth width. The presence of the tooth crack is translated into the model as a reduction in the second moment of area and the area of the cross-section. The effects of tooth profile modifications, applied torque and gear tooth root crack on the mesh stiffness were investigated for both low contact and high contact ratio gears [85].

Meng et al. [103] investigated the vibration of a spur gear pair in the presence of tooth root crack and spalling by analytically defining the gear mesh stiffness. Like in the previous model, the potential energy method is applied with the fillet-foundation and Hertzian contact stiffnesses. In order to establish the gear mesh stiffness with a tooth root crack or spalling, the tooth cross-section and second moment of area are modified accordingly. The impact of different crack lengths, spalling widths, spalling lengths and spalling locations on the gear mesh stiffness is studied.

The gear mesh stiffness with the desired tooth damage is inserted in a six degrees of freedom lumped-parameter model to analyze the fault characteristics in the dynamic response [103].

Wang and Zhu [104] took advantage of the potential energy method, the nonlinear Hertzian contact stiffness and the FE corrected fillet-foundation stiffness to define the mesh stiffness of spur gears with spalled teeth and time-varying coefficient of friction. As it is commonly found in analytical models with tooth surface defects, the spall is defined as a rectangle and affects the tooth stiffness by modifying its cross-section area and the second moment of area. The friction coefficient under mixed elasto-hydrodynamic lubrication is obtained considering a weighting factor function and the coefficients of friction in boundary and full film lubrication. The gear mesh stiffness with time-varying friction coefficient and spalled teeth are studied separately [104].

Liu et al. [105] combine an analytical geometry description of external and internal spur gears with tip chipping and the potential energy method to accurately evaluate their mesh stiffness. Five energy components were included in the potential energy method for the calculation of the gear mesh stiffness: bending, shear, axial compressive, fillet-foundation and Hertzian contact. The analytical model is discussed separately for external-external and external-internal spur gears and accounts for the damage variations along the tooth width. The analytical procedure was validated by a finite element analysis for both external-external and external-internal spur gears. The tip chipping can vary along the involute profile (point A), addendum tooth tip (point B) and tooth width (point C) as shown in Figure 2.6. The left side of Figure 2.6 displays the entire tooth while the right side presents a damaged cross-section. The mesh stiffness of different tip chipping shapes is investigated resorting to the comparison of mesh stiffness curves, differences in stiffness amplitude and attenuation rate relatively to a healthy tooth mesh. The results provided evidence that the position along the involute profile (point A) has the highest impact on the mesh stiffness [105].

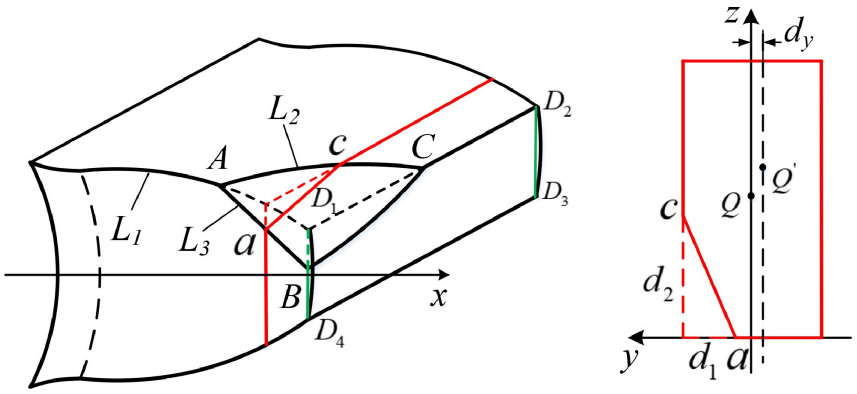

Figure 2.6: Illustration of tooth with tip chipping. Reprinted [105].

Chen et al. [106] employ the potential energy method to research the effect of wear on the gear mesh stiffness of external spur gears. To include the wear in the analytical model, Archard's wear prediction model is applied and the tooth related energies are modified to account the evolution of wear. Only the bending, shear and axial compressive energies were affected while the remaining, Hertzian contact and fillet-foundation energies, were not altered by this phenomenon. Figure 2.7, presented by Shen et al. [107] in an investigation on the effect of wear on the mesh stiffness of a planetary gear set, shows how wear influences the shape of a gear tooth profile. The potential energy method together with the deformation compatibility equations give the gear mesh stiffness for both single and double tooth pair contact regions. The model is found to be validated by comparing the results with a finite element model for both healthy and worn gears.

The mesh stiffness of gears with different number of revolutions (N) is analyzed, concluding that wear mainly affects the double tooth contact region and that the mean mesh stiffness reduction has an approximately linear relation with the maximum wear depth for $N < 5 \times 10^5$ [106].

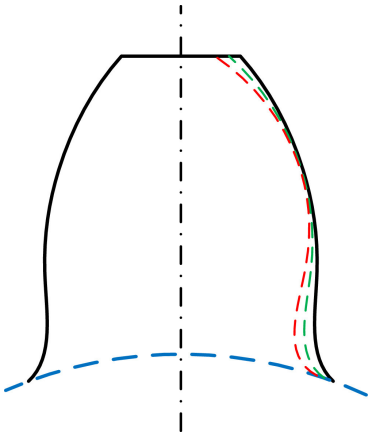

Figure 2.7: Example of gear tooth profiles with different wear cycles. Reprinted from [107].

Chen and Ji [108] examine the gear mesh stiffness and transmission error of spur gear teeth including wear, profile modifications, extension of contact and structure coupling (influence of the neighboring teeth deflections). To accomplish this objective, the potential energy method was implemented (bending, shear, axial compressive, Hertzian contact and fillet-foundation components) with a fillet-foundation formulation developed in [79] that accounts for the deflections on the neighboring teeth. Wear, profile modifications and extension of contact are incorporated by the application of the principle of rotation displacement coordination (deformation compatibility equations) which require the amount of wear, profile modification and separation distances. The amount of profile modification is defined by the designer, the separation distance only depends on the gear geometry and the amount of wear is established via the Archard's wear prediction model. A successful validation was acquired through a finite element analysis of two distinct gear geometries with and without profile modifications. A combination of profile modifications and cycles of wear was analyzed which lead to the conclusion that even if the maximum wear depth is smaller than the amount of profile modification, it can have the most significant influence on the gear mesh stiffness [108].

Yousfi et al. [109] assessed the gear mesh stiffness of spur gears considering more realistic surface defects instead of using, as it is commonly found in the literature, specific geometries like circles, rectangles or triangles. The gear mesh stiffness is defined by a developed contact detection algorithm and the potential energy method which involves the bending, shear, axial compressive, fillet-foundation and Hertzian contact stiffnesses. The gear tooth surface is discretized in the length and width directions granting the possibility of varying the defect depth in the two directions. This way, irregular surface defects can be modeled without defining their mathematical expressions. The coordinates of the contact points in the path of contact during meshing considering the irregular defects are defined in the contact detection algorithm by minimizing the distance between two points, one on the pinion surface and other on the wheel surface. The model was validated for an healthy gear by comparing with finite element and analytical models. Upon validation, the gear mesh stiffness under different nonuniform shaped spalls and pitting defects is studied. The nonuniform shaped defects are generated by a MATLAB® function that creates two-dimensional random rough surfaces with a Gaussian height distribution. Even though this approach was taken to define the irregular defects, the true potential of this model relies in the possibility of considering real damaged tooth surfaces without any mathematical expression.

This is, with the proper equipment, direct tooth surface measurements can be introduced in the model for the calculation of the gear mesh stiffness [109].

Chen et al. [110] resorted to the potential energy method and the slicing method to determine the mesh stiffness of helical gear pairs with spalling. The mesh stiffness considers bending, shearing, axial compressive, fillet-foundation with correction coefficients and Hertzian stiffnesses. For each slice it is verified whether it is a healthy or spalling meshing position - see Figure 2.8 for an example of a tooth slice with spalling. In case of a faulty meshing point, the effect of the spalling in the gear mesh stiffness is introduced through a spalling correction coefficient. The developed procedure allows to evaluate the mesh stiffness for different spalling lengths, widths and positions. The proposed method was compared with a finite element model under different types of spalling defects and the results obtained are in good agreement [110].

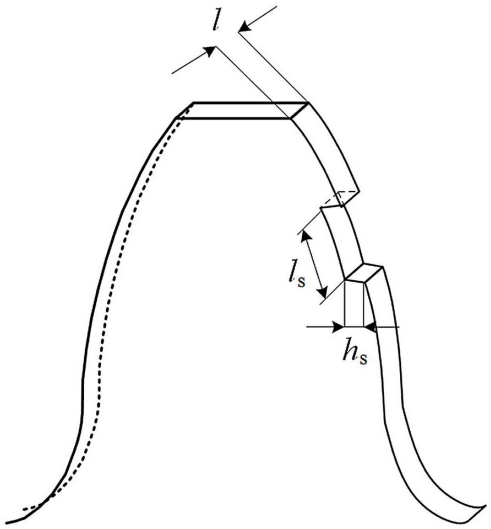

Figure 2.8: Sliced tooth with spalling. Reprinted and adapted from [110].

Wan et al. [111] developed the accumulated potential energy method to define the mesh stiffness of a helical gear pair. The accumulated potential energy method arises from the application of the potential energy method, used for spur gear, to helical gears. Assuming that a helical gear can be viewed as a series of staggered spur gears with no elastic coupling (valid for narrow-faced gears with low helix angles), the stiffness of the helical tooth can be achieved by integration along facewidth, therefrom the name accumulative potential energy method. The mesh stiffness of a helical gear pair with cracked tooth was evaluated in this model (modification in the effective cross-section area and second moment of area) by assuming the cracked tooth as a cantilevered beam and that the crack depth changes linearly with the facewidth. The model was validated with comparison to a FE model and the ISO 6336. The presence of a tooth crack and the effects of normal module, helix angle and facewidth on the mesh stiffness of a helical gear pair were investigated. Moreover, the mesh stiffness obtained by this method was included in a dynamic model to evaluate the dynamic response of a helical gear pair with the variation of geometric parameters and containing a cracked tooth [111].

Jiang and Liu [112] modeled the mesh stiffness of helical gears containing tooth cracks. The potential energy and slice methods are used to determine the stiffness of the tooth as well as the deflection of the gear body. The cantilever beam model presented consists of half the gear body (fixed along the gear center) with a single tooth. The stiffness of each sliced pair is obtained by adding the bending, shear and axial compressive tangential components; the bending, shear and

torsional axial components and the Hertzian contact stiffness. The implemented cantilever beam model allows to account for the contributions of the tooth crack in both the gear tooth and gear body deflections. So, in the presence of tooth crack, the second moment of area, cross-section area and the polar moment of area are all suitably modified. The single tooth pair mesh stiffness is computed by integrating the stiffness of each sliced tooth pair along the contact line, then the gear mesh stiffness is given by the sum of all gear tooth pairs in mesh. Since this model describes the crack depth along the tooth width and integrates the tooth slices along the contact lines, healthy and damaged tooth slices are properly assessed. The proposed model is validated by comparing the gear mesh stiffness results with a finite element analysis under three different circumstances, they are, in the presence of tooth crack considering or not the gear body deflection, ignoring or not certain stiffness components and different crack propagation scenarios [112].

Discussion In the analytical models of damaged gears, the tooth defects are usually taken into account in the tooth stiffness by modifying its cross-section area and second moment of area. It is common to find in these models non-realistic defects such as rectangles or circles to simulate pitting and/or spalling. They might be a good approximation for some situations but they are not valid for most of them. To overcome this, Yousfi et al. [109] developed a model where it is possible to introduce realistic shapes from real tooth surface measurements. The best results are obtained when the model is as close to reality as possible.

Finally, when modeling gears with defects that are not uniform along the entire tooth width, there will be damaged and healthy gear slices so, in order to properly include them, the slice coupling effect needs to included. In addition, if only the damaged slice is considered for the calculation, it is almost the same as considering that the defect is in the entire tooth width (cross-section area accounts for tooth width damage). Care must be taken to the simplifications/approximations performed when dealing with damaged gears. Table 2.4 compiles all the works presented on analytical models of damaged gears along with their main characteristics. There is no column for the tooth width errors since pitting, spalling and tooth cracks can be seen as errors along the tooth width. From Table 2.4, it can be concluded that there is not any work with slice tooth coupling in damaged gears.

Table 2.4: Summary of damaged gears analytical models.

Analytical Model	Transverse and Contact Stiffnesses	Axial Stiffness	Fillet-foundation Stiffness	FE corrected Fillet-foundation Stiffness	Profile Errors	Tooth Friction	Slice Coupling Stiffness	Pitting and/or Spalling	Tooth Cracks	Wear	Tip Chipping	Realistic Tooth Surface
Chen and Shao [85]	✓	-	✓	-	✓	-	-	-	✓	-	-	-
Meng et al. [103]	✓	-	✓	-	-	-	-	✓	✓	-	-	-
Wang and Zhu [104]	✓	-	-	✓	-	✓	-	✓	-	-	-	-
Liu et al. [105]	✓	-	✓	-	-	-	-	-	-	-	✓	-
Chen et al. [106]	✓	-	✓	-	-	-	-	-	-	✓	-	-
Chen and Ji [108]	✓	-	✓[1]	-	✓	-	-	-	-	✓	-	-
Yousfi et al. [109]	✓	-	✓	-	✓[2]	-	-	✓	-	-	-	✓
Chen et al. [110]	✓	-	✓	-	-	-	-	✓	-	-	-	-
Wan et al. [111]	✓	-	-	✓	-	-	-	-	✓	-	-	-
Jiang and Liu [112]	✓	✓	✓	-	-	-	-	-	✓	-	-	-

[1] analytical formulation in [79].
[2] the realistic tooth surface allows for profile errors.

2.3. Finite element models

The finite element method (FEM) is a procedure used to find numerical solutions of equations that define the behavior of any system. These problems are usually defined resorting to the laws of physics, algebraic equations, differential equations or integrals. Concerning structural analysis, FEM is a powerful tool to calculate displacements, stresses and deformations of loaded structures [113–115].

This numerical method is characterized for dividing a continuous domain of a problem into several non-overlaped subdomains, the finite elements. The finite elements are interconnected by nodes and together they create a mesh that discretizes the entire domain. The number and location of the nodes depends of the geometry of the elements and the polynomial approximation used. For each element the solution is approximated by the combination of the values at each node and by assembling all the elements, the entire problem is solved. The assembly process is conducted considering that the solution is continuous along the elements. Moreover, this process depends on the boundary conditions and initial conditions of the problem. The solution can only be found after imposing these conditions [113–115].

However, no method is perfect and FEM is no exception. FEM has errors associated to the modeling of the problem, discretization of the domain and from numerical computation. The modeling errors can be minimized by improving the conceptual and structural models that describe the system's behavior. The errors that arise from the approximation of the domain through finite elements - discretization process - are usually taken care by selecting a more appropriate element, by increasing the precision of the selected element or by increasing the number of elements. The computational errors, which are normally small, are associated to the capacity of the computer in representing data by finite numbers which, for the finite element method, is aggravated due to its accumulation [113–115].

In short, the finite element method allows the analysis of a system with complex geometries, boundary conditions, loadings and material properties as well as nonlinear configurations whether due to the material or geometry, meaning it is a powerful calculation and analysis tool [113–115].

For the gear mesh stiffness, the finite element method comes in handy, as its determination involves very complicated geometry, loading and, in some situations, material properties. The high precision of the finite element method allows to account for many different effects that are, sometimes, neglected in analytical methods, for instance, corner and back contact, border effects and, for helical gears, axial deformations. The main disadvantage of the finite element method is its high computational effort which may not be, in some situations, affordable.

Common applications of the finite element method regarding the gear mesh stiffness are validation of other techniques (the finite element method is considered the most accurate), analysis of mesh stiffness with tooth crack, spalling and pitting, study of gear geometrical parameters on the mesh stiffness and assessment of the mesh stiffness for dynamic purposes.

2.3.1. Details of finite element method

The purpose of this section is to describe details of the application of the finite element method to the gear mesh stiffness. The addressed points are softwares, system modeling, commonly used elements, mesh discretization and mesh stiffness extraction.

- **Softwares:** Table 2.5 shows commonly used softwares for finite element analysis of the gear mesh stiffness as well as the corresponding works that use them.

Table 2.5: Softwares used to perform finite element analysis of the gear mesh stiffness.

Softwares	ABAQUS®	ANSYS®	Calyx®	COSMOS/M®	MSC Software® (Nastran solver)
Works	[116]	[15; 16; 110; 117–120]	[9]	[121]	[122]

- **Gears' modeling:** There are different ways to model the gears for the finite element method and they vary according to what is desired to analyze. The full gear can be modeled, this is, the entire body with all the teeth, or only some of the teeth might be represented in the entire gear body. Also, partial gear body and corresponding gear teeth can also be utilized (sector models). Table 2.6 summarizes the different types of gear modeling found.

Table 2.6: Modeling of gears for finite element analysis of the gear mesh stiffness.

Type of Gear Modeling	Full Gear	Gear Body with a Single Tooth	Gear Body with Several Teeth	Single Tooth Sector Model	Three Teeth Sector Model
Works	[9; 15; 118; 120]	[121]	[16; 110; 117; 122]	[116]	[116; 119]

- **Type of elements:** A finite element model can contain different types of elements so that the most appropriate elements are utilized according to the intended purpose. Table 2.7 resumes the types of elements used for the works analyzed.

Table 2.7: Types of elements for finite element analysis of the gear mesh stiffness.

Type of Elements	Gap Elements	High Stiffness Truss Elements	3-noded Plane Stress Elements	4-noded Plane Stress Elements	Linear Elements: SOLID185	Contact Elements: CONTA174 TARGE170	20-node Structural Elements	8-node Linear Brick Elements (C3D8)	8-node Trilinear Hexahedral Elements	10-node Tetrahedral Elements
Liang et al. [15]	-	-	-	-	✓	-	-	-	-	-
Feng et al. [16]	-	-	-	-	✓	✓	-	-	-	-
Chen et al. [110]	-	-	-	-	✓	✓	-	-	-	-
Thirumurugan and Gnanasekar [116]	-	-	-	-	-	-	-	✓	-	-
Zhan et al. [117]	-	-	-	-	✓	✓	-	-	-	-
Wang and Howard [118]	-	-	-	✓	-	-	-	-	-	-
Zouari et al. [119]	-	-	-	-	-	-	✓	-	-	-
Liang et al. [120]	-	-	-	-	✓	-	-	-	-	-
Arafa and Megahed [121]	✓	✓	✓	✓	-	-	-	-	-	-
Hedlund and Lehtovaara [123]	-	-	-	-	-	-	-	-	✓	-
Natali et al. [122]	-	-	-	-	-	-	-	-	-	✓

- **Elements' size:** The elements' size is most critical when analyzing the contact between gear teeth for a proper incorporation of the Hertzian contact effects and the tooth root regions due to the high stresses involved. The meshes are usually made in order to obtain the best results with the minimum computational effort, therefore finer meshes are only applied when strictly necessary. There are different approaches for meshing in order to minimize the computational time: adaptive meshing is a technique where at each step there is a remeshing of the contact area, that is, the contact zone is always finely meshed independently of its location; layer meshing is the application of a layer of fine elements along the tooth profile and teeth meshing consists in refining the entire teeth that are going to mesh. Coy and Chao [124] developed a method of selecting the grid size for the

finite element study of gear tooth deflection in order to include the full effects of Hertzian deformations. This method was established resorting to the analysis of two cylinders in line contact and it was determined that the ratio of element size to Hertz contact width ($e/(2b_{\mathrm{H}})$) is related to grid aspect ratio (c/e: element dimension in the direction normal to the loaded edge divided by the element size measured along the loaded edge) according to equation (2.42). In [118] it is ensured that the maximum allowable element edge in the contact zone is equal to half the contact zone considering the maximum tooth contact stress at the tooth tip, whereas in [121] the elements' size in the contact region is 1/10 of half the Hertz contact width. The average element dimension at the contact region in [122] is 0.14 mm.

$$\frac{e}{2b_{\mathrm{H}}} = -0.2\left(\frac{c}{e}\right) + 1.2, \quad \text{where } 0.9 < \frac{c}{e} < 3 \tag{2.42}$$

- **Mesh stiffness extraction:** There are two main ways to extract the gear mesh stiffness. One of them requires the rotational displacement (transmission error) and the other the deflections in the direction of the applied load. The previously mentioned data are related to the torsional mesh stiffness (rotational displacement) and the linear mesh stiffness (linear deflections) which in turn can be related with each other, as it was previously explained (see equation (2.6)). Depending on the boundary conditions included in the developed finite element model, the computation of either the rotational or linear displacements can be more accessible. There are models where the rotational displacement of the output gear can be directly obtained from the finite element results, meaning that the torsional stiffness can be determined in a straightforward process. This methodology is usually associated with the creation of a master node that represents the total rotational displacement of the entire gear body [16; 110; 117; 118]. When only the linear displacements are available, there are two possible approaches. One considers the linear displacements in the load direction, which can be applicable to both 2D or 3D models. However, in order to apply this approach for 3D models either the averaging of the displacements along the tooth width or the displacements at a particular position have to be determined ([116; 119; 121; 122]). The other approach consists in computing the tangential displacements at a specified radius with averaging or curve fitting of the results which allows for the computation of the rotational displacement ([9; 15; 120]).

2.3.2. Literature review on finite element models

In this section, the literature review on the usage of the finite element method to acquire the gear mesh stiffness is exhibited. The models presented only take advantage of the finite element method to reach the gear mesh stiffness. The subsequent works are shortly described. For further details consult the references.

Cooley et al. [9] compared different approaches for the calculation of the gear tooth mesh stiffness: the average slope method (secant stiffness) and the local slope method (tangent stiffness). The gear tooth mesh stiffness is determined by applying the two methods to the force-deflection curve obtained with the finite element method. With the average slope method the gear mesh stiffness is obtained by dividing the mesh force by the mesh deflections at each point whereas the local slope method is the actual slope of the force-deflection curve at a specific point (first-order finite difference approximation). Attend to Figure 2.9 to see a graphical representation of the average and local slope methods. Both approaches are compared for unmodified teeth, teeth with profile modifications and teeth with lead crown. Overall, the local slope method presents higher average mesh stiffness. The main shape differences are found in the transition between one and two teeth

pairs in contact and in the double teeth contact area. The average slope method is significantly more affected than the local slope model when teeth modifications are applied. Upon an analysis to the mesh forces, it became clear that the average slope stiffness captures the gear deflections relative to an unloaded state while the local slope stiffness evaluates the deflections of the gears relative to a loaded state. Therefore, it was concluded that for static conditions, e.g. load sharing ratio, the average slope stiffness should be used. Although, for dynamic gear models where there is an oscillation around a static deflection, the local slope stiffness is more appropriate [9].

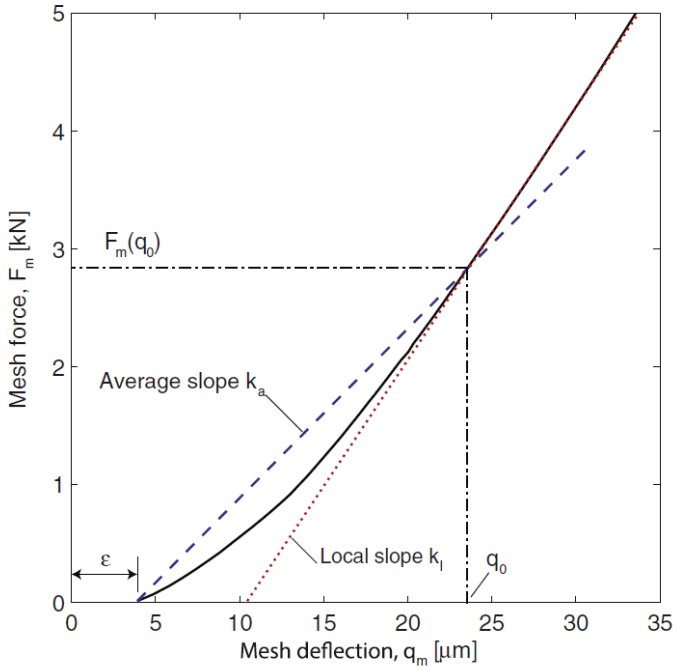

Figure 2.9: Finite element calculation of the force-deflection curve with representation of different stiffness approaches. Reprinted from [9].

Arafa and Megahed [121] created a FE model to evaluate the mesh compliance of spur gears. In this work, the modeling is performed in the commercial package COSMOS/M® and uses gap elements for the contact between the engaging teeth. Some of the assumptions included are that there is no sliding friction between the mating teeth; the load distribution along the tooth facewidth is uniform in order to apply a 2D finite element analysis with plane stress conditions; there are no geometrical errors and the effect of lubricant oil film pressure is neglected. The gears are modeled with a single tooth and in order for the tooth deflections to be independent of the rim effects, the rim thickness is set to 2.5 times the tooth height. Concerning the boundary conditions, one of the gears has its bore rigidly fixed while the other can only rotate about its center. The latest boundary condition is applied by connecting the bore nodes to a center node with high stiffness truss elements. The torque is applied on the gear that rotates by loading it with two equal and opposite tangential loads at two diametrically opposed nodes at the gear bore. The mesh consists of three- and four-node isoparametric plane stress elements. The elements' size in the contact area is equal to 1/10 of half the Hertz contact width and they were applied along the contacting involute profiles so that remeshing is avoided. The elements' size increases as the distance to the contacting zone increases. The results of the model are validated by comparing with other analytical, numerical and experimental methods. The model is then used to analyze the compliance, load sharing ratio and mesh stiffness of gears [121].

Liang et al. [15] established three finite element models for the mesh stiffness assessment of standard involute spur gears. The three-dimensional finite element models were implemented in ANSYS® and used hexahedral SOLID185 elements with the pinion's and wheel's nodes coupled in advance to avoid contact finite elements. The first model (model 1) assumes that the gear body and teeth are elastic but the bore surface of the wheel is assumed to be rigid. A rigid bore surface was implemented by coupling every node of the bore surface with a fixed distance from each other. Attend to Figure 2.10 to see the finite element model developed. The angular displacement of the wheel bore surface was then withdrew from the finite element results to compute the mesh stiffness. Two other existing finite element models were implemented for comparison purposes. It was concluded that the gear body deflection cannot be neglected since that yields significantly different mesh stiffness values. Model 2 takes on the same approach as model 1 but with an elastic bore surface. In this model, the angular deflections of the end surface circle of the gear bore are determined for a number of points evenly distributed along the end surface circle and fitted to a cosine curve. Then, the minimal angular deflection according to the approximation curve is used to obtain the mesh stiffness for the corresponding meshing position. The process is repeated for each meshing position. The results obtained from model 1 and 2 are in agreement. The last model presented (model 3) has the same assumptions as model 2, however instead of obtaining the angular deflection of several distributed points at the end surface circle of the gear bore, only an arbitrary position of that circle is required. By doing this, it is necessary to rotate the gear by angles corresponding to the mesh period in order to obtain the entire end surface circle angular deflections and perform the cosine curve fitting. From this point on, the process is the same as previously explained. The mesh stiffness computed from model 3 is in accordance with the one of model 2. Since there is the possibility that the gear bore radius affects the mesh stiffness, a study was conducted where different bore radius were applied. Models 2 and 3 revealed to be in agreement with model 1 for the different bore radius applied [15].

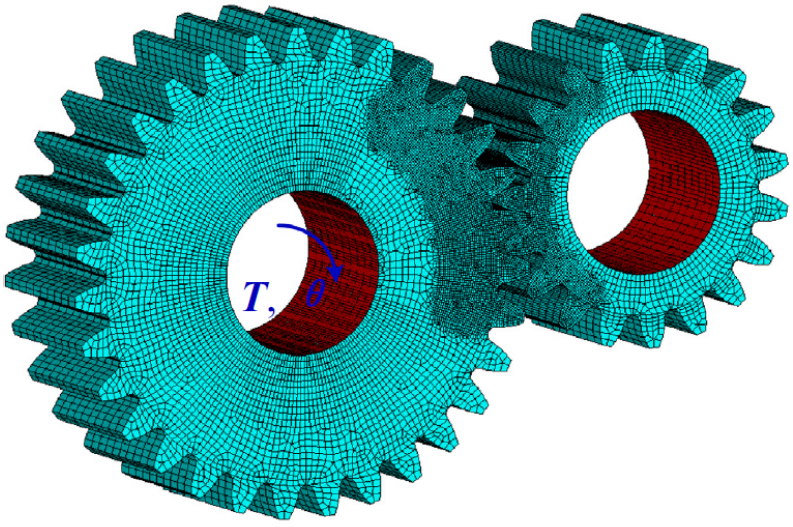

Figure 2.10: Finite element model of a spur gear pair with bore surfaces highlighted. Reprinted from [15].

Natali et al. [122] implemented different approaches of FE models, hybrid models and analytical models with the objective of comparing them and studying particular critical parameters. Within those models, Natali et al. developed a FE model that consists on three finite element analysis, two linear analysis (full and partial models) and a nonlinear analysis of a contacting tooth pair.

While the linear analysis has the purpose of obtaining the linear global deflections, the nonlinear analysis is intended to establish the local nonlinear contact deflections. Two linear finite element analysis are required to reach the global deflections because the incorrect local displacements given by the application of a nodal load at the contact position need to be removed. The full model (gear body with six teeth and fixed hub surface) will give the tooth bending, gear body and incorrect local deformations and the partial model (single tooth restrained to avoid bending and gear body deflections) will only yield the incorrect local deformations. The nonlinear single tooth pair model has all surfaces not related to the tooth contact rigidly connected to the center of the corresponding gear. The wheel tooth is fixed and the pinion tooth has the imposed torque. The finite element models are meshed with free mapped 3D tetrahedral elements with ten nodes and an average size of 1.35 mm. For the nonlinear analysis contact elements are applied and the contact zones are refined, attaining an average element dimension of 0.14 mm. The FE analysis were all run in the MSC Nastran solver by MSC Software®. Concluding, a comparison between the different models in terms of mesh stiffness accuracy and computation times is performed [122].

Feng et al. [16], whose analytical method for calculating the gear mesh stiffness of helical gears was previously presented, utilized the finite element method to validate the analytical model. ANSYS® was used to perform the FE analysis. The gear was modeled with five teeth and meshed with solid elements (SOLID185) and contact elements (TARGE170 and CONTA174) for the contact between the teeth surfaces. A layer of finer mesh was defined along the teeth profiles on the contact areas. The inner ring nodes of the driving gear are coupled to a master node at its center which is allowed to rotate freely. However, the inner ring nodes of the driven gear and the end-faces of both gears are constrained. The torque was applied on the driving gear. The results of the analytical model and others found in the literature were compared taking the finite element method described here as a reference [16].

The finite element models presented until now were dedicated to the analysis of the meshing stiffness of spur and helical gears without any kind of modification or damage. The following works [117; 118] use the finite element method to investigate the influence of tip fillet, misalignment and profile modifications on the gear mesh stiffness.

Zhan et al. [117] developed an CAD-FEM-QSA integrated technique to study the effect of tip fillet and misalignment on the gear mesh stiffness. The technique is divided into three main steps: (i) CAD modeling; (ii) finite element analysis and (iii) results generation (quasi-static algorithm). For the first step, the software NX is used for the modeling of the gear pair where five teeth are modeled on each gear. Then the finite element analysis is conducted with ANSYS® Workbench. Each gear only has the rotational degree of freedom as their hubs are connected with Body-Ground Revolute joints, one joint is assigned a very low rotational speed and the other a drive torque. The contact of the gear pair is defined resorting to frictionless and contact elements, CONTA174 and TARGE170. Only three of the five teeth are modeled with a fine mesh (the three teeth that will contact) in order to reduce the computational time. Linear finite elements SOLID185 are applied to mesh the teeth and gear body. The relative rotation between the gears can be obtained directly using the joint probe. The torsional and linear mesh stiffness can then be obtained. The tip fillet radius study showed that there is a decrease in the length of the double tooth pair contact region and an increase in the single tooth pair contact region due to the increasing tip fillet radius. The presence of misalignment reduced the mesh stiffness magnitude, affecting more significantly the double tooth contact region [117].

Wang and Howard [118] studied the effect of different profile modifications on the meshing of high contact ratio spur gears resorting to a finite element analysis. Customized ANSYS® APDL looping programs calculate the transmission error, torsional gear mesh stiffness, load sharing

ratio, contact stress and the maximum tooth root stress for various input loads over a mesh cycle. The 2D FE analysis used 4-node quadrilateral plane stress elements with an adaptive mesh for the contact points. The elements' size was defined considering the local Hertzian contact, which if not established carefully can deteriorate the quality of the numerical solution with chaotic solutions and unconverged data points. The mesh obtained is characterized by its high density on the contact points with a controlled transition to larger elements at the gear body - entire gear is modeled. The output of the numerical analysis is the torsional displacement of the driving gear hub. The hub nodes are all radially constrained and coupled to a master node at the driving gear's center of rotation. The driven gear hub was completely restrained. For each meshing position the quasi-static transmission error is obtained and after applying consecutive angular increments, the entire quasi-static transmission error curve is established. The gear mesh stiffness can be acquired by dividing the input load and the quasi-static transmission error. Four types of profile modifications were evaluated on high contact ratio spur gears with a very constructive analysis considering the applied load, contact stress, root stress, transmission error, meshing stiffness and load sharing ratio [118].

As previously stated, one of the advantages of the finite element method is the high precision representing complex geometries. By taking advantage of that, several authors developed models to study damaged gears with tooth cracks, pitting and spalling.

Zouari et al. [119] used a 3D finite element model to evaluate the effect of teeth foot cracks on the gear mesh stiffness. Only a portion of the entire gear is modeled (three teeth sector model) being clamped at its inner diameter and two lateral borders. 3D 20-node structural elements are used to mesh the three teeth considering a constant load along their width. The displacements are computed in the direction of the applied load for each meshing position. With the previously data retrieved, the gear mesh stiffness can be established and the effect of crack depth, propagation direction and position on the mesh stiffness can be evaluated [119].

Thirumurugan and Gnanasekar [116] studied the effect of different FE models, load distribution and load sharing ratio on the crack propagation path of spur gear drives resorting to ABAQUS®. Even though this work ([116]) is not focused on the analysis of the mesh stiffness of gears, it is still determined to obtain the load sharing ratio and hence the finite element model is going to be summarized. Two different 3D FE models are used, namely, a three teeth sector model (TTSM) and a single tooth sector model (STSM). Both models are meshed with linear brick elements with 8-nodes (C3D8) and constrained in the direction normal to the sector surfaces. In the TTSM, the adjacent teeth are loaded according to the meshing position. The stiffness is acquired by dividing the applied load by the deflection due to that load. The STSM and TTSM are employed to evaluate the SIFs (Stress Intensity Factors) at the crack initiation stage and the crack propagation. The FE simulation with actual load distribution showed very similar results to the experimental tests for the crack path [116].

Liang et al. [120] analyzed the effect of tooth pitting on the mesh stiffness of a spur gear pair with analytical expressions from the potential energy method and then validated them by comparing the results with a finite element computation in ANSYS®. The 3D analysis is conducted by modeling the entire gears. SOLID185 elements are used, which are mapped hexahedral for the gear body and healthy teeth but tetrahedral for the pitted tooth. The mesh is refined for six teeth when the middle one or two teeth are in mesh. As for boundary conditions, the driven gear bore is fixed and the driving gear bore is under an applied torque. The linear mesh stiffness is calculated with the angular displacement and compared with the results of the analytical model. The analytical model presented results which are in agreement with the finite element model meaning that the analytical model can estimate the gear mesh stiffness of spur gears with pitting [120].

Chen et al. [110] developed an analytical model resorting to the potential energy and slicing methods to investigate the mesh stiffness of helical gears with spalling. In order to validate the model, a finite element analysis on ANSYS® was conducted. The gear body was modeled with five teeth to improve the computational efficiency and the spalling was simplified as a parallelepiped. The mesh implemented consisted of SOLID185, CONTA174 and TARGE170 elements, being the last two types of elements used to establish the contact between the gears. The teeth in mesh are refined along their profiles. The inner hole nodes of each gear were connected to a master node at the center of each gear. Each master node was defined as a mass element (MASS21). The master node of the driven gear was fully constrained while the master node of the driving gear, which was loaded with the torque, was only allowed to rotate. The end faces of both gears were constrained to remove the effects of the axial force. The linear mesh stiffness was determined through the angular displacement [110].

Discussion Among the works presented, there are not many investigations on the effect of geometrical parameters/modifications on the gear mesh stiffness. The reason for this is the high computational costs of FEM, which is emphasized by the repeated simulations required for this kind of analysis. For these situations, analytical/approximate analytical models are the preferred choice.

When developing a finite element model for gears there are some aspects that should not be overlooked. An accurate definition of the mesh size is one of those aspects, specially for the contact and tooth root regions. Regarding the mesh on the contact region Coy and Chao [124] defined the required mesh size to properly include the Hertzian effects. Nevertheless, a convergence study must be conducted to understand the effect of the mesh applied on the output and perform an accuracy/computational cost analysis.

The finite element models are considered the most accurate and for that reason, are used as a validation tools for other types of models. However, the finite element models should be validated themselves. It is very common to find the definition of the models but not their validation. The finite element models could be validated by comparing the results with other models in the literature and/or experimental results. Just because this kind of models are very accurate it does not mean it was correctly implemented and that the results are legitimate. The finite element method is not flawless.

On a last note, the ability of the finite element method to obtain accurate results should not be exploit to validate other models. When using the finite element method, the simulation should be as close to reality as possible and not simplified so that the results are the same as the model being validated. The simplifications performed on a finite element model should neither significantly deteriorate the quality of the results nor eliminate any effect.

2.4. Hybrid models

Hybrid models are characterized by having two components, one of them is the finite element method and the other usually is an analytical method - that is why these models can also be named analytical-FE models. While the finite element method is used to compute the global deformations, the analytical method is applied to determine the local (Hertzian) deformations. By doing this, the mesh does not need to be as refined as when only using the finite element method. That being said, the major purpose of hybrid models is to reduce the computational cost of the finite element method while trying to keep a precise result. There is no detailed explanation for the hybrid models since they consist of a combination of previously displayed

methods. The following works employ hybrid models as a technique to study the mesh stiffness of gears.

Lars Vedmar [125; 126] is one of the earliest researchers to propose a hybrid model to study external involute gears. Vedmar's methodology allows to determine the gear tooth stiffness by superposition of three different cases. The first two cases correspond to a finite element analysis with concentrated loads applied at the contact position (global deflections) while the third case consists on analytically computing the local displacements. The global deflections are equal to the sum of two finite element models, namely, the full and partial models. When applying the concentrated load on the full model (first case), the results close to the nodal load will be incorrect due to local distortions, hence the need of the partial model to remove the local contribution of the displacements. This partial model (second case) is defined by a fixed layer of thickness h parallel to the tooth flank. The distance h is required to be large enough to comprise the displacements around the application point. The displacements from the second case, considering the same load as in the global model, are subtracted to the deflections of the first case thus eliminating all local displacements. In the third and final case the Hertzian displacements along the fixed layer are included by an analytical expression derived by Weber and Banascheck [125; 126].

Hedlund and Lehtovaara [123] evaluate the mesh stiffness of a helical gear pair resorting to a parameterized numerical model comprised by a finite element method for the structural analysis and a Hertzian contact analysis. The intent of using the Hertzian contact analysis is to reduce the high computational cost derived from the dense meshes required for a proper Hertzian analysis in the finite element method. The 3D FE study, developed in MATLAB®, employs eight-node trilinear hexahedral elements to model a single tooth with an elliptical foundation. The mesher automatically applies a finer mesh just bellow the teeth since that is a high stress concentration location. The structural stiffness is obtained by applying equivalent nodal loads according to the contact line. The displacement is not measured on the surface, but a few elements bellow to minimize the effect of local contact deformations. For the Hertzian contact analysis, the contact along the line of action is modeled as roller contact with radii that changes for each meshing position. The radii of curvature is calculated numerically through a circumradius method and included in the Hertzian line contact formula. The single tooth pair stiffness is computed by assuming that the structural stiffness of each tooth and the Hertzian stiffness are all in series. Then, the total mesh stiffness is obtained by summing the single tooth pair stiffness of every teeth pair in mesh. The effect of the FE mesh on the mesh stiffness results was evaluated and an analysis on the frequency domain to the mesh stiffness variation was conducted [123].

Rincon et al. [11] created an hybrid model which uses the finite element method and an analytical formulation to obtain the gear mesh stiffness for a dynamic model. The formulation of the gear mesh is comprised by three main steps, namely, the definition of the tooth geometry, the location of the contact points and the determination of the contact points' deflection. Regarding the tooth geometry, this is established based on a rack-type tool following Litvin's vector approach. The location of the contact points, which is done analytically, is accomplished by defining the separation distance between the tooth profiles. For this calculation, involute-involute and involute-rounding tip contacts as well as direct and reverse contacts are considered. The deflections of the contact points are divided into global and local deflections. The global deflections include the tooth body deflections created by the linear effects of bending, shearing and compression while the local deflections consider the nonlinear Hertzian deformations. To acquire the global deformations two FE models (global and partial models) are used, observe Figure 2.11 for a schematic of this procedure. The global model corresponds to an entire gear with only the necessary number of teeth according to the contact ratio. The usage of this kind of models

introduces a local distortion where the nodal load is applied. So, the partial model (composed by the active flank of the gear tooth) takes action to remove the distortions - the procedure consists on applying a unitary load, with opposite direction of the load applied in the global model, to the node being corrected while the nodes at the interface with the tooth are fixed. By adding the two previously mentioned FE models, one reaches the global deflections. The nonlinear local deflections are introduced via analytical formulae. The gear meshing forces are obtained by solving a nonlinear system of equations with inequality constraints. The effects of the sliding friction are also included in this model assuming a Coulomb model with constant friction coefficient and considering the direction variation of the sliding friction forces. The model was validated by comparing it with other formulations and used to study how the transmitted torque, friction and variation of the center distance affect the gear mesh stiffness. Moreover, this model was applied in other works to study the efficiency of spur gear transmissions [127–129] and the effect of manufacturing and assembly errors on the gear transmission dynamics [86; 130].

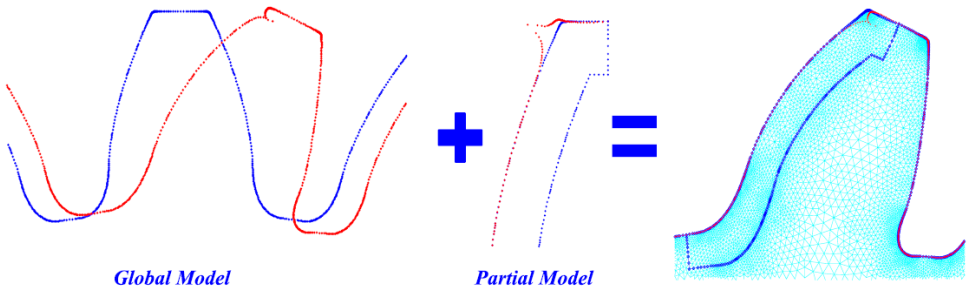

Figure 2.11: Global and partial FE models. Reprinted from [11].

Chang et al. [12] developed a model to determine the mesh stiffness of cylindrical gears which incorporates the finite element method and a local analysis of elastic bodies. The purpose of such division is to separate the linear global deformations from the nonlinear local deformations, which are calculated by the finite element method and an analytical local analysis, respectively. The usage of the finite element method for the calculation of the linear global deformations has the advantage that the mesh does not need to be as refined as it generally is for contact problems. However, one needs to extract the local deformations from the FE model. To achieve this, two FE models are employed: a full model that obtains all deformations and a partial model to determine the local distortions, see Figure 2.12. The full model is a simplification of an entire gear with three teeth while the partial model is a single tooth constrained to prevent tooth bending and gear body deflection. The global deformations are obtained by subtracting the local distortions to the deformations of the full model. The nonlinear local contact deformation was calculated from analytical formulae. The mesh stiffness model was validated and the results were in agreement with other methods. This model was then used to evaluate the effect of gear parameters on the mesh stiffness [12]. The methodology used here ([12]) to obtain the gear mesh stiffness is implemented by Yuan et al. [131] to serve as an input to a three-dimensional dynamic contact model with the aim of investigating the dynamic behavior and dynamic load distribution of cylindrical gear pairs [131].

Langlois et al. [132] implemented a hybrid Hertzian and FE-based approach to determine the transmission error of helical gears. A finite element model is responsible for incorporating the bending stiffness and base rotation of the teeth while the Hertzian contact stiffness is included via an analytical formulation. The FE model considers multiple teeth so that the compliance of adjacent teeth is taken into account. Local displacements need to be removed from the FE model due to the distortions created by the nodal load and because the contact stiffness is introduced

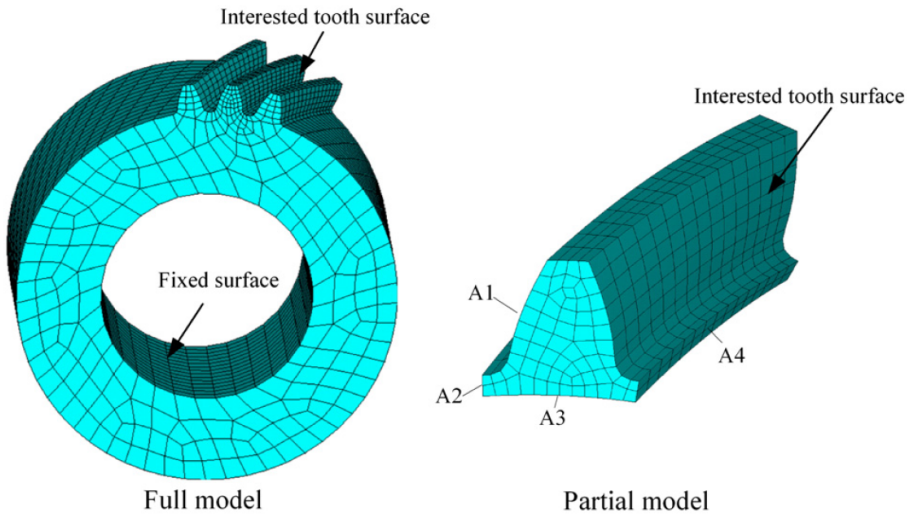

Figure 2.12: Full and partial FE models. Reprinted from [12].

by an analytical procedure. A second FE model replicating the nodal load is created to remove the local displacements. The difference is that this second model is considered to be fixed at the tooth centerline in order to disregard/minimize the tooth bending and base rotation deflections. The results from a full finite element model developed in ANSYS® corroborated the model. The influence of contact extension is evaluated, concluding that significant differences can be found on account of this effect. Furthermore, Langlois et al. also compare the transmission error curves from several model and discuss the reasons for the discrepancies encountered [132].

Chen et al. [133] created an analytical-finite element model to calculate the mesh stiffness of spur gears with complex foundation types and cracks. MATLAB® is used to develop the 2D finite element analysis which is responsible to determine the global deformations. Each gear is modeled with five teeth and the nodes located at the hub circles are constrained. A local area near the contact zone is defined as rigid in order to avoid local deformations in the FE model. This rigid area was defined with a Young's modulus 1000 times higher than the remaining body and its size, according to extensive testing, should be 0.2 the module. Figure 2.13 shows the finite element model (left) and tooth contact model (right) which enlighten the previous statements. The global stiffness is obtained with the displacements along the line of action. A nonlinear load dependent Hertzian compliance - analytical procedure - is included to account for the local deformations. The effect of the extended tooth contact was also added by considering the separation distances and the potential contact points via the deformation compatibility equation. To model the gear foundation, the planar elements' thickness is adjusted according to the gear body part they are associated to. Figure 2.14 (left side) shows the elements of the web structure in red which need to have their thickness modified to the web thickness. The 3D model used to verify this procedure is also shown in Figure 2.14 (right side). Regarding the crack path, it is included in the model by performing a separate simulation. The simulation uses a fixed crack propagation increment (0.2 mm) and a crack propagation angle which depends on the stress intensity factors - computed with a finite element model. The mesh stiffness determined by this method was validated by comparison with the potential energy method and the finite element method. The influence of the web and rim thicknesses on the mesh stiffness was evaluated and it was found that the web thickness is more impactful [133]. Huangfu et al. [134] use the same model ([133]) to estimate the gear mesh stiffness with wear for a subsequent gear dynamic analysis. The amount of wear is defined by Archard's wear prediction model and introduced as profile error in the deformation

compatibility equations. The maximum relative difference between the mesh stiffness from this model ([134]) and a finite element model for gears with different tip reliefs and wear cycles was under 6%.

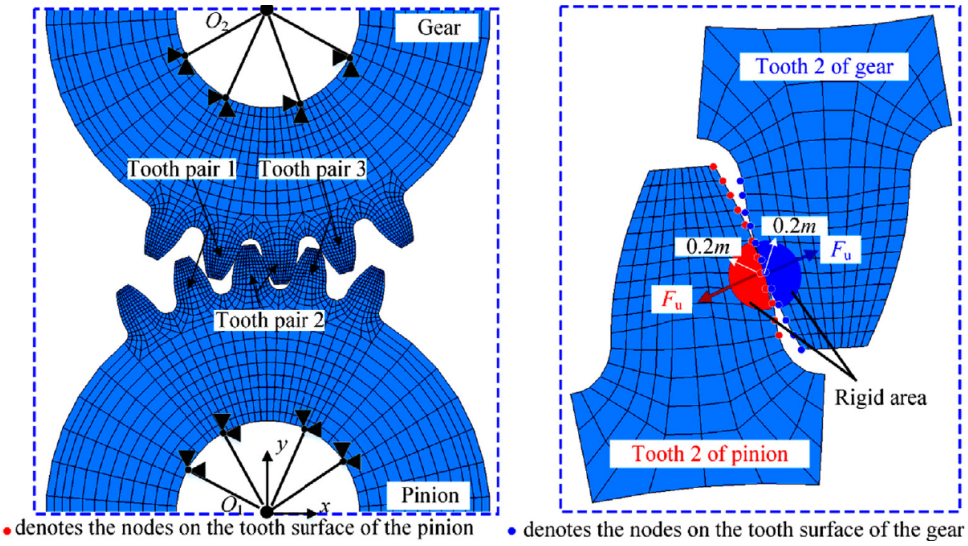

Figure 2.13: Finite element model (left) and tooth contact model (right). Reprinted from [133].

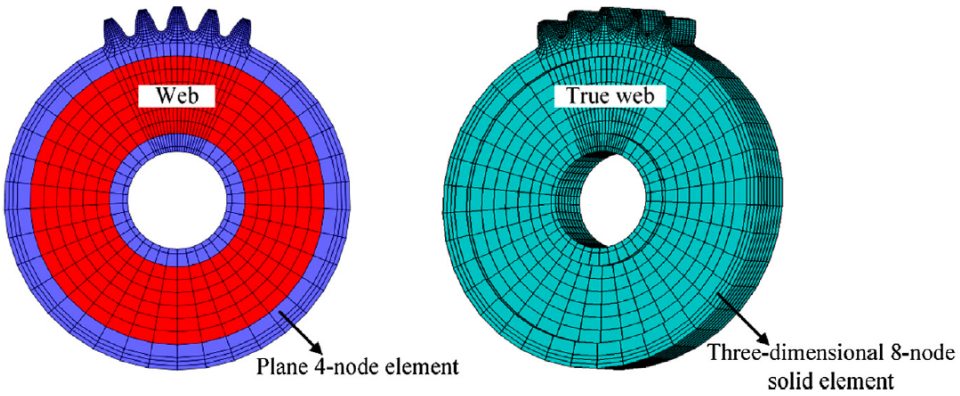

Figure 2.14: Web structure for the proposed finite element model (left) and the three-dimensional finite element model (right). Reprinted from [133].

Beinstingel et al. [82] combined a finite element analysis with an analytical description of the contact deformation to establish the mesh stiffness of cylindrical gears. The finite element method, employed to determine the global compliance factors, resorts to an isogeometric analysis to numerically describe the solid volume by means of Non-Uniform Rational B-Splines (NURBS). The global compliance factors (α_{ij}) include the tooth bending and gear body deformations in the direction normal to the contact point i for both the pinion and the wheel when a normal load is applied at contact point j. There is also a parameter that defines the theoretical distance between the pinion and the wheel along the line of action allowing to consider manufacturing errors, profile modifications and extension of contact. The coupling effects between the different gear teeth are neglected since the analysis is only conducted for a single tooth pair. The local contact deformation is introduced in the compliance matrix through analytical formula. Several mesh discretizations were tested so that the best mesh considering the relation between accuracy and computational cost is selected. The gear mesh stiffness for spur and helical gears calculated with

this model is validated and compared with other research and software tools. The approaches of the different gear mesh tools are analyzed and the reasons for the deviations found discussed [82].

Discussion Hybrid models are mainly differentiated by the strategy employed to remove the local deformations from the FE model. Three distinct techniques were used: (i) displacement of the FE model measured a few elements below the surface; (ii) definition of a rigid local area near the contact zone and (iii) an extra local FE model. The last option requires the development of another finite element model which, when compared to the other options is much more time consuming in both preparation and computation times. The other two methodologies are more straightforward since with some modifications in the FE model, the local deformations are not included. In the first technique, the local deformations are not actually removed from the model but the measurement procedure of the global deformations minimizes their effects. The second approach removes the local deformations because the location where they occur is rigid. This last technique seems to be the most balanced in terms of preparation time, computational costs and effectiveness in removing the local deformations.

2.5. Approximate analytical models

Approximate analytical models have the lowest computational cost off all models as they only require a few simple numerical steps to obtain the gear mesh stiffness. In this group of models, complex phenomena that involve many steps and high numerical computation are represented by a direct and effortless expression.

The simplicity of these models is specially highlighted while using iterative processes. In these cases, as the same calculations have to be constantly repeated, with a simple model, computation time can be drastically reduced [135]. As an example, this is the case for gear dynamic modeling and iterative gear design optimization.

The models in this section have been divided according to the approximation developed, that is, estimation of the single tooth pair mesh stiffness and estimation of the gear mesh stiffness from an analytical description of contact lines' length.

2.5.1. Models for the estimation of the single tooth pair mesh stiffness

Parabolic model

Cai and Hayashi [136] performed a linear approximation to the nonlinear equation for the rotational vibration of spur gear pairs. The analytical solution was determined and validated by comparing with the numerically calculated result of the nonlinear vibration and experimental testing [136].

During the linearization and normalization processes, the normalized equivalent error was defined. This variable is the static force-induced displacement which is a function of the normalized stiffness and normalized profile errors. Focusing on the normalized stiffness, a parabolic approximation for the stiffness of a tooth pair was developed, attend on equation (2.43) [136].

$$\hat{k^{\mathrm{tp}}} = \left[\frac{-1.8}{(\varepsilon_\alpha t_\mathrm{z})^2}t^2 + \frac{1.8}{\varepsilon_\alpha t_\mathrm{z}}t + 0.55\right]/(0.85\varepsilon_\alpha) \tag{2.43}$$

where t is the meshing time of tooth pairs, t_z is the meshing period time and ε_α is the contact

ratio. An example of the normalized single tooth pair stiffness for a gear with $\varepsilon_\alpha = 1.5$ is shown in Figure 2.15 [136].

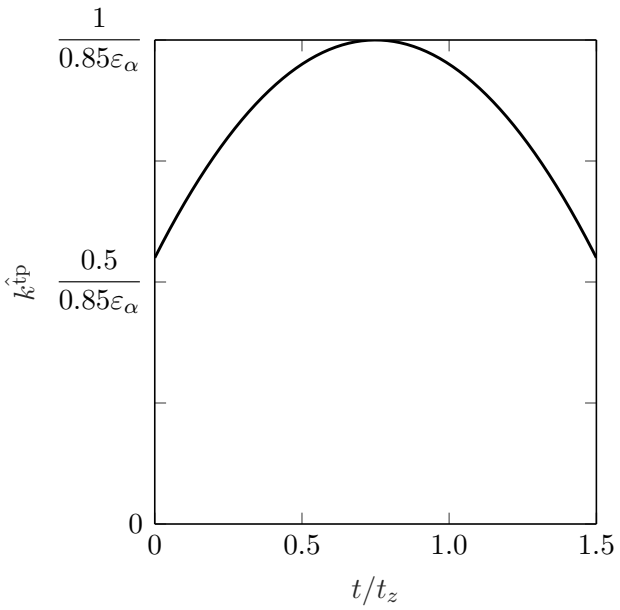

Figure 2.15: Normalized single tooth pair stiffness ($\varepsilon_\alpha = 1.5$) according to equation (2.43).

The total gear mesh stiffness is established by adding the mesh stiffness of all tooth pairs in mesh and it is normalized according to the integral average stiffness of the gear pair - K_{avg}.

The analytical approximation for the single tooth pair stiffness presented by Cai and Hayashi [136] is widely used, either for comparison with other methods or implementation in other models [136]. Later, Cai [97] developed a stiffness function for a helical involute tooth pair based on the study of Umezawa et al. [137] for a helical gear rack pair. The work of Cai [97] improved the work of Umezawa et al. [137] so that the single tooth pair mesh stiffness function took into account the number of teeth and the profile shift coefficients. This improvement was attained based on the 1990 Draft of ISO 6336 to calculate the gear stiffness value at the pitch point, equation (2.44). The helical tooth pair stiffness function agrees with other theoretical calculations and the resonance frequency estimated is in line with experimental results [97]. The single tooth pair mesh stiffness for helical gears can be calculated by equations (2.44) to (2.49).

$$K^{\mathrm{p}} = \frac{b_{\mathrm{avg}}}{c_0 + c_1\left(\frac{1}{z_{\mathrm{v1}}} + \frac{1}{z_{\mathrm{v2}}}\right) + c_2\left(\frac{x_1}{z_{\mathrm{v1}}} + \frac{x_2}{z_{\mathrm{v2}}}\right) + c_3\left(\frac{1}{z_{\mathrm{v1}}^2} + \frac{1}{z_{\mathrm{v2}}^2}\right) + c_4\left(x_1 + x_2\right) + c_5\left(x_1^2 + x_2^2\right)} \tag{2.44}$$

In equation (2.44) c_0 is defined according to equation (2.45).

$$c_0 = \frac{2.25}{\left[-0.166\ \left(b_{\mathrm{avg}}/H_{\mathrm{t}}\right) + 0.08\right]\left(\beta\frac{180}{\pi} - 5\right) + 44.5} \tag{2.45}$$

The coefficients c_1 to c_5, presented in equation (2.44), were adjusted using the least squares approximation, resulting in: $c_1 = -0.00854$; $c_2 = -0.11654$; $c_3 = 2.9784$; $c_4 = -0.00635$ and

$c_5 = 0.00529$. b_{avg} is the effective gear facewidth and H_{t} is the total tooth depth, defined respectively in equations (2.46) and (2.47).

$$b_{\text{avg}} = \frac{b_1 + b_2}{2} \tag{2.46}$$

$$H_{\text{t}} = 2.25\ m \tag{2.47}$$

The single tooth pair mesh stiffness was then calculated according to equation (2.48), where C_{a} was defined according to equation (2.49).

$$k^{\text{tp}}(t) = K^{\text{p}} \exp\left(C_{\text{a}} \left| \frac{t - (\varepsilon t_{\text{z}})/2}{1.125\ \varepsilon_\alpha t_{\text{z}}} \right|^3\right) \tag{2.48}$$

$$C_{\text{a}} = 0.322\ (\beta \frac{180}{\pi} - 5) + [0.23\ (b_{\text{avg}}/H_{\text{t}}) - 23.26] \tag{2.49}$$

Cosine model

Sánchez et al. [19] approached a previously developed load distribution model based on the potential energy method [73] from the stiffness point of view in order to easily introduce the effects of Hertzian stiffness [19].

The single tooth pair stiffness (k^{tp}), which depends on the contact point ξ_{C}, is given by equation (2.50) [19].

$$k^{\text{tp}}(\xi_{\text{C}}) = \left(\frac{1}{k_1^{\text{st}}} + \frac{1}{k_2^{\text{st}}}\right)^{-1} = \left(\frac{1}{k_{\text{b1}}} + \frac{1}{k_{\text{s1}}} + \frac{1}{k_{\text{a1}}} + \frac{1}{k_{\text{b2}}} + \frac{1}{k_{\text{s2}}} + \frac{1}{k_{\text{a2}}}\right)^{-1} \tag{2.50}$$

Equation (2.50) shows that the single tooth pair stiffness is obtained by adding the tooth stiffness of the pinion (k_1^{st}) and the wheel (k_2^{st}). Further, each tooth stiffness is the sum of the bending (k_{b}), shear (k_{s}) and compressive (k_{a}) stiffnesses. It was verified that the shape obtained when plotting equation (2.50) for different gears was always very similar. By considering a normalization so that $K_{\text{max}}^{\text{tp}}$ is equal to 1, an approximate equation to the normalized single tooth pair stiffness can be defined as shown in equation (2.51) [19].

$$\hat{k^{\text{tp}}}(\xi_{\text{C}}) \simeq \cos\left(b_0\ (\xi_{\text{C}} - \xi_{\text{m}})\right) \tag{2.51}$$

where b_0 and ξ_{m} are presented in equations (2.52) and (2.53), respectively [19].

$$b_0 = \left[\frac{1}{2}\left(1 + \frac{\varepsilon_\alpha}{2}\right)^2 - 1\right]^{-1/2} \tag{2.52}$$

$$\xi_{\text{m}} = \xi_{\text{inn}} + \frac{\varepsilon_\alpha}{2} \tag{2.53}$$

ξ_{inn} is the normalized coordinate for the start point of meshing.

The approximation defined by equations (2.51) to (2.53) does not include the contributions of the Hertzian deflections. Updating the single tooth pair stiffness (equation (2.50)) to include the Hertzian stiffness leads to equation (2.54) [19].

$$k^{\mathrm{tp}}(\xi_{\mathrm{C}}) = \left(\frac{1}{k^{\mathrm{tp}}} + \frac{1}{k_{\mathrm{H}}}\right)^{-1} = \left(\frac{1}{k_{\mathrm{b1}}} + \frac{1}{k_{\mathrm{s1}}} + \frac{1}{k_{\mathrm{a1}}} + \frac{1}{k_{\mathrm{b2}}} + \frac{1}{k_{\mathrm{s2}}} + \frac{1}{k_{\mathrm{a2}}} + \frac{1}{k_{\mathrm{H}}}\right)^{-1} \tag{2.54}$$

The Hertzian stiffness is defined according to equation (2.55) [19].

$$k_{\mathrm{H}} = \frac{\pi}{4}\frac{Eb}{1-\nu^2} \tag{2.55}$$

E is the modulus of elasticity, b is the gear width and ν is the Poisson's ratio.

Modifications to the approximate formulation given by equations (2.51) to (2.53) are required to introduce the effects of the Hertzian stiffness. According to the authors [19], equations (2.51) and (2.53) are kept the same and only the parameter b_0 is adjusted, see equation (2.56) [19].

$$b_0 = \left[\frac{1}{2}\left(1.11 + \frac{\varepsilon_\alpha}{2}\right)^2 - 1.17\right]^{-1/2} \tag{2.56}$$

In order to validate the Cosine approximation with Hertzian stiffness - equations (2.51), (2.56) and (2.53) - two different separate studies for low and high contact ratio spur gears were conducted. 3775 cases for low contact ratio spur gears and 2835 cases for high contact ratio spur gears were compared with the numerical results obtained by integration. Note that these spur gear geometries were obtained by combining geometrical parameters in a limited range. The Cosine approximation model with Hertzian effects was successfully validated and applied in the calculation of contact and tooth root stresses [19].

This model was further improved by the introduction of the extension of contact and profile modifications [138; 139]. In [138] the authors enhanced the model and analyzed the influence of profile modifications on the mesh stiffness, transmission error and load sharing ratio for spur gears. Then, by taking advantage of such model, optimum tip reliefs for minimum peak-to-peak amplitude of quasi-static transmission error and minimum dynamic load where obtained [139]. In the latest work, Pleguezuelos et al. [140] study, with this model, the gear meshing of spur gears with profile modifications under non-nominal/variable loading conditions [140].

2.5.2. Models based on the analytical description of the contact lines' length

Fourier model

Gu et al. [13] investigated an analytical description for the mesh stiffness of solid spur and helical gears. For this method, the thin-slice approach is applied so gears are defined as the stack of infinitesimal width gears that are staggered for helical gears. This approach also divides the contact lines, therefore infinitesimal contact segments of length dM are created. The overall mesh stiffness, presented in equation (2.57), can be defined associating a normal stiffness per unit of contact length, $K^M(\tau)$, with every length segment [13].

$$K(\tau) = \int_{L_{\mathrm{gm}}(\tau)} K^M(\tau)\,\mathrm{d}M \tag{2.57}$$

τ is the time normalized to the mesh period and $L_{\mathrm{gm}}(\tau)$ is the time-varying contact length. $K^M(\tau)$ consists on the pinion and the wheel structural stiffness as well as the contact stiffness [13].

There are two effects that are neglected due to the usage of the formulation presented in equation (2.57). One of them is the intertooth elastic couplings and the other is the elastic couplings between the points of contact on the same tooth pair [13].

The normal stiffness for an ideal unmodified tooth pair of infinitesimal width, $K^M(\tau)$, can be established in equation (2.58) [13].

$$K^M(\tau) = k_0 \left(1 + \alpha_{\mathrm{Fourier}}\, \varphi_M(\tau)\right) \tag{2.58}$$

In equation (2.58), k_0 is the average mesh stiffness per unit of contact length which is defined, for example, according to ISO 6336 [141]. $\alpha_{\mathrm{Fourier}}$ is the relative variation in stiffness amplitude and $\varphi_M(\tau)$ represents the shape variation during meshing, which is approximated by the parabolic expression in equation (2.59) [13].

$$\varphi_M(\tau) \cong A + B\tau + C\tau^2 \tag{2.59}$$

The integral in equation (2.57) can be determined by a discrete summation over the instantaneous contact lines and resorting to a Fourier series. Fourier series are utilized to represent the meshing conditions as they are repeated every mesh period.

The dimensionless time-varying mesh stiffness function, presented in equation (2.60), can be computed considering the previous statements [13].

$$\begin{aligned}\hat{K}(\tau) = 1 + \sum_{k=1}^{\infty} \frac{\mathrm{Sinc}\left(k\varepsilon_\beta\right)}{\pi k \varepsilon_\alpha} \Bigg[& 2\sin\left(\pi k \varepsilon_\alpha\right)\cos\left(\pi k\left(2\tau - \varepsilon_\alpha - \varepsilon_\beta\right)\right) + \\ & + \alpha_{\mathrm{Fourier}} \left(-A + \frac{C}{2\pi^2 k^2}\right) \sin\left(\pi k\left(-2\tau + \varepsilon_\beta\right)\right) + \\ & + \alpha_{\mathrm{Fourier}} \left(A + B\varepsilon_\alpha + C\varepsilon_\alpha^2 \left(1 - \frac{1}{2\pi^2 k^2 \varepsilon_\alpha^2}\right)\right) \sin\left(\pi k\left(2\varepsilon_\alpha - 2\tau + \varepsilon_\beta\right)\right) + \\ & + \alpha_{\mathrm{Fourier}} \left(-\frac{B}{2\pi k}\right) \cos\left(\pi k\left(-2\tau + \varepsilon_\beta\right)\right) + \\ & + \alpha_{\mathrm{fourier}} \left(\frac{B}{2\pi k} + \frac{C\varepsilon_\alpha}{\pi k}\right) \cos\left(\pi k\left(2\varepsilon_\alpha - 2\tau + \varepsilon_\beta\right)\right) \Bigg]\end{aligned} \tag{2.60}$$

$\hat{K}(\tau) = K(\tau)/K_{\mathrm{avg}}$ and $\mathrm{Sinc}(X) = \sin(\pi X)/\pi X$ is the sine cardinal function [13].

The values of the coefficients for the stiffness time-variations (A, B and C) can be established assuming that the tooth pair stiffness for any infinitesimal spur gear is symmetric between approach and recess. Normalizing the function so that $\varphi_M(\tau = 0) = \varphi_M(\tau = \varepsilon_\alpha) = -1$ and by applying $\int_0^{\varepsilon_\alpha} \varphi_M(\tau) d\tau = 0$, the values $A = -1$, $B = 6/\varepsilon_\alpha$ and $C = -6/\varepsilon_\alpha^2$ are reached. The relative variation in stiffness amplitude $\alpha_{\mathrm{Fourier}}$ was set to 0.3 which is an average value considering the works of other authors in the literature [13].

The expression for the dimensionless time-varying mesh stiffness can be further simplified by

replacing the coefficients by their values, as presented in equation (2.61) [13].

$$\hat{K}(\tau) = 1 + 2\sum_{k=1}^{\infty} \Xi_k(\varepsilon_\alpha)\,\mathrm{Sinc}(k\varepsilon_\beta)\cos(\pi k(2\tau - \varepsilon_\alpha - \varepsilon_\beta)) \tag{2.61}$$

where the function $\Xi_k(\varepsilon_\alpha)$ is defined in equation (2.62).

$$\Xi_k(\varepsilon_\alpha) \cong \left(0.7 + \left(0.09/k^2\varepsilon_\alpha^2\right)\right)\mathrm{Sinc}(k\varepsilon_\alpha) - \left(0.09/k^2\varepsilon_\alpha^2\right)\cos(\pi k\varepsilon_\alpha) \tag{2.62}$$

The model established in equation (2.60) and (2.61) was validated resorting to refined 2D finite element models and benchmark results from the literature [13].

The Fourier model shows that the mesh stiffness fluctuations can be controlled by only a few parameters. Moreover, it gives fast mesh stiffness estimations that allow to perform parametric studies and be included in dynamic models.

Heaviside model

In past investigations, Marques et al. [135] introduced the Heaviside analytical contact line length and mesh stiffness models [135; 142], which were used to study the length of a gear pair's contact lines and to obtain a new gear design with reduced vibrations and dynamic overload as well as potential noise reduction [8].

Continuing to improve on these investigations [135], Marques et al. [143] have introduced an analytical mesh stiffness/load sharing ratio and friction torque models that rely on the same contact lines' length description based on the Heaviside function [143]. The model is valid for parallel axis spur and helical gears and it has no limitations in the admissible range for overlap and contact ratios. One of the main innovations of this work is in the mathematical approach that was introduced which allowed a continuous description of the gearing phenomena without using piecewise functions. Furthermore, the contact line stiffness and line load sharing functions were not assumed uniform. The work [143] is quite lengthy and goes into the details of establishing each equation that was proposed. Here, only the main and essential equations related to the determination of the gear mesh stiffness will be presented and discussed.

Marques et al. [143] start by defining a set of normalized coordinates based on the gear geometry, ξ and η. ξ is the coordinate along the path of contact with origin at the theoretical start point of meshing, point A in Figure 2.16, and normalized using the transverse base pitch, p_{bt}. η is the coordinate along a contact line normalized by the quantity $b/\cos\beta_{\mathrm{b}}$, which has either the ξ axis ($\xi < \varepsilon_\alpha$) or the line of the theoretical end point of meshing EE' ($\xi > \varepsilon_\alpha$) as an origin - see Figure 2.16 [143].

It is based on this coordinate system that the analytical description of the length of the contacting lines using the Heaviside approach is presented. The Heaviside function was selected due to its step like shape which is representative of the behavior of the length of the lines of contact for spur gears. In addition, the Heaviside function can be combined with linear functions to replicate the behavior of helical gears. The Heaviside function was approximated using equation (2.63) using a value of $K_H = 10^4$ [143].

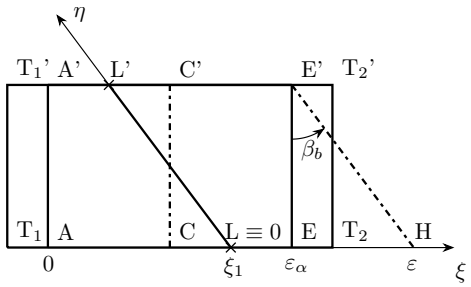

Figure 2.16: Definition of coordinates ξ and η for a gear with an arbitrary overlap ratio, ε_β. Reprinted from [143].

$$H(\xi) = \lim_{K_H \to +\infty} \left(\frac{1}{1 + e^{-2\,K_H\,\xi}} \right) \tag{2.63}$$

Equations (2.64) and (2.65) represent the length of the lines of contact over tooth i for spur and helical gears respectively. This way for a tooth pair that is currently in mesh, the length of the lines of contact for all the meshing tooth pairs that will enter the contact can be accounted for by making $i = -\,\text{floor}(\varepsilon) : 1 : \text{floor}(\varepsilon)$. In equations (2.64) and (2.65), ε_α is the contact ratio, ε_β is the overlap ratio, ε is the total contact ratio ($\varepsilon = \varepsilon_\alpha + \varepsilon_\beta$) and floor is a rounding down function [143].

$$Ul_i^s(\xi, i) = \Big[H(\xi - i) - H(\xi - \varepsilon_\alpha - i) \Big] \tag{2.64}$$

$$\begin{aligned} Ul_i^h(\xi, i) = \frac{1}{\varepsilon_\beta} \Big[& H(\xi - i)\,(\xi - i) - H(\xi - \varepsilon_\beta - i)\,(\xi - \varepsilon_\beta - i) \\ & - H(\xi - \varepsilon_\alpha - i)\,(\xi - \varepsilon_\alpha - i) H(\xi - \varepsilon - i)\,(\xi - \varepsilon - i) \Big] \end{aligned} \tag{2.65}$$

In order to establish the single tooth pair mesh stiffness, it is assumed that a gear can be viewed as a stack of coupled thin slices, where the coupling stiffness between slices can be described using a parabolic function, k_L, along the contact line (coordinate η). The single tooth pair slice stiffness along the path of contact (coordinate ξ), $k_i^{s,h}$, is also assumed parabolic. The maximum single tooth pair mesh stiffness was calculated according to ISO 6336 [141] ($K_\mathrm{max}^\mathrm{ISO}$), therefore, due to the parabolic line load assumption, in order to keep a compatibility between this standard and the proposed model, a stiffness correction factor is introduced, equation (2.66). In equation (2.66), ε_L is the maximum length of a line of contact normalized to $\frac{b}{\cos\beta_\mathrm{b}}$, which is equal to 1 for spur gears ($\varepsilon_\mathrm{L} = 1$), while for helical gears it depends on the relationship between ε_α and ε_β, as described by equation (2.67) [143].

$$K_\mathrm{max}^\mathrm{ISO}\,\varepsilon_\mathrm{L} = c_\mathrm{f}^{s,h}\,K_\mathrm{max}^\mathrm{ISO} \int_0^{\varepsilon_\mathrm{L}} \left[k_i^{s,h} \left(\frac{\varepsilon}{2}, \eta, 0 \right)\; k_L \left(\frac{\varepsilon}{2}, \eta, 0 \right) \right] \mathrm{d}\eta \tag{2.66}$$

$$\varepsilon_\mathrm{L} = \frac{1}{\varepsilon_\beta} \Big[\varepsilon_\beta - H(\varepsilon_\beta - \varepsilon_\alpha)\,(\varepsilon_\beta - \varepsilon_\alpha) \Big] \tag{2.67}$$

The normalized single tooth pair mesh stiffness can then be established using equation (2.68) [143].

$$\hat{k^{\mathrm{tp}}}(\xi, i) = c_{\mathrm{f}}^{s,h} \int_0^{Ul_i^{s,h}} \left(k_i^{s,h}\ k_{\mathrm{L}}\right) \mathrm{d}\eta \tag{2.68}$$

The aforementioned principle (equation (2.68)) is applied to spur and helical gears. Marques et al. [143] concluded that the normalized single tooth pair mesh stiffness of spur gears is not affected by the stiffness distribution along a contact line, resulting in the product between lines' length and single slice tooth mesh stiffness, equation (2.69). The normalized unbounded single tooth pair mesh stiffness for spur gears is defined according to equation (2.70) [143].

$$\hat{k^{\mathrm{tp}^s}}(\xi, i) = Ul_i^s\ \hat{k_U^{\mathrm{tp}^s}} \tag{2.69}$$

$$\hat{k_U^{\mathrm{tp}^s}}(\xi, i) = \frac{4(\alpha_k - 1)}{\varepsilon_\alpha^2}(\xi - i)^2 - \frac{4(\alpha_k - 1)}{\varepsilon_\alpha}(\xi - i) + \alpha_k \tag{2.70}$$

The application of this principle (equation (2.68)) to helical gears brought additional complexity which is mainly related to the mathematical description of the problem for $\xi > \varepsilon_\alpha$. The same principles that were described still apply, however the necessary equations are different and necessarily more complex. For this reason, only the equations essential to the implementation of this model are presented. The details behind each equation are exhaustively discussed in Marques et al. [143].

From the adoption of equation (2.68) to helical gears, the normalized single tooth pair mesh stiffness is obtained, equation (2.71). Note that the correction factor for the maximum normalized single tooth pair mesh stiffness for helical gears c_{f}^h, defined in equation (2.72), does not cancel out and therefore appears in equation (2.71) [143].

$$\begin{aligned}
\hat{k^{\mathrm{tp}^h}}(\xi, i) = Ul_i^h \Bigg[& \varepsilon_\beta^2 \frac{AB}{5} Ul_i^{h\,4} - \varepsilon_\beta \frac{AB}{4} Ul_i^{h\,3} \Big[\varepsilon_\beta \varepsilon_{\mathrm{L}} - \varepsilon_\alpha + 2\big(\xi - \phi_i^{\mathrm{L}} \varepsilon_\beta - \kappa\big)\Big] \\
& + \frac{Ul_i^{h\,2}}{3} \Bigg[\alpha_{\mathrm{L}} B \varepsilon_\beta^2 + A\Big[\alpha_k + B\Big(\kappa\big(2\varepsilon_\beta\big(2\phi_i^{\mathrm{L}} - \varepsilon_{\mathrm{L}}\big) - 2\xi + \varepsilon_\alpha\big) \\
& - \xi\big(2\varepsilon_\beta\big(2\phi_i^{\mathrm{L}} - \varepsilon_L\big) + \varepsilon_\alpha\big) + \varepsilon_\beta\big(\phi_i^{\mathrm{L}} \varepsilon_\beta\big(\phi_i^{\mathrm{L}} - \varepsilon_{\mathrm{L}}\big) - \varepsilon_\alpha\big(\varepsilon_{\mathrm{L}} - 2\phi_i^{\mathrm{L}}\big)\big) + \kappa^2 + \xi^2\Big)\Big]\Bigg] \\
& + \frac{Ul_i^h}{2} \Bigg[\alpha_{\mathrm{L}} B \varepsilon_\beta\big(2\kappa - 2\xi + \varepsilon_\alpha\big) - A\Big[\alpha_k\big(\varepsilon_{\mathrm{L}} - 2\phi_i^{\mathrm{L}}\big) + B\Big(\kappa\big(2\phi_i^{\mathrm{L}} \varepsilon_\beta\big(\varepsilon_{\mathrm{L}} - \phi_i^{\mathrm{L}}\big) + \\
& \big(\varepsilon_\alpha - 2\xi\big)\big(\varepsilon_{\mathrm{L}} - 2\phi_i^{\mathrm{L}}\big)\big) + \varepsilon_\beta \phi_i^{\mathrm{L}}\big(\phi_i^{\mathrm{L}} - \varepsilon_{\mathrm{L}}\big)\big(2\xi - \varepsilon_\alpha\big) \\
& + \big(\kappa^2 + \xi^2 - \varepsilon_\alpha \xi\big)\big(\varepsilon_{\mathrm{L}} - 2\phi_i^{\mathrm{L}}\big)\Big)\Big]\Bigg] \\
& + \Big(\alpha_{\mathrm{L}} + A\phi_i^{\mathrm{L}}\big(\phi_i^{\mathrm{L}} - \varepsilon_{\mathrm{L}}\big)\Big)\Big(\alpha_k + B\big(\kappa - \xi\big)\big(\kappa - \xi + \varepsilon_\alpha\big)\Big)\Bigg] c_{\mathrm{f}}^h
\end{aligned} \tag{2.71}$$

$$c_{\mathrm{f}}^{h} = \varepsilon_{\mathrm{L}}\left[\frac{1}{120}\left(10\alpha_{\mathrm{L}}\varepsilon_{\mathrm{L}}\left(12\alpha_k + B\left(\varepsilon_\beta^2\left(4\varepsilon_{\mathrm{L}}^2 - 6\varepsilon_{\mathrm{L}} + 3\right) + 12\varepsilon_\beta\psi\left(\varepsilon_{\mathrm{L}} - 1\right) + 12\psi^2 - 3\varepsilon_\alpha^2\right)\right)\right.\right.$$
$$\left.\left. - A\varepsilon_{\mathrm{L}}^3\left(20\alpha_k + B\left(\varepsilon_\beta^2\left(6\varepsilon_{\mathrm{L}}^2 - 10\varepsilon_{\mathrm{L}} + 5\right) + 20\varepsilon_\beta\psi\left(\varepsilon_{\mathrm{L}} - 1\right) + 20\psi^2 - 5\varepsilon_\alpha^2\right)\right)\right)\right]^{-1} \tag{2.72}$$

Equations (2.71) and (2.72) depend on the parameters defined by equations (2.67) and (2.73) to (2.79) [143].

$$\phi_i^{\mathrm{L}}(\xi, i) = \frac{1}{\varepsilon_\beta}H(\xi - i - \varepsilon_\alpha - (1 - \varepsilon_{\mathrm{L}})\,\varepsilon_\beta)\,(\xi - i - \varepsilon_\alpha - (1 - \varepsilon_{\mathrm{L}})\,\varepsilon_\beta) \tag{2.73}$$

$$A = \frac{4\,(\alpha_{\mathrm{L}} - 1)}{{\varepsilon_{\mathrm{L}}}^2} \tag{2.74}$$

$$B = \frac{4\,(\alpha_k - 1)}{\varepsilon_\alpha^2} \tag{2.75}$$

$$\kappa = i + \phi_i \tag{2.76}$$

$$\phi_i(\xi, i) = \varepsilon_\beta\left[Ul_i^\infty - Ul_i^h\right] \tag{2.77}$$

$$Ul_i^\infty(\xi, i) = \frac{1}{\varepsilon_\beta}\Big[H(\xi - i)\,(\xi - i) - H(\xi - \varepsilon_\beta - i)\,(\xi - \varepsilon_\beta - i)\Big] \tag{2.78}$$

$$\psi = \frac{\varepsilon}{2} - H\left(\frac{\varepsilon}{2} - \varepsilon_\beta\right)\,\left(\frac{\varepsilon}{2} - \varepsilon_\beta\right) - \varepsilon_\beta\varepsilon_{\mathrm{L}} \tag{2.79}$$

Taking into account the necessary equations, for spur or helical gears, the normalized gear mesh stiffness can be calculated by superposition of effects according to equation (2.80) [143].

$$\hat{K^{s,h}}(\xi) = \left[\sum_{i=-\mathrm{floor}(\varepsilon)}^{\mathrm{floor}(\varepsilon)} \hat{k^{\mathrm{tp}}}\right] Tl^{s,h} \tag{2.80}$$

$Tl^{s,h}(\xi)$, equation (2.81), is a function whose purpose is to trim and bound $\hat{K^{s,h}}(\xi)$, so that $\hat{K^{s,h}}(\xi) \neq 0$ only for $\xi \in [0; \varepsilon]$ [143].

$$Tl^{s,h}(\xi) = H(\xi) - H(\xi - \varepsilon) \tag{2.81}$$

The absolute gear mesh stiffness can then be estimated by taking the product of the maximum single tooth pair mesh stiffness from ISO 6336 [141] ($K_{\mathrm{max}}^{\mathrm{ISO}}$) and the normalized gear mesh

stiffness ($\hat{K^{s,h}}(\xi)$, equation (2.80)), resulting in equation (2.82) [143].

$$K(\xi) = K_{\max}^{\mathrm{ISO}} \cdot \hat{K^{s,h}}(\xi) \tag{2.82}$$

In equations (2.70), (2.71) and (2.72) , α_k is the ratio between the single tooth pair (slice) stiffness at $\xi = 0$ and $\xi = \varepsilon_\alpha$ and its value at $\xi = \frac{\varepsilon_\alpha}{2}$ [143].

Due to its importance, an equation for the estimation of α_k is also presented, equation (2.83), where $\mathcal{R}$ is the load sharing ratio for a spur gear at the start of meshing ($\xi = 0$). It is relevant to point out that equation (2.83) is only valid for $\varepsilon_\alpha \in]1;2[$. From the AGMA 925-03 [144] and the work of Sánchez et al. [19] a value of $\mathcal{R} = 0.36$ is suggested [143].

$$\alpha_k = -\frac{4\mathcal{R}\left(\varepsilon_\alpha - 1\right)}{\varepsilon_\alpha^2\left(2\mathcal{R} - 1\right) - 4\mathcal{R}\varepsilon_\alpha + 4\mathcal{R}} \tag{2.83}$$

Additionally, in equations (2.71) and (2.72) α_{L} is the ratio between the contact line stiffness at $\eta = 0$ and $\eta = 1$ and its value at $\eta = \frac{1}{2}$. Based on the work of Yu and Mechefske [14], a guiding value of $\alpha_{\mathrm{L}} = 0.25$ is suggested. Note that for a value of $\alpha_{\mathrm{L}} = 1$, the line stiffness sharing function becomes uniform, thus removing the slice coupling effect, making it comparable to the Fourier model suggested by Gu et al. [13].

Discussion The approximate analytical models require a balance between accuracy and computation time. The approximation performed cannot neither be computational expensive nor deteriorate the quality of the results. Four approximate analytical models were presented, which can be divided in two groups: models based on the approximation of the single tooth pair stiffness and models based on the analytical description of the length of the contact lines.

In the first group are the models from Cai and Hayashi [136] (parabolic approximation) and Sánchez et al. [19] (cosine approximation) which are both very similar regarding computational time and effectiveness in the approximation for spur gears. The models of Cai and Hayashi [136] and Cai [97] can be applied to spur and helical gears, while the model of Sánchez et al. [19] was developed exclusively for spur gears. The model of Sánchez et al. [19] explicitly considered the Hertzian contact stiffness while the works of Cai and Hayashi [97; 136] did not.

Regarding the second group, the Fourier series in Gu et al. [13] and the Heaviside function in Marques et al. [143] are used to describe the length of the contacting lines. These two models also resort to a quadratic approximation of the single tooth pair slice stiffness to determine the gear mesh stiffness. In addition, the model proposed by Marques et al. [143] considers slice coupling through a parabolic stiffness sharing function along the contact line, while the Fourier model does not. The Gu et al. [13] model, based on Fourier series, presents overshoot at step like discontinuities (Gibbs phenomenon) whereas the Heaviside function describes the contact line length behavior of spur gears the best since they both theoretically behave like step functions. Furthermore, in the Fourier model the contribution of each meshing tooth pair cannot be separated from the gear mesh stiffness, while in the Heaviside model this is possible.

As for the computational cost among the approximate analytical models, the Fourier model should be the most expensive model due to the need to sum a large amount of harmonics to obtain a reasonably accurate solution while the remaining models ought to have similar costs. Although, for dynamic analysis, the Fourier model is more suitable due to the ease in separating the gear mesh stiffness in its fundamental harmonics. Both Fourier and Heaviside models depend on an

adjusting parameter (α_{Fourier} and α_k) that describes the relationship between the maximum of the single tooth pair slice mesh stiffness and its values at the start and end points of meshing. A relationship between each of the adjusting parameters can be established such as $\alpha_{\text{Fourier}} = 1 - \alpha_k$.

A final note on the coordinate systems used to describe the gear mesh stiffness along the path of contact according to the different models should be made. The works of Cai [97]; Cai and Hayashi [136] and Gu et al. [13] take advantage of the meshing time normalized to the mesh period, counting from the start of meshing (point A in Figure 2.16). The model proposed by Marques et al. [143] has a similar approach, but instead of considering time quantities, their spatial equivalents are used, resulting in a mathematical similarity between the coordinate of these three models, as stated in equation (2.84).

$$\tau = \frac{t}{t_z} = \xi \tag{2.84}$$

Despite Sánchez et al. [19] considering the spatial coordinate normalized to the spatial mesh period, the starting point for the coordinate is the contact point tangent at the base circle of the driving gear, point T_1 in Figure 2.16. In order to represent the model of Sánchez et al. [19] in the same coordinate system as the other three models, the transformation stated in equation (2.85) must be considered.

$$\xi_C = \xi + \xi_{\text{inn}} \tag{2.85}$$

2.6. Polymer gears

A dedicated section to polymer gears is presented since the majority of gear mesh stiffness investigations are devoted to steel gears and there are significant differences on the gear mesh stiffness modeling for each type of material. Polymer gears have a lightweight nature, self-lubricating ability, are quieter, more resistance to corrosion and have lower mass production costs than steel gears [145–151]. On the other hand, this type of gears have, when compared to steel gears, reduced load capacity, inferior temperature resistance and thermal conductivity, worse manufacturing tolerances, might be sensible to humidity and have a short running life, limiting the applicability of these gears [146–148; 151]. All these different characteristics lead to distinct failure modes which are reported in [152]. The meshing of polymer gears is more complex than metal gears because of the added dependencies on the displacement, temperature and humidity (depending on the hygroscopic behavior of the material). Hence, to properly establish the mesh stiffness of polymer gears these factors need to be accounted for.

In the following works, not all of them directly investigate the mesh stiffness of polymer gear, although they analyze the meshing characteristics mainly through the transmission error, which can be related to the gear mesh stiffness. Besides that, the models developed on those works can be used to extract the gear mesh stiffness, hence, these investigations are summarily presented.

Tsai and Tsai [145] performed a multi-tooth contact analysis using the finite element method, more precisely, the contact option of the finite element package MARC to study the static transmission error of plastic spur gears. A four or five teeth sector gear model is employed where the two contacting teeth are more refined. The elements used for the mesh are quadrilateral plane strain elements. Concerning the boundary conditions, the driven gear is fixed while the driving gear is, at every increment, rotated by a small angle. Two different configurations were implemented, them being, steel/plastic gears and plastic/plastic gears. The finite element results

were compared with an analytical method for steel gears which did not consider the extension of contact. It was concluded that the large tooth deflections in plastic gears cannot be disregarded as it leads to significant deviations in the determination of the transmission error. The mentioned analytical model was modified to include the extension of contact and the new results were significantly improved to the extent that only slight differences can now be detected [145].

Lin and Kuang [146] determined the mesh stiffness of plastic spur gears for a dynamic model resorting to the finite element method. The model consists of a full gear and a partial cylinder that changes its radius of curvature according to the contact point being analyzed. The gear has a finer mesh on the measured teeth and even more refined mesh near the contact region. The MARC finite element package is used with its contact elements to obtain the single tooth stiffness. The stiffness results for Nylon 66 at 20°C are curve-fitted and defined by the number of teeth, profile shift coefficient, loading position, pitch radius and module. Five characteristic loading points are selected for the approximation. From the simulations conducted, the single tooth stiffness for POM at 20°C is approximated as 1.5 times the single tooth stiffness of Nylon 66. In order to include the effects of temperature on the gear mesh stiffness, a linear relationship between the stiffness and the Young's modulus was considered. The single tooth stiffness for any temperature is acquired by describing the Young's modulus as a function of temperature. The gear mesh for the plastic gear is finally defined considering the number of tooth pairs in contact and that each tooth pair is formed by two springs in series. The mesh stiffness is inserted in a dynamic model to study the relations between the dynamic contact loads and the tooth profile wear [146].

Karimpour et al. [147] investigated the meshing kinematics of polymer spur gears resorting to the finite element model in ABAQUS® and analytical procedures in the BS ISO 6336. The contact behavior of polymer gears was analyzed through the load sharing ratio, bending stresses and contact stresses. There is not a direct study of either the transmission error or the mesh stiffness, nevertheless, a finite element model for polymer gears is presented along with an evaluation of the load sharing ratio and the extension of the path of contact under different conditions. For the FEM analysis, the entire gear body with ten teeth was modeled with two tooth pairs having a higher density structured mesh along the involute profile and the remaining ones a coarse mesh. The elements employed were plane strain 4-node bilinear with reduced integration and hourglass control (CPE4R). The nodes of the gear hub were attached to a rigid-body shaft which is then used to apply the boundary conditions. The driving and driven gears were under opposing torques, creating a resistance torque, and the driving gear was rotated in order to obtain a mesh cycle for at least one tooth pair. The developed model, which assumed a isotropic linear elastic material model, allowed to perform simulations at different but constant temperatures by modification of the material's Young modulus as well as different torques and friction coefficients. With the increasing torque and temperature, the maximum load sharing ratio decreased whereas with the increase of the friction coefficient, the opposite was found to be true [147].

Letzelter et al. [148] developed a model to establish the loaded mechanical behavior of polyamide 6.6 gears. This model takes advantage of the generalized Kelvin model to determine the viscoelastic properties of the material which includes the wide relaxation time spectrum and depends on the temperature and humidity (time temperature superposition principle). By incorporating the viscoelastic model within a previously developed quasi-static load sharing model, the loaded transmission error, mesh stiffness, load sharing ratio and tooth root stresses at different temperatures, humidity and rotating speeds can be established. Even though it is possible to obtain the gear mesh stiffness with this model, only the transmission error is analyzed and compared with experimental results from a developed testing device. The experimental and simulated transmission error curves have similar shape and amplitude which proves the

validity of the model. Nevertheless, the model defined here can still be improved since it assumes that the temperature is constant during operation which is shown not to be true. The temperature variation during operation should not be neglected specially considering the sensitivity of polymeric materials with the temperature [148].

Cathelin et al. [149] compared the transmission error of polymer gears from a developed numerical model and experimental measurements. The numerical model comprises three main steps: (i) definition of the real tooth geometry, (ii) kinematics simulation and (iii) loaded calculation. The gear geometry is obtained by simulating the manufacturing process and then, in an unloaded kinematics simulation, the potential contact regions are established. In the last step, the transmission error is calculated considering the viscoelastic displacement and loading history of the polymeric material based on the generalized Kelvin-Voigt method. The measurement of the transmission error is performed in a dedicated test bench with optical encoders. The simulation results without deviations and inclination errors showed similar trend and amplitudes. However, variations in the positions of the axis were noticed during the experimental procedure. Other simulations were conducted under different deviations, inclinations and center distances which led to an approximation to the experimental measurements. Other measurements and simulations at a higher rotating speed suggested that the shorter loading time caused a smaller displacement and consequently a reduction in the transmission error amplitude. The source of this phenomenon was assigned to the time dependent viscoelastic properties of the material. In order to improve the correlation between the numerical and experimental results, it was suggested to acquire precise information of the center distance, deviation and inclination during meshing as these proved to have great impact on the transmission error [149].

Kodeeswaran et al. [150] studied the transmission characteristics of steel-polymer gear mesh with FEM and compared it with experimental results. Both the transmission error and gear mesh stiffness were analyzed. Regarding the geometric nonlinear finite element analysis in ABAQUS®, the gear was designed with a full body and five teeth for reduced computational cost. The mesh size was defined resorting to a convergence study. The tooth root and contact regions were the most refined regions with elements of 8µm and 55µm, respectively. Plain stress 4-node bilinear elements with reduced integration and hourglass control were implemented and the material model was set to isotropic linear elastic. The hub of the driven gear was completely constrained while the hub center of the driving gear had a kinematic constrain to the gear hub diameter and was only allowed to rotate. It is on this reference node (driving gear hub center) that the torque is applied. A coefficient of friction equal to 0.1 was imposed for every simulation conducted. From the numerical results, it was concluded that both the transmission error and the gear mesh stiffness increased with the increase in the applied torque. In addition, both parameters showed an increase in the single and double tooth contact regions. When FEM results were compared with the experimental tests, a high relative error in the single and double tooth pair contact regions was found for every applied load. The encountered discrepancies were attributed to the poor manufacturing quality of the polymer gear, practical difficulties in the experimental measurement and the variations found along the single and double tooth pair contact regions [150].

Roda-Casanova et al. [151] proposed two 2D finite element models in ABAQUS® to perform the thermal-stress analysis of polymer gears. This heating contact analysis considers the heating produced by friction between the gear teeth and the nonlinear properties of the material. A transient coupled thermal-stress model is firstly presented. The pinion and the wheel are discretized into linear quadrilateral finite elements which comprise displacement and temperature degrees of freedom (CPE4T). On the boundary conditions, the gear bore edges are defined as rigid and are linked to the references nodes (center of rotation) of each gear. It is on these

reference nodes, which are only allowed to rotate, that the torque and velocity are applied. While a torque is imposed on the pinion reference node, an angular velocity is defined at the wheel's reference node. A constant coefficient of friction ($\mu = 0.3$) is imposed at the contact even tough it is possible to make this parameter temperature dependent. The heat is transferred by conduction and convection. The second FE model (simplified model) was developed to reduce the high computational time and cost of the first model. This is done by dividing the entire process in two separate and sequential stages, each one with its own FE model: (i) heating during contact and (ii) cooling while unmeshed. The model in the first step (simplified heating contact analysis) is very similar to the previously described full model but only part of the gear body is modeled. The cooling FE model uses elements that only contain temperature degrees of freedom (DC2D4) to model the same gear parts as in the simplified heating contact model. Also, there are no contacting parts during this step, allowing to treat the pinion and the wheel as two separate bodies. The simplified model is validated by comparing, with the coupled thermal-stress model, the temperature variations with time for several nodes. Transmission error curves are plotted for different meshing cycles showing that the increase in temperature causes an increase in the transmission error and consequently a reduction in the mesh stiffness. However, from the results presented, only the single tooth pair regions have a noticeable increase in the transmission error [151].

Discussion Since polymer gears have more particularities than steel gears, and consequently a more extensive exploration field, it would be expected to find more works on this topic. Although, from the analysis shown, it is clear that the amount of works is severely reduced when compared to steel gears. On top of that, there is not much diversity on the type of models used, only finite element models (majority) and analytical models (a few) were implemented, and there are not mesh stiffness/transmission error results for any other than type of polymer gears but spur gears.

The mesh stiffness modeling of polymer gears has the potential to be more explored and exploited than steel gears due to the nonlinear behavior of polymer properties with temperature, displacement and humidity as well as the large geometrical distortions during the meshing process. Nevertheless, there is still a long way to go on this area but when the right step is taken, a whole new spectrum of possibilities will be available.

2.7. New trends and the gear mesh stiffness

There are two aspects that must be highlighted regarding new trends and gear mesh stiffness, electric vehicles (EVs) and polymer gears. The impact of electric vehicles at both industrial and environmental levels is of great proportions, specially considering the increase in production volume over the last few years. Two common drivetrain configurations can be found in electric vehicles. For small EVs, the electric motor (low/average speed motor) is typically attached directly to the wheels while for EVs with the objective of replacing the internal combustion engine vehicles, the electric motor (high speed motor) is coupled to a transmission [153]. The high speed motors typically work between 8900 and 16000 rpm [154] (but it is expected to reach 30000 rpm) which completely changes the design requirements for gears and bearings [155]. This modifies the modeling of the gear mesh stiffness since some effects are enhanced and new ones need to be accounted for, to name a few, Hertzian dampening, extension of contact, loss of contact, centrifugal expansion, manufacturing errors, teeth friction, precession and gyroscopic effect. There are gear mesh stiffness models that consider some of these phenomena although there is not a model that includes all of them simultaneous; a demand for proper modeling of this transmissions.

The application of polymer gears has been increasing for the last decades, nevertheless, there are not many models analytically describing the mesh stiffness or transmission error for this kind of gears. The main gear mesh modeling tool for polymer gears is the finite element method. This numerical method is the tool of choice mainly due to the ease in incorporating the nonlinear material properties with the temperature and displacement. The significantly lower Young modulus compared to steel gears leads to higher deflections and hence the extension of contact is mandatory for any polymer gear mesh stiffness model, for instance, the associated increase in the contact ratio must be considered in the calculation of the tooth root stress of polymer gears [156; 157]. The aforementioned phenomena highlight the need to include, for example, the manufacturing errors and misalignment which become more significant for polymer gears [149; 158]. In addition, the influence of the temperature on the gear mesh stiffness of polymer gears has shown to be of great importance and therefore it must be studied - some investigations on the temperature distribution of polymer gear teeth have been conducted in [159–163]. Temperature variations directly influence the mesh stiffness by modifying the material's Young modulus, moreover, due to the higher thermal coefficient of expansion and lower conductivity of polymer gears, their geometry will certainly change. Kashyap et al. [164] developed analytical models to describe the gear geometry considering the thermal expansion with the purpose of incorporating them in the prediction of load sharing distribution, mesh stiffness and transmission error. In many situations, polymer gears mesh with steel gears, resulting in stiffness imbalance, which impacts the gear mesh stiffness by increasing its peak-to-peak amplitude [165]. All these effects must not be disregarded when designing/modeling polymer gears.

There is a lack of optimization studies on polymer gears even though there are a lot of interesting topics to explore [23] - this might be related to the absence of analytical models. As previously discussed, analytical models are suited for optimization purposes, contrary to the finite element models which, on account of the high computational costs, are not the best option. Precision gearing, an application of polymer gears where the transmission error is of major importance, is one of the fields that can benefit from the analytical modeling of the gear mesh stiffness. An optimization of the transmission error would surely improve the design of polymer gears. There are a lot of other areas to be investigated on polymer gears, namely, composite materials, new design approaches, friction, lubrication, coatings, vibration and noise, revealing a great potential for improvements and expansion of their applicability.

2.8. Closure

As it was demonstrated along the review, gear mesh stiffness has always been a topic of great concern among gears' researchers and the fact that it is still being studied proves its importance and complexity.

In the analytical models, the most commonly used method is the potential energy method. This method is extensively used due to its good results and high flexibility in incorporating geometrical modifications to the tooth, for example, tip relief, tooth cracks and spalling. The potential energy method is described with detail and several works for both spur and helical gears are presented. This method shows results close to those from the finite element method with a reduced computational time. Nevertheless, the computational cost of the potential energy method is not the lowest due to the need of the numerical integration, besides that, due to the extensive expressions required to code, there is a reasonable implementation time with the chance of programming errors. The analytical models emerge as an option for any situation, whether it is gear design, optimization or dynamics yet one must be aware that this type of models may not comprise the required phenomena for a particular investigation and further developments

must be performed. The implementation of new phenomena demands its comprehension and description which might be difficult to do analytically.

The calculation of the gear mesh stiffness with the finite element method is also reviewed. Details regarding the softwares, gear modeling, types of elements and their sizes as well as the mesh stiffness extraction are summarized. A description of some works and their objectives in using the finite element method for the gear mesh stiffness computation is presented. The main disadvantage found for the finite element method consists on performing consecutive analysis for different gear geometries owing to the high computational time and different modelings required - making it very time consuming for gear design/optimization purposes. On the other hand, the finite element method allows for a geometrical and contact accuracy that is not attainable in other methods and exhibits great flexibility regarding materials and geometries.

The hybrid models try to solve the problem of the high computational time of the finite element method by calculating the nonlinear Hertzian component separately. The Hertzian deformations are the main restriction to the selection of the elements' mesh as they require a fine mesh to be properly calculated. Hence, in hybrid models, the finite element method is used for a global analysis and an analytical procedure is applied to compute the contact deformations. A comprehensive analysis is not conducted as hybrid models combine previously presented techniques, this is, the finite element method and analytical procedures. From the literature review, hybrid models present a reduction in the computational time while keeping an accuracy close to the finite element method models. Hence, the applicability range of this kind of model is expanded compared to that of the finite element method, making it more appropriate for consecutive analysis.

The final type of gear mesh stiffness models presented are the approximate analytical models. The principle behind this kind of models is reducing a phenomena defined by expensive numerical calculations to an approximate and simple function. Four approximate analytical methods were presented, they were named the Parabolic model (Cai and Hayashi [136] and Cai [97]), the Cosine model (Sánchez et al. [19]), the Fourier model (Gu et al. [13]) and the Heaviside model (Marques et al. [143]). In short, the Parabolic model uses a quadratic function to approximate the single tooth pair mesh stiffness whereas the Cosine model uses the cosine trigonometric function for the same purpose. Gu et al. [13] and Marques et al. [143] take advantage of the Fourier series and the Heaviside function, respectively, to describe the length of the contacting lines for the estimation of the gear mesh stiffness. These models are very similar to the analytical methods regarding both benefits and drawbacks however the simpler and more direct expressions they present facilitate the implementation procedure and reduce the computation time by orders of magnitude as it is shown in the comparative study for spur gears performed by Natali et al. [122]. The approximate analytical models give reliable results in a very short computational time, in fact, its ratio between accuracy and computational cost is one of, if not, the best.

Mesh stiffness models for cylindrical gears are reviewed with great detail. Any researcher/practitioner, either experienced or novice, can find here a complete source of information to get an update or rapidly know what was and is currently done in the field of gear mesh stiffness and how to do it.

The selection of the absolute best gear mesh stiffness model is not possible since it depends on the needs, knowledge and interests of each individual. What can be stated is that the best model for a certain individual contains all the necessary effects for the intended application and is within the implementation capabilities of the individual. It should be clarified that including all possible effects that exist for the modeling of gear mesh stiffness is not the best approach, including unnecessary/unused effects is useless and can even be pernicious due to the increased

computational cost it might bring.

A comparison between key characteristics of each group of models is performed in Table 2.8 to supply information for deciding which class of model is the most suited for a specific investigation. The parameters compared in Table 2.8 are the accuracy of the results, computation time/repeatability, easiness in the implementation procedure and required resources for modeling. Note that this is a general overview of the models and that these are the expected outcomes for each class of model - there might be exceptions. The gear mesh stiffness modeling categories are classified from the best (1st) to the worse (4th) for each parameter.

Table 2.8: Comparison between the different types of gear mesh stiffness models.

Model	**Accuracy**	**Computation cost**	**Implementation procedure**	**Resources**
Analytical	3	2	2	2
Finite Element	1	4	3	4
Hybrid	2	3	4	3
Approximate Analytical	4	1	1	1

Table 2.8 grants the possibility to verify which aspect is the most challenging or needs further improvement for each kind of model. From Table 2.8 it can be concluded:

- Considering a correct and equivalent implementation for every type of model, finite element models are the most accurate. The high accuracy of these models makes them the preferred choice for many researcher/practitioners. The accuracy decreases when selecting hybrid models, analytical models and approximate analytical models;

- Approximate analytical models have the lowest computational cost. The simple and direct procedures that define these models lead to a significant reduction in the computational cost and allow their repeatability, crucial for optimization algorithm and gear dynamic analysis. Oppositely to these models are the finite element models and between the remaining models, hybrid models are closer to finite element, as expected by their similarities;

- Hybrid models are selected as being the hardest to implement since they require the combination of the finite element method and analytical expressions as well as a procedure to remove the local deformations from the finite element model. Next are the finite element models, which even resorting to finite element softwares/solvers require a solid basis of knowledge on the topic. Programming finite element models from scratch is even harder and requires high level of mathematical and programming skills. The analytical and approximate analytical models can be implemented with the minimum mathematical/programming skills but analytical models are more prone to implementation errors due to the need of performing the integrals;

- Resources classify the utilities and computational power necessary to perform the analysis for each model, therefore, this topic is closely related to the computation time. Finite element models are at the bottom as powerful machines are needed for an adequate analysis - some finite element models are not worth solving if the computational machine available cannot solve the problem within demanded/reasonable time. At the top are the approximate analytical models which are affordable in almost every computer.

Lastly, there is one question that comes to mind: what would be the perfect gear mesh stiffness model? The perfect gear mesh stiffness model can accurately represent the mesh stiffness of any gear mesh under any condition within a computation time that allows it to be used as a tool for any application. As this is not attainable yet, the focus is on the new trends and how they modify the current gear mesh stiffness models.

Next Comparing the different types of models and taking into account the goal of reaching an accurate and low computational cost gear mesh stiffness model, using an approximate analytical model is the best strategy - Heaviside model [135] used as a basis. Early implementations of the Heaviside model [135] to include extension of contact on spur gears revealed some inconsistencies when comparing the results with KISSsoft® in terms of magnitude and for gears with $u \neq 1$. After further investigation, the former discrepancies were attributed to the definition of the maximum stiffness value (established according to ISO 6336 [141]) while the latter to the symmetrical shape of the single tooth pair mesh stiffness that was being assumed since for gears with gear ratio $u = 1$ full agreement was found. Later, in the work of Marques et al. [143] (improved Heaviside model) there is a strong dependence of the model on the parabolic approximation for the definition of the single tooth pair slice mesh stiffness. This expression results in a symmetric shape for the stiffness component and relies on the definition of a free parameter which, in the state it is presented, has no correlation with the gear geometry. Three key issues must be addressed for the quality of the estimation given by the approximate analytical models to be improved: (i) definition of a single tooth pair (slice) mesh stiffness shape accounting for the possible asymmetries; (ii) determination of the free parameter depending on gear geometry and (iii) improved estimation of the maximum stiffness value. This was found to be the first major step towards the development of the gear mesh stiffness model.

Chapter 3

Single tooth pair slice mesh stiffness

In many gear mesh stiffness models, the single tooth pair mesh stiffness is commonly approximated as having a parabolic-like symmetric shape along the path of contact with a fixed or contact ratio dependent amplitude. Even though this is a valid approximation under certain conditions, there is an asymmetry being disregarded and an amplitude being roughly approximated. In this chapter, a new straightforward analytical expression for the single tooth pair slice mesh stiffness is defined resorting to a parabolic approximation of the tooth pair structural stiffness that requires the definition of the asymmetry, relative amplitude and maximum value as a function of the gear parameters. In order to assess the developed work in terms of applicability and accuracy, a random sample of gears have their tooth pair structural stiffness approximation tested. The established asymmetry, relative amplitude and maximum value allow, in a fast and simple fashion, to obtain an accurate approximation. Different formulations of the single tooth pair slice mesh stiffness are compared, highlighting the importance of including the asymmetry and showing the improvements due to the new parameters.

3.1. Background

There are many different kinds of gear mesh stiffness models, ranging from analytical, finite element, hybrid and approximate. Each type of model comprises their own advantages and drawbacks, so the selection of the right type of model depends, to some extent, of the requirements imposed by the user. When it comes to situations where the number of gear mesh stiffness computations can be very high, for instance, optimization of gear design and gear dynamics, the approximate gear mesh stiffness models are the best option [166]. In this type of models, it is very common to find approximations to the single tooth pair (slice) mesh stiffness, either giving them parabolic or trigonometric shape functions [13; 19; 135; 136; 143]. Therefore, the accuracy of the single tooth pair (slice) mesh stiffness will influence the results of the gear mesh stiffness. Bearing that in mind, an analysis of the current applications of single tooth pair mesh stiffness approximations is conducted to stress out the main characteristics of each one of them.

Cai and Hayashi [136] developed the parabolic approximation for the stiffness of a tooth pair when working on the linearization process of the nonlinear equation for the rotational vibration of spur gear pairs. The approximate single tooth pair mesh stiffness is normalized by the average

Contents in Chapter 3: Single tooth pair slice mesh stiffness are reproduced with permission of the respective publisher from João D.M. Marafona, Pedro M.T. Marques, Ramiro C. Martins, and Jorge H.O. Seabra. Approximate expression for the single tooth pair slice mesh stiffness. *Mechanism and Machine Theory*, 187:105367, 2023.

gear mesh stiffness value and, as displayed in equation (3.1), is a function of the contact ratio (ε_α), meshing period (t_z) and meshing time (t).

$$\hat{k^{\mathrm{tp}}} = \left[\frac{-1.8}{(\varepsilon_\alpha t_\mathrm{z})^2}t^2 + \frac{1.8}{\varepsilon_\alpha t_\mathrm{z}}t + 0.55\right]/(0.85\varepsilon_\alpha) \tag{3.1}$$

Analyzing equation (3.1), the amplitude of the curve depends on the contact ratio and is equal to $0.45/(0.85\,\varepsilon_\alpha)$. By performing this approximation, it is being assumed that the meshing of the tooth pairs occurs symmetrically.

Gu et al. [13] also made use of a parabolic and symmetrical approximation, to establish the normalized, with respect to the average stiffness value, single tooth pair mesh stiffness for an analytical description of the mesh stiffness of solid spur and helical gears - attend to equation (3.2).

$$\hat{k^{\mathrm{tp}}} = 1 + \alpha_{\mathrm{Fourier}}\left(\frac{-6}{\varepsilon_\alpha^2}\tau^2 + \frac{6}{\varepsilon_\alpha}\tau - 1\right) \tag{3.2}$$

In equation (3.2), τ is the time normalized by the meshing period. In the approximation proposed by Gu et al. [13], the amplitude depends on the value applied for $\alpha_{\mathrm{Fourier}}$ - relative variation in stiffness amplitude - which varies between 0.25 and 0.35. This range of values was obtained by computing $\alpha_{\mathrm{Fourier}}$ for different gear geometries and according to various procedures. An average value of $\alpha_{\mathrm{Fourier}} = 0.3$ is implemented, making the amplitude equal to 0.45.

Marques et al. [143] presented a continuous analytical solution for the gear mesh stiffness of involute spur and helical gears considering a non-uniform contact line stiffness distribution. This model resorts to a symmetrical parabolic approximation to define the single tooth pair stiffness for a spur gear slice, as shown in equation (3.3).

$$\hat{k^{\mathrm{tp,s}}} = \frac{4(\alpha_k - 1)}{\varepsilon_\alpha^2}\xi^2 - \frac{4(\alpha_k - 1)}{\varepsilon_\alpha}\xi + \alpha_k \tag{3.3}$$

The variable ξ in equation (3.3) is the distance from the start of meshing divided by the transverse base pitch. The value for α_k, which defines the minimum stiffness ratio along the path of contact was studied and a relationship between α_k and $\mathcal{R}$ (load sharing ratio at the theoretical start of the meshing process for gears with $1 < \varepsilon_\alpha < 2$) was established according to equation (3.4).

$$\alpha_k = -\frac{4\mathcal{R}\,(\varepsilon_\alpha - 1)}{\varepsilon_\alpha^2(2\mathcal{R} - 1) - 4\mathcal{R}\varepsilon_\alpha + 4\mathcal{R}} \tag{3.4}$$

Since the amplitude of this parabolic approximation is $1 - \alpha_k$, it depends on the value of $\mathcal{R}$ and the transverse contact ratio. Considering the evaluation conducted in [143], several studies suggest that a value of $\mathcal{R} = 0.36$ would give results close to reality. Unlike the previously discussed works, this curve is normalized by the maximum single tooth pair mesh stiffness value.

Sánchez et al. [19] use the cosine trigonometric function to approximate the single tooth pair mesh stiffness and, with that formulation, evaluate the contact and tooth root stresses of spur gears. The applied approximation is shown in equation (3.5).

$$\hat{k^{\mathrm{tp}}} = \cos\left(b_0\left[\xi_C - \left(\xi_{\mathrm{inn}} + \frac{\varepsilon_\alpha}{2}\right)\right]\right) \tag{3.5}$$

where b_0 is defined according to equation (3.6) and ξ_{inn} is the point where the tooth pair starts meshing. The coordinate ξ_C defines the contact point and is equal to the length along the line of action normalized by the transverse base pitch.

$$b_0 = \left[\frac{1}{2}\left(1.11 + \frac{\varepsilon_\alpha}{2}\right)^2 - 1.17\right]^{-\frac{1}{2}} \tag{3.6}$$

Establishing the minimum stiffness ratio along the path of contact for the cosine approximation leads to equation (3.7), which presents very similar values to equation (3.4) when $\mathcal{R} = 0.36$ [143].

$$\alpha_k^{\text{Sanchez}} = \cos\left(\frac{\varepsilon_\alpha}{2}\left[\frac{1}{2}\left(1.11 + \frac{\varepsilon_\alpha}{2}\right)^2 - 1.17\right]^{-\frac{1}{2}}\right) \tag{3.7}$$

Even though only symmetrical approximations are presented in the work of Sánchez et al. [19], it is referred that modifications must be applied in situations where the addendum of the standard basic rack tooth profile is different than one ($h_{aP}^* \neq 1$) and for non-standard center distance. Furthermore, in other works [73; 167; 168], the influence of undercut at the tooth root and non-equal tooth addendum on the pinion and the wheel on the load distribution along the line of contact is evaluated. Asymmetrical curves need to be considered when reduced tooth height, vacuum gearing at pinion root, enlarged tooth height and modifications to the standard center distance have to be included in the single tooth pair mesh stiffness approximations. The solutions proposed in [73; 167; 168] to these cases resort to a fictitious contact ratio which neglects all those modifications and consequently leads to fictitious gear geometries. Then, by considering the actual starting and ending points of teeth contact, the fictitious curve is trimmed and the final result, which can be asymmetric or not, is obtained.

When it comes to approximate gear mesh stiffness models, three key features were found (a discussion between approximate gear mesh stiffness models can be found in [166]): (i) the curve is (most times) considered to be symmetric, (ii) these models rely on the ISO 6336-1 [141] standard to establish an absolute value for the single tooth pair mesh stiffness and (iii) there are different formulations for the relative amplitude of the curves. Upon this analysis, there are a number of questions that can be raised, for instance, what is the relationship between gear geometry/parameters and shape of the single tooth pair mesh stiffness? Also, how far can the ISO 6336-1 [141] describe the maximum value for the single tooth pair mesh stiffness? Even though approximate gear mesh stiffness models mostly deal with the single tooth pair mesh stiffness, the single tooth pair slice mesh stiffness is, conceptually, a broader parameter that gives a wider range of modeling, allowing the mesh stiffness estimation for both spur and helical gears. Taking the aforementioned into account, there is the need to define these parameters as a function of the gear geometry, giving better estimations for approximate gear mesh stiffness models. For that purpose, an extensive study on the single tooth pair slice mesh stiffness where its shape, relative amplitude and maximum absolute value are evaluated is required to shed some light on this topic and expand the modeling range of approximate gear mesh stiffness model.

For that purpose it is necessary to be capable of accurately computing the single tooth pair slice mesh stiffness multiple times. Considering the aforementioned restrictions, the potential energy method (PEM) is the selected gear mesh stiffness model to determine the single tooth pair slice mesh stiffness [166]. The potential energy method is a well-established analytical procedure

for the calculation of the single tooth pair and gear mesh stiffnesses. This method views the gear tooth as a non-uniform cantilever beam fixed at its dedendum circle and estimates its total potential energy due to external work resorting to analytical expressions from mechanics of materials [72; 166]. The potential energy method can be employed to compute the gear mesh stiffness of spur [17; 83; 87; 88; 90] and helical [14; 16; 99–101] gears including profile and width modifications/errors as well as damaged gears (both spur and helical) from pitting, spalling, cracked teeth and wear [85; 105; 106; 109–111].

For this work, the potential energy method is used to study the tooth pair structural stiffness, this means that the components considered for the computation are the bending, shear and axial compressive energies of both the pinion and the wheel. Consequently, the contact stiffness and fillet-foundation stiffness are not taken into account for this investigation. In fact, there is currently no need to further investigate these stiffness components since both the contact [77] and the fillet-foundation [78; 79] deflections already have analytical, simple and computationally inexpensive expressions. This chapter focuses on defining the tooth pair structural stiffness by simple analytical expressions without any numerical method so that the contact and fillet-foundation components can be combined to establish the single tooth pair slice mesh stiffness.

To reach that goal, the tooth pair structural stiffness is approximated by a quadratic expression including two parameters to define its shape plus a third parameter to establish its maximum value. Firstly, the shape parameters, asymmetry parameter and relative amplitude parameter, of the tooth pair structural stiffness are evaluated. Then, the maximum single tooth pair mesh stiffness from the ISO 6336-1 [141] is adapted to fit the maximum tooth pair structural stiffness according to the potential energy method. This study is centered on slices of both spur and helical gears. When approximate gear mesh stiffness models are implemented for parallel axis cylindrical gears, most times, they resort to the slicing method [14; 16; 99–101; 166] and therefore gears are viewed as a series of staggered spur gears, which are the slices. In addition, the research is conducted for the ISO 53 [169] Profile A ($\alpha = 20°$, $h^*_{\mathrm{aP}} = 1$, $h^*_{\mathrm{fP}} = 1.25$ and $\rho^*_{\mathrm{fP}} = 0.38$) and considering a linear elastic behavior of the gears' material.

As an output, analytical expressions for the asymmetry, relative amplitude and maximum value of the parabolic approximation of the tooth pair structural stiffness are established which together with the existing contact and fillet-foundation stiffness give an unique formulation for the single tooth pair slice mesh stiffness. By defining these parameters as a function of the gear geometry/parameters, there is no need to rely on further simplifications or on free/user-defined parameters, thus improving the accuracy and reliability of approximate gear mesh stiffness models. This improvement in accuracy will be highlighted when the extension of contact (contact outside the path of contact) is considered since it is influenced by the stiffness at the starting and ending points of contact [138; 140]. The load sharing distribution, friction losses and location of critical points for bending and wear calculations can also be better estimated considering the newly established approximation for the single tooth pair slice mesh stiffness.

3.2. Potential energy method

In this section, the potential energy method is described together with the presentation of the expressions necessary to determine the gear tooth potential energy so that the tooth pair structural stiffness can be established. According to the potential energy method, the total potential energy of a gear tooth (U_{t}), shown in equation (3.8), due to the external work done in deforming it can be separated into three components: the bending energy (U_{b}), the shear energy (U_{s}) and the axial compressive energy (U_{a}). Each of these energy components is defined

by equations (3.9) to (3.11) [72; 166].

$$U_{\mathrm{t}} = U_{\mathrm{b}} + U_{\mathrm{s}} + U_{\mathrm{a}} \tag{3.8}$$

$$U_{\mathrm{b}} = 6\frac{F^2\cos^2(\alpha_C)}{Eb}\int_{y_p}^{y_C}\frac{(y_C-y)^2}{e^3(y)}\,\mathrm{d}y \tag{3.9}$$

$$U_{\mathrm{s}} = 0.6\frac{F^2\cos^2(\alpha_C)}{Gb}\int_{y_p}^{y_C}\frac{\mathrm{d}y}{e(y)} \tag{3.10}$$

$$U_{\mathrm{a}} = \frac{F^2\sin^2(\alpha_C)}{2Eb}\int_{y_p}^{y_C}\frac{\mathrm{d}y}{e(y)} \tag{3.11}$$

where y is the coordinate given by the axis defined along the tooth centerline with origin at the gear rotation center, F is the involute profile normal load, α_C is the load angle, b is the facewidth, $e(y)$ is the tooth chordal thickness at section y. E and G are, respectively, the modulus of elasticity and transverse modulus of elasticity of the material. The integration limits, y_p and y_C, are the values of y corresponding to the fixed boundary of the tooth and the load section. The fixed boundary is given by the chordal tooth root line while the load section is defined by the intersection of the line of action and the tooth centerline [73; 166]. The tooth pair structural stiffness can then be obtained by using the single tooth total potential energy of the pinion and the wheel.

3.3. Shape parameters

In previous works [8; 135; 143], the single tooth pair (slice) mesh stiffness was approximated by a parabolic expression to define its shape and by the ISO 6336-1 [141] to specify its maximum absolute value. For the approximation of the tooth pair structural stiffness, a similar expression is employed, where the amplitude parameter α_k is kept and a new parameter to characterize the asymmetry of the curve λ is added, attend to equation (3.12).

$$\hat{k^{\mathrm{str}}} = \frac{4(\alpha_k-1)}{\varepsilon_\alpha^2}(\xi-\lambda)^2 - \frac{4(\alpha_k-1)}{\varepsilon_\alpha}(\xi-\lambda) + \alpha_k \tag{3.12}$$

The amplitude α_k is, for a symmetric curve, the ratio between the minimum and maximum tooth pair structural stiffness along the path of contact. The asymmetric parameter is the quantity which the parabolic curve is shifted to the right (if $\lambda > 0$) or to the left (if $\lambda < 0$). Figure 3.1 shows an example of how the shape parameters influence the behavior of the normalized tooth pair structural stiffness curve according to equation (3.12) - this shows the high variability of the curves with the shape parameters.

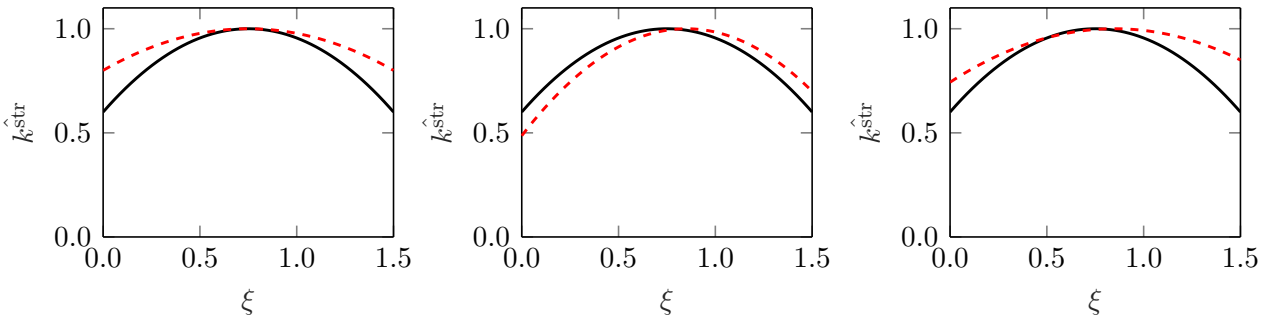

(a) Variation of α_k: - - - $\alpha_k = 0.8$ and $\lambda = 0$.

(b) Variation of λ: - - - $\alpha_k = 0.6$ and $\lambda = 0.1$.

(c) Variation of α_k and λ: - - - $\alpha_k = 0.8$ and $\lambda = 0.1$.

Figure 3.1: Example of the effect of the shape parameters on the tooth pair structural stiffness: — $\varepsilon_\alpha = 1.5$, $\alpha_k = 0.6$ and $\lambda = 0$.

3.3.1. Asymmetry parameter, λ

The effect of the gears' geometrical parameters on the asymmetry is evaluated for each parameter individually. However, since the helix angle, module and facewidth do not create asymmetries, these are not studied. That being said, for the number of teeth, profile shift coefficients and addendum reduction, expressions are developed. The asymmetry parameter is defined by equation (3.13) where λ_{GR}, λ_{PS} and λ_{AS} are the asymmetries caused by the number of teeth, the profile shift coefficients and the addendum shortening - each parameter is discussed in its own section. From the different fitting approaches that were tried, it was found that the topology used for equation (3.13) is the simplest given that the contribution of each parameter can be individually approximated.

$$\lambda = \lambda_{\text{GR}} + \lambda_{\text{PS}} + \lambda_{\text{AS}} \tag{3.13}$$

To determine λ, the first step is to obtain the tooth pair structural stiffness from PEM. Then, the PEM curve is normalized such that its maximum value is equal to one. Following that, a parabolic interpolation of the region near its maximum value is performed to accurately obtain its location. Finally, λ^{PEM} is computed from the difference between the position of the actual maximum value and the position where the maximum would be if the tooth pair structural stiffness was considered symmetric, this is, halfway between the start and end of meshing. Once λ^{PEM} is determined, it is approximated according to the gear parameters in study and thus λ is achieved.

Number of teeth

On the asymmetries caused by the number of teeth, it should be noted that there are no asymmetries when the gear ratio is equal to one ($z_1 = z_2$) and if the profile shift coefficients are $x_1 = x_2$ - meaning that under these circumstances, one can alter the number of teeth that the tooth pair structural stiffness will remain symmetric. Although, this does not mean that only the gear ratio has influence on the asymmetries because for different values of z_1 and a fixed value of gear ratio, different values of asymmetries can be found. Starting by defining the unbalance in the path of contact imposed by the number of teeth ψ_{GR} leads to equation (3.14).

$$\psi_{\mathrm{GR}} = \frac{1}{2\,p_{\mathrm{bt}}}\left[\left(-\frac{1}{2}(z_2 - z_1)m_{\mathrm{t}}\sin(\alpha_{\mathrm{t}})\right) + \sqrt{\left(\frac{1}{2}m_{\mathrm{t}}z_2 + m_{\mathrm{n}}\right)^2 - \left(\frac{1}{2}z_2 m_{\mathrm{t}}\cos(\alpha_{\mathrm{t}})\right)^2} - \sqrt{\left(\frac{1}{2}m_{\mathrm{t}}z_1 + m_{\mathrm{n}}\right)^2 - \left(\frac{1}{2}z_1 m_{\mathrm{t}}\cos(\alpha_t)\right)^2}\right] \tag{3.14}$$

When comparing the asymmetry parameter from PEM (λ^{PEM}) with ψ_{GR}, it was discovered that they shared the same shape, although the amplitude required to be adjusted by a factor of 0.9642. This result was determined by varying the number of teeth between 18:300 and the gear ratio between 1:8 while keeping the module equal to 8 mm and the facewidth to 20 mm - see Table 3.1. The values attributed to the module and facewidth have no particular reason for their selection and impose no influence in the results.

Table 3.1: Gear parameters for the number of teeth evaluation.

Gear parameters	**Range**
$\boldsymbol{z_1}$/-	18:300
$\boldsymbol{z_2}$/-	$z_1\times$ 1:8
$\boldsymbol{m}_{\mathrm{n}}$/mm	8
$\boldsymbol{\alpha}$/°	20
$\boldsymbol{\beta}$/°	0
$\boldsymbol{b}$/mm	20
$\boldsymbol{x_1}$/-	0
$\boldsymbol{x_2}$/-	0
$\boldsymbol{E}$/GPa	206

Taking the aforementioned into account, equation (3.15) describes the asymmetries caused by the variation in the number of teeth.

$$\lambda_{\mathrm{GR}} = 0.9642\ \psi_{\mathrm{GR}} \tag{3.15}$$

Profile shift coefficients

The asymmetries imposed by the profile shift coefficients are evaluated for the geometries presented in Table 3.2.

The analysis begins by determining the modifications on the starting and ending points of meshing created by x_1 and x_2. These are established by equation (3.16) for x_1 and equation (3.17) for x_2.

Table 3.2: Gear parameters for the profile shift coefficients evaluation.

Gear parameters	**Range**
$\boldsymbol{z_1}$/-	18:300
$\boldsymbol{z_2}$/-	z_1
$\boldsymbol{m_n}$/mm	8
$\boldsymbol{\alpha}$/°	20
$\boldsymbol{\beta}$/°	0
$\boldsymbol{b}$/mm	20
$\boldsymbol{x_1}$/-	-1:1*
$\boldsymbol{x_2}$/-	-1:1*
$\boldsymbol{E}$/GPa	206

* limited by undercut for z_1

$$\psi_{\mathrm{PSA}} = \frac{1}{2\,p_{\mathrm{bt}}}\left[-\sqrt{\left(\frac{1}{2}m_{\mathrm{t}}z_2 + m_{\mathrm{n}}(1+x_2)\right)^2 - \left(\frac{1}{2}z_2 m_{\mathrm{t}}\cos(\alpha_{\mathrm{t}})\right)^2} + \sqrt{\left(\frac{1}{2}m_{\mathrm{t}}z_2 + m_{\mathrm{n}}\right)^2 - \left(\frac{1}{2}z_2 m_{\mathrm{t}}\cos(\alpha_{\mathrm{t}})\right)^2}\,\right] \tag{3.16}$$

$$\psi_{\mathrm{PSB}} = \frac{1}{2\,p_{\mathrm{bt}}}\left[\sqrt{\left(\frac{1}{2}m_{\mathrm{t}}z_1 + m_{\mathrm{n}}(1+x_1)\right)^2 - \left(\frac{1}{2}z_1 m_{\mathrm{t}}\cos(\alpha_{\mathrm{t}})\right)^2} - \sqrt{\left(\frac{1}{2}m_{\mathrm{t}}z_1 + m_{\mathrm{n}}\right)^2 - \left(\frac{1}{2}z_1 m_{\mathrm{t}}\cos(\alpha_{\mathrm{t}})\right)^2}\,\right] \tag{3.17}$$

Then, considering the deviations caused by the profile shift coefficients on the path of contact (ψ_{PSA} and ψ_{PSB}), the procedure is divided in two stages. On the first stage, only symmetric profile shift coefficients ($x_1 = -x_2$) are modeled, leading to equation (3.18).

$$\lambda_{\mathrm{PS}}^{\mathrm{sym}} = \frac{1}{7.3678\times10^{-2}z_2 + 1.2945}\,\psi_{\mathrm{PSA}} + \frac{1}{7.3678\times10^{-2}z_1 + 1.2945}\,\psi_{\mathrm{PSB}} \tag{3.18}$$

On the second stage, $x_1 = 0$ is fixed and x_2 is varied between -1 and 1. The ratio between λ^{PEM} and $\lambda_{PS}^{\mathrm{sym}}$ is computed to find out that it can be replicated by a linear function in x_i whose coefficients are a parabolic and linear functions of z_i - resulting in the final form of λ_{PS}, displayed in equation (3.19) accompanied by equations (3.20) and (3.21).

$$\lambda_{\mathrm{PS}} = \gamma_1\,\psi_{\mathrm{PSA}} + \gamma_2\,\psi_{\mathrm{PSB}} \tag{3.19}$$

$$\gamma_1 = \frac{(-2.513\times10^{-6}z_2^2 + 1.498\times10^{-3}z_2 - 0.5824)x_2 - 7.651\times10^{-5}z_2 + 1.029}{7.3678\times10^{-2}z_2 + 1.2945} \tag{3.20}$$

$$\gamma_2 = \frac{(-2.513 \times 10^{-6} z_1^2 + 1.498 \times 10^{-3} z_1 - 0.5824) x_1 - 7.651 \times 10^{-5} z_1 + 1.029}{7.3678 \times 10^{-2} z_1 + 1.2945} \tag{3.21}$$

Addendum shortening

The last parameter to be studied for the asymmetric shift is the addendum shortening k_{ad} which is the height removed to the tooth normalized by the normal module. Since this process consists in the reduction of the teeth's height by removal of the correspondent material, it leads to a reduction on the path of contact. Even though the path of contact is reduced, the stiffness values are kept the same owing to the fact that the contact points between the gears are exactly in the same position. That being said, for the addendum shortening, an exact expression for the asymmetries can be established, resulting in equation (3.22). Note that this addendum shortening can also include any further desired tooth height reduction.

$$\begin{aligned}\lambda_{\mathrm{AS}} = \frac{1}{2\,p_{\mathrm{bt}}} \Bigg[& \sqrt{\left(\frac{1}{2} m_{\mathrm{t}} z_2 + m_{\mathrm{n}}(1 - k_{\mathrm{ad}})\right)^2 - \left(\frac{1}{2} z_2 m_{\mathrm{t}} \cos(\alpha_{\mathrm{t}})\right)^2} - \\ & \sqrt{\left(\frac{1}{2} m_{\mathrm{t}} z_2 + m_{\mathrm{n}}\right)^2 - \left(\frac{1}{2} z_2 m_{\mathrm{t}} \cos(\alpha_{\mathrm{t}})\right)^2} - \\ & \sqrt{\left(\frac{1}{2} m_{\mathrm{t}} z_1 + m_{\mathrm{n}}(1 - k_{\mathrm{ad}})\right)^2 - \left(\frac{1}{2} z_1 m_{\mathrm{t}} \cos(\alpha_{\mathrm{t}})\right)^2} + \\ & \sqrt{\left(\frac{1}{2} m_{\mathrm{t}} z_1 + m_{\mathrm{n}}\right)^2 - \left(\frac{1}{2} z_1 m_{\mathrm{t}} \cos(\alpha_{\mathrm{t}})\right)^2} \Bigg]\end{aligned} \tag{3.22}$$

3.3.2. Amplitude parameter, α_k

The amplitude parameter to be approximated is the one that minimizes the difference between the potential energy method and the normalized approximate function for the tooth pair structural stiffness in equation (3.12) while using the asymmetric parameter established by the potential energy method. A first analysis has unveiled that the amplitude parameter depends on the number of teeth, helix angle and the profile shift coefficients. The resulting expression for the amplitude parameter is of the type shown in equation (3.23).

$$\alpha_k = \alpha_k^z \, \alpha_k^\beta \, \alpha_k^x \tag{3.23}$$

where α_k^z, α_k^β and α_k^x are functions that account for the influence of the number of teeth, helix angle and profile shift coefficients in the amplitude parameter, respectively. α_k^z is estimated first to be used as a reference. Then, α_k^β and α_k^x are introduced to account for the variations imposed by the profile shift coefficients as well as the helix angle. The three following sections are dedicated to the investigation of the aforementioned parameters in α_k.

Number of teeth

The value of the amplitude parameter is computed for the gears established by Table 3.1, maintaining the range that is used for λ_{GR}. When looking at the results, the amplitude

parameter took a very similar shape for every value of gear ratio, which can be described by a power function of z_1, as in equation (3.24).

$$\alpha_k^z = A_z z_1^{B_z} + C_z \tag{3.24}$$

The parameters A_z, B_z and C_z in equation (3.24) control the shape of the power function with the gear ratio. Upon determining these values, they are correspondingly fitted by expressions shown in equations (3.25), (3.26) and (3.27).

$$A_z = 2.746 \times 10^{11} \exp\left(-28.88 \, \frac{z_2}{z_1}\right) + 1.095 \exp\left(0.03794 \, \frac{z_2}{z_1}\right) \tag{3.25}$$

$$B_z = -0.7036 \left(\frac{z_2}{z_1}\right)^{0.08683} \tag{3.26}$$

$$C_z = 0.2851 \left(\frac{z_2}{z_1}\right)^{0.004734} \tag{3.27}$$

Helix angle

The helix angle of the analyzed gears is varied between 0° and 40° as it can be seen from Table 3.3 which shows all gear parameters for α_k^β.

Table 3.3: Gear parameters for the helix angle evaluation.

Gear parameters	**Range**
$\boldsymbol{z_1}$/-	18:300
$\boldsymbol{z_2}$/-	z_1
$\boldsymbol{m}_\mathrm{n}$/mm	8
$\boldsymbol{\alpha}$/°	20
$\boldsymbol{\beta}$/°	0:40
$\boldsymbol{b}$/mm	20
$\boldsymbol{x_1}$/-	0
$\boldsymbol{x_2}$/-	0
$\boldsymbol{E}$/GPa	206

The results of α_k are divided by the ones obtained when $\beta = 0°$ prior to the modeling - the achieved ratio is a surface with axis z_1 and β. To develop the fitting function, the average value of the ratio for every β is taken. Ergo, the dependence on z_1 is removed and the function given by equation (3.28) is established.

$$\alpha_k^\beta = \frac{0.9896\beta^2 - 64.76\beta + 1349}{\beta^2 - 65.81\beta + 1347} \tag{3.28}$$

Profile shift coefficients

The procedure taken for modeling the amplitude parameter considering the profile shift coefficients is the same as for assessing the influence of the profile shift coefficients on the asymmetry parameter, described in section 3.3.1. The values of the amplitude parameter according to Table 3.2 are divided by α_k^z prior to their examination, leading to α_k^x and thus guaranteeing that equation (3.23) holds true. This procedure gives rise to a second degree polynomial function on x_1 and x_2 to approximate α_k^x, as expressed in equation (3.29), with functions A_x, B_x, C_x and D_x dependent on z_1 - shown from equation (3.30) to (3.33).

$$\alpha_k^x = A_x - B_x(x_2 + x_1) + C_x(x_2^2 + x_1^2) + D_x x_2 x_1 \tag{3.29}$$

$$A_x = -1.4 \times 10^5 z_1^{-5.429} + 0.9982 \tag{3.30}$$

$$B_x = \frac{0.004049 z_1^2 + 3.236 z_1 - 17.06}{z_1^2 - 48.98 z_1 + 1444} \tag{3.31}$$

$$C_x = 6.449 z_1^{-0.9202} \tag{3.32}$$

$$D_x = -11.74 z_1^{-1.143} \tag{3.33}$$

3.4. Maximum stiffness

The maximum value for the tooth pair structural stiffness is studied resorting to the potential energy method and the standard ISO 6336-1 [141]. The ISO 6336-1 [141] is used as a basis which is reworked by different functions to give results in accordance with the potential energy method. Different gear parameters are analyzed, such as, the number of teeth, helix angle, module, facewidth, profile shift coefficients and Young's modulus of the gear's material. The maximum single tooth pair stiffness, $K_{\max}^{\mathrm{ISO}}$ is expressed by equation (3.34).

$$K_{\max}^{\mathrm{ISO}} = c' \, \frac{b}{\cos(\beta_{\mathrm{b}})} \, 10^6 \tag{3.34}$$

where c' is computed according to the ISO 6336-1 [141] standard.

The overall procedure to adapt the maximum stiffness value from ISO 6336-1 [141] to be consistent with the maximum values obtained for the tooth pair structural stiffness from the potential energy method comprises two parts. The first part consists in the computation of the maximum tooth pair structural stiffness with the PEM for several gear geometries where only the geometrical parameter to be studied is modified. In the second part, the ratio between the PEM and ISO* maximum stiffness (R^K, equation (3.35)) is evaluated to find a fitting function. When this function is found, one can multiply it by the ISO maximum stiffness to obtain the maximum tooth pair structural stiffness from PEM. So, for each parameter that requires adjustment, a fixing function is developed and a new maximum ISO stiffness $K_{\max}^{\mathrm{ISO}^*}$ is obtained. Upon establishing a fixing function, these are kept for the analysis of the following gear parameter. The final result is the maximum tooth pair structural stiffness, $K_{\max}^{\mathrm{STR}}$, as shown by equation (3.36).

$$R^K = \frac{K_{\max}^{\text{PEM}}}{K_{\max}^{\text{ISO}^*}} \tag{3.35}$$

$$K_{\max}^{\text{STR}} = K_{\max}^{\text{ISO}} \times f_z \times f_\beta \times f_x \times f_E \tag{3.36}$$

3.4.1. Number of teeth

The first parameter to be evaluated is the number of teeth. The maximum tooth pair structural stiffness with the potential energy method is computed for the gears defined by Table 3.1 but with $z_1 = z_2$. After acquiring the results, the ratio between the maximum stiffness from PEM and ISO is evaluated, giving Figure 3.2.

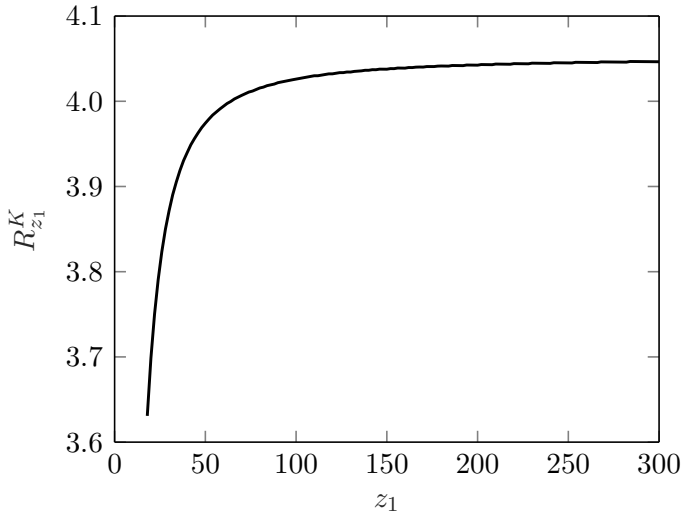

Figure 3.2: Stiffness ratio between the PEM and the ISO* maximum stiffness for each z_1.

It was found that the function given by equation (3.37) fits the ratio curve very accurately for the studied range. Even though the variation of the number of teeth z_1 is already accounted for, the fact that different gear ratios can be applied is not. Therefore, a new run is required where both z_1 and z_2 are varied. On that account, $z_1 = 18{:}100$ and $z_2 = z_1 \times 1{:}8$, where the gear ratio was changed for every z_1 (gears from Table 3.1). When the stiffness ratio was plotted, it was noticed that it was very close to 1 for every point. These results indicate that the standard ISO 6336-1 properly accounts for the variation of the gear ratio considering the adjustment already performed for the number of teeth z_1 and, consequently, there is no need for an extra fixing function.

$$f_z = -53.4\, z_1^{-1.677} + 4.05 \tag{3.37}$$

3.4.2. Helix angle

The range of values for the gear parameters used in order to determine how the helix angle affects the maximum value of the tooth pair structural stiffness are displayed in Table 3.3 - the same for the evaluation of the helix angle in α_k. The outcome revealed that there is a dependence with both the number of teeth and the helix angle. The fixing function for the helix angle, displayed in equation (3.38), is a double exponential function with coefficients A_β, B_β, C_β and D_β which are a function of z_1, attend on equations (3.39) to (3.42).

$$f_\beta = A_\beta \exp(B_\beta \beta) + C_\beta \exp(D_\beta \beta) \tag{3.38}$$

$$A_\beta = 0.9159 \exp\left(-4.93 \times 10^{-6} z_1\right) - 0.1216 \exp(-0.1426 z_1) \tag{3.39}$$

$$B_\beta = -0.001563 \exp(-0.06567 z_1) - 0.003835 \exp\left(-4.806 \times 10^{-5} z_1\right) \tag{3.40}$$

$$C_\beta = 0.1015 \exp(-0.1235 z_1) + 0.07971 \exp\left(3.44 \times 10^{-5} z_1\right) \tag{3.41}$$

$$D_\beta = -0.1636 z_1^{-0.9882} + 0.06932 \tag{3.42}$$

3.4.3. Module and facewidth

According to the ISO 6336-1 [141], the value of the maximum single tooth pair stiffness does not depend on the module and is proportional to the facewidth. When running the gears presented in Table 3.4, the outcome demonstrated that the ISO 6336-1 [141] successfully describes the behavior for these parameters and thus, no further modifications are required.

Table 3.4: Gear parameters for the module/facewidth evaluation.

Gear parameters	**Module**	**Facewidth**
$\boldsymbol{z_1}$/-	18:300	
$\boldsymbol{z_2}$/-	z_1	
$\boldsymbol{m_n}$/mm	DIN 780*	8
$\boldsymbol{\alpha}$/°	20	
$\boldsymbol{\beta}$/°	0	
$\boldsymbol{b}$/mm	20	5:100
$\boldsymbol{x_1}$/-	0	
$\boldsymbol{x_2}$/-	0	
$\boldsymbol{E}$/GPa	206	

* all module values from DIN 780 Series I

3.4.4. Profile shift coefficients

To analyze the effect of the profile shift coefficients on the maximum tooth pair structural stiffness, they are both varied simultaneously for every number of teeth and according to the data presented in Table 3.2. This makes it so that the stiffness ratio for each number of teeth z_1 is a surface. In order to fit each surface, a quadratic bivariate polynomial function such as in equation (3.43) is selected. Then, each of the coefficients A to F are expressed as functions ruled by z_1, as it can be seen from equation (3.44) to (3.49).

$$f_x = A + B\ x_2 + C\ x_1 + D\ x_2^2 + E\ x_2\ x_1 + F x_1^2 \tag{3.43}$$

$$A = -1.105 \times 10^{-5} \exp\left(0.0208\ z_1\right) + 0.9964 \exp\left(2.944 \times 10^{-5}\ z_1\right) \tag{3.44}$$

$$B = 10.26\ z_1^{-1.187} - 0.0341 \tag{3.45}$$

$$C = 8.587\ z1^{-1.01} - 0.1288 \tag{3.46}$$

$$D = \frac{0.03383\ z_1^2 - 3.775\ z_1 + 52.73}{z_1^2 - 30.96\ z_1 + 251.6} \tag{3.47}$$

$$E = \frac{-0.006403\ z_1^2 + 14.8\ z_1 - 213.9}{z_1^2 - 3.057\ z_1 - 215.8} \tag{3.48}$$

$$F = \frac{0.104\ z_1^2 - 6.334\ z_1 + 77.86}{z_1^2 - 28.87\ z_1 + 211.1} \tag{3.49}$$

3.4.5. Young's modulus

The Young's modulus is the only parameter studied which is not a geometrical parameter. In this investigation, the material is assumed to have a linear elastic behavior. Therefore, a linear fixing function of E is necessary, giving rise to equation (3.50).

$$f_E = \frac{E}{206} \tag{3.50}$$

3.5. Assessment process

To conclude the analysis of the tooth pair structural stiffness, both the shape parameters and the maximum stiffness are tested for a sample of varied gear geometries to verify its accuracy and applicability. Firstly, the intervals for the gear geometrical parameters need to be defined. On that regard, the ISO 53 [169] Profile A tooth proportions ($\alpha = 20°$, $h^*_{\mathrm{aP}} = 1$, $h^*_{\mathrm{fP}} = 1.25$ and $\rho^*_{\mathrm{fP}} = 0.38$) together with the boundaries for the gear geometrical parameters in Table 3.5 and restrictions on cutting interference, mating interference as well as on the tooth crest width [170] define the possible gears to be evaluated. The number of teeth z_2 is obtained by rounding the result of $u \times z_1$ to the closest integer, also z_2 cannot be higher than 300.

Secondly, the number of gears to be examined needs to be determined. For that purpose, Yamane's sample size formula, given by equation (3.51), is used to guarantee that the sample is representative of all possibly gear geometries in the previously mentioned conditions. For a precision, $e = 0.01$ and considering all possible combinations of the gear parameters as the total population $N = 1.8839 \times 10^{13}$, the sample size ($n$) should be $n = 10000$.

$$n = \frac{N}{1 + N\ e^2} \tag{3.51}$$

Thirdly and lastly, the asymmetry parameter, the amplitude parameter and the maximum stiffness value are computed with the developed expressions as well as with the potential energy

method for every gear in the random sample.

Table 3.5: Interval of gear parameters for the assessment.

Gear parameters	**Range**
$\boldsymbol{z_1}$/-	18:100
$\boldsymbol{u = z_2/z_1}$/-	1:6
$\boldsymbol{m_n}$/mm	DIN 780*
$\boldsymbol{\alpha}$/°	20
$\boldsymbol{\beta}$/°	0:40
$\boldsymbol{b}$/mm	3 m_n:14 m_n
$\boldsymbol{x_1}$/-	-1:1
$\boldsymbol{x_2}$/-	-1:1
$\boldsymbol{E}$/GPa	180:220

* all module values from DIN 780 Series I

3.5.1. Shape parameters

To assess the shape parameters (asymmetry and amplitude) the normalized curves of the tooth pair structural stiffness from the approximate expression, equation (3.12), and the potential energy method are compared. Figure 3.3 shows the histogram of the R-squared values of each set of curves.

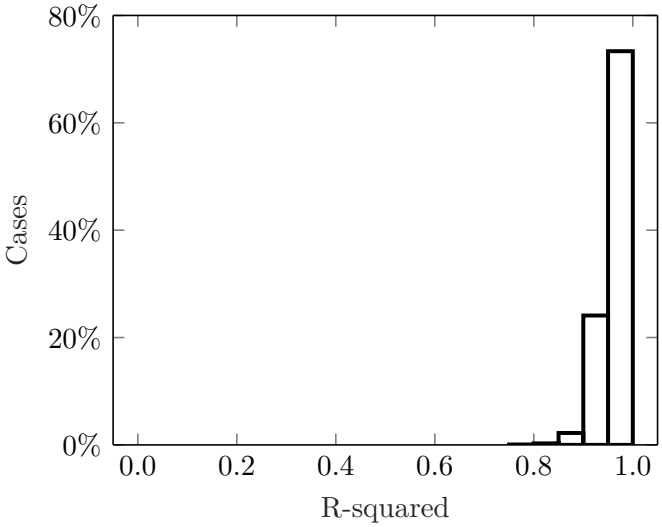

Figure 3.3: Histogram of the R-squared values for the tooth pair structural stiffness shape.

According to the results displayed in Figure 3.3, 73% of the cases have an R-squared above 0.95 and 97% are over 0.90. The average R-squared value is 0.9544. Next, the best and worst cases of fitting are presented, which correspond to the gear parameters given by Table 3.6.

Figure 3.4 shows the best and worst fit obtained for the tooth pair structural stiffness shape. The worst result presented is expected to be the worst case that one would face from all possible gears in the range of the established parameters, showing how solid the model is. From this analysis, the shape parameters are found to be in agreement with the potential energy method for the tooth pair structural stiffness.

Table 3.6: Gear parameters for the best and worst cases.

Gear parameters	**Best**	**Worst**
z_1/-	22	31
z_2/-	26	124
m_n/mm	16	0.7
α/°	20	20
β/°	21	21
b/mm	119	6.1
x_1/-	-0.18	0.74
x_2/-	-0.23	-0.87
E/GPa	220	205

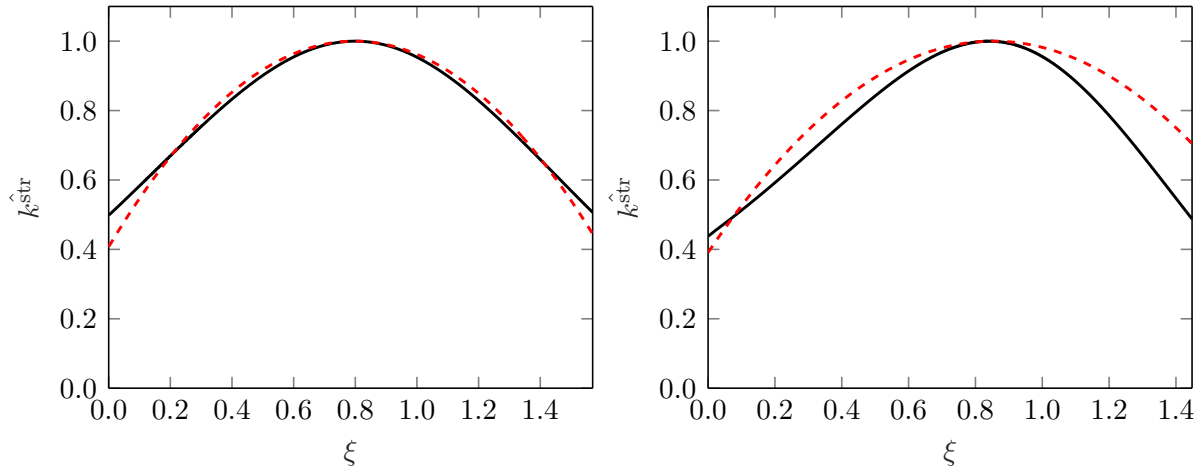

(a) Best fit. $R^2 = 0.9858$.

(b) Worst fit. $R^2 = 0.7687$.

Figure 3.4: Comparison between the potential energy method (——) and the model (- - -) curves for the tooth pair structural stiffness shape.

Next, in order to understand how the independent variables affect the fit of the tooth pair structural stiffness shape, Figure 3.5 is plotted. Figure 3.5 has the domain of the variable in study divided into intervals. The results comprised in each interval are shown by a modified box plot as described by the legend in Figure 3.5a. Analyzing each variable leads to the following conclusions:

- z_1 (Figure 3.5a): there is a clear correlation between the number of teeth and the R-squared values. The mean, boxes and whiskers all follow the same pattern, that is, with the increase number of teeth there are higher R-squared values.
- u (Figure 3.5b): the mean and boxes show the maximum R-squared values at around $u = 2.2$ and tend to decrease as u moves away from this value. Although, the whiskers do not show any type of relation as they are randomly distributed.
- β (Figure 3.5c): the boxes are all comprised for R-squared > 0.90 and the lowest mean value of R-squared is around 0.95 - both increasing with β. There is not a relation between β and the whiskers but it can be verified that the whiskers show higher values when β is in its upper limit.

- x_1 (Figure 3.5d): regarding mean and boxes, the region slightly to the left of zero is where the maximum values of R-squared are found. The further away x_1 is from this region, the lower the R-squared values are. The whiskers are dispersed along the domain.
- x_2 (Figure 3.5e): two distinct behaviors are found for this variable, one to the left and another to the right of $x_2 \approx -0.3$. On one hand, in the right side, R-squared values shows a small decrease. On the other hand, there is an abrupt decrease in the quality of fitting when analyzing the left side. However, it must be mentioned that the lowest mean is 0.88 and that there are very few generated gears in this region.

To sum up, the number of teeth of the pinion is the only variable has a consistent relation with the quality of the tooth pair structural stiffness shape fitting. This is, the trend of the mean value, the boxes as well as the whiskers is the same - higher R-squared values for higher number of teeth.

3.5.2. Maximum stiffness

The maximum value for the tooth pair structural stiffness is computed according to equation (3.52). Each of the functions f_z, f_α, f_x and f_E are established by equations (3.37), (3.43) - (3.49) and (3.50), respectively.

$$K_{\max}^{\mathrm{STR}} = K_{\max}^{\mathrm{ISO}} \times f_z \times f_\beta \times f_x \times f_E \tag{3.52}$$

Figure 3.6 shows the relative error of the maximum tooth pair structural stiffness according to equation (3.52) compared to the maximum tooth pair structural stiffness obtained from the potential energy method.

From Figure 3.6 there is a high concentration of cases between -5% and 5% of relative error which consist on 72% of the cases. Also, 90% of the sample have an absolute relative error $< 10\%$. Overall, the average absolute relative error is 4.1%. Concluding, the values of the maximum single tooth pair mesh stiffness from ISO 6336-1 [141] were successfully modified for the tooth pair structural stiffness.

The distribution of the relative error for each variable is presented in Figure 3.7. Taking an overview of Figure 3.7, it shows that there is a correlation between the relative error for the maximum stiffness values and z_1, x_1 as well as x_2 since the mean, boxes and whiskers all follow the same same trend. Detailing more the analysis to each variable:

- z_1 (Figure 3.7a): the relative error decreases with the increase in the number of teeth, as it was found for the fitting of the tooth pair structural stiffness shape.
- β (Figure 3.7b): almost constant values in the entire domain with slight increase for high values of helix angle.
- x_1 (Figure 3.7c): the mean, boxes and whiskers all show the same behavior with x_1. The minimum relative error is found around $x_1 = 0$. Also, the relative error is proportional to $|x_1|$ in an almost symmetrical manner.
- x_2 (Figure 3.7d): similar conclusions to x_1 can be performed but for x_2 the increase is higher when x_2 is negative. Note that there is a small number of generated gears for x_2 around -1.

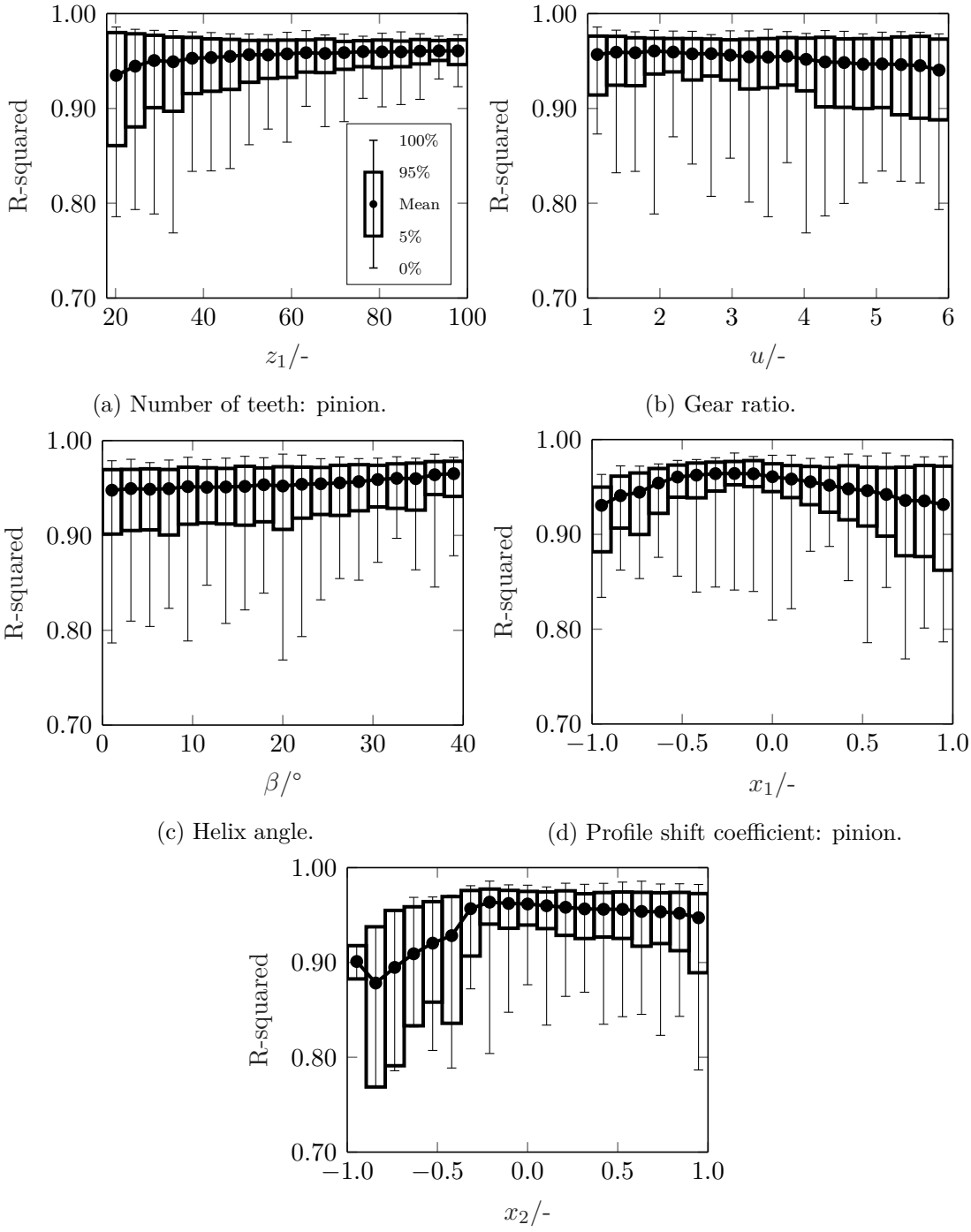

(a) Number of teeth: pinion.

(b) Gear ratio.

(c) Helix angle.

(d) Profile shift coefficient: pinion.

(e) Profile shift coefficient: wheel.

Figure 3.5: Influence of independent variables in the tooth pair structural stiffness shape.

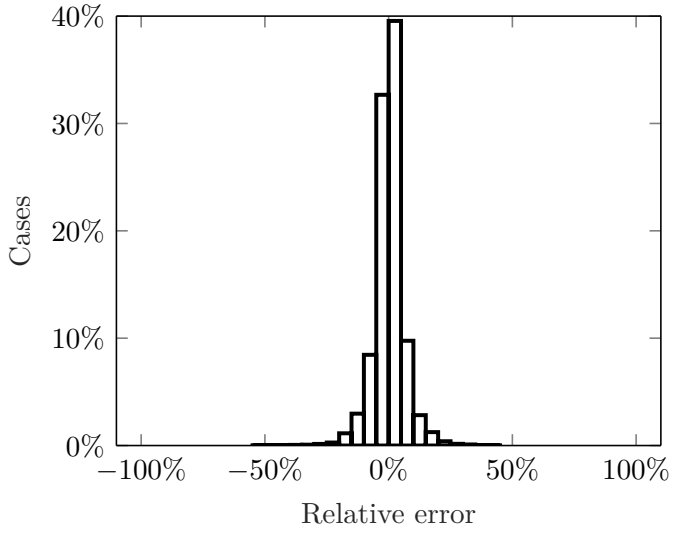

Figure 3.6: Histogram of the maximum tooth pair structural stiffness relative error comparing to PEM.

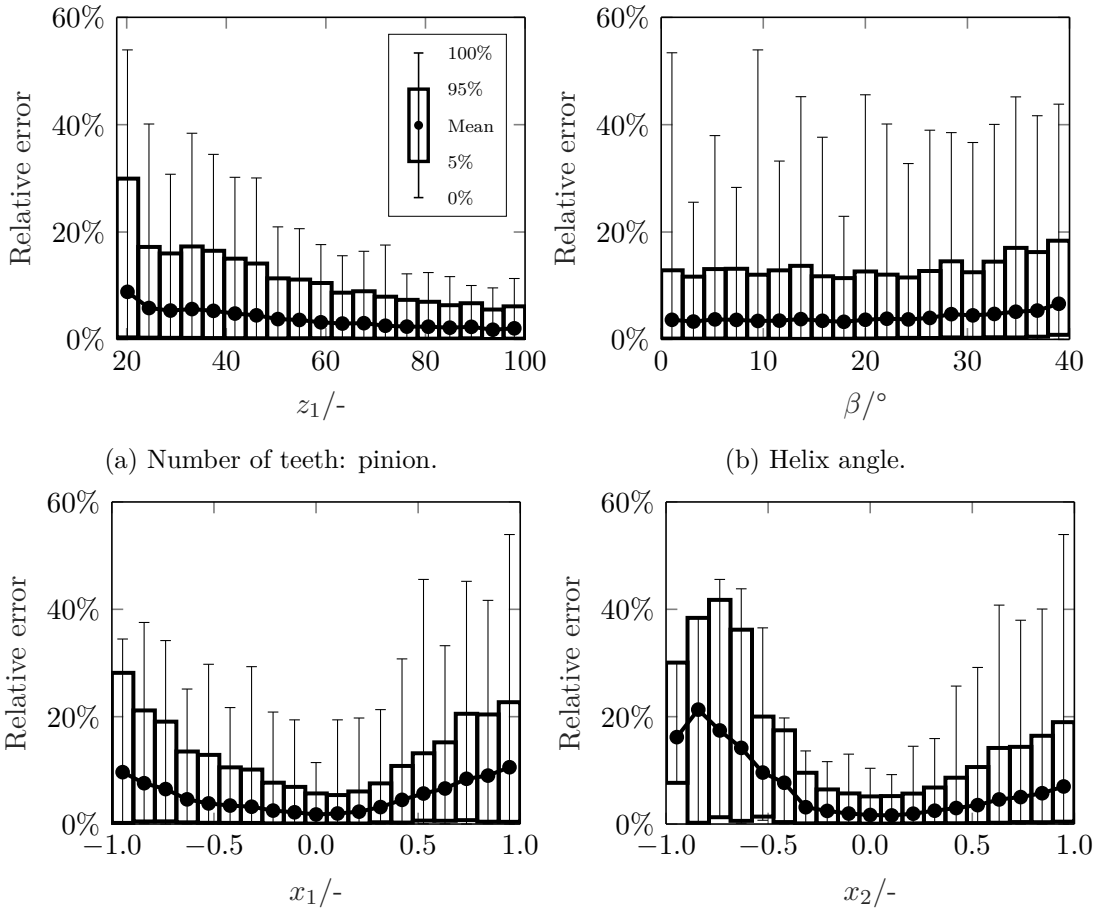

(a) Number of teeth: pinion.

(b) Helix angle.

(c) Profile shift coefficient: pinion.

(d) Profile shift coefficient: wheel.

Figure 3.7: Influence of independent variables in the maximum tooth pair structural stiffness value.

3.6. Single tooth pair slice mesh stiffness

As it was previously noted, there are three main components for the single tooth pair slice mesh stiffness, them being, tooth pair structural stiffness, the fillet-foundation stiffness and the contact stiffness. In this chapter, an approximate expression for the tooth pair structural stiffness is settled. By combining the new tooth pair structural stiffness formulation with other closed-form analytical expressions for the fillet-foundation [78] and contact stiffnesses [77], one can reach an accurate and computational inexpensive expression for the single tooth pair slice mesh stiffness, which is set by equation (3.53).

$$k^{\mathrm{tp,\,s}} = \left(\frac{1}{k^{\mathrm{str}}} + \frac{1}{k_{\mathrm{f1}}} + \frac{1}{k_{\mathrm{f2}}} + \frac{1}{k_{\mathrm{H}}} \right)^{-1} \tag{3.53}$$

In equation (3.53), k^{str} is the tooth pair structural stiffness defined by equation (3.54). The parameters required for its definition are λ, α_k and $K_{\mathrm{max}}^{\mathrm{STR}}$ and are established by equations (3.13), (3.23) and (3.36), respectively; k_{f1} and k_{f2} are the fillet-foundation stiffnesses computed according to Sainsot et al. [78] and k_{H} is the contact stiffness determined with the formulation presented in Sainsot and Velex [77].

$$k^{\mathrm{str}} = \left[\frac{4(\alpha_k - 1)}{\varepsilon_\alpha^2} (\xi - \lambda)^2 - \frac{4(\alpha_k - 1)}{\varepsilon_\alpha} (\xi - \lambda) + \alpha_k \right] K_{\mathrm{max}}^{\mathrm{STR}} \tag{3.54}$$

Next, and since the stiffness components from equation (3.53) are successfully assessed, some examples of application of the approximate expression for the single tooth pair slice mesh stiffness for the spur and helical gears presented in Table 3.7 are discussed.

Table 3.7: Gear parameters for the example gears.

Gear parameters	**C14**	**H501**
$\boldsymbol{z_1}$/-	16	20
$\boldsymbol{z_2}$/-	24	30
$\boldsymbol{m}_{\mathrm{n}}$/mm	4.5	3.5
$\boldsymbol{\alpha}$/°	20	20
$\boldsymbol{\beta}$/°	0	15
$\boldsymbol{b}$/mm	14	23
$\boldsymbol{x_1}$/-	0.1817	0.1809
$\boldsymbol{x_2}$/-	0.1715	0.0891
$\boldsymbol{E}$/GPa	210	210
$\boldsymbol{r}_{\mathrm{hub}}$/mm	15	15

The single tooth pair slice mesh stiffness from the developed model is compared with the results from PEM and an approximate stiffness model from the literature, Marques et al. [143] model, attend on Figure 3.8. It is noteworthy here that Figure 3.8a represents the single tooth pair mesh stiffness for the spur gear while Figure 3.8b shows the single tooth pair slice mesh stiffness when 93 slices are considered in the helical gear.

When looking at the results for the C14 (Figure 3.8a), the new model can replicate the single tooth pair stiffness from PEM, however the literature model [143] shows a lower maximum

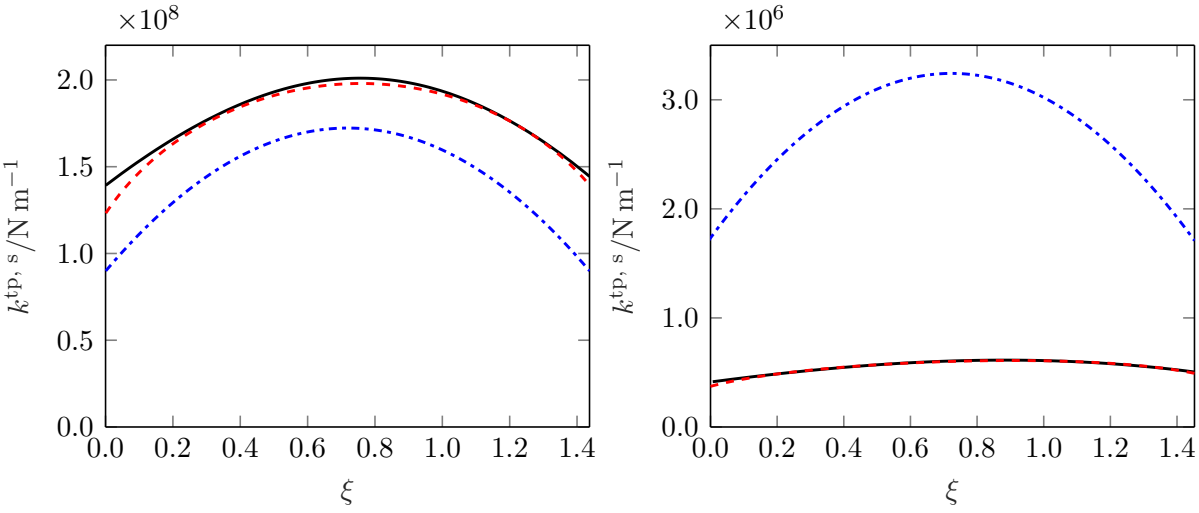

(a) C14. (b) H501.

Figure 3.8: Comparison between the potential energy method (——), the developed model (- - -) and the Marques et al. [143] model (-·-·-) curves for the single tooth pair slice mesh stiffness.

stiffness value as well as a lack of asymmetry. The results for the H501 (Figure 3.8b) clearly exhibit the limitation of the ISO 6336 [141] on estimating the maximum stiffness on the literature model - issue solved with the new formulation of maximum tooth pair structural stiffness of this work. In addition, the H501 curve is actually highly asymmetric, presenting for the PEM curve a difference between the starting and ending points of contact normalized by the maximum stiffness value equal to 14%. Due to the introduction of the asymmetry parameter, the model presented in this chapter can keep up with asymmetric shapes. These examples highlight the possible improvements given by the new model when comparing with other type of approximate models that do not consider the asymmetry, define the relative amplitude with fixed/contact ratio dependent values and use the ISO 6336 [141] to establish the stiffness value.

3.7. Closure

A new expression to approximate the single tooth pair slice mesh stiffness is developed in this chapter. The tooth pair structural stiffness, fillet-foundation stiffness [78] and contact stiffness [77] are the stiffness components included. A new formulation for the tooth pair structural stiffness, which can replace the potential energy method with a faster estimation, is developed, allowing the prompt and accurate computation of the tooth pair structural stiffness. This formulation relies on a parabolic approximation of the tooth pair structural stiffness with three parameters to define its asymmetry, relative amplitude and maximum stiffness value. Each of these parameters was assessed for a random sample of gears representative of every possible gear pair within a broad range of gear parameters, thus proving the authenticity and applicability of the expressions. In addition, when evaluating how the expression behaves with its variables, it was found that the number of teeth of the pinion is the independent variable that better correlates with the quality of the approximation.

The single tooth pair slice mesh stiffness is computed for a spur and helical gear with three distinct models, the potential energy method, the developed model and an approximate stiffness model from the literature. The approximate stiffness model reveals the limitations of the simplifications performed in the literature while the developed model is in accordance with the

potential energy method.

Concluding, this work provides a significant contribution for approximate analytical gear mesh stiffness models as it enables an easy implementation with fast and accurate results for the single tooth pair slice mesh stiffness. To compare the computational cost between the potential energy method and the developed approximate expressions, the necessary time (intel(R) core(TM) i7-9700 CPU with 64 GB of memory RAM at 2667 MHz - MATLAB® R2023a) to estimate the tooth pair structural stiffness is used. Considering the sample of 10000 random gear geometries already created for this work, the potential energy method takes for the estimation of the tooth pair structural stiffness an average of 2.04 s per estimation while the developed approximate expression needs 0.021 ms - reduction in the necessary time by 5 orders of magnitude. The integration of the developed approximate analytical expression in a gear mesh stiffness model makes it feasible to perform extensive gear parametric and optimization studies.

Next The accomplishment of the approximate expression for the single tooth pair slice mesh stiffness solves the major accuracy issue of approximate gear mesh stiffness models. The following phase is to develop a gear mesh stiffness model with the work in this chapter as a basis. The gear mesh stiffness model is built while keeping in mind a sound yet flexible implementation, in the sense that it needs to include fundamental effects that characterize the mesh stiffness and also allow to be easily modified for further phenomena.

Chapter 4

Gear modeling

There are certainly a lot of different gear mesh stiffness models in the literature, nonetheless, it is not possible to find comprehensive and in-depth gear parametric studies that sweep the gear geometrical domain. To do so, it is required to have a fast and accurate gear mesh stiffness model, which is precisely one of the main developments of this chapter. By taking advantage of this new model, a parametric study on the influence of tooth pair structural stiffness asymmetry is conducted. This investigation evaluates how the referred stiffness asymmetry affects the gear mesh stiffness, dynamic displacements and load distribution by performing an extensive number of simulations that cover the entire selected gear geometry spectrum - two randomly generated populations of gears, one for spur and another for helical, are tested with and without the tooth pair structural stiffness asymmetry. It is concluded that tooth pair structural stiffness asymmetry cannot be neglected since it can lead to significant modifications on the frequency content of the gear mesh stiffness as well as the dynamic behavior of the geared system.

4.1. Background

Geared transmissions are core elements of contemporary machinery. Noise, vibration and efficiency are factors whom without, it is not possible to understand or control the behavior of these systems. Two of the necessary pieces to link the noise, vibration and efficiency to the geared transmission are the gear mesh stiffness and dynamic modeling. These three parameters cannot be obtained if, somewhat along the way, the gear mesh stiffness is not estimated or a dynamic model is not developed.

Marafona et al. [171] developed an approximate expression for the single tooth pair slice mesh stiffness resorting to a parabolic function of the tooth pair structural stiffness and existing formulations for the fillet-foundation [78; 79] and contact [77] stiffnesses. The single tooth pair slice mesh stiffness expression [171] does not require integration of the tooth profile for every point and therefore is a much faster and easier to incorporate alternative to the potential energy method. The single tooth pair slice mesh stiffness approximation [171], defined in equation (4.1), depends on the tooth pair structural stiffness, fillet-foundation stiffness [79] and contact stiffness [77]. Approximate gear mesh stiffness models [13; 73; 136; 143] typically consider the single tooth

Contents in Chapter 4: Gear modeling are reproduced with permission of the respective publisher from João D.M. Marafona, Pedro M.T. Marques, Stephane Portron, Ramiro C. Martins, and Jorge H.O. Seabra. Gear mesh stiffness and dynamics: Influence of tooth pair structural stiffness asymmetry. *Mechanism and Machine Theory*, 190:105447, 2023.

pair slice mesh stiffness as being a symmetric curve with respect to the middle of the theoretical path of contact ($\varepsilon_\alpha/2$, Figure 4.2), which is not necessarily true. Asymmetric single tooth pair mesh stiffness curves are discussed in [73; 167; 168] but referring to asymmetries caused by non-standard center distance, non-equal tooth addendum and undercut, not due to differences in the number of teeth and profile shift coefficients between the pinion and the gear, as it is done in [171]. With the formulation presented in [171], the single tooth pair stiffness asymmetries from the fillet-foundation and contact stiffness are included in the respective formulations and the tooth pair structural stiffness asymmetry is established by λ; equation (4.2) defines the tooth pair structural stiffness where the amount of asymmetry (λ) is included. In order to understand if the tooth pair structural stiffness asymmetry (λ) can be neglected or not for gear modeling, a study covering a wide range of gear geometries is necessary. A detailed discussion on how the different approximate gear mesh stiffness models approach the single tooth pair (slice) mesh stiffness can be found in reference [171].

In this chapter, two different approaches are taken to evaluate the influence of the tooth pair structural stiffness asymmetry: a quasi-static approach and a dynamic approach. Either way, extensive computations of the stiffness and dynamic response are required, so a fast, reliable and complete gear mesh stiffness model is necessary for such purposes. Looking into gear mesh stiffness models, there are four different categories, analytical models [14; 17; 84; 87; 89; 90; 99; 100; 102], finite element models [9; 15; 118; 120; 122], hybrid models [11; 12; 123; 126; 132; 133] and approximate analytical models [13; 73; 136; 138; 143; 172–174]. The type of models that have the lowest computation time are analytical and approximate analytical models [166]. Focusing on analytical/approximate models for spur gears, the works [17; 84; 87; 89; 90; 138; 173] consider tooth profile error, which include separation distance and/or profile modification. Regarding helical gears, the slicing method, which consists in viewing the helical gear pair as a set of staggered spur gears, is commonly used. However, these slices must be coupled so that the deformation of one slice has influence on the neighboring ones and thus guaranteeing continuity [14; 99; 100; 102]. Extension of contact and profile modifications in helical gears is a much less discussed topic in the literature when compared to spur gears. Including profile modification for the estimation of the gear mesh stiffness of helical gears is found in [99; 172–174].

For the dynamic approach, gear dynamic systems show a wide applicability and can reach results that compare well with experimental tests with a proper description of the dynamic system [175–182]. Blankenship and Singh [175] estimated the forces/moments produced and transferred through the gear mesh interface in a dynamic model. The developed formulation allows the comparison, in a mathematical level, of several simplifying assumptions commonly applied in gear dynamic systems [175]. To study a mechanical system with parametric excitation and clearance type nonlinearity, Blankenship and Kahraman [176] presented a single degree-of-freedom gear torsional model which is validated with experimental results. Velex and Maatar [177] treated the gear meshing from a dynamic perspective. The dynamic transmission error and dynamic tooth loads are obtained as a result of the proposed model which separates the rigid body displacements from the elastic displacements in its formulation. Both quasi-static and dynamic solutions show agreement with experimental and analytical results from the literature. The impact of geometrical errors and profile modifications on the gear dynamics is evaluated resorting to the developed methodology [177]. Kubur et al. [179] developed and validated experimentally a helical gear-shaft-bearing system to then analyze a multi-shaft helical gear transmission. The model employs time-invariant gear mesh stiffness, Timoshenko beam elements for the shafts, lumped stiffnessess for the bearings and, if necessary, the housing flexibility by a condensed stiffness matrix derived from the finite element method [179]. Ajmi and Velex [183] developed a model to simulate the quasi-static and dynamic behavior of solid wide-faced gears. Gear bodies

were modeled resorting to two node shaft finite elements in bending, torsion and traction; tooth bending and shear deflections including coupling effects were modeled with the Pasternak's foundation model; contact deflections were introduced with the classical approximation based on semi-infinite elastic spaces; tooth shape deviations and alignment errors were included as normal deviations. It was found that gear body flexibility is relevant for the quasi-static and dynamic conditions of wide-faced gears and that the tooth coupling effects are less significant in dynamic conditions [183]. Kang and Kahraman [181] conducted an experimental study on double-helical gear pair systems comprising shafts and bearings. Alongside the experimental investigation, the dynamic modeling of the same system was also performed where the double-helical gear pair was modeled as a combination of two single helical gear pairs. For that purpose, the gear bodies of the single helical gear pair were assumed to be rigid and connected by a spring representing the gear mesh stiffness. The gear mesh stiffness was fixed to its average value and nonlinearities related with tooth separations were neglected. Shafts are introduced via Euler beam elements and the bearings as time-invariant stiffnessess. It was shown that the developed dynamic model can successfully predict the dynamic behavior of double-helical systems [181].

For this work, an approximate gear mesh stiffness model that takes advantage of the formulation developed by Marafona et al. [171] for the single tooth pair slice mesh stiffness as well as the line stiffness distribution by Marques et al. [143] for the coupling stiffness between the slices is developed. In addition, the effect of the extension of contact/contact outside the path of contact, profile modifications and buttressing are also included in the model - showing significant improvements to the previous approximate gear mesh stiffness model [143]. The developed approximate gear mesh stiffness model is fast, accurate and easy to implement. With it, it is possible to estimate the gear mesh stiffness and the load sharing ratio of a large amount of gears in a very short time, thus allowing detailed gear parametric studies and optimization of gear design. For the dynamic evaluation, a single stage gear-shaft-bearing transmission is modeled. The gears are approximated as rigid disks connected through a time-varying gear mesh stiffness, the shafts are modeled by applying the finite element method and bearings are introduced via lumped stiffnesses. First, the developed gear mesh stiffness model is thoroughly explained and assessed. Second, the dynamic model is described and then verified with results from the literature. Third, the influence of the tooth pair structural asymmetry is investigated by creating two random samples of gears, one for spur and another for helical gears. Then, the gear mesh stiffness, dynamic transmission error and load distribution of the gears are computed with and without the asymmetry parameter. Finally, one can conclude if the tooth pair structural stiffness asymmetry (λ) should or should not be included in the modeling of the mesh stiffness and dynamic behavior for the generality of spur and helical gears. That being said, there are two main outputs of the current study that are relevant at both academic and industrial levels:

- improvement of approximate gear mesh stiffness models: these models are praised for being very fast with a straightforward implementation. On the other hand, their main disadvantage (inherent due to the approximations applied to make them simple) is in their relatively low accuracy when compared to other types of gear mesh stiffness models like finite element and hybrid models. In this chapter, every necessary step for the implementation of a new, complete and more accurate approximate gear mesh stiffness model is presented;

- presentation of large scale gear exploratory study: it is shown that approximate gear mesh stiffness models can perform gear geometry exploratory studies where it is required to compute the gear mesh stiffness multiple times. This is applied, in this chapter, to investigate the effect of tooth pair structural stiffness asymmetry (stiffness modeling parameter) on the gear mesh stiffness model in order to improve approximate models.

Other examples of applicability are gear design optimization and nonlinear/iterative gear dynamic models where for each point the gear mesh stiffness is updated.

4.2. Gear mesh stiffness model

A new approximate gear mesh stiffness model that considers extension of contact, profile modifications and single tooth pair stiffness asymmetry is presented. This model estimates the gear mesh stiffness of spur and helical gears based on the slicing method and an approximation of the single tooth pair slice mesh stiffness. An overall view of the employed methodology is displayed in Figure 4.1 and is briefly described as follows: the algorithm starts by processing the gear geometry and then moves to the determination of the slice transmission error, which is the transmission error for each slice without considering the extension of contact. Then, it enters the process of including the extension of contact where it is first necessary to compute the distance that separates the teeth from contacting each other. Next, the algorithm starts an iterative cycle consisting on the computation of the extension distance (where both the slice transmission error and the separation distance are necessary), the transmission error with the effect of the extension of contact and the slice load sharing ratio. At this point, if the convergence criteria is not accomplished it returns to the computation of the extension distance with the updated slice transmission error and repeats the cycle. Once convergence is found, the algorithm computes the transmission error and the gear mesh stiffness.

As it was aforementioned, the problem is analyzed using the slicing method, meaning that the helical gear is viewed as a combination of staggered slices, each slice being equivalent to a spur gear. Therefore, for spur gears, the developed model can be simplified if no axial modifications are introduced - slicing method not required. Nevertheless, the most generic methodology is going to be presented. Note that each of the following sections matches with a process from Figure 4.1, thus allowing a parallel analysis for better comprehension of the algorithm.

4.2.1. Slice transmission error

To define the slice transmission error, the single tooth pair slice mesh stiffness from [171] is taken and combined with a coupling stiffness distribution function and the buttressing effect. The applied coordinate system is shown in Figure 4.2 where the plane of action of a random helical gear is presented with some theoretical contact lines. There are two coordinates used for the description of the gear model: ξ and b_s. ξ is the coordinate along the path of contact normalized by the transverse base pitch, which is zero at the theoretical start point of meshing, point A in Figure 4.2. b_s is the axial coordinate defined along the gear facewidth.

First, the slice mesh stiffness of tooth pair i is defined as in equation (4.1).

$$k^{\mathrm{tp,s}}(\xi, b_\mathrm{s}, i) = \left(\frac{1}{k^{\mathrm{str}}} + \frac{1}{k_{\mathrm{f1}}} + \frac{1}{k_{\mathrm{f2}}} + \frac{1}{k_\mathrm{H}} \right)^{-1} \tag{4.1}$$

where k^{str} is the tooth pair structural stiffness defined by equation (4.2) and requires the parameters λ, α_k and $K^{\mathrm{STR}}_{\mathrm{max}}$ which are established in [171] as well as the coordinate b_s to characterize the shift of the stiffness curve along the gear facewidth; k_{f1} and k_{f2} are the fillet-foundation stiffnesses computed according to [78; 79] and k_H is the contact stiffness determined with the formulation presented in Sainsot and Velex [77].

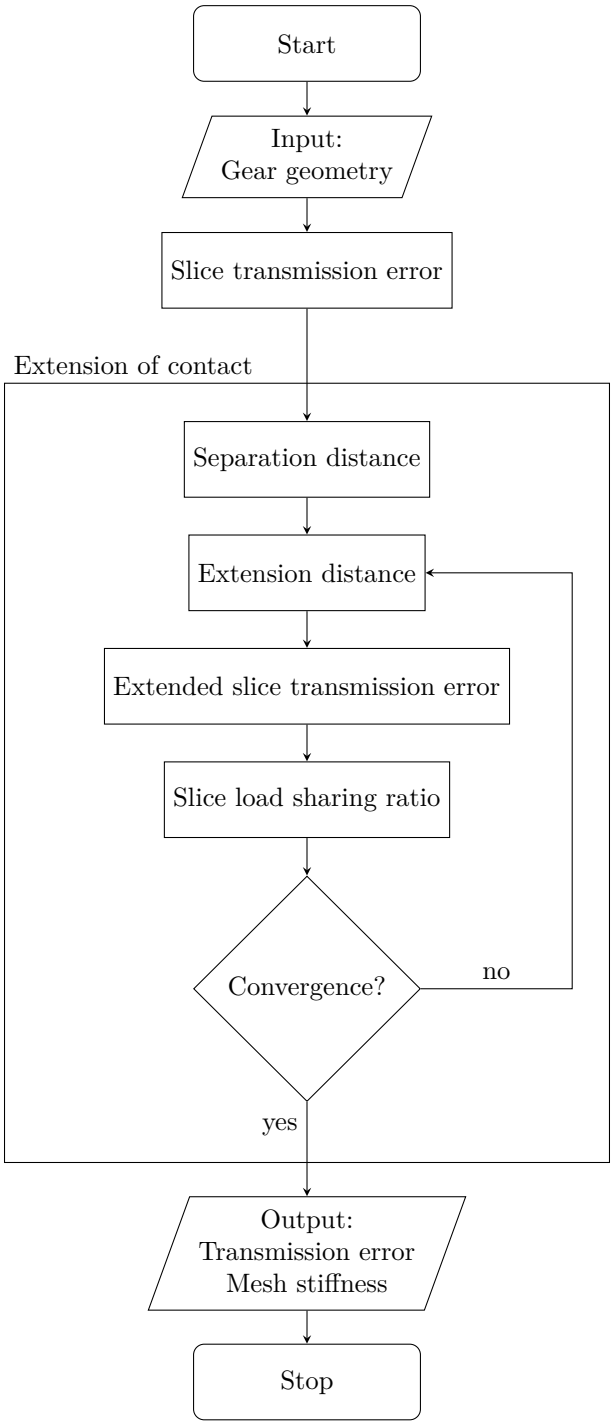

Figure 4.1: Flowchart of the gear mesh stiffness model.

$$k^{\mathrm{str}}(\xi, b_{\mathrm{s}}, i) = \left[\frac{4(\alpha_k - 1)}{\varepsilon_\alpha^2}(\xi - \frac{b_{\mathrm{s}}}{b}\varepsilon_\beta - \lambda - i)^2 - \frac{4(\alpha_k - 1)}{\varepsilon_\alpha}(\xi - \frac{b_{\mathrm{s}}}{b}\varepsilon_\beta - \lambda - i) + \alpha_k\right] K_{\max}^{\mathrm{STR}} \quad (4.2)$$

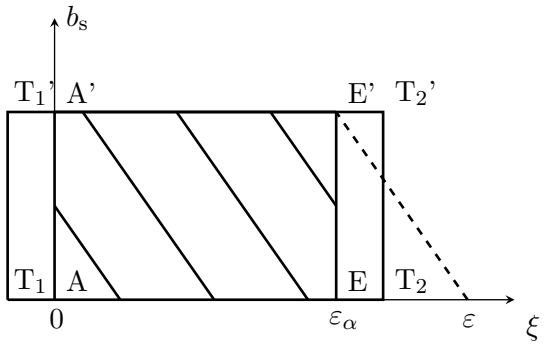

Figure 4.2: Definition of the coordinate system.

It is in equation (4.2) that the tooth pair structural stiffness asymmetry (parameter in study), defined by λ, appears. This parameter makes the parabolic curve of the tooth pair structural stiffness shift right or left and thus modifies the stiffness values along the path of contact - the asymmetry parameter can cause significant stiffness changes in the theoretical start and end of the path of contact.

Second, the coupling stiffness distribution is defined as a parabolic function along the contact lines [143], see equation (4.3).

$$k_{\mathrm{L}}(\xi, b_{\mathrm{s}}, i) = c_{\mathrm{f}} \left[\frac{4(\alpha_{\mathrm{L}} - 1)}{\varepsilon_{\mathrm{L}}^2} \left(\frac{b_{\mathrm{s}}}{b} + \phi_{\mathrm{L}} - \frac{\phi}{\varepsilon_\beta} \right)^2 - \frac{4(\alpha_{\mathrm{L}} - 1)}{\varepsilon_{\mathrm{L}}} \left(\frac{b_{\mathrm{s}}}{b} + \phi_{\mathrm{L}} - \frac{\phi}{\varepsilon_\beta} \right) + \alpha_{\mathrm{L}} \right] \tag{4.3}$$

where c_{f}, ε_{L}, ϕ_{L} and ϕ are established by equations (4.4), (4.5), (4.6) and (4.7) according to [143].

$$c_{\mathrm{f}} = \left[\frac{2 + \alpha_{\mathrm{L}}}{3} \right]^{-1} \tag{4.4}$$

$$\varepsilon_{\mathrm{L}} = \frac{1}{\varepsilon_\beta} \Big(\varepsilon_\beta - H(\varepsilon_\beta - \varepsilon_\alpha) \cdot (\varepsilon_\beta - \varepsilon_\alpha) \Big) \tag{4.5}$$

$$\phi_{\mathrm{L}}(\xi, i) = \frac{1}{\varepsilon_\beta} H(\xi - i - \varepsilon_\alpha - (1 - \varepsilon_{\mathrm{L}})\varepsilon_\beta) \cdot (\xi - i - \varepsilon_\alpha - (1 - \varepsilon_{\mathrm{L}})\varepsilon_\beta) \tag{4.6}$$

$$\phi(\xi, i) = H(\xi - i - \varepsilon_\alpha) \cdot (\xi - i - \varepsilon_\alpha) - H(\xi - i - \varepsilon) \cdot (\xi - i - \varepsilon) \tag{4.7}$$

Third, in helical gears, the stiffness on the side edges is reduced when there is not a full tooth normal section supporting the load in the normal direction - this reduction is referred to as buttressing or border weakening factor. In order to incorporate such phenomenon in the computation of stiffness, a correction factor R is introduced as proposed by KISSsoft® [81], see equation (4.8).

$$R = \left(\frac{\bar{s}^{\mathrm{red}}}{\bar{s}} \right)^{0.5} \tag{4.8}$$

In equation (4.8), $\bar{s}^{\mathrm{red}}$ is the reduced chordal tooth thickness at the pitch point and $\bar{s}$ is the normal tooth thickness at the pitch normal for every contact point.

Forth, the final form of the single tooth pair slice mesh stiffness with the effects of the coupling stiffness distribution and the buttressing effect is obtained by equation (4.9).

$$k^{\mathrm{s},i}(\xi, b_{\mathrm{s}}, i) = k^{\mathrm{tp,\ s}} \cdot k_{\mathrm{L}} \cdot R \tag{4.9}$$

It is possible to compute the gear slice mesh stiffness by adding the stiffness of all tooth pairs in contact, as shown by equation (4.10). Notice that i (integer number obtained by the rounding down function "floor") makes a translation of the stiffness curves so that all necessary tooth pairs are accounted for the stiffness estimation along the path of contact.

$$K^{\mathrm{s}} = \sum_{i=-\mathrm{floor}(\varepsilon_\alpha)}^{\mathrm{floor}(\varepsilon_\alpha)} k^{\mathrm{s},i} \tag{4.10}$$

In order to determine the transmission error for each slice, it is required to determine the load applied in each slice. For that purpose, the constrained expression for elastic potential energy, equation (4.11), is specified.

$$I(F^1, ..., F^{NS}, \Lambda) = \sum_{\mathrm{s}=1}^{NS} \frac{1}{2} \frac{F^{\mathrm{s}2}}{K^{\mathrm{s}}} + \Lambda \left(\sum_{\mathrm{s}=1}^{NS} F^{\mathrm{s}}\, r_{\mathrm{b}2} - T_2 \right) \tag{4.11}$$

where F^{s} is the load applied on slice s and K^{s} is the gear slice mesh stiffness, NS is the total number of slices and Λ is the Lagrange multiplier. Minimizing the total elastic potential energy of the system leads to equation (4.12) for the load applied in each slice and equation (4.13) for the Lagrange multiplier.

$$F^{\mathrm{s}} = \frac{T_2}{r_{\mathrm{b}2}} \frac{K^{\mathrm{s}}}{\sum_{\mathrm{s}=1}^{NS} K^{\mathrm{s}}} \tag{4.12}$$

$$\Lambda = -\frac{T_2}{r_{\mathrm{b}2}^2} \frac{1}{\sum_{\mathrm{s}=1}^{NS} K^{\mathrm{s}}} \tag{4.13}$$

Finally, the transmission error for each slice s is given by equation (4.14).

$$\delta^{\mathrm{s}} = \frac{F^{\mathrm{s}}}{K^{\mathrm{s}}} \tag{4.14}$$

4.2.2. Extension of contact

The extension of contact results from the deformation of the gear teeth which makes their contact begin earlier and end later than the theoretical points thus leading to contact outside the path of contact [35; 92–95]. The application of the extension of contact is divided in three main

steps which correspond to: (1) computation of the separation distance; (2) determination of the extension distance which requires the transmission error and separation distance and (3) calculation of the extended transmission error, which is the modification of the transmission error to consider the extension of contact. The procedure presented is applied for a gear slice, thus is valid for both spur and helical gears.

Separation distance

The separation distance (Δ_s) is the distance that separates two teeth from contacting each other and is divided into the geometrical separation distance (Δ_g) and the profile modification separation distance (Δ_p), equation (4.15).

$$\Delta_s = \Delta_g + \Delta_p \tag{4.15}$$

The geometrical separation distance is computed resorting to the formulation developed by Munro et al. [95]. The profile modification separation distance can be determined by the imposed profile modifications according to equation (4.16).

$$\begin{aligned}\Delta_p = &\left[C\left(\frac{\xi-(\varepsilon_\alpha-L^C)}{L^C}\right)^{n^C}\right]\left[H(\xi-(\varepsilon_\alpha-L^C))-H(\xi-\varepsilon_\alpha)\right]+\\ &\left[C\left(\frac{L^C-\xi}{L^C}\right)^{n^C}\right]\left[H(\xi)-H(\xi-L^C)\right]\end{aligned} \tag{4.16}$$

In equation (4.16), C is the amount of relief, L^C is the length of the modification normalized by the transverse base pitch and n^C defines the type of modification, which can either be linear ($n^C = 1$) or parabolic ($n^C = 2$). Notice that the total separation distance can be divided into approach and recess distances, which refers to the distances separating the teeth as they enter and leave contact.

Extension distance

The applied load on the gear pair will make the teeth deform and consequently increase the path of contact, making the contact start earlier and end later: phenomena of extension of contact. While the teeth deformations are higher than the distance that separate them, contact will remain. So, the actual starting and ending points are given by the location where the separation distance equals the tooth pair deflection, attend on Figure 4.3 for a graphical example of this phenomena. Since the transmission error can be viewed as the deflection caused by the applied load, together with the separation distance, the extension distance can be acquired. Thus, extension distance approach/recess is the distance between the actual and theoretical starting/ending points - extension distance is considered positive when the path of contact increases. For the example shown in Figure 4.3, the extension distance is given by the width of the shaded areas which are extended double tooth contact regions.

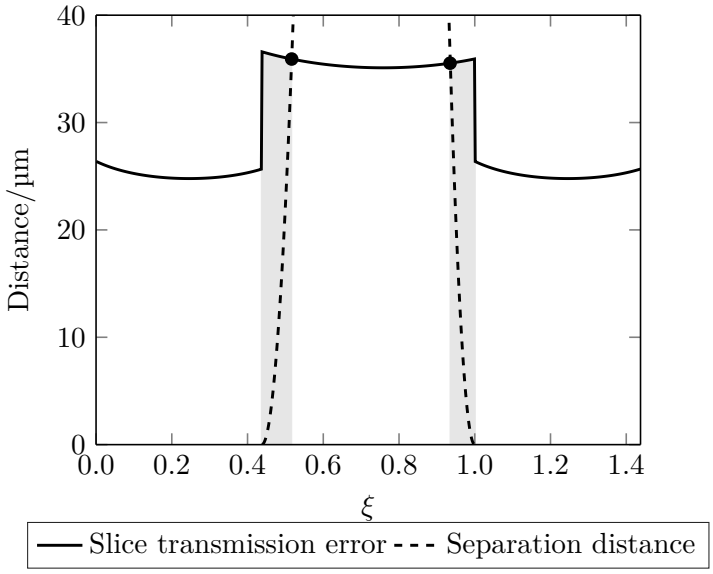

Figure 4.3: Theoretical transmission error and separation distances in recess and approach for teeth.

Extended slice transmission error

The load supported by a given slice (F^{s}) is always the same regardless the number of teeth in contact, thus equation (4.17) can be written.

$$F^{\mathrm{s}} = k^{\mathrm{s},1} \cdot \left(\delta^{\mathrm{s},1} - \Delta_{\mathrm{s}}^{\mathrm{s},1}\right) + k^{\mathrm{s},0} \cdot \left(\delta^{\mathrm{s},0} - \Delta_{\mathrm{s}}^{\mathrm{s},0}\right) + k^{\mathrm{s},-1} \cdot \left(\delta^{\mathrm{s},-1} - \Delta_{\mathrm{s}}^{\mathrm{s},-1}\right) \tag{4.17}$$

where $k^{\mathrm{s},i}$ is the final single tooth pair slice mesh stiffness of pair i, $\delta^{\mathrm{s},i}$ is the slice transmission error of tooth pair i and $\Delta_{\mathrm{s}}^{\mathrm{s},i}$ is the total separation distance of tooth pair i in slice s.

The single tooth pair slice mesh stiffness is not defined beyond the theoretical starting and ending points of contact. In order to define the transmission error beyond the theoretical points, it will be assumed that the single tooth pair slice mesh stiffness for the approach and recess extension region are constant and equal to the value at the theoretical starting and ending points, respectively.

The slice transmission error of tooth pair i is defined by equation (4.18) where $F^{\mathrm{s},i}$ is the load applied on tooth pair i of slice s. Developing equation (4.18), leads to the conclusion that the slice transmission error for every tooth pair is the same and equal to the slice transmission error.

$$\delta^{\mathrm{s},i} = \frac{F^{\mathrm{s},i}}{k^{\mathrm{s},i}} = F^{\mathrm{s},i} \cdot \frac{1}{k^{\mathrm{s},i}} = \frac{k^{\mathrm{s},i}}{K^{\mathrm{s}}} F^{\mathrm{s}} \cdot \frac{1}{k^{\mathrm{s},i}} = \frac{F^{\mathrm{s}}}{K^{\mathrm{s}}} = \delta^{\mathrm{s}} \implies \delta^{\mathrm{s},1} = \delta^{\mathrm{s},0} = \delta^{\mathrm{s},-1} \tag{4.18}$$

Combining equations (4.17) and (4.18), the extended transmission error is established in equation (4.19). The transmission error considering the extension of contact for any situation can be computed according to equation (4.19) and only depends on the single tooth pair slice mesh stiffness modified to include the extended regions, the load on each slice and the total separation distance for every tooth pair of each slice.

$$\delta^{\mathrm{s}} = \frac{F^{\mathrm{s}} + \sum_{i=-\mathrm{floor}(\varepsilon_\alpha)}^{\mathrm{floor}(\varepsilon_\alpha)} k^{\mathrm{s},i} \cdot \Delta_{\mathrm{s}}^{\mathrm{s},i}}{K^{\mathrm{s}}} \tag{4.19}$$

Slice load sharing ratio

The load applied in each slice is modified considering the extended slice transmission error from equation (4.19) and thus must be recalculated - the constrained expression for the elastic potential energy is given by equation (4.20).

$$I(F^1, ..., F^{NS}, \Lambda) = \sum_{\mathrm{s}} \frac{1}{2} F^{\mathrm{s}} \delta^{\mathrm{s}} + \Lambda \left(\sum_{\mathrm{s}} F^{\mathrm{s}}\, r_{\mathrm{b2}} - T_2 \right) \tag{4.20}$$

After rearranging the terms, the load is defined by equation (4.21) and the Lagrange multiplier by equation (4.22).

$$F^{\mathrm{s}} = K^{\mathrm{s}} \left[r_{\mathrm{b2}}\, \Lambda - \frac{\frac{1}{2} \sum_{i} k^{\mathrm{s},i} \cdot \Delta_{\mathrm{s}}^{\mathrm{s},i}}{K^{\mathrm{s}}} \right] \tag{4.21}$$

$$\Lambda = -\frac{\frac{T_2}{r_{\mathrm{b2}}} + \frac{1}{2} \sum_{\mathrm{s}} \sum_{i} k^{\mathrm{s},i} \cdot \Delta_{\mathrm{s}}^{\mathrm{s},i}}{r_{\mathrm{b2}} \sum_{\mathrm{s}} K^{\mathrm{s}}} \tag{4.22}$$

To conclude the iteration cycle, an updated slice transmission error is determined with the slice load along with the calculation of the slice load sharing ratio, shown in equation (4.23).

$$\mathcal{L}^{\mathrm{s}} = \frac{k^{\mathrm{s},i} \left(\delta^{\mathrm{s}} - \Delta_{\mathrm{s}}^{\mathrm{s},i} \right)}{\sum_{i} k^{\mathrm{s},i} \left(\delta^{\mathrm{s}} - \Delta_{\mathrm{s}}^{\mathrm{s},i} \right)} \tag{4.23}$$

4.2.3. Mesh stiffness and transmission error

The next step consists in computing the transmission error, which is used as the control variable for the convergence criteria. The transmission error is the product of the Lagrange multiplier (directly obtained from the minimization of the potential energy of the system) and the base radius of the wheel, see equation (4.24).

$$\delta = r_{\mathrm{b2}}\, \Lambda \tag{4.24}$$

The implemented convergence criteria is defined by equation (4.25), which considers the trans-

mission error from the previous iteration (δ_{ref}) and the latest transmission error (δ).

$$C_{\text{iter}} = \sqrt{\sum_{\xi} \left(\frac{2\left(\delta_{\text{ref}} - \delta\right)}{\delta_{\text{ref}} + \delta} \right)^2} \tag{4.25}$$

Once the convergence criteria is met, the gear mesh stiffness can be determined by equation (4.26), as the ratio between the total normal load and the transmission error. Concerning the load sharing ratio of the gear pair, it is given by equation (4.27), as the combination of the slice load sharing ratio and the slice load divided by the nominal transverse load in the plane fo action (F_{bt}).

$$K = \frac{F_{\text{bt}}}{\delta} \tag{4.26}$$

$$\mathcal{L} = \frac{\sum_{\text{s}} \mathcal{L}^{\text{s}} F^{\text{s}}}{F_{\text{bt}}} \tag{4.27}$$

4.2.4. Assessment process

The assessment of the gear mesh stiffness model consists in comparing results found in the literature which are obtained using the finite element method with the ones acquired with the approximate analytical model to prove its effectiveness. The assessment for spur gears is performed with an example from Ma et al. [17] and for helical gears from Wang et al. [101] - ISO 53 [169] Profile A tooth proportions ($\alpha = 20°$, $h^*_{\text{aP}} = 1$, $h^*_{\text{fP}} = 1.25$ and $\rho^*_{\text{fP}} = 0.38$) with remaining gear parameters established in Table 4.1. Both FE models resort to master nodes at the center of each gear body to which their inner hole nodes are connected to. The external torque is applied to the pinion while the wheel is fixed. The FE analysis for the assessment of spur gears uses a 2D model with contact elements [17] while in the case of helical gears resorts to 3D contact surfaces [101].

Table 4.1: Gear parameters for the assessment gears.

Gear parameters	z_1/-	z_2/-	m_{n}/mm	β/°	b/mm	r_{hub}/mm	C/µm	L^C/-	n^C/-	ρ/kg m^{-3}	E/GPa	ν/-	T_1/N m
Spur	28	28	3.175	0	6.35	20	15	0.3201	1	7850	210	0.3	100
Helical	35	35	5	15	20	14	-	-	-	7850	210	0.3	200

Figure 4.4 shows the gear mesh stiffness curves achieved by the approximate and finite element models. These results are very similar, capturing even the smallest details. For instance, in Figure 4.4a, the model is capable of replicating the change in slope found in the FEM just before $\xi = 0.2$ and after $\xi = 0.8$. Regarding the helical gear, the curves are very close to each other, presenting a round shape just near the start and end of the plateaus. This round shape appears in the model because contact extension is taken into account, otherwise the curve would have sharp edges in the transition areas. Overall, a good agreement is found between the approximate model and the FEM. An average absolute relative difference of 3.0% and 4.0% is found respectively for the spur and helical gear with corresponding maximum absolute relative difference of 8.2% and 6.3%.

Even though two examples are presented here, other gears were tested to guarantee the reliability

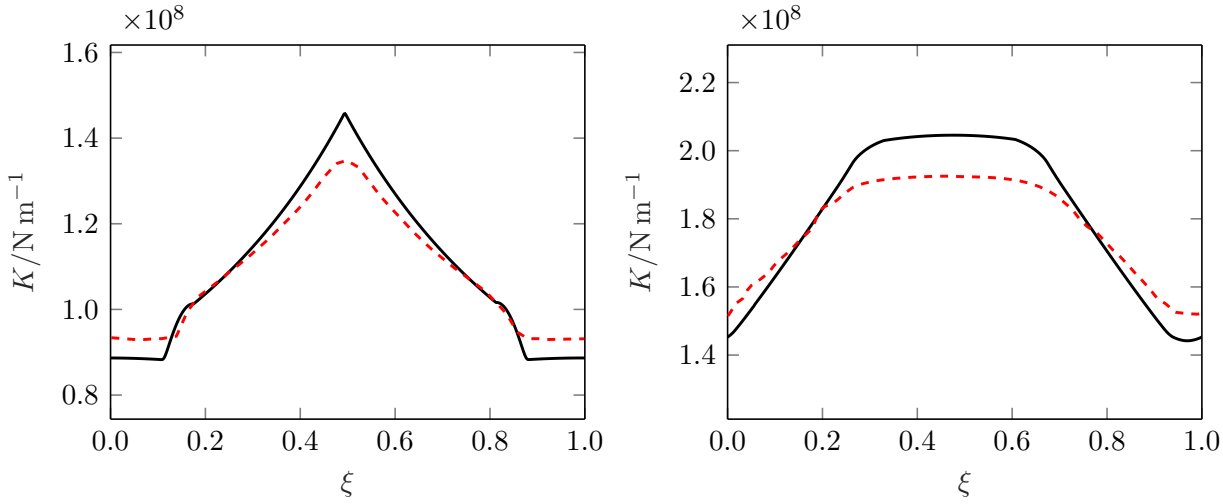

(a) Spur gear.

(b) Helical gear.

Figure 4.4: Gear mesh stiffness assessment: comparison between the developed model (——) and FEM (- - -).

of the approximate model - in general, a good agreement was observed. Additionally, this assessment is more directed towards the methodology implemented to estimate the gear mesh stiffness since all the expressions employed in the model were already successfully assessed in other works. Therefore, not requiring a wide range of tested gears.

The last step in the assessment process consists in finding the number of points per mesh period that leads to the convergence of the gear mesh stiffness. Three different gears were used to perform this evaluation, a spur gear, an helical gear with $\varepsilon_\alpha > \varepsilon_\beta$ and another helical gear but with $\varepsilon_\alpha < \varepsilon_\beta$. The number of points/slices is increased until no relevant modification is found in the gear mesh stiffness. It was concluded that it is enough to keep 100 points per mesh period and a number of slices equal to rounding up 100 ε_β, therefore this is the discretization used for the gear mesh stiffness study. It is noteworthy here that the model has an approximately linear relationship between the number of points used in the discretization and the computational cost.

4.3. Dynamic model

The dynamic model is a representation of a single stage gear-shaft-bearing transmission, as exemplified in Figure 4.5. The system has two shafts, the input shaft and the output shaft, both modeled resorting to the finite element method. A rotating speed is imposed on the input shaft while a resisting torque is applied on the output shaft. Also, each shaft is supported by two bearing elements - housing is assumed to be infinitely rigid. The gear pair, either spur or helical, connects both shafts through their meshing. The following sections explain the gear, shaft and bearings components; the formulation of the equations of motion and the algorithm implemented.

4.3.1. Gear components

The gears are approximated as rigid disks by their base radius and connected through a time-varying gear mesh stiffness which is established with the previously presented gear mesh stiffness model. Nonlinearities related to tooth separations are considered but the contact frictional forces are disregarded as it was shown that tooth friction has negligible effect on the torsional, axial and line-of-action motions of the gear pair [181; 184; 185].

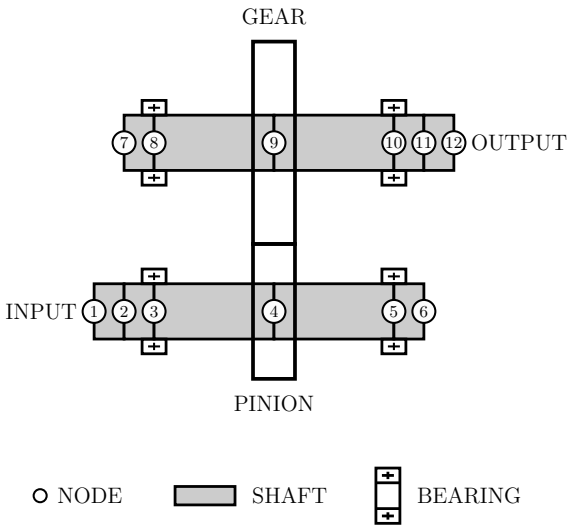

Figure 4.5: Schematic of the dynamic system.

That being said, a 12 degree-of-freedom subsystem is developed for the gear pair - see Figure 4.6, where the equations of motions are determined by the Lagrange equations, expressed in generalized coordinates (q_j) in equation (4.28).

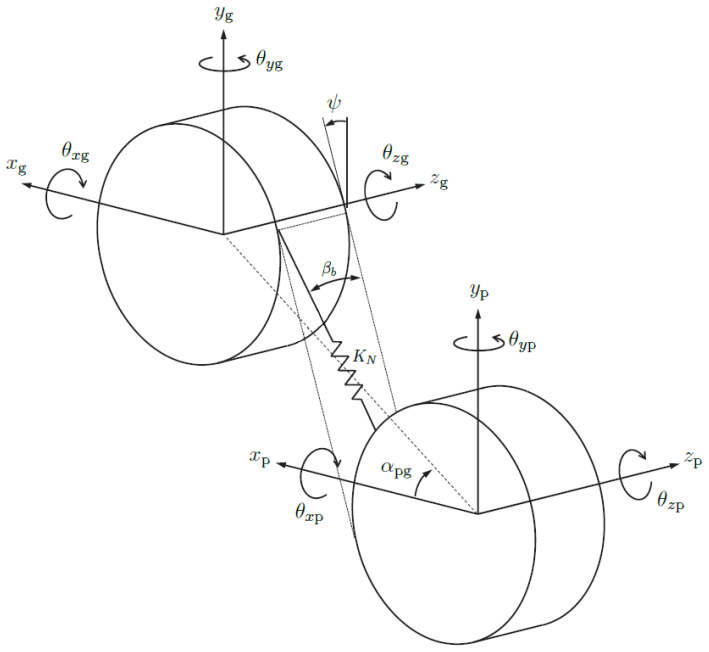

Figure 4.6: Gear subsystem. Adapted from [181].

$$\frac{d}{dt}\left(\frac{\partial T}{\partial \dot{q}_j}\right) - \frac{\partial T}{\partial q_j} + \frac{\partial V}{\partial q_j} = Q_j \qquad j = 1, \ldots, n. \tag{4.28}$$

with Q_j being the generalized forces of each coordinate, T is the kinetic energy of the subsystem and V is the potential energy of the subsystem. In Figure 4.6, α_{pg} is the angle between the line formed by the centers of the gear bodies and the positive x-axis; and ψ is the angle given by the

plane of action and the positive y-axis. The kinetic and potential energies of the subsystem are defined by equations (4.29) and (4.30).

$$\begin{aligned} T = \frac{1}{2}\Big[& m_1\left(\dot{x_{\mathrm{p}}}^2 + \dot{y_{\mathrm{p}}}^2 + \dot{z_{\mathrm{p}}}^2\right) + I_1\left(\dot{\theta_{x\mathrm{p}}}^2 + \dot{\theta_{y\mathrm{p}}}^2\right) + J_1\dot{\theta_{z\mathrm{p}}}^2 + \\ & m_2\left(\dot{x_{\mathrm{g}}}^2 + \dot{y_{\mathrm{g}}}^2 + \dot{z_{\mathrm{g}}}^2\right) + I_2\left(\dot{\theta_{x\mathrm{g}}}^2 + \dot{\theta_{y\mathrm{g}}}^2\right) + J_2\dot{\theta_{z\mathrm{g}}}^2\Big] \end{aligned} \tag{4.29}$$

$$V = \frac{1}{2}K_{\mathrm{N}}(t)\Delta l^2 \tag{4.30}$$

where 1 or "p" relates the quantities to the pinion and 2 or "g" to the wheel. m is the mass, I and J are mass moment of inertia, $K_{\mathrm{N}}(t)$ is the time-varying mesh stiffness in the normal direction and Δl is the reference displacement in the tooth normal direction as a function of the degrees-of-freedom. The time-varying normal stiffness can be obtained with the gear mesh stiffness (K), which is established in the transverse direction, by considering that the total elastic energy introduced by K in the system is the same as K_{N} - resulting in equation (4.31).

$$V(K_{\mathrm{N}}) = V(K) \Leftrightarrow K_{\mathrm{N}} = \frac{K}{\cos^2(\beta_{\mathrm{b}})} \tag{4.31}$$

The displacement of the spring (Δl) is defined as positive when its length is increased by the degrees-of-freedom. Hence, it is established by equation (4.32).

$$\begin{aligned} \Delta l = & (x_{\mathrm{g}} - x_{\mathrm{p}})\sin(\psi)\cos(\beta_{\mathrm{b}}) + (y_{\mathrm{g}} - y_{\mathrm{p}})\cos(\psi)\cos(\beta_{\mathrm{b}}) + (z_{\mathrm{p}} - z_{\mathrm{g}})\sin(\beta_{\mathrm{b}}) + \\ & (-r_{\mathrm{b}1}\sin(\psi)\sin(\theta_{x\mathrm{p}}) - r_{\mathrm{b}2}\sin(\psi)\sin(\theta_{x\mathrm{g}}))\sin(\beta_{\mathrm{b}}) + \\ & (-r_{\mathrm{b}1}\cos(\psi)\sin(\theta_{y\mathrm{p}}) - r_{\mathrm{b}2}\cos(\psi)\sin(\theta_{y\mathrm{g}}))\sin(\beta_{\mathrm{b}}) + \\ & (-r_{\mathrm{b}1}\theta_{z\mathrm{p}} - r_{\mathrm{b}2}\theta_{z\mathrm{g}})\cos(\beta_{\mathrm{b}}) \end{aligned} \tag{4.32}$$

Since external loads are not considered in this subsystem and the damping is going to be included in modal form for the entire system. Applying equation (4.28) to equations (4.29) and (4.30), gives the equations of motion for pinion and the wheel, which are, correspondingly, equations (4.33) and (4.34).

$$\begin{cases} m_1\ddot{x_{\mathrm{p}}} - K_{\mathrm{N}}\Delta l\sin(\psi)\cos(\beta_{\mathrm{b}}) = 0 \\ m_1\ddot{y_{\mathrm{p}}} - K_{\mathrm{N}}\Delta l\cos(\psi)\cos(\beta_{\mathrm{b}}) = 0 \\ m_1\ddot{z_{\mathrm{p}}} + K_{\mathrm{N}}\Delta l\sin(\beta_{\mathrm{b}}) = 0 \\ I_1\ddot{\theta_{x\mathrm{p}}} - K_{\mathrm{N}}\Delta l\ r_{\mathrm{b}1}\sin(\psi)\sin(\beta_{\mathrm{b}}) = 0 \\ I_1\ddot{\theta_{y\mathrm{p}}} - K_{\mathrm{N}}\Delta l\ r_{\mathrm{b}1}\cos(\psi)\sin(\beta_{\mathrm{b}}) = 0 \\ J_1\ddot{\theta_{z\mathrm{p}}} - K_{\mathrm{N}}\Delta l\ r_{\mathrm{b}1}\cos(\beta_{\mathrm{b}}) = 0 \end{cases} \tag{4.33}$$

$$\begin{cases} m_2\ddot{x_{\mathrm{g}}} + K_{\mathrm{N}}\Delta l\sin(\psi)\cos(\beta_{\mathrm{b}}) = 0 \\ m_2\ddot{y_{\mathrm{g}}} + K_{\mathrm{N}}\Delta l\cos(\psi)\cos(\beta_{\mathrm{b}}) = 0 \\ m_2\ddot{z_{\mathrm{g}}} - K_{\mathrm{N}}\Delta l\sin(\beta_{\mathrm{b}}) = 0 \\ I_2\ddot{\theta_{x\mathrm{g}}} - K_{\mathrm{N}}\Delta l\ r_{\mathrm{b}2}\sin(\psi)\sin(\beta_{\mathrm{b}}) = 0 \\ I_2\ddot{\theta_{y\mathrm{g}}} - K_{\mathrm{N}}\Delta l\ r_{\mathrm{b}2}\cos(\psi)\sin(\beta_{\mathrm{b}}) = 0 \\ J_2\ddot{\theta_{z\mathrm{g}}} - K_{\mathrm{N}}\Delta l\ r_{\mathrm{b}2}\cos(\beta_{\mathrm{b}}) = 0 \end{cases} \tag{4.34}$$

Putting equations (4.33) and (4.34) in matrix form leads to the equation of motion of the gear subsystem, equation (4.35).

$$\boldsymbol{M}_G\ \ddot{\boldsymbol{q}}_G(t) + \boldsymbol{K}_G(t)\ g(t)\ \boldsymbol{q}_G(t) = 0 \tag{4.35}$$

$\boldsymbol{q}_G(t)$ is the vector containing the degrees-of-freedom of the gear subsystem, $\boldsymbol{M}_G$ is the gear diagonal elemental mass matrix, $\boldsymbol{K}_G(t)$ is the gear elemental time-varying stiffness matrix and $g(t)$ is the contact loss function described by equation (4.36).

$$g(t) = \begin{cases} 1, & -\boldsymbol{w}_G^T\ \boldsymbol{q}_G(t) \geq 0, \\ 0, & -\boldsymbol{w}_G^T\ \boldsymbol{q}_G(t) < 0. \end{cases} \tag{4.36}$$

Equation (4.36) depends on the displacements in the normal direction, $-\boldsymbol{w}_G^T\ \boldsymbol{q}_G(t)$, that is, the product between the gear projection vector ($\boldsymbol{w}_G^T$) and the gear displacements ($\boldsymbol{q}_G(t)$). The contact loss function, equation (4.36), considers the loss of contact between the gear teeth. However, it does not take into account the amount of backlash and, therefore, regardless the amount of displacement, there is not back-side contact.

4.3.2. Shaft components

The shafts of the gearbox are introduced via Timoshenko beam elements. The hollow cylindrical shaft elements comprise two nodes with six degrees-of-freedom per node, thus leading to 12×12 mass and stiffness elemental matrices ($\boldsymbol{M}_S$ and $\boldsymbol{K}_S$). The description of the components incorporating the elemental mass and stiffness matrices are presented in [186; 187].

4.3.3. Bearing components

The bearing elements are implemented by lumped stiffnesses, which means that six linear elastic and time-invariant springs are introduced to the node where this element supports the shaft. The 6×6 diagonal bearing matrix ($\boldsymbol{K}_B$) includes k_{xx} and k_{yy} as radial stiffnesses, k_{zz} as axial stiffness, $k_{\theta_x\theta_x}$ and $k_{\theta_y\theta_y}$ as torsional stiffnesses in the radial direction and $k_{\theta_z\theta_z}$ as torsional stiffness in the axial direction. The torsional stiffness in the axial direction is set to zero.

4.3.4. Equations of motion

With the mass and stiffness matrices of the individual gearbox components determined, the equation of motion of the entire system is shown in equation (4.37).

$$\boldsymbol{M}\ \ddot{\boldsymbol{q}}(t) + \boldsymbol{C}\ \dot{\boldsymbol{q}}(t) + \boldsymbol{K}(t)\ \boldsymbol{q}(t) = \boldsymbol{f} \tag{4.37}$$

The vector $\boldsymbol{q}(t)$ contains the degrees-of-freedom of the entire gearbox system and the matrices $\boldsymbol{M}$ and $\boldsymbol{K}(t)$, mass and stiffness matrices of the system, are assembled according to equations (4.38) and (4.39), where $\mathcal{A}(\cdot)$ is the assembly operator to localize the gear, shaft and bearing elemental matrices in the global matrices of the system.

$$\boldsymbol{M} = \mathcal{A}\left(\boldsymbol{M}_G\right) + \mathcal{A}\left(\boldsymbol{M}_S\right) \tag{4.38}$$

$$\boldsymbol{K}(t) = \mathcal{A}\left(\boldsymbol{K}_G(t)\ g(t)\right) + \mathcal{A}\left(\boldsymbol{K}_S\right) + \mathcal{A}\left(\boldsymbol{K}_B\right) \tag{4.39}$$

If any other elements, such as discrete inertias or elastic couplings, need to be included then they

are added as lumped parameter elements to the intended node.

Regarding the damping matrix $\boldsymbol{C}$, it is introduced by modal damping. Hence, the problem of the eigenvalues ($\boldsymbol{\Omega^2}$) and eigenvectors ($\boldsymbol{\Phi}$) of the system is solved considering the mass matrix of the system, equation (4.38), and a time-invariant stiffness matrix $\boldsymbol{K}_{\text{eig}}$ where the contact loss function is removed and the time-varying mesh stiffness (K_{N}) is replaced by its average value. The projection of the damping matrix in the modal system is given by equation (4.40) and allows to determine the damping matrix of the system by imposing a damping ratio ζ to the system.

$$\boldsymbol{\Phi}^{\text{T}}\boldsymbol{C}\boldsymbol{\Phi} = 2\zeta\boldsymbol{\Omega} \tag{4.40}$$

Finally, the system has a fixed output torque which needs to be imposed at a node of the output shaft and corresponding location in the external load vector $\boldsymbol{f}$.

4.3.5. Algorithm

The algorithm starts by getting all the necessary inputs on every component (gears, shafts, bearings) and working conditions, as seen in Table 4.2. Following the inputs, the individual mass and stiffness matrices required for the gearbox components are built. Then, the gear, shafts and bearings components are assembled in a single matrix according to the degrees-of-freedom. At this point, the damping matrix is computed and the equations of motion completely defined. To solve the equations of motion of the gearbox dynamic model, a Newmark integration algorithm is used with the constants that make it unconditionally stable ($\delta = 0.5$ and $\alpha = 0.25$). The gear mesh stiffness for the dynamic model is estimated considering a discretization of 50 points per mesh period (100 points if $\beta \geq 35$) as well as 100 slices per unit of overlap ratio (rounded up to an integer number); time discretization is the same as for the gear mesh stiffness. Steady-state conditions are considered to be reached after one complete turn of the pinion.

Table 4.2: Inputs for gearbox dynamic model.

Gear inputs
Number of teeth
Pressure angle
Helix angle
Facewidth
Normal module
Profile shift coefficients
Profile modification (type)
Amount
Length
Density
Young's modulus
Poisson's ratio
Nr. points per period

Shaft inputs
Outside diameter
Inside diameter
Length
Density
Young's modulus
Poisson's ratio
Nr. elements

Bearing inputs
Radial stiffness
Axial stiffness
Torsional stiffness (radial direction)

Working conditions
Start speed
End speed
Speed step
Torque
Damping ratio

4.3.6. Dynamic parameters

The displacements resulting from the dynamic model need to be processed to give a clear representation of the gears behavior for every speed. Hence, the dynamic transmission error (DTE) is determined for every speed that is simulated. There are different approaches when it comes to computing the DTE, which is evaluated as seen from the transverse plane. On one hand, the DTE can be computed considering the transverse displacements of the gear teeth, which would result in equation (4.41). Note that even though vector $\boldsymbol{q}(t)$ contains the displacements of the entire system, the projection vector $\boldsymbol{w}^T$ only relates to the displacements of the pinion and wheel bodies. On the other hand, the DTE can be obtained only considering the rotations along the z-axis for the pinion and wheel, in which case, it is defined by equation (4.42).

$$\mathrm{DTE} = \frac{-\boldsymbol{w}^T}{\cos(\beta_\mathrm{b})}\,\boldsymbol{q}(t) \tag{4.41}$$

$$\mathrm{DTE}_{\theta_z} = r_{\mathrm{b}2}\theta_{z\mathrm{g}} + r_{\mathrm{b}1}\theta_{z\mathrm{p}} \tag{4.42}$$

Regardless of the DTE approach, its oscillating component around the quasi-static solution of the system (QSTE, quasi-static transmission error) is obtained by equation (4.43).

$$\mathrm{DTE}_\mathrm{osc} = \mathrm{DTE} - \mathrm{QSTE} \tag{4.43}$$

where the degrees-of-freedom necessary to compute the QSTE, according to either specification of the DTE (equation (4.41) or (4.42)), are given by equation (4.44).

$$\boldsymbol{q}(t)_\mathrm{QS} = \boldsymbol{K}(t)^{-1}\boldsymbol{f} \tag{4.44}$$

The dynamic transmission error is a time dependent variable, meaning that it evaluates the behavior of the system for a single speed. Therefore, to look at the performance of the system throughout all imposed speeds, root-mean-square functions are applied - equation (4.45) defines the root-mean-square and equation (4.46) specifies the equivalent root-mean-square.

$$\mathrm{RMS(X)} = \sqrt{\frac{1}{T_\mathrm{m}}\int_0^{T_\mathrm{m}} \mathrm{X}^2} \tag{4.45}$$

$$A_\mathrm{RMS}(\mathrm{X}) = \sqrt{A_1^2 + A_2^2 + A_3^2} \tag{4.46}$$

In equations (4.45) and (4.46), X is the variable in study, T_m is the meshing period and A_1, A_2 and A_3 are the magnitude of the first three harmonics from the Fast Fourier Transforms of X.

4.3.7. Assessment process

To verify that the dynamic model is properly implemented, the single stage drive model presented in the work of Raclot and Velex [178] is replicated. Results for both a spur gear and helical gear setup are shown and all the necessary data is given in [178]. Figure 4.7 shows the TE (transmission error) shape factor using two different methods, the Spectral and Newmark methods, as given by [178] together with the results from the implemented model. For the spur gear,

Figure 4.7a, the model correlates with the other results: location of the peaks is in complete agreement with minor differences in the magnitude values. Regarding the TE shape factor for the helical gear, Figure 4.7b, the shape of the curves are all very close to each other with a small difference in magnitude at around 6000 rpm.

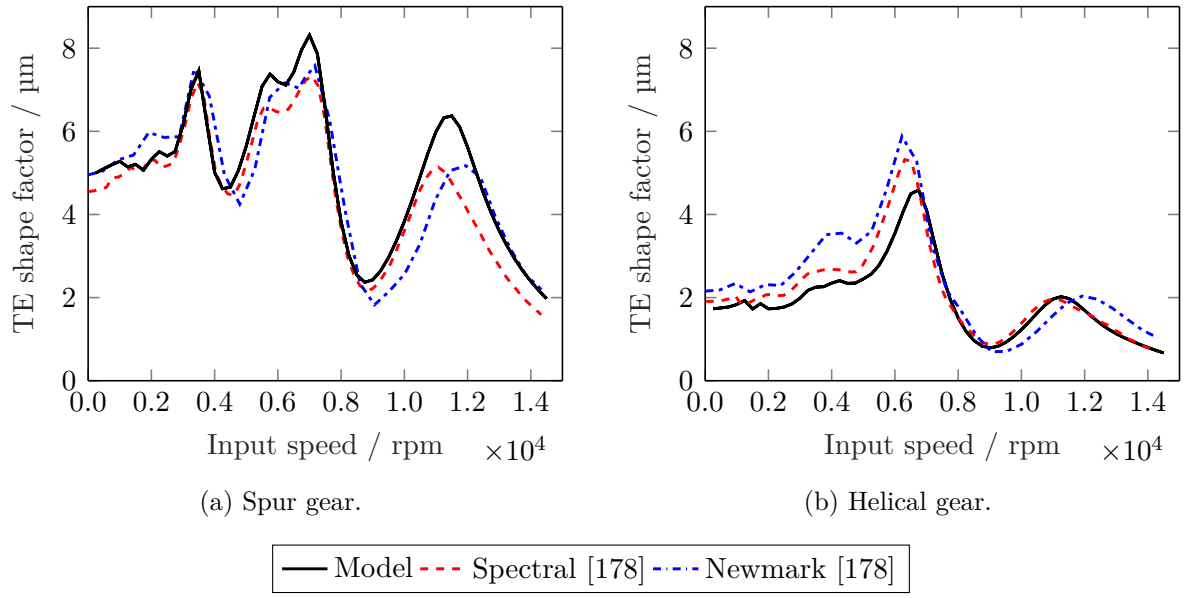

(a) Spur gear.

(b) Helical gear.

Figure 4.7: Dynamic assessment: comparison between the implemented model and Raclot and Velex [178].

4.4. Effect of asymmetry

The effect of the tooth pair structural stiffness asymmetry is investigated in spur and helical gears separately. To perform such an evaluation, random samples of spur and helical gears with ISO 53 [169] Profile A tooth proportions and steel material properties ($\rho = 7830$ kg m^{-3}, $E = 206$ GPa and $\nu = 0.3$) are generated. The limits for the geometric parameters are established in Table 4.3 to which restrictions on cutting interference [170], mating interference [170], tooth crest width [170] as well as z_2 being equal to the closest integer given by $u \times z_1$ are added. Due to the existing validity domains for the fillet-foundation stiffness models, the gear geometric parameters in Table 4.3 end up being considerably restricted. The model developed by Xie et al. [79] only allows for the number of teeth to be between $37 \leq z_i \leq 75$, constraining the maximum allowable gear ratio in this study to $u_{max} = 2.0$. The other analytical option for the fillet-foundation stiffness would be the one developed by Sainsot et al. [78] which is much less restrictive, however, it leads to a significant overestimation of the gear mesh stiffness in the regions where there are more than one tooth pair in contact. For this reason, it is opted to go with the formulation of Xie et al. [79] and thus restricting the evaluated domain for the sake of having more accurate results.

An estimation for the necessary sample size is given by Yamane's formula, equation (4.47), considering a precision $e = 0.01$ and a population size of $N_{spur} = 2.3258 \times 10^{11}$ and $N_{helical} = 9.3033 \times 10^{12}$, yielding $n = 10000$.

$$n = \frac{N}{1 + N\, e^2} \tag{4.47}$$

Next, the generated samples have their gear mesh stiffness and dynamic behavior estimated twice,

Table 4.3: Interval of gear parameters for the evaluation of the asymmetry effect.

Gear parameters	**Range**
$\boldsymbol{z_1}$/-	37:75
$\boldsymbol{u = z_2/z_1}$/-	1:2
$\boldsymbol{m_n}$/mm	DIN 780*
$\boldsymbol{\alpha}$/°	20
$\boldsymbol{\beta}$/°	0:40
$\boldsymbol{b}$/mm	3 m_n:14 m_n
$\boldsymbol{x_1}$/-	-1:1
$\boldsymbol{x_2}$/-	-1:1

* all module values from DIN 780 Series I

once including the tooth pair structural stiffness asymmetry (λ [171]) and another one disregarding it ($\lambda = 0$). Note that the gear geometry is random, therefore there are a few parameters that need to be adjusted so that every gear mesh stifffness/dynamic behavior evaluation is equivalent to each other. For instance, the load applied in each gear pair is calculated so that it reaches 80% of the maximum allowable stress according to Dufailly [188]. The same type of adjustment also needs to be done for the gear hub radius which was defined as being equal to 30% of the dedendum radius for both the pinion and the wheel. Regarding the dynamic system, the shafts' diameter is adjusted for the hub diameter and the length is made proportional to the gear facewidth using the FZG test gearbox with the C14 assembled as the reference [8; 189] - meaning that each shaft has a length of 7.8571 b. The shafts' material properties are $\rho = 7830\ \mathrm{kg\,m^{-3}}$, $E = 206$ GPa and $\nu = 0.3$. The bearing stiffnesses are as displayed in Table 4.4 and the damping ratio is set to $\zeta = 0.1$ [178] for every simulation. The selection of the speed range is determined by using a Campbell diagram, see Figure 4.8 for an example: the natural frequencies of the system are filtered so that only the ones that have more than 5% of gear mesh stiffness contribution are considered; then, the intersection of the third gear mesh frequency with the lowest filtered natural frequency of the system gives the lower bound and the intersection of the first gear mesh frequency with the highest filtered natural frequency of the system gives the upper bound. To make sure all effects within that interval are captured, the speed interval (uniformly divided into 100 points) is established as 0.9 the lower bound and 1.1 the upper bound.

Table 4.4: Bearing stiffnesses for each shaft.

Bearing inputs	**Pinion's shaft**	**Wheel's shaft**
Radial stiffness / $\mathrm{N\,m^{-1}}$	1.40×10^8	2.50×10^8
Axial stiffness / $\mathrm{N\,m^{-1}}$	3.50×10^7	6.00×10^7
Torsional stiffness (radial direction) / $\mathrm{N\,m\,rad^{-1}}$	1.00×10^{12}	1.00×10^{12}

4.4.1. Gear mesh stiffness

The results for the influence of the tooth structural asymmetry on the gear mesh stiffness are summarized in Figure 4.9 for spur gears and Figure 4.10 for helical gears. The tooth pair structural asymmetry is represented in the x-axis, and there are two y-axis. The left y-axis corresponds to the average absolute relative difference and the right y-axis shows how many gears are within an established λ interval. Also, for the left y-axis, the maximum and minimum

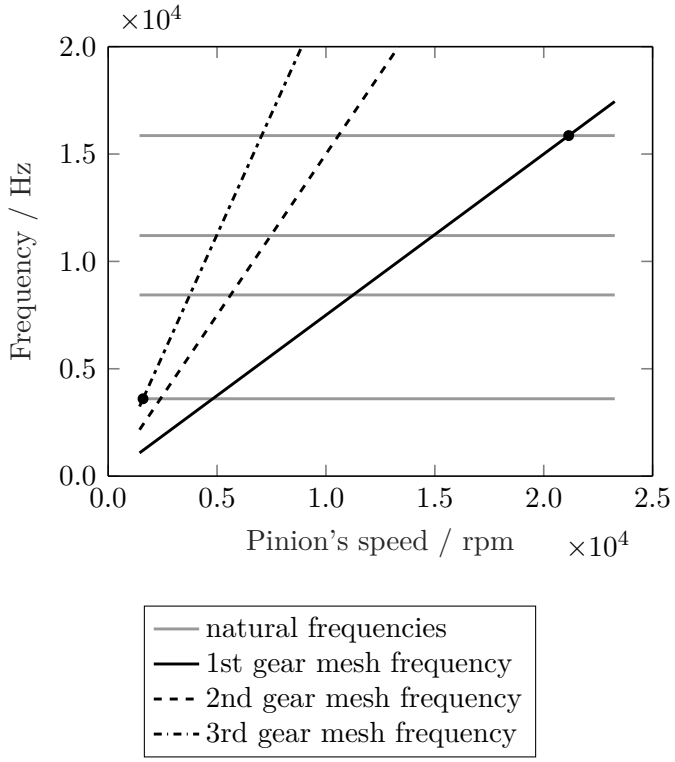

Figure 4.8: Example of Campbell's diagram for selection of the speed range.

values of differences for each group of gears in that λ are plotted. Note that both y-axis share the same x-axis, so the results are grouped for the same λ interval. To reach the average absolute relative difference for a gear, one computes the relative difference for every point of the path of contact and then determines its mean absolute relative difference, $\overline{E}/\%$. Then, it is a matter of grouping the gears by their λ values and calculate the average value of each group.

First, looking at the distribution of the number of cases along λ, very similar distributions are found for both spur and helical gears. Although, the range of values for λ is broader for spur gears. Figures 4.9 and 4.10 show that most gear pairs have values of λ around 0.

Identical relative difference values are obtained for both spur and helical gears but they exhibit different shapes. Although, as expected, the relative difference is close to zero for λ near 0 and it increases as the amount of asymmetry increases. The maximum average absolute relative difference found between all spur gears is of 2.38% while the same parameter reaches a value of 2.33% for helical gears.

It is noteworthy here that since λ is straightforward to implement, any improvement in accuracy it brings is welcome. Also, the range of values for the average absolute relative differences can be within the same order of values as the ones that the approximate model presents when compared to the finite element method in the assessment process. Superimposing the differences inherent to the approximate gear mesh stiffness model with the ones from disregarding the tooth pair structural stiffness asymmetry can potentially cause relevant differences in the gear mesh stiffness shape due to cumulative effects. Thus, the asymmetry should not be neglected when modeling the gear mesh stiffness.

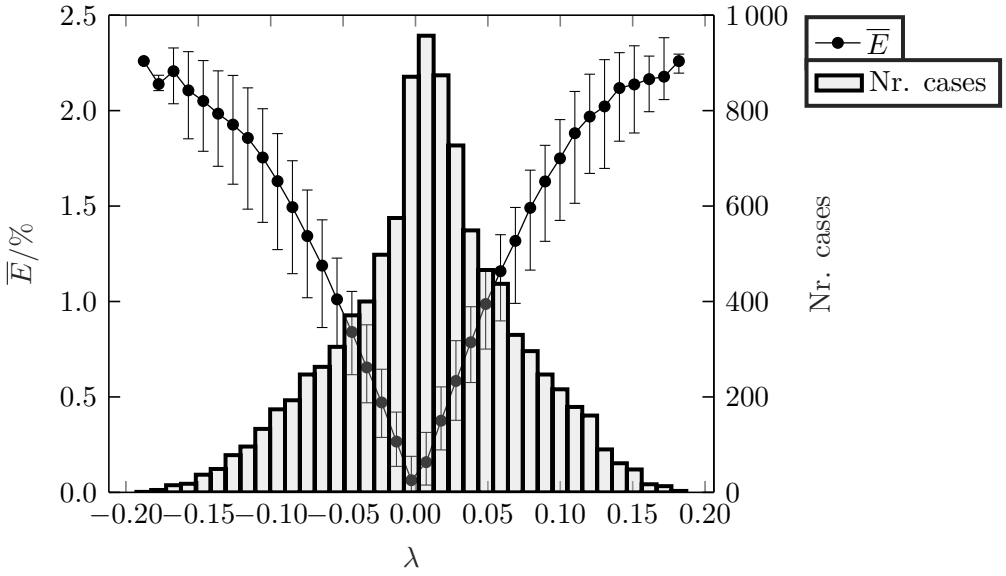

Figure 4.9: Effect of asymmetry on the gear mesh stiffness: spur gears.

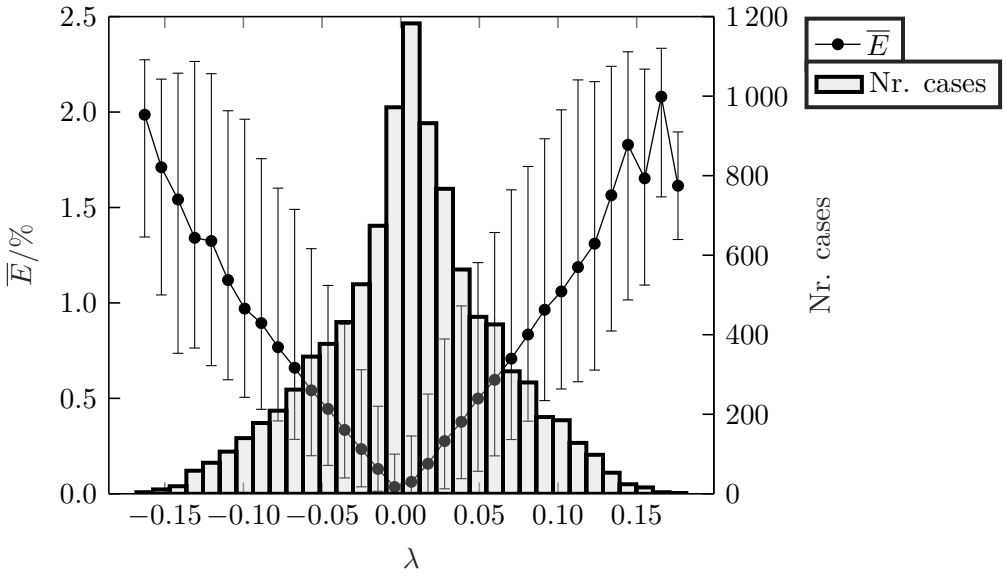

Figure 4.10: Effect of asymmetry on the gear mesh stiffness: helical gears.

4.4.2. Dynamic transmission error

For the analysis of the dynamic transmission error, the relative difference in the $A_{\mathrm{RMS}}(\mathrm{DTE}_{\mathrm{osc}})$ is taken as the reference parameter - attend on equations (4.41) to (4.46) for the definition of this parameter. Figures 4.11 and 4.12 show very similar average values of absolute relative difference: maximum average relative difference of 3.49% and 2.55% for spur and helical gears respectively. However, when analyzing the maximum absolute difference for each λ interval, the values can go up to 37.1%/28.3% for spur/helical gears. This result is unexpected considering that every system is equivalent to each other and that the gear mesh stiffness is the only excitation of the dynamic model, where the results, apparently, do not exhibit significant differences.

To better understand the reasons behind the high relative difference in this dynamic analysis, the

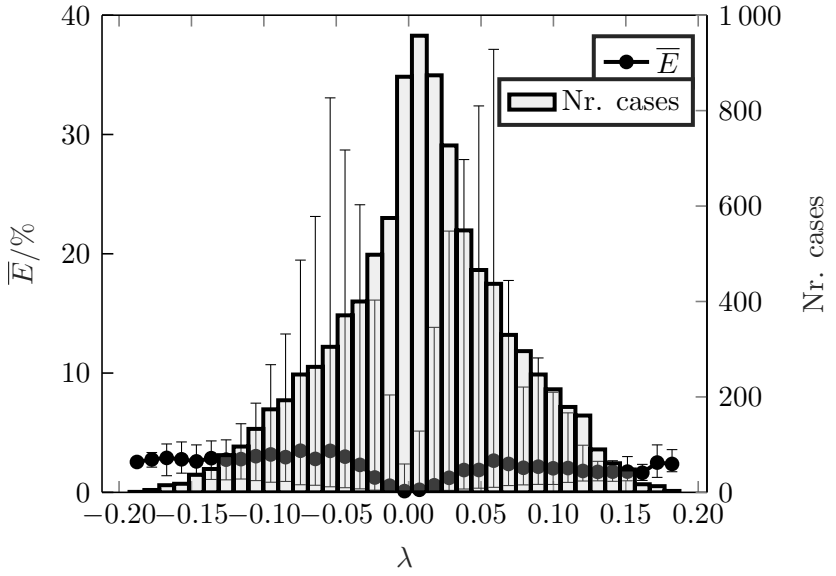

Figure 4.11: Effect of asymmetry on gear dynamics: spur gears.

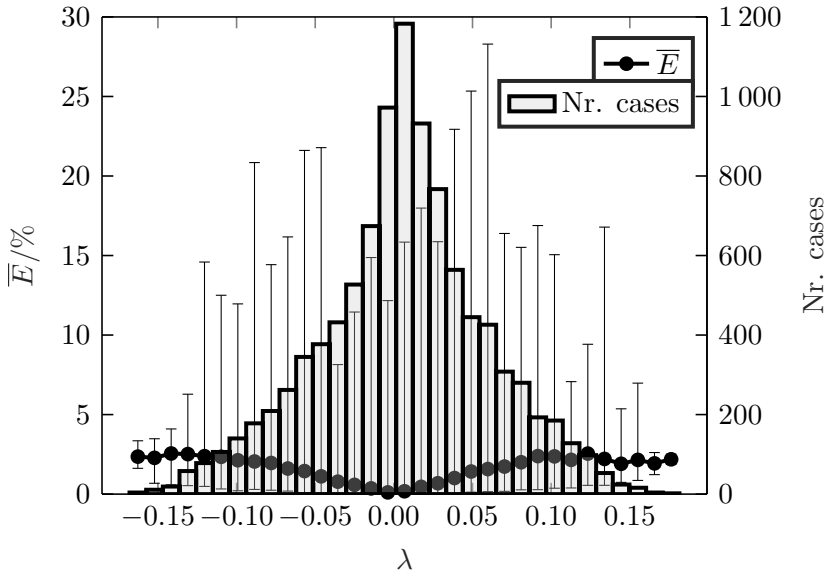

Figure 4.12: Effect of asymmetry on gear dynamics: helical gears.

group spur and helical gears that have the highest absolute relative differences are investigated. Figure 4.13 shows the $A_{\mathrm{RMS}}(\mathrm{DTE}_{\mathrm{osc}})$ for the spur gear with the highest absolute relative difference ("worst spur gear"). It can be concluded that the high relative differences comes from the gap in the magnitude for the whole speed range because the location of the peaks are very close to each other.

Figure 4.14a shows the mesh stiffness along the path of contact with and without λ. The mean absolute relative difference between them is only around 1.0%, so it is not a simple difference in the stiffness magnitude that can explain the differences in the dynamic response. In order to go further in the analysis, the mesh stiffness has been decomposed using an FFT - the decomposition is shown in Figure 4.14b. The relative difference for each of the first three harmonic is of 17.1%, 71.6% and 48.3%, which explains the differences in the dynamic response.

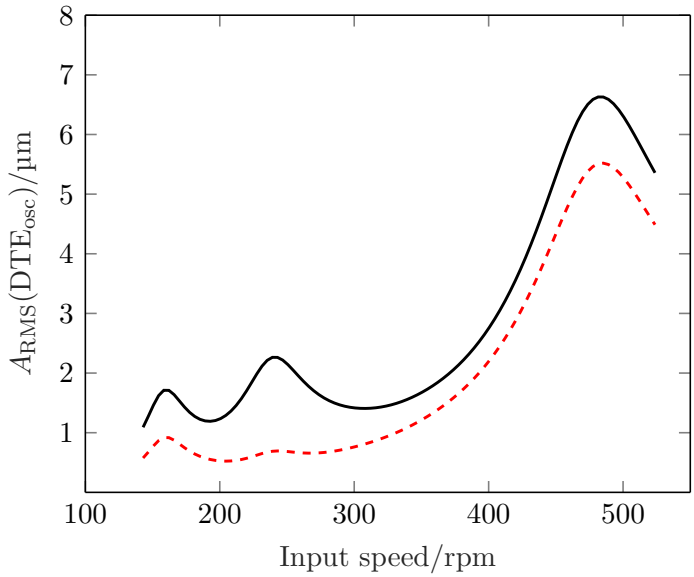

Figure 4.13: Dynamic analysis for the worst spur gear: with (——) and without (- - -) asymmetry.

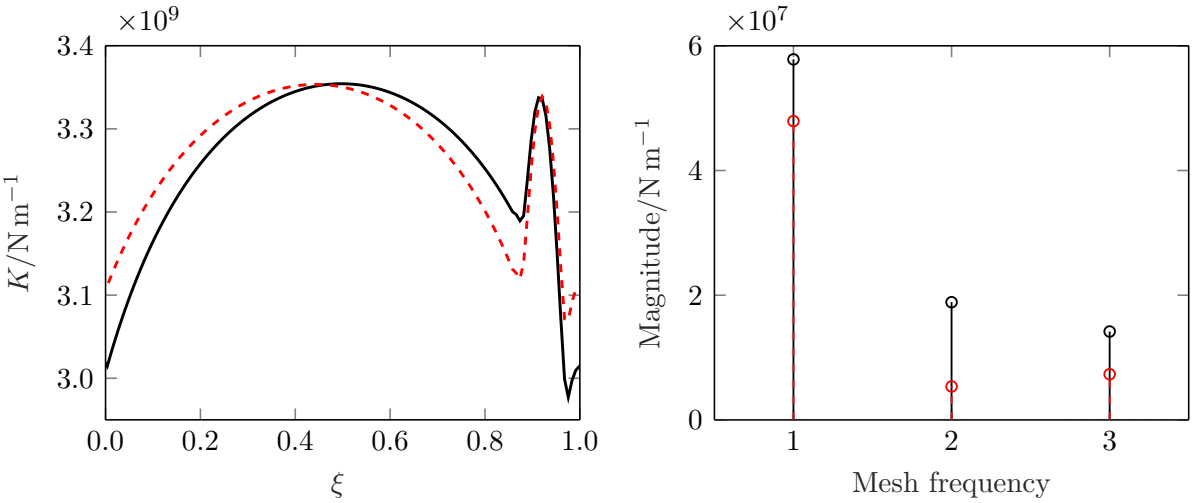

(a) Gear mesh stiffness.

(b) Spectrum of gear mesh stiffness (K).

Figure 4.14: Stiffness analysis for the worst spur gear: with (——) and without (- - -) asymmetry.

Concerning the dynamic transmission error oscillations of the "worst helical gear" with and without λ, from Figure 4.15 it can be concluded that the curves have very similar shapes with different values which leads to the average relative difference of 28.1%.

The gear mesh stiffness for this helical gear is studied by analyzing its shape, Figure 4.16a, and the magnitude of its first three gear mesh stiffness harmonics, Figure 4.16b. The relative difference in the gear mesh stiffness has an average value of approximately 0.9%. Also, note that there is an effect of an extra tooth pair in contact in the transverse plane, in other words, the contact ratio, which is theoretically lower than 2, due to the contact extension increases to a value higher than 2 and thus creates the peaks located at the start and end of the meshing period. The FFT analysis to the gear mesh stiffness, Figure 4.16b, shows a relative difference

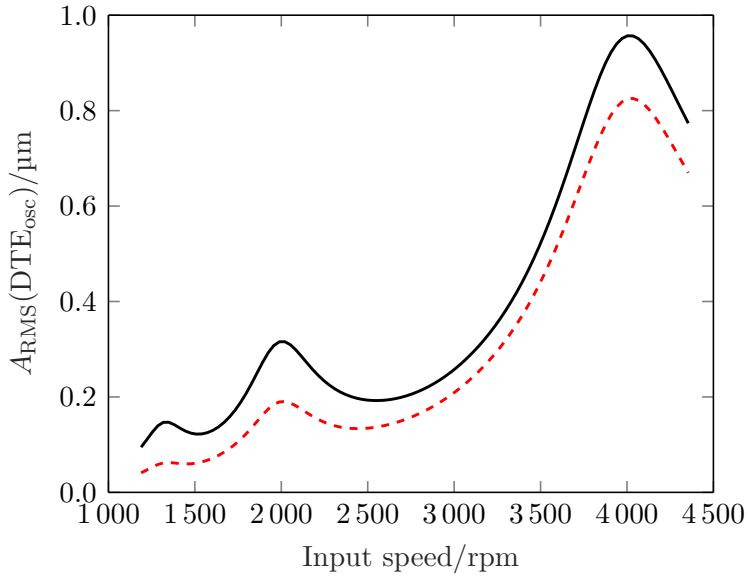

Figure 4.15: Dynamic analysis for the worst helical gear: with (——) and without (- - -) asymmetry.

in the magnitude of the first three harmonics of 13.1%, 41.9% and 57.8%. Despite having a very low average point by point absolute relative difference, the magnitude of each harmonic are considerably different. From a dynamics point of view, the differences in the magnitude of the harmonics justify the mismatch between having very similar shapes of gear mesh stiffness and distinct modeled dynamic transmission error fluctuations.

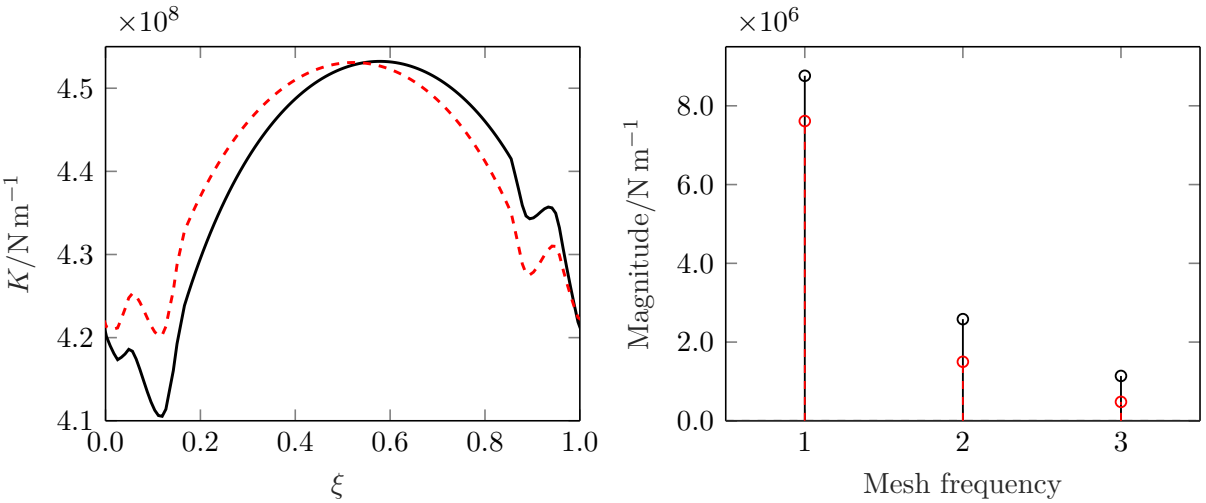

(a) Gear mesh stiffness.

(b) Spectrum of gear mesh stiffness (K).

Figure 4.16: Stiffness analysis for the worst helical gear: with (——) and without (- - -) asymmetry.

To sum up, even though the gear mesh stiffness might have similar shape, the dynamic transmission error oscillations of those gears is not necessarily close to each other. The top 5 "worst" spur and helical gears were submitted to a stiffness analysis as shown in this section. A common factor found between those gears is the addition of another tooth pair in the gear meshing process, for

instance, the triple tooth contact region located between $0.8 < \xi < 1$ for Figure 4.14a and the extra tooth pair in the transverse plane for Figure 4.16a shown at the start and end of the meshing period. The tooth structural asymmetry affects the stiffness values at the theoretical start and end of the path of contact, therefore it makes sense that with higher extension of contact, the influence of λ becomes more pronounced. One of the main modifications that the extension of contact can produce to the gear mesh stiffness, is the introduction of another tooth pair in the gear meshing. It is precisely under those conditions that the tooth structural asymmetry cannot be neglected as, according to the presented analysis, accounting for it remarkably changes the dynamic modeling results.

4.4.3. Load distribution

Load distribution is of interest for gear analysis since it affects the estimations of tooth bending, pitting and meshing efficiency performances. When it comes to gear quasi-static behavior, the load sharing ratio is the parameter of reference. Under dynamic conditions, to evaluate the load distribution, the dynamic mesh force is determined.

Quasi-static analysis

In order to compare the results of the load sharing ratio with and without the tooth pair structural stiffness asymmetry, the relative point-by-point difference between the load sharing ratios is taken as presented in equation (4.48).

$$\Delta\mathcal{L} = \left| \frac{\mathcal{L}^{\lambda_0} - \mathcal{L}^{\lambda}}{\mathcal{L}^{\lambda}} \right| \tag{4.48}$$

In equation (4.48), $\mathcal{L}^{\lambda}$ and $\mathcal{L}^{\lambda_0}$ are the load sharing ratios of the gears with and without the asymmetry parameter, respectively. The mean value of $\Delta\mathcal{L}$ ($\overline{\Delta\mathcal{L}}$) is computed for every gear. These results are averaged for the gears in the same range of λ with whiskers representing the group's extreme values, as shown in Figure 4.17 for spur gears and Figure 4.18 for helical gears.

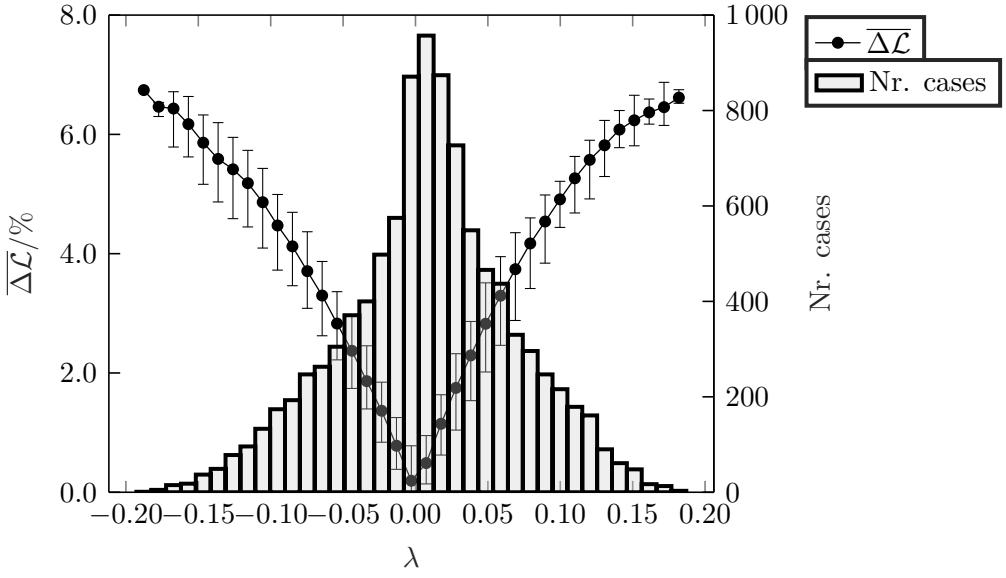

Figure 4.17: Effect of asymmetry on load sharing ratio: spur gears.

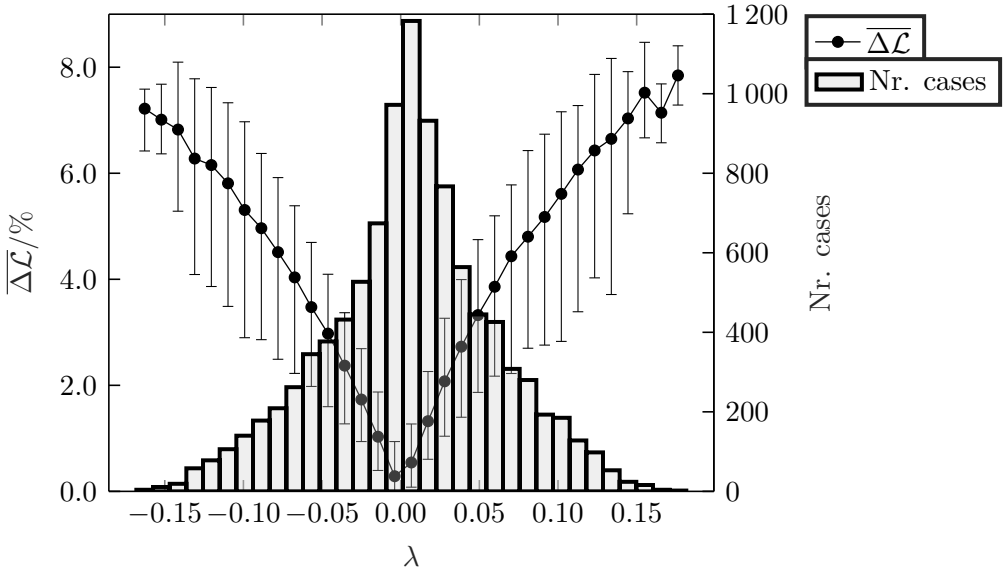

Figure 4.18: Effect of asymmetry on load sharing ratio: helical gears.

Figures 4.17 and 4.18 show much higher relative difference when compared to the results obtained for gear mesh stiffness (Figures 4.9 and 4.10). The shape of the curves, when comparing spur and helical gears with their respective gear mesh stiffness analysis, follow the same trend, increasing with the higher asymmetry values. The significant increase in the relative difference can be explained by the definition of the load sharing ratio, equations (4.23) and (4.27). The single tooth pair mesh stiffness takes an important role in the definition of the load sharing ratio. Also, since the effect of the tooth pair structural stiffness asymmetry is more noticeable on the single tooth pair mesh stiffness than on the gear mesh stiffness, it originates this increased relative difference. A maximum average relative difference of correspondingly 6.7% and 7.8% for spur and helical gears with the worst results (spur: 6.9% and helical: 8.5%) for each λ range not presenting any drastic increase from their average values. That being said, the importance of the tooth pair structural stiffness asymmetry is more relevant for the load sharing ratio than for the gear mesh stiffness. Therefore, its effect must not be disregarded.

Dynamic analysis

The dynamic analysis of the load distribution is performed using the dynamic mesh force oscillating component, as defined in equation (4.49), which takes the dynamic mesh force (DMF), seen as the force in the gear mesh due to dynamic displacements, and subtracts its static component (F_{bt}).

$$\mathrm{DMF}_{\mathrm{osc}} = K \cdot \mathrm{DTE} - F_{\mathrm{bt}} \tag{4.49}$$

There is a steady-state dynamic mesh force curve for every speed evaluated. Thus, this data needs to be compacted into a single value for each speed. To do so, for each pinion rotating speed, the equivalent root-mean square of the dynamic mesh force oscillating component ($A_{\mathrm{RMS}}(\mathrm{DMF}_{\mathrm{osc}})$) is computed. Then, for each speed, the relative difference between the two gear pairs (one with and another without asymmetry) is determined according to equation (4.50).

$$\Delta\text{DMF} = \left| \frac{A_{\text{RMS}}(\text{DMF}_{\text{osc}})^{\lambda_0} - A_{\text{RMS}}(\text{DMF}_{\text{osc}})^{\lambda}}{A_{\text{RMS}}(\text{DMF}_{\text{osc}})^{\lambda}} \right| \tag{4.50}$$

The values calculated for every speed are averaged, resulting in a single value for the two gear pairs being compared - $\overline{\Delta\text{DMF}}$. Figures 4.19 and 4.20 summarize the results for the dynamic mesh force for the spur and helical gears respectively.

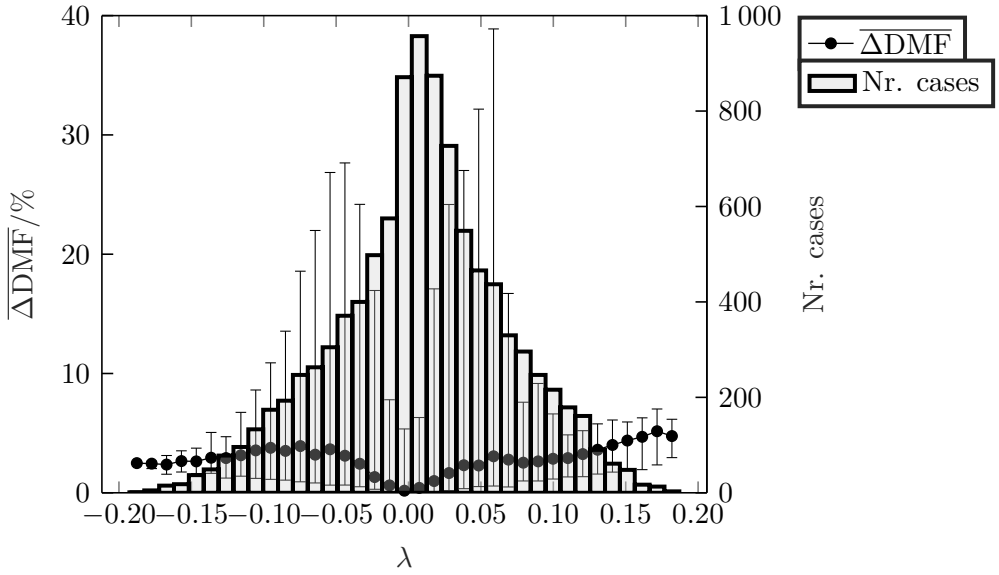

Figure 4.19: Effect of asymmetry on dynamic mesh force: spur gears.

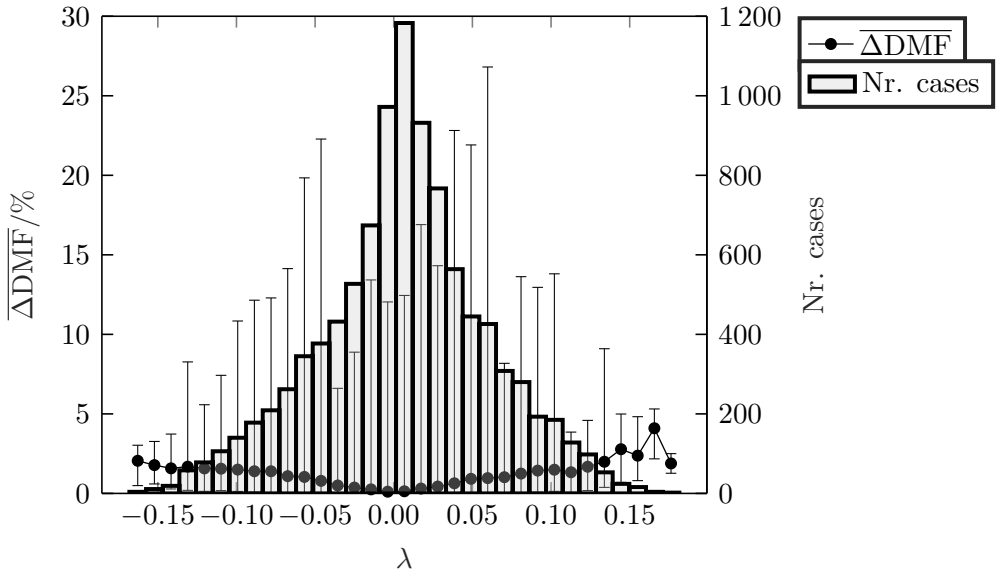

Figure 4.20: Effect of asymmetry on dynamic mesh force: helical gears.

When looking at the dynamic load distribution results with λ in Figures 4.19 and 4.20, the average relative differences for each λ interval are, overall, in line with their dynamic displacement counterpart (Figures 4.11 and 4.12), presenting maximum average values of 5.2% (spur) and 4.1% (helical). Moreover, the magnitude of the maximum relative difference values along λ are

close to the ones shown for the dynamic transmission error (38.9%/26.8% for dynamic mesh force and 37.1%/28.3% for dynamic transmission error: spur/helical). Even their distributions with λ are very similar. An examination to the "worst" results in the dynamic load distribution disclosed that it is due to the same phenomena (distinct frequency content of the gear mesh stiffness) of the dynamic displacement that the dynamic mesh force has its highest values, with the same gears appearing in both cases. So, the combination of an extra tooth pair in the gear meshing with the tooth pair structural stiffness asymmetry causes pronounced differences in the dynamic mesh force oscillating component.

4.5. Closure

Throughout this chapter, a new approximate gear mesh stiffness model was developed for spur and helical gears. This model takes advantage of an approximate expression for the single tooth pair slice mesh stiffness [171] and includes the effects of coupling between gear slices, contact extension, profile modifications and buttressing. Thanks to the low computational cost of this gear mesh stiffness model, it is now feasible to perform large parametric studies on gears with good accuracy. Along with the gear mesh stiffness model, a gear-shaft-bearing dynamic model has also been implemented. From the large-scale analysis on the effect of tooth structural stiffness asymmetry on spur and helical gears, it was concluded that:

- the low computational cost feature of the gear mesh stiffness model developed can be evaluated using the computational time as a measurement. Taking the two 10000 random gear geometries as samples, the average gear mesh stiffness estimation time (intel(R) core(TM) i7-9700 CPU with 64 GB of memory RAM at 2667 MHz - MATLAB® R2023a) is 5.1 ms for a spur gear and 1.0 s for a helical gear.

- the tooth structural stiffness asymmetry does not significantly modify the shape of the gear mesh stiffness: highest average absolute relative difference is around 2.4%. However, superimposing the differences inherent to the approximate gear mesh stiffness model with the ones from disregarding the tooth pair structural stiffness asymmetry can potentially cause relevant differences in the gear mesh stiffness shape due to cumulative effects;

- for gear dynamic displacements, the asymmetry must be considered since it can lead to relative differences of up to 37.1%. Although small differences can be found in the shape of the gear mesh stiffness, the magnitude of the gear mesh stiffness harmonics can be drastically modified, causing different dynamic behavior;

- the differences caused by λ in the load sharing ratio (quasi-static load distribution) are increased in comparison with the ones for the gear mesh stiffness, maximum relative difference of 8.5%. The dynamic mesh force analysis revealed differences in the same range of values as for the gear dynamic displacement (maximum of 38.9%). Worst cases are obtained under the same circumstances of the gear dynamic displacement, having matching worst gear sets;

- the phenomena leading to significant differences in the results at a dynamic level is a combination of neglecting the tooth pair structural stiffness asymmetry with the fact that, due to the applied load and consequently elastic deformations, an extra tooth pair enters the gear meshing. Thus, this can occur depending on the applied load, gear mesh stiffness magnitude and contact/overlap ratios of the gear being analyzed.

Taking the aforementioned into account, it can be stated that the tooth pair structural stiffness asymmetry cannot be neglected and should be included for the modeling of gear mesh stiffness (which enters in the dynamic evaluation) and load distribution. Moreover, it is shown that the approximate gear mesh stiffness model is effective and reliable for gear exploratory studies.

Next At this point, a set of tools for gear quasi-static and dynamic evaluation is acquired with the achievement of the gear mesh stiffness model and the implementation of a gear-shaft-bearing dynamic model. With it, the next chapter is dedicated to the exploration of a previously presented gear design concept - integer overlap ratio helical gears [8].

Chapter 5

Integer overlap ratio gears: preliminary study

In previous works it was found that for certain combinations of overlap and contact ratios, the fluctuation of the theoretical length of the lines of contact was zero, promoting an almost constant gear mesh stiffness. This led to the design of integer overlap ratio helical gears in order to reach an almost constant gear mesh stiffness. Being the overlap ratio the central parameter for the design of these new gears, it is relevant to evaluate how the gears mesh stiffness, dynamic behavior and noise level are affected by it. Resorting to the developed gear mesh stiffness model, the implemented gear-shaft-bearing dynamic model and Masuda's noise level equation, a correlation between the overlap ratio, gear mesh stiffness fluctuations, dynamic transmission error as well as gear noise level is found. Integer overlap ratio gears present better overall performance.

5.1. Background

One of the main sources of vibration in a geared transmission system is the gear pair. Its mesh stiffness fluctuations excite the entire system. The generated vibration energy passes through the shafts and bearings to then reach the gearbox housing. The gearbox housing vibrates and radiates noise accordingly [190–192]. Therefore, designing a gear pair whose gear mesh stiffness fluctuations are non-existent or insignificant would result in an overall improved dynamic performance of the system [135; 142].

Several authors [8; 193–195] showed with distinct methodologies that for integer values of the contact/overlap ratios, the theoretical length of the contact lines is constant. Under these circumstances, the gear has an almost constant gear mesh stiffness [8; 135; 142]. By taking advantage of this concept, Marafona et al. [8] developed a gear design algorithm to create integer overlap ratio gears considering the tooth bending strength, surface durability as well as gear meshing efficiency. The newly designed gears were tested showing reduced dynamic transmission error oscillations and lower dynamic overload.

The basis of this work is the concept of integer overlap ratio (IOR) gears. For the development of

Contents in Chapter 5: Integer overlap ratio gears: preliminary study are reproduced with permission of the respective publisher from João D.M. Marafona, Pedro M.T. Marques, Ramiro C. Martins, and Jorge H.O. Seabra. Effect of overlap ratio on gear dynamic behavior and noise level. In VDI Wissensforum GmbH, editor, *International Conference on Gears 2023*, volume 2422 of *VDI-Berichte*. VDI Verlag, Düsseldorf, 2023. doi: doi.org/10.51202/9783181024225.

this new concept, gears need to be manufactured and then experimentally tested. This chapter consists on a preliminary numerical study, prior to experimental testing, on the effect of varying the overlap ratio of a gear in its dynamic behavior. First, the previously developed algorithm [8] is used to design IOR gears. The overlap ratio is varied between 0.5 and 2.5 for the designed gear by changing its facewidth. To keep an equivalent analysis for all evaluated cases, the maximum contact pressure is fixed for all gears. Second, the gear mesh stiffness is investigated with the model developed in [196]. As for the dynamic behavior, the employed model comprises Timoshenko beam elements for the shafts, lumped stiffness for the bearing elements and the previously estimated gear mesh stiffness [196]. The overall noise level emitted by the gearbox is determined with the semi-empirical equation developed by Masuda et al. [197]. Finally, the gear mesh stiffness, gear dynamic behavior and emitted noise level are related to the overlap ratio with focus on integer values.

5.2. Gear design

To design the gears for the dynamic evaluation of the overlap ratio, a previously developed gear design algorithm [8] is made use of while taking into account the test rig available (FZG test rig) - this way, the gears can be manufactured and experimental tests can then be performed. A brief description of the algorithm employed for the development of the IOR gears is presented here but a detailed explanation can be found in [8].

The algorithm requires a gear geometry to initiate the optimization procedure. Two different gear geometries are used as starting points, the H501 and the H951, as defined in Table 5.1. The H501 is a standard helical gear while the H951 is a "low loss" helical gear pair. Note that the parameters that define the starting gear geometries in Table 5.1 are the same given as the output of the algorithm.

Table 5.1: Geometrical parameters of the H501 and H951 gears.

Gear	**H501**		**H951**	
	Driving	Driven	Driving	Driven
z/-	20	30	38	57
m/mm	3.5		1.75	
β/°	15		15	
b/mm	23		23	
x/-	+0.1809	+0.0891	+1.6915	+2.0003
ρ^*_{fP}/-	0.38		0.38	

ρ^*_{fP}: root fillet radius of the basic rack for cylindrical gears per module

Data regarding the geometry (pressure angle, working center distance and velocity ratio), operating conditions, gears' material and lubricant properties needs to be given as an input for the algorithm - Table 5.2 shows the information required and used in this optimization procedure.

Concerning the constraints imposed, they are the limitation of the contact ratio, imposition of the gear ratio, impossibility of interference, equal maximum specific sliding and assurance of the correct center distance.

The definition of the objective function, established in equation (5.1), involves the calculation of the gear surface durability and tooth bending strength [141], which are introduced in the equation through their respective safety factors, S_H and S_F. Moreover, the objective function accounts for the gear meshing efficiency through the gear loss factor H_V^G [142]. Finally, to include

Table 5.2: Parameters imposed for the development of the IOR gears.

Parameters	**Value**
$\boldsymbol{\alpha}$/°	20
$\boldsymbol{a}$/mm	91.5
$\boldsymbol{u}$/-	1.5
$\boldsymbol{n_1}$/rpm	1200
$\boldsymbol{T_1}$/N m	477.78
Material/-	16MnCr5 (Class Eh)
$\boldsymbol{R_a}$/µm	0.35
$\boldsymbol{R_{z\ root}}$ / µm	20
$\boldsymbol{R_{z\ flank}}$/µm	2.5
$\boldsymbol{K_A}$/-	1.25
Accuracy Grade/-	6
Lubricant/-	ISO-VG 220 (Mineral-oil base)
Required Service Life/hours	20000

all the different parameters in a single objective function, the constants C_i are introduced as weights for each term.

$$\text{Obj. Fun.}=C_1|S_{\text{Fmin1}}-S_{\text{F1}}|+C_2|S_{\text{Fmin2}}-S_{\text{F2}}|+C_3|S_{\text{Hmin}}-S_{\text{H}}|+C_4H_{\text{V}}^{\text{G}} \tag{5.1}$$

Since the implemented algorithm [8] is going to find the minimum of the objective function while satisfying the constraints, the calculated safety factors tend to the imposed safety factors ($S_{\text{min}} = 2.0$) and the gear loss factor is going to be minimized.

A wide variety of gears is intended from the algorithm so that when choosing the gears, a broader range of alternatives is available. From all the obtained gears, the selected gears are presented in Table 5.3 along with the C14 and C40 which are reference gears for the test and slave gearboxes of the FZG test rig. The new gears are named Integer Overlap Ratio (IOR) Gears followed by their total number of teeth. Table 5.3 shows the starting gear geometry and constants applied in the objective function for each gear. In addition, the gear geometrical parameters, contact ratio and overlap ratio are also included. The safety factors and power loss shown in Table 5.3 were calculated in KISSsoft®. The conditions employed for their computation were a torque of $T_1 = 477.8$ Nm at the pinion and a pinion rotating speed $n_1 = 1200$ rpm (non-mentioned conditions are KISSsoft®'s default values). The gears developed from the algorithm vary from high safety factor gears to high efficiency gears, from low to high helix angles and from overlap ratios equal to one and two.

The C14 and C40 (Table 5.3) are the standard gears used in the FZG gear test rig so their safety factors are taken as a reference for the IORGears. The IORGears are displayed in Table 5.3 ordered by increasing total number of teeth. It can be verified that the power loss is related with the size and number of teeth of the gear pair - the higher the number and the smaller the teeth are, the more efficient the gear pair is. Moreover, a correlation with the safety factors can also be made: as the meshing efficiency increases, the safety factors decrease.

The IOR55 was selected to be a replacement for the C40 so their safety factors are as high as the C40. The higher power loss of the IOR55 comparing to the C40 does not stand a problem as this

Table 5.3: Parameters for the IOR gears developed.

Gear	**C14**	**C40**	**IOR55**	**IOR60**	**IOR651**	**IOR652**	**IOR70**	**IOR85**	**IOR100**
Starting Gear	-	-	H501	H501	H951	H951	H951	H501	H951
C_1	-	-	1.00	0.90	0.10	1.00	0.15	0.00	0.40
C_2	-	-	1.00	0.90	0.10	1.00	0.15	0.00	0.40
C_3	-	-	1.00	0.90	0.10	1.00	0.15	0.00	0.40
C_4	-	-	1.00	0.50	0.70	0.70	0.80	1.00	0.60
z_1/-	16	16	22	24	26	26	28	34	40
z_2/-	24	24	33	36	39	39	42	51	60
m/mm	4.50	4.50	3.00	2.75	2.75	2.50	2.50	2.00	1.75
β/°	-	-	28.1147	25.5926	12.4733	23.1225	11.3236	18.3101	15.9554
b/mm	14	40	40	40	40	40	40	40	40
x_1/-	0.1817	0.1817	-0.1021	0.1147	0.1218	0.6354	0.4824	0.4947	0.1923
x_2/-	0.1715	0.1715	-0.5303	-0.1055	-0.1347	0.7557	0.4997	0.5575	0.0953
ρ^*_{fP}/-	0.38	0.38	0.25	0.25	0.25	0.25	0.25	0.25	0.25
ε_α/-	1.438	1.438	1.482	1.423	1.605	1.218	1.410	1.399	1.598
ε_β/-	-	-	2.000	2.000	1.000	2.000	1.000	2.000	2.000
S_{F1}/-	0.84	2.34	2.42	1.95	1.64	1.47	1.32	1.16	1.07
S_{F2}/-	0.87	2.43	2.35	1.93	1.63	1.44	1.30	1.13	1.05
S_{H1}/-	0.54	0.91	1.01	1.05	1.07	1.04	1.07	1.08	1.09
S_{H2}/-	0.59	0.99	1.02	1.06	1.08	1.05	1.08	1.09	1.10
P_{VZP}/W	634.0223	609.1162	767.0451	666.4143	572.8135	524.6879	475.1985	448.9556	428.4298

gear is supposed to be mounted on the slave box. In fact, this can be seen as a positive aspect, as it was concluded in [142], a high power loss gear with low dynamic excitation would be the ideal gear for power loss studies of the lubricant. The high power loss and low dynamic effects allow for a better experimental torque measurement due to the almost constant high torque loss level output.

The IOR60 is another high safety factor gear that when compared with the IOR55 has lower helix angle, safety factors and power loss - this gear is another option for the replacement of the C40.

Two gears with a total of 65 teeth were obtained so an extra number corresponding to the overlap ratio was added to their names. These are very similar gears, being their main differences on the module and helix angle - geometrical parameters that contribute for the overlap ratio. Still, these differences lead to higher safety factors for the IOR651 and a more efficient gear meshing for the IOR652.

The other gear made with an overlap ratio equal to 1 is the IOR70. It is clear the difference in the helix angle between the gears with different overlap ratios. The IOR70 and IOR651 both show the lowest helix angles among all the developed gears. A major benefit of low helix angles is the lower axial loads transmitted to bearings which contribute to a higher efficiency of the entire system. The IOR70 presents the best balance between power loss and safety factors of all gears in Table 5.3.

Finally, the IOR85 and IOR100 are the gears with the best meshing efficiency and the lowest safety factors. Regardless, they both show safety factors higher than the C14. Between these two

gears, the IOR100 has higher total contact ratio, lower helix angle and higher meshing efficiency. Hence, after analyzing this data, it is expected that the IOR100 leads to an improved system efficiency and lower dynamic excitation when comparing to the IOR85.

Figures 5.1 and 5.2, the IOR maps, show the facewidth as a function of the helix angle in order to obtain an overlap ratio equal to 1 and 2, respectively, for the range of modules presented in Table 5.3 - it can be extended for any module. For each module presented in Figures 5.1 and 5.2, the point closest to the origin gives the geometrical parameters for the IORGear with the lowest possible helix angle and facewidth. Also, the lower the gear module, the closer the curve is to the origin and therefore an IORGear with a lower facewidth and helix angle can be obtained. The IOR maps help to understand the relation between all variables that define the overlap ratio and can also be used as transformation maps, meaning that, one can easily find the facewidth required to modify an existing helical gear pair to make it an IOR gear.

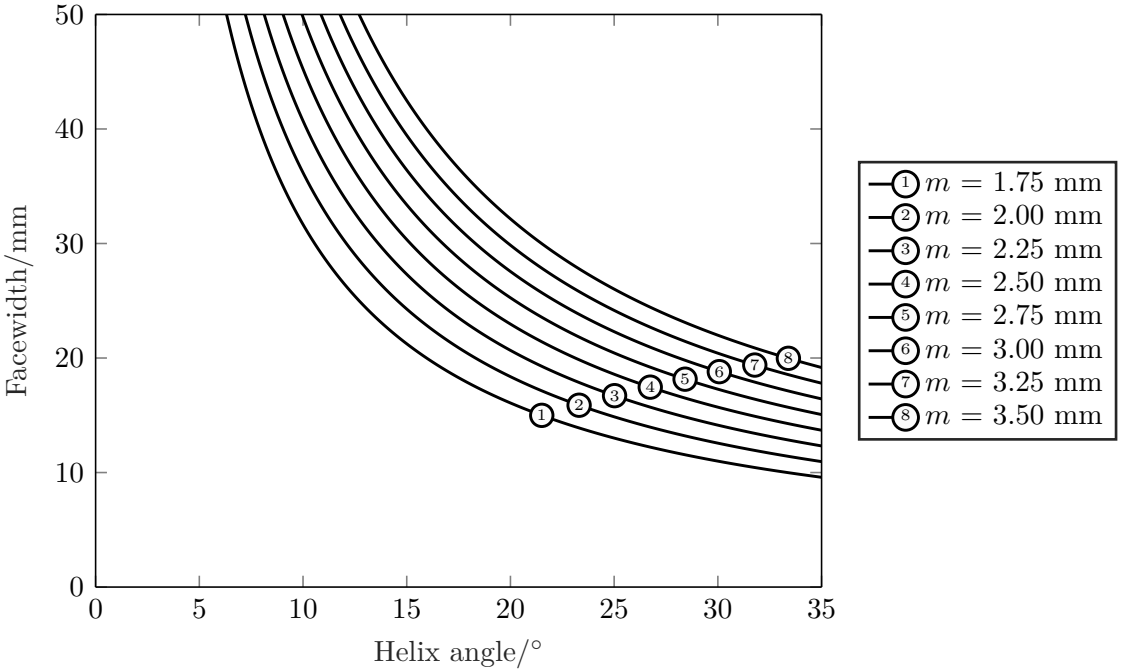

Figure 5.1: IOR map for $\varepsilon_\beta = 1$.

Upon a thorough discussion on the obtained IOR gears (Table 5.3), a geometry for the evaluation of the dynamic behavior with the overlap ratio needs to be selected. To do so, the facewidth of the selected gears is changed to obtain the desired overlap ratios. The modification of the gear facewidth is the less intrusive option to vary the overlap ratio as every tooth proportion in the transverse plane is exactly the same for every overlap ratio studied. Nevertheless, this imposes an issue on how to select a proper loading torque for an equivalent analysis of every case. The criteria used is that the load selected is the one that gives the same maximum contact pressure according to the Hertz theory.

The values intended for the overlap ratios are $\varepsilon_\beta = 0.50$, 0.75, 1.00, 1.25, 1.5, 1.75 and 2.00. Given the options presented in Table 5.3, the IOR651 and IOR70 cannot have their facewidth further increased due to the limitation of the available gearbox and are therefore not an option to perform this study. From the remaining gears, the IOR100 is the selected gear pair as it presents the lowest helix angle and the lowest power loss.

Given the options presented in Table 5.3, the IOR651 and IOR70 cannot have their facewidth

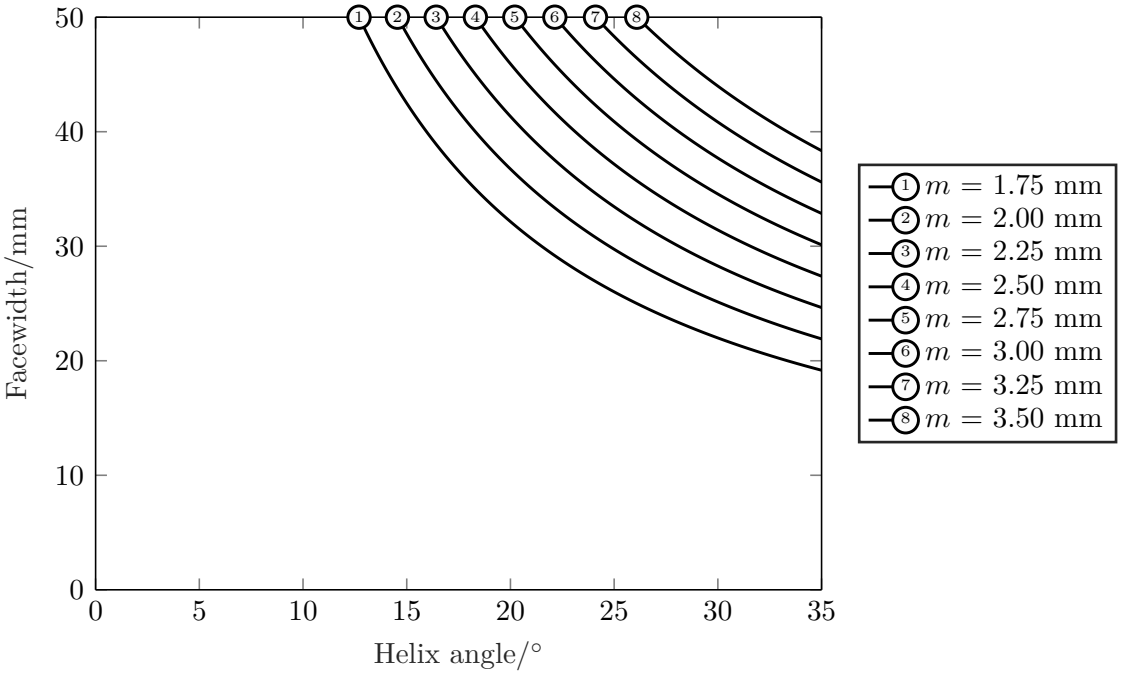

Figure 5.2: IOR map for $\varepsilon_\beta = 2$.

further increased due to the size of the available gearboxes. From the remaining gears, the IOR100 is the one selected since it presents the lowest power loss and helix angle. Table 5.4 shows the geometrical parameters of the IOR100 and its variants with their corresponding contact and overlap ratios.

Table 5.4: Parameters for the IOR100 variants.

Gear	**IOR100-200**	**IOR100-175**	**IOR100-150**	**IOR100-125**	**IOR100-100**	**IOR100-075**	**IOR100-050**
$\boldsymbol{z_1}$/-	40	40	40	40	40	40	40
$\boldsymbol{z_2}$/-	60	60	60	60	60	60	60
$\boldsymbol{m}$/mm	1.75	1.75	1.75	1.75	1.75	1.75	1.75
$\boldsymbol{\beta}/^\circ$	15.9554	15.9554	15.9554	15.9554	15.9554	15.9554	15.9554
$\boldsymbol{b}$/mm	40	35	30	25	20	15	10
$\boldsymbol{x_1}$/-	0.1923	0.1923	0.1923	0.1923	0.1923	0.1923	0.1923
$\boldsymbol{x_2}$/-	0.0953	0.0953	0.0953	0.0953	0.0953	0.0953	0.0953
$\boldsymbol{\rho^*_{fP}}$/-	0.25	0.25	0.25	0.25	0.25	0.25	0.25
$\boldsymbol{\varepsilon_\alpha}$/-	1.598	1.598	1.598	1.598	1.598	1.598	1.598
$\boldsymbol{\varepsilon_\beta}$/-	2.000	1.750	1.500	1.250	1.000	0.750	0.500

On the nominal testing conditions, the torque does not impose any restriction as a great variety is available and different values can easily be added to the accessible test rig. Thus, a nominal torque of $T_1 = 200$ N m is selected for the reference gear, IOR100-200. The torques for the remaining gears are computed by making the maximum Hertz pressure the same for every gear pair. Regarding the range of rotating speeds, the test rig available can currently go up to 4500 rpm. Nevertheless, a nominal rotating speed for the pinion equal to 5000 rpm is selected. Table 5.5 shows the torque values for every IOR100 variant and their safety factors under the nominal conditions according to KISSsoft®- all gears have their safety factors above the

minimum required [81].

Table 5.5: Experimental tests safety factors for the IOR100 variants.

Gear	**IOR100-200**	**IOR100-175**	**IOR100-150**	**IOR100-125**	**IOR100-100**	**IOR100-075**	**IOR100-050**
n_1/rpm	5000	5000	5000	5000	5000	5000	5000
T_1/Nm	200	175	150	125	100	75	50
S_{F1}/-	1.779	1.788	1.797	1.806	1.828	1.762	1.700
S_{F2}/-	1.758	1.767	1.776	1.785	1.807	1.742	1.680
S_{H1}/-	1.416	1.418	1.421	1.422	1.429	1.374	1.326
S_{H2}/-	1.434	1.436	1.438	1.440	1.447	1.395	1.351

Since the results presented in this work consist on a preliminary numerical analysis of the effect of the overlap ratio on the gear mesh stiffness and gear dynamic behavior, the number of gears and range of overlap ratios studied is increased. 41 gears uniformly distributed between $\varepsilon_\beta = 0.5$ and 2.5 are analyzed, meaning that a gear is evaluated for every increment of 0.05 in the overlap ratio. These values of overlap ratio are obtained by varying the facewidth and the torque is determined as it was aforementioned. In addition, the spectrum of testing conditions is broaden in what regards the speed range. The dynamic behavior of the gears is simulated between 50 rpm and 10000 rpm.

5.3. Gear mesh stiffness

The gear mesh stiffness of the IOR100 gears is analyzed by resorting to a previously developed model [196]. The model used [196] is an approximate gear mesh stiffness model that employs the slicing method. The stiffness of each slice is estimated with the expression from Marafona et al. [171] and the slices are coupled with a parabolic contact line stiffness distribution. This gear mesh stiffness model also considers extension of contact, profile modifications as well as the border weakening effect in helical gears. For this research, the number of points per mesh period is set to 100 while the number of slices is made proportional to the overlap ratio with 100 slices per unit of overlap ratio. The gears' material properties are as in Table 5.6.

Table 5.6: Gears' material properties.

Properties	**Value**
E /GPa	206
ν /-	0.3
ρ /kg m^{-3}	7830

Figure 5.3 shows the gear mesh stiffness of part of the gears studied. Two key features of Figure 5.3 must be stressed out, one of them is the increasing average stiffness value with the increasing overlap ratio. The other one is that the mesh stiffness for the gears with integer overlap ratios is close to being a straight line and therefore it is almost constant.

To investigate the fluctuation of the gear mesh stiffness, the average gear mesh stiffness value is subtracted to each stiffness curve (ΔK), resulting in Figure 5.4. This parameter highlights the very low amplitude of the gear mesh stiffness as a consequence from imposing integer overlap ratios. Moreover, from Figure 5.4, the gears can be divided into four groups where even though they can have completely different average gear mesh stiffness values, their variation is basically

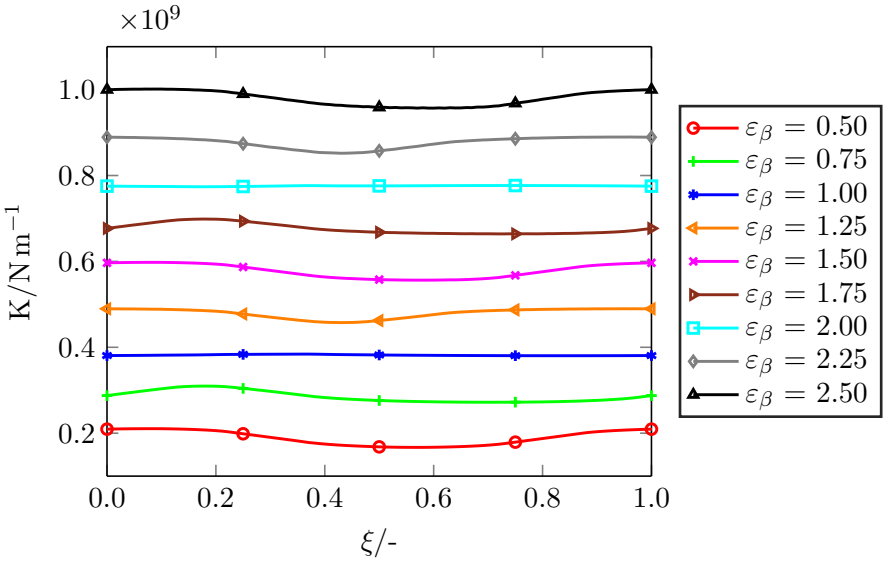

Figure 5.3: Gear mesh stiffness.

the same. These groups consist on the gears that have the same decimal places, for instance, the gears with $\varepsilon_\beta = 0.50$, 1.50 and 2.50 show almost coincident curves. Of course if these values are normalized by the average stiffness, their amplitudes would differ. Within each group, a higher average gear mesh stiffness would result in a lower relative amplitude.

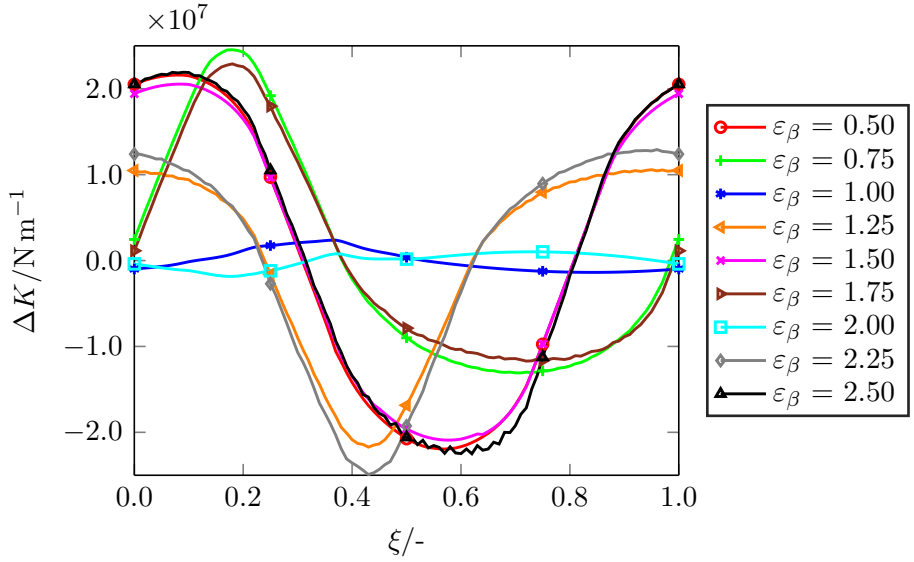

Figure 5.4: Gear mesh stiffness fluctuation around its average.

The peak-to-peak amplitude (PPA) of the gear mesh stiffness and the root-mean-square (RMS) of the gear mesh stiffness fluctuation are shown in Figures 5.5 and 5.6. These parameters attribute a unique value to each gear, classifying the mesh stiffness for each value of the overlap ratio. The trend of the curves in Figures 5.5 and 5.6 match each other showing minimum values for integer values of the overlap ratio and maximum values when $\varepsilon_\beta = 0.50$, 1.50 and 2.50.

Figure 5.7 shows the RMS of the gear mesh stiffness fluctuation normalized by its average value. When compared to Figure 5.6, Figure 5.7 has the minimum and maximum values located at the

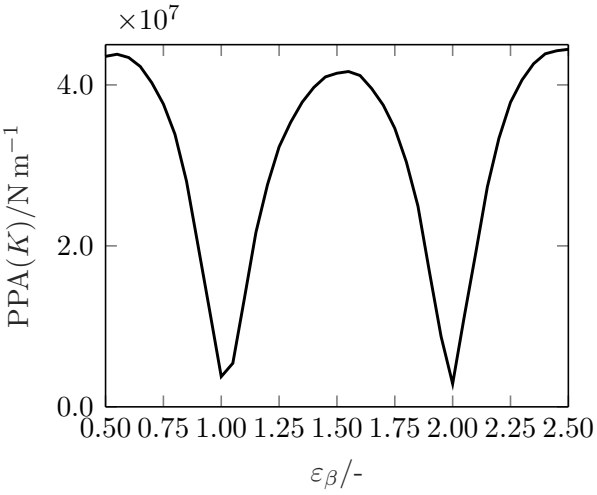

Figure 5.5: Peak-to-peak amplitude of the gear mesh stiffness amplitude.

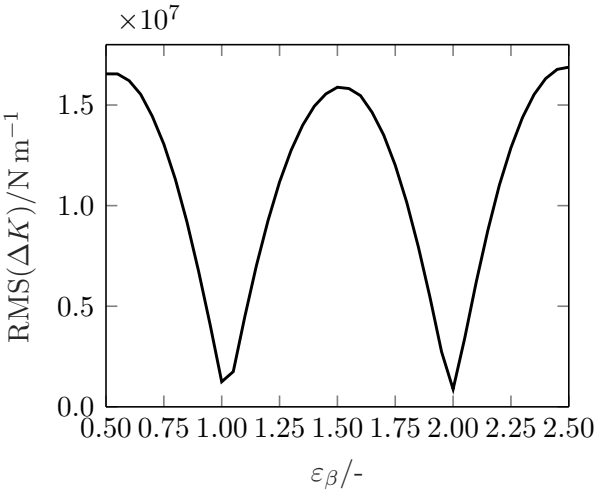

Figure 5.6: RMS of the gear mesh stiffness fluctuation around its average.

same overlap ratios. However, with the normalization, there is a decrease in the values with the overlap ratio due to the increasing average gear mesh stiffness.

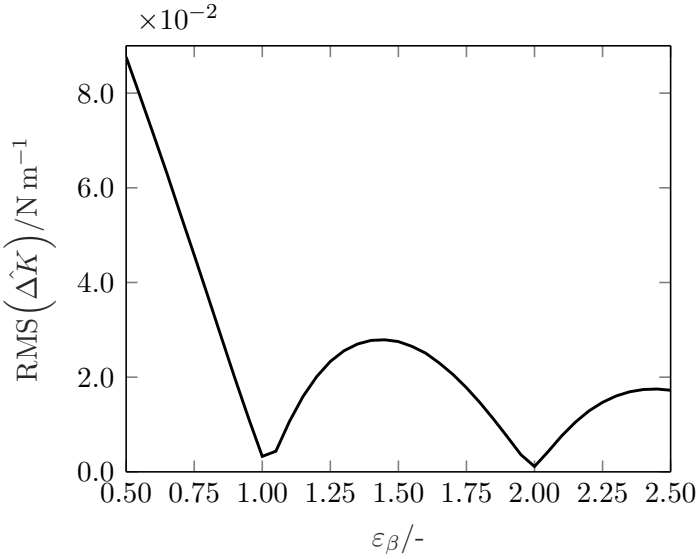

Figure 5.7: RMS of the normalized gear mesh stiffness fluctuation around its average.

5.4. Gear dynamics

The dynamic analysis of the gears is conducted considering the FZG test gearbox as a reference for the dimensions. Accordingly, a single stage gear-shaft-bearing transmission is modeled. Figure 5.8 shows a representation of the dynamic system being modeled, where the rotating speed is imposed on the input shaft and a torque is applied on the output shaft. The gear pair being tested connects the two shafts which are supported by two bearings elements each. The gears are modeled as rigid disks by their base radius which are connected by a time-varying mesh stiffness estimated by the approximate gear mesh stiffness model in [196]. Timoshenko beam elements are employed for the shafts and the bearing elements are introduced via lumped

stiffnesses. The damping matrix is determined using modal damping. Once the equations of motion are established, they are solved with the unconditionally stable Newmark integration algorithm ($\delta = 0.5$ and $\alpha = 0.25$); time discretization is the same as for the time-varying mesh stiffness, 50 points per period (50 slices per unit of overlap ratio). Steady-state conditions are considered to be reached after one complete turn of the pinion. More details on the formulation of the equations of motion and the algorithm implemented can be found in [196].

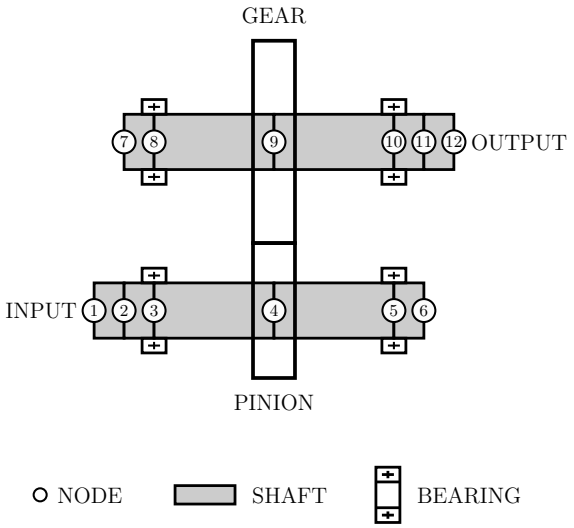

Figure 5.8: Schematic of the dynamic system.

The shafts of the system are defined in Table 5.7 where two different finite element lengths are used, one of 10 mm and other of 40 mm. Table 5.8 shows the bearing stiffness implemented on both shafts. A damping ratio of 0.10 is employed to determine the damping matrix. Gears are tested from 50 rpm up to 10000 rpm in steps of 50 rpm.

Table 5.7: Shaft data.

Shaft inputs	**Diameter** /mm	**Length** /mm	$\boldsymbol{E}$ /GPa	$\boldsymbol{\nu}$ /-	$\boldsymbol{\rho}$ /kg m^{-3}
Pinion's shaft	30	110	206	0.3	7830
Wheel's shaft	30	110	206	0.3	7830

Table 5.8: Bearing data.

Bearing inputs	**Pinion's shaft**	**Wheel's shaft**
Radial stiffness / N m^{-1}	1.40×10^8	2.50×10^8
Axial stiffness / N m^{-1}	3.50×10^7	6.00×10^7
Torsional stiffness (radial direction) / N m rad^{-1}	1.00×10^{12}	1.00×10^{12}

The evaluation of the dynamic response is based on the two parameters. The first one is the peak-to-peak amplitude of the dynamic transmission error (DTE), which is shown in Figure 5.9 for every simulated rotating speed. It can be noted that there is not a consistent decrease in the PPA(DTE) with the increase of the overlap ratio. The IOR gears have significantly lower peak-to-peak amplitudes for the speeds tested, even when compared with gears that have more than the double of the overlap ratio.

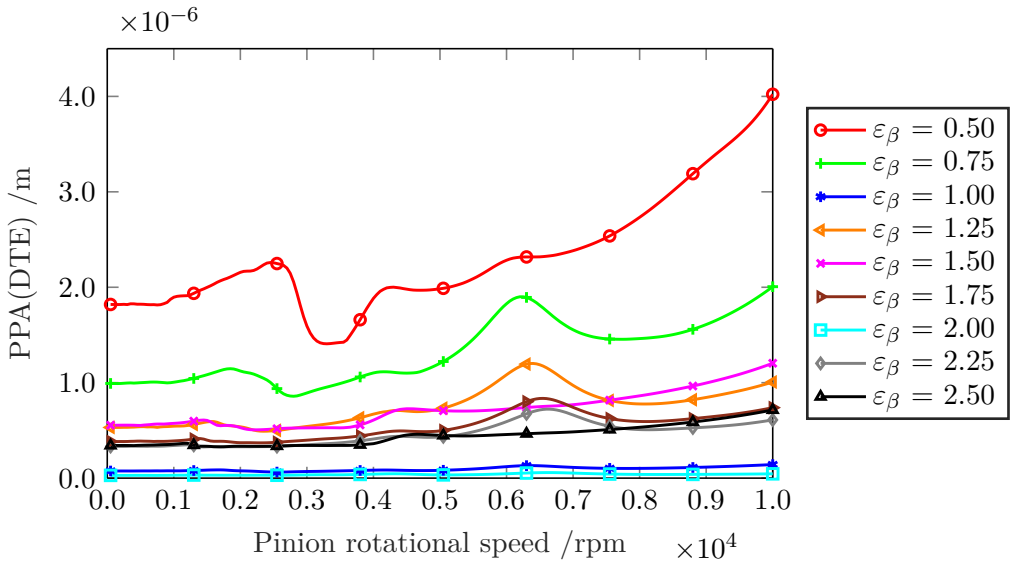

Figure 5.9: Peak-to-peak amplitude of the DTE.

The second parameter is $A_{RMS}(DTE_{osc})$ which is the equivalent root-mean-square (A_{RMS}) of the oscillating component of the DTE (DTE_{osc}). Looking at Figure 5.10, the location of the peaks for $A_{RMS}(DTE_{osc})$ changes between gears due to the variation in both mass and gear mesh stiffness introduced by varying the gears' facewidth. Nevertheless, the gears with $\varepsilon_\beta = 0.75$, 1.25, 1.75 and 2.25 show very similar shapes with deceasing magnitudes. On the other hand, the gears with $\varepsilon_\beta = 1.50$ and 2.50 do not present a peak at around 6200 rpm and pass below these curves. The integer overlap ratio gears are placed at the very bottom.

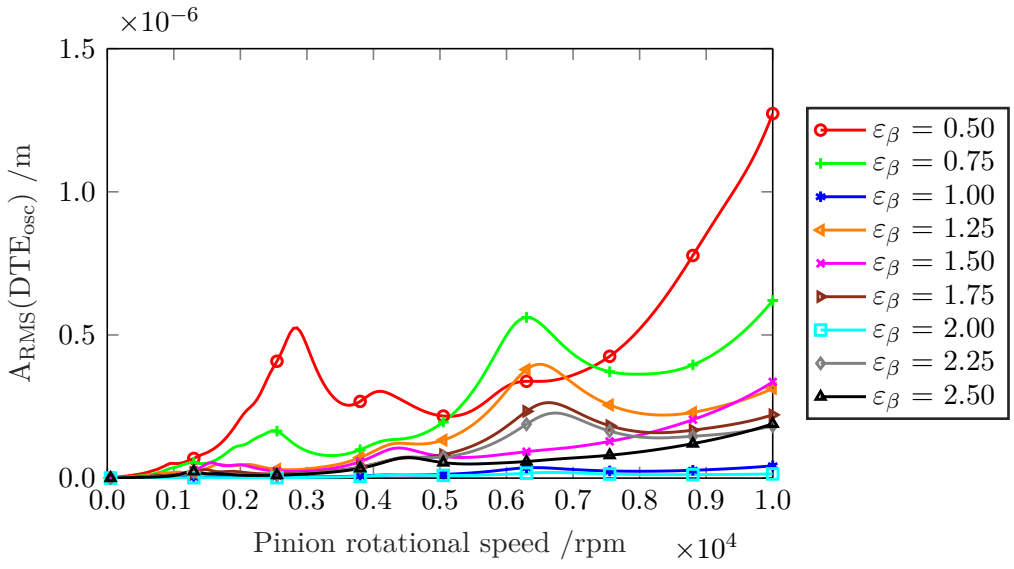

Figure 5.10: Variation of the first three harmonic amplitudes of DTE_{osc}.

Figures 5.9 and 5.10 are summed up for every gear by computing the average value for each curve, this way their variation with the overlap ratio can be shown, resulting in Figures 5.11 and 5.12, respectively. Just like the results presented for the gear mesh stiffness (Figures 5.5, 5.6 and 5.7), there is always a minimum for integer overlap ratios. On the other hand, the decreasing amplitude of stiffness parameter with the overlap ratio only occurs in Figure 5.7 for the normalized stiffness

parameter, whereas this trend is always verified in the dynamic parameters. Moreover, there is a reduction of the average A_{RMS} of the DTE oscillating component, Figure 5.10, for $\varepsilon_\beta = 1.5$ and 2.5. This occurs because in the speed range being tested, it is the second gear mesh stiffness frequency that is being excited. Since the amplitude of the second gear mesh stiffness frequency is significantly smaller for $\varepsilon_\beta = 1.5$ and 2.5 when compared to nearby overlap ratios, it exhibits this decrease.

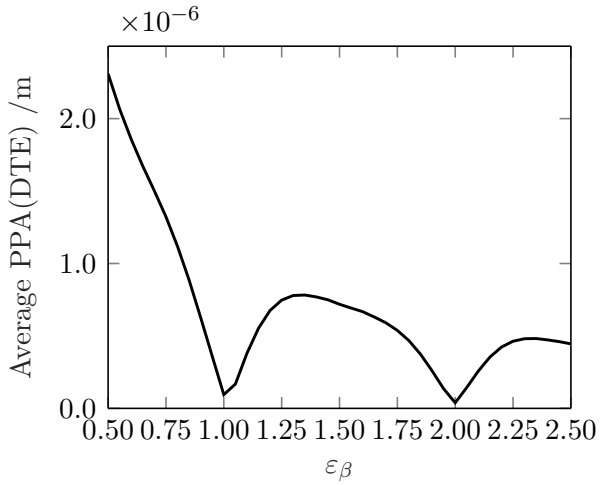

Figure 5.11: Average DTE peak-to-peak amplitude.

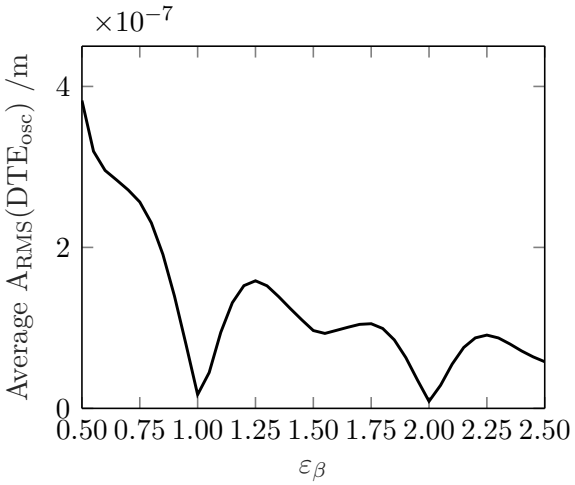

Figure 5.12: Average A_{RMS} of the DTE oscillating component.

5.5. Gear noise level

The noise level equation presented by Masuda et al. [197] is an improvement of a previous semi-empirical equation. Besides modifying the speed factor that was previously employed, a dynamic parameter is also introduced. Masuda et al. [197] found that for a wide variety of finishing methods and operating conditions, the noise level has a strong dependence with both transmitted power and vibration amplitude. According to Masuda et al. [197], the overall noise level at 1 meter from the gearbox (L^{1m} [dB(A)]) can be estimated according to equation (5.2).

$$L^{1m} = \frac{20(1-\tan(\beta/2))u^{1/8}}{{\varepsilon_\alpha}^{1/4}}\sqrt{\frac{5.56+\sqrt{v}}{5.56}} + 20\log(W) + 20\log\left(\tilde{X}\right) + 20 \tag{5.2}$$

Equation (5.2) is a semi-empirical expression that depends on six gear pair parameters: helix angle (β), gear ratio (u), contact ratio (ε_α), pitch line velocity (v [m s^{-1}]), transmitted power (W [kW]) and peak-to-peak amplitude of the DTE normalized by the transmission error ($\tilde{X}$). To determine the vibration amplitude, Masuda et al. [197] used a torsional vibration model where the stiffness of a tooth pair is approximated by a half-sine wave. For helical gears, only the increase in the total contact ratio due to the helix angle in taken into account - no other modifications are applied [197].

Figure 5.13 presents the different noise levels computed according to equation (5.2) for a set of rotating speeds. Notice that the only terms that are modified in equation (5.2) when evaluating the different gear geometries are the power transmitted and the normalized vibration amplitude ($\tilde{X}$). That being said, it is not clear enough that for a given speed there is a reduction of the noise level for $\varepsilon_\beta = 2.00$. However there is a decrease in the noise level when $\varepsilon_\beta = 1.00$, which

for some speeds it is the gear with lowest noise level.

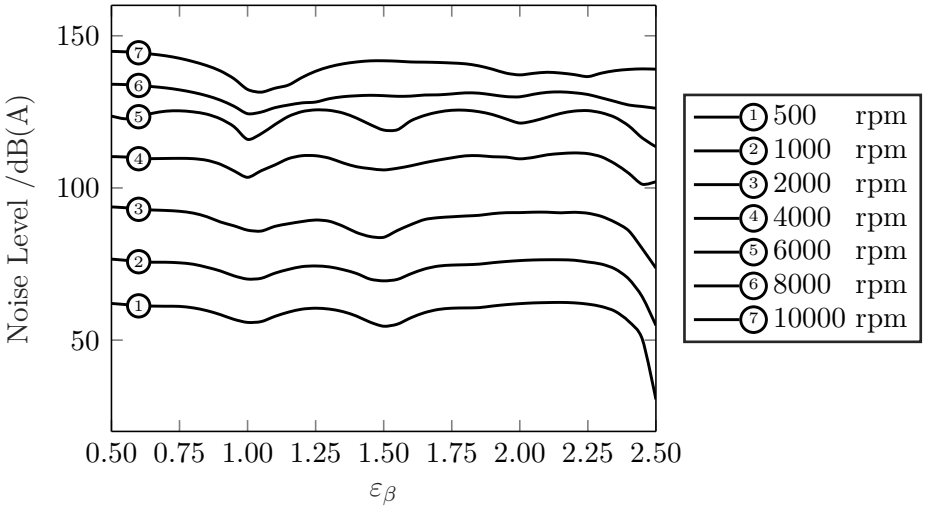

Figure 5.13: Overall noise level at different rotating speeds.

5.6. Closure

Three approaches to evaluate the influence of the overlap ratio on the gear behavior were taken. These are from the point of view of gear mesh stiffness, dynamic behavior and noise emission. To conduct this work, an integer overlap ratio was designed resorting to a previously developed gear design algorithm. Then, the gear facewidth is modified to achieve the desired overlap ratios for investigation. Considering the numerical simulations performed, it can be concluded that:

- Stiffness: increasing the overlap ratio does not necessarily lead to a reduction of the gear mesh stiffness peak-to-peak amplitude. Although, since it leads to an increase of the average gear mesh stiffness value, consequently, the fluctuations normalized by the average stiffness value are decreased. Nevertheless, it is for integer overlap ratios that gear mesh stiffness fluctuations are at their lowest regardless of the parameter used.
- Dynamics: the gears' dynamic behavior is investigated with a gear-shaft-bearing system. Results show that there is an overall decrease of the dynamic excitation with the increase of the overlap ratio. Though, minimums for dynamic fluctuations are found for integer overlap ratio gears.
- Noise: the overall noise level was evaluated for distinct overlap ratios at given rotating speeds. Considering the different torques applied at each gear, for the same rotating speed the gears with higher overlap ratio are transmitting more power. Nevertheless, an increase in the noise level with the overlap is not found as the normalized vibration amplitude tends to decrease with the overlap ratio. Minimums of noise levels are achieved for $\varepsilon_\beta = 1.00$, 1.50, 2.00 and 2.50 depending on the speed in study. However, there is a consistent decrease in the noise level for $\varepsilon_\beta = 1.00$.

Integer overlap ratios lead to a reduction of gear mesh stiffness fluctuations as well as reduced dynamic excitation. However, for noise emission, a clear connection between integer overlap ratios and overall noise levels was not found. Given the conclusions presented, the developed

IOR maps are a useful tool for a quick and easy starting point for the design of helical gears with low transmission error fluctuations and improved dynamic performance.

Next Another prime applicability of the gear analysis tool set developed is optimization of gear transmissions which can currently be performed at several levels, for instance, definition of gear macro- and/or micro-geometry, shaft dimensions, bearing stiffness. These variables can be defined with different objectives regarding gear mesh stiffness, gear transmission dynamic behavior or volume as well as gear meshing efficiency. The following and last chapter focuses on a investigation of gear design optimization approaches - different objective functions are put face-to-face for solving two distinct gear design optimization problems.

Chapter 6

Gear design optimization

Optimization is a flexible methodology for gear design since it allows for diverse approaches according to current demands. Thus, lightweight, efficient, small, quiet or robust gears can all be achieved according to the designers' needs. However, these problems can easily become a computational burden due to the large amount of calculations necessary. In this chapter, a macro-geometry gear design optimization problem solved by a genetic algorithm is investigated to find the best approach to reach minimum dynamic excitation, comparing as objective functions gear mesh stiffness and dynamic behavior. Given that gear dynamic evaluation can be significantly more computationally expensive than gear mesh stiffness evaluation, the goal is to discuss how optimizing a gear design towards minimum gear mesh stiffness fluctuations compares with optimizing for minimum dynamic excitation. Two gear optimization problems, one more restrictive than the other, are solved with the two objective functions. A genetic algorithm is implemented so that the evolution can be considered equivalent regardless the objective function. From the results obtained, a computationally efficient yet effective gear design optimization approach is proposed.

6.1. Background

The application of optimization to engineering design results in a structured approach, sustained by mathematical principles, to find designs of engineering systems with superior performance by optimizing a design objective subject to a set of design constraints that define the search domain. When considering gear design, optimization gives the freedom to reach any type of required design while also taking into account the system it is inserted in. This means that one can consider any type of design variable, for instance, number of teeth, module, profile shift coefficients, facewidth, profile modification parameters, amount of backlash and also variables related to the shafts, bearings and gearbox. Following the same thought, the objective function and restrictions of the optimization can be the manufacturing costs, volume, efficiency, emitted noise, robustness, vibration and/or stiffness. One way of dividing gear design optimization is according to the type of gear geometrical parameters used as design variables, them being, (i) macro-geometry and (ii) micro-geometry gear design optimization. According to the data presented in [23], macro-geometry gear optimization is more directed towards mass, volume

Contents in Chapter 6: Gear design optimization are reproduced with permission of the respective publisher from João D.M. Marafona, Gonçalo N. Carneiro, Pedro M.T. Marques, Ramiro C. Martins, Carlos C. António, and Jorge H.O. Seabra. Gear design optimization: stiffness *versus* dynamics. *Mechanism and Machine Theory*, 191:105503, 2024.

and meshing efficiency while micro-geometry gear optimization is more for transmission error fluctuations or emitted noise which can be related to dynamic behavior.

Regarding gear macro-geometry design optimization, Yokota et al. [198] solved the optimal spur gear weight problem using a genetic algorithm. The problem variables are the facewidth, pinion/wheel diameters, number of teeth of the pinion and module. Five constraints were applied, namely regarding the bending strength, surface durability, torsional strength of both shafts and center distance. The adopted approach led to a reduction of 48.8% in the weight as well as a 33.6% decrease in the gear pair average surface area [198]. Savsani et al. [199] compared the solutions of spur gear pair weight optimization problem by a genetic algorithm, particle swarm optimization and simulated annealing. Two different cases were evaluated (based on the formulation by Yokota et al. [198]) where the design vector consists mainly on gear macro-geometry and constraints on gear bending strength, gear surface durability, torsional strength of the shafts and center distance. All the algorithms in study are applicable for spur gear weight optimization problems but depending on the design variables and constraints included particle swarm optimization and simulated annealing can present better solutions [199]. Miler et al. [200] studied the influence of including the profile shift coefficients as variables for the gear pair volume optimization process. Two identical optimizations were performed where in one of them the profile shift coefficients were set to zero ($x_1 = x_2 = 0$) and the other where the profile shift coefficients were used as design variables. In both optimization problems, there were constraints regarding the gear tooth root stress as well as surface durability. Results indicate that profile shift coefficients should be considered as design variables when the goal is to minimize the gear pair volume since it lead to gear pair volumes more than 30% lower when compared to not using the profile shift coefficients for optimization [200]. In another work, Miler et al. [201] performed multi-objective optimization of a gear pair to reduce its volume and power loss. An analytical description of the power loss is implemented to decrease computational cost. The variables are the number of teeth of the pinion, facewidth, module and both profile shift coefficients. The problem is constrained so that tooth root strength and surface durability conditions are fulfilled along with the continuity of action ($\varepsilon_\alpha \geq 1.2$). The Pareto optimal solutions for different sets of data (nominal working conditions and gear material) are analyzed. Correlation between the design variables and the two objectives are discussed. Given the results, it is recommended, as a general guideline, to select a low facewidth, high number of teeth of the pinion and positive profile shift coefficients to achieve a good spur gear design in terms of volume and efficiency [201]. Salomon et al. [202] employed active robust optimization method to define the number of gear stages as well as their ratios to minimize production cost and energy consumption. This optimization procedure proved to be effective since a set of robust solutions were found given the uncertainty of the demanded load [202].

Moving to researches that consider gear micro-geometry for design variables, Younes et al. [203] studied the optimization of a gear unit in terms of power loss and gear meshing excitation resorting to both macro and micro gear geometrical parameters. For that purpose, two multi-objective problems were implemented, where both include the root-mean-square of the transmission error variation. However, while one only considers the gear meshing power loss, the other takes into account power losses of the entire transmission via a thermal network. The problem is constrained by ensuring a minimum contact ratio and guaranteeing tooth root bending and contact integrity. Different combinations of variables, including macro-geometry (pressure angle and helix angle) and/or micro-geometry (tip relief) were studied. Using the micro-geometry for the optimization variables remarkably enhanced the gear unit efficiency [203]. Bonori et al. [21] used a genetic algorithm to optimize the tip and root reliefs of spur gears. Two objective functions based on the static transmission error are employed: the peak-to-peak of static transmission error

and the average value of the static transmission error harmonics. 2D plain strain nonlinear finite element analysis are conducted to determine the static transmission error for the objective function. Even though a static objective function was employed, the optimization was effective in reducing the gears vibrations. A reliability analysis considering manufacturing errors is done, revealing that the GA was capable of finding robust results [21]. Velex et al. [204] minimize the dynamic mesh forces on multi-mesh systems by minimizing the transmission errors as a direct mathematical correlation between the two parameters was shown. A genetic algorithm is used to find the optimum symmetric tip relief (depth and length of modification). Two distinct multi-mesh systems are optimized; results corroborate the proposed methodology for minimization the dynamic mesh forces. In addition, the profile modifications obtained by the optimization agreed with the ones from the analytical master curves [205] derived to minimize the transmission error variations [204]. With the goal of improving the quasi-static behavior of a geared transmission, Lagresle et al. [206] optimized the micro-geometry of the gears by a modified particle swarm optimization algorithm. Multi- and single-objective functions are evaluated which can include the maximum contact pressure on the gear flanks, the variation of the loaded transmission error signal, the tooth bending stress and a pressure-speed factor. The optimization procedure showed tendency to apply long tip reliefs for the minimization of the transmission error fluctuations with symmetrical linear tip reliefs as well as for the optimization of contact pressures. Applying a robustness procedure for different misalignment conditions proved to be effective; there was a significant reduction on the average value of objective function under various misalignment circumstances when compared to the non-modified version [206]. Lei et al. [207] used a particle swarm optimization algorithm in order to optimize the micro-geometry of gears of an electric bus gearbox for reduced vibration and noise. According to the conducted studied, a weighted multi-objective function considering peak-to-peak value of the transmission error, amplitude of the transmission error harmonics as well as the maximum tooth surface load is found to be a better approach for reducing vibration and noise than single-objective function considering the peak-to-peak value of the transmission error. This is because by reducing the transmission error harmonics' amplitude, the excitation of the remaining system is prone to be reduced. The optimized gear pair was tested in the noise bench showing the effectiveness of the optimization procedure in reducing the noise levels [207]. Bozca and Fietkau [208] optimized a gearbox considering an empirical average rattle noise level expression for the objective function. Constraints for bending stress, contact stress and constant center distance were included. The optimization variables are the module, number of teeth, axial clearance and backlash. The optimized gearbox showed a reduction of 14% in the rattle noise when compared to the sample gearbox. In addition, it was found that increasing the module and number of teeth lead to increased rattle noise [208].

For more details on optimization of cylindrical gear pairs, a comprehensive review is performed by Miler and Hoić [23], analyzing the selection of design variables, objective functions and constraints of several optimization works in the literature while also providing gear design optimization guidelines.

Optimization is a process that requires multiple evaluations of the objective function. The gear design problem in hands is finding the gear macro-geometry that reduces gear dynamic excitation. Micro-geometry, such as tip/root relief, is not included in this work even though the implemented models can account for them because it requires a separate study to evaluate the different possible approaches: should it be a simultaneous, sequential or multi-level optimization. Nevertheless, this does not change the fact that computing the steady-state dynamic response for an entire speed range has a high computational cost and therefore, other alternatives must be considered. The minimization of the gear mesh stiffness fluctuation is a possible approach since

the gear mesh stiffness can be the main excitation of a gear system and there are fast and reliable models for its estimation. So, in this chapter, two optimization problems are solved, with an implemented genetic algorithm, for two objective functions each, one for minimizing gear mesh stiffness fluctuations and other for minimizing gear vibration over a speed range. Among the constraints included are minimum requirements for safety factors and gear meshing efficiency. It is due to these constraints that the two optimization problems differ: one is less restricted than the other since it does not include an efficiency restriction and requires less demanding nominal working conditions, hence has a bigger search domain. The goal is to compare the evolution as well as understand the connections, through an optimization point of view, between the stiffness and dynamic objective functions in order to reach a feasible and effective gear design criteria for minimum dynamic excitation.

To start, the gear design optimization problem is explained which includes the description of the single-stage transmission system being considered, definition of the optimization problem statement (design variables, constraints and penalty problem), explanation of the models employed for the determination of the objective functions as well as the characterization of the implemented genetic algorithm. Then, for each optimization problems, namely relaxed (less restricted/bigger search domain) and full problems, the optimum solutions are analyzed in terms of geometry, gear mesh stiffness and dynamic behavior; the evolution of the stiffness and dynamic fitness value of the best individual for each objective function and the individuals with the highest fitness values from each optimization approach are related in terms of stiffness, dynamic behavior and noise level. Lastly, there is an overall discussion of the presented results with highlight to the main conclusions and a proposal of a gear design optimization methodology for minimization of the dynamic excitation.

6.2. Gear design optimization problem

The proposed optimization problem consists in finding gear designs for a single-stage transmission system based on the FZG test gearbox, schematically shown in Figure 6.1. The system comprises a gear transmission, two shafts (connected through the gear pair) and four bearing elements, two supporting each shaft. A rotating speed is imposed on the input shaft and a resisting torque on the output torque.

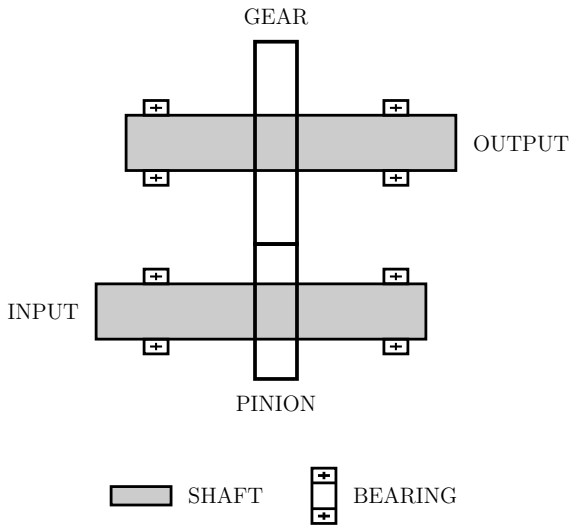

Figure 6.1: Schematic of the single-stage transmission system.

In more detail, the system has two 30 mm diameter shafts with 110 mm length. The bearing to bearing distance is 80 mm and the shafts' short end measured from the bearing element is 10 mm. Gears are centered in between the bearing elements and have ISO 53 [169] Profile A tooth proportions ($\alpha = 20°$, $h^*_{\mathrm{aP}} = 1$, $h^*_{\mathrm{fP}} = 1.25$ and $\rho^*_{\mathrm{fP}} = 0.38$). The center distance ($a$) is fixed at 91.5 mm and the gear ratio (u) is 1.5. The material of the gears and shafts has the following properties: $\rho = 7830\ \mathrm{kg\,m^{-3}}$; $E = 206$ GPa and $\nu = 0.3$. Table 6.1 specifies other desired and imposed details of the single-stage gear system.

Table 6.1: Parameters from the single-stage gear system.

Parameters	**Value**
$\boldsymbol{a}$/mm	91.5
$\boldsymbol{u}$/-	1.5
Gears' material/-	16MnCr5 (Class Eh)
$\boldsymbol{R}_{\mathrm{z}}$/µm	4.8
$\boldsymbol{K}_{\mathrm{A}}$/-	1.25
Accuracy grade/-	6
Lubricant/-	ISO-VG 150 (oil bath)
Required service life/hours	20000

Next, the gear design optimization problem is formulated in view of the implemented genetic algorithm. The numerical tools for the computation of the objective functions in study, namely, the gear mesh stiffness and gear-shaft-bearing dynamic models, are briefly explained as a comprehensive presentation of both models can be found in [196]. Lastly, the genetic algorithm is explained.

6.2.1. Problem statement

This section is dedicated to the formulation of the gear design optimization problem. It starts by establishing the **design variables**, which are the gear macro-geometry parameters:

$$\boldsymbol{X} = \{z_1, m_{\mathrm{n}}, b, x_1, \beta\} \in S \text{ with } S = \left\{ \boldsymbol{X} : \sum_{j=1}^{4} h_j(\boldsymbol{X}) = 4 \right\}$$

where z_1 is an integer variable representing the number of teeth of the pinion; m_{n} is a real-valued discrete variable with normalized values from DIN 780; b, x_1 and β are continuous variables, respectively depicting the facewidth, profile shift coefficient of the pinion and helix angle. The functions $h_j(\boldsymbol{X})$ are introduced to guarantee that the gears can be evaluated in the gear mesh stiffness model [196]. These functions have as an output value of 1 when the gear can be evaluated and 0 when it does not respect any of the required conditions. The functions $h_j(\boldsymbol{X})$ are:

$h_1(\boldsymbol{X})$: feasible domain considering the limitations from the fillet-foundation stiffness model [79] and single tooth pair slice mesh stiffness model [171], namely, (i) the root radius of both gear bodies need to be comprised between $30 \leq r_{\mathrm{pi}} \leq 75$ [79]; (ii) z_1 cannot be equal to 36 [79] and (iii) profile shift coefficient of the wheel is between $-1 \leq x_2 \leq 1$ [171];

$h_2(\boldsymbol{X})$: exclude gears with cutter interference [170];

$h_3(\boldsymbol{X})$: mating interference is not permitted [170];

$h_4(\boldsymbol{X})$: limitation on the minimum tooth crest width, $s^*_{\text{ai}} \geq 0.4$ [170].

The lower and upper bounds for the design variables are restricted given the limitations of the models used for computing the objective function as well as characteristics of the system being optimized:

$36 \leq z_1 \leq 50$: these bounds are established by the limitation on the tooth root half-angle ($0.04 \leq \theta_p \leq 0.08$) from the fillet-foundation stiffness model [79] used within the gear mesh stiffness model which limits the number of teeth between [37; 75]. Combining this with the imposition on the gear ratio ($u = 1.5$), results that the upper limit is $z_1 \leq 50$ as it will result in $z_2 > 75$. Even though $z_1 = 36$ is used as a lower bound, this value is not admissible since it is out of the domain S;

$0.7 \leq m_{\text{n}} \leq 4$: other limitation of the fillet-foundation stiffness model [79] is on the ratio between the tooth root radius and hub radius ($2 \leq h \leq 5$). Considering the bounds for all the other variables involved in this coefficient, the lowest and highest admissible values for the module are achieved;

$2.1 \leq b \leq 40$: minimum facewidth value is determined as three times the lowest module value. The maximum facewidth value is set at 40 mm since this value is the maximum allowable in the system being studied and it is lower than maximum permissible facewidth to module ratio ($b_{\max} = 14\ m_{\text{n}}$);

$-1 \leq x_1 \leq 1$: the profile shift coefficients are contained in this interval due to the single tooth pair slice mesh stiffness approximate expression [171];

$0 \leq \beta \leq 30$: an upper limit of $\beta = 30°$ is selected to keep the compatibility between the different methods in DIN 3990 and the ISO 6336.

The proposed gear design problem has the **primal problem** established as:

$$\min\ f(\boldsymbol{X})$$

$$\text{subjected to } g_j(\boldsymbol{X}) \leq 0,\ j = 1, 2, \ldots, 11$$

$f(\boldsymbol{X})$ represents the objective function of the design problem and the functions g_j represent the constraints of the optimization problem. There are several sets of constraints, namely, functions g_1 to g_6 are geometrical restrictions for the design space:

$g_1(\boldsymbol{X}) = 1 - \varepsilon/1.2$: minimum contact ratio $\varepsilon \geq 1.2$

$g_2(\boldsymbol{X}) = \varepsilon/4 - 1$: maximum total contact ratio $\varepsilon \leq 4$;

$g_3(\boldsymbol{X}) = 1 - \varepsilon_\alpha/0.9$: minimum contact ratio $\varepsilon_\alpha \geq 0.9$;

$g_4(\boldsymbol{X}) = \varepsilon_\alpha/3 - 1$: maximum contact ratio $\varepsilon_\alpha \leq 3$;

$g_5(\boldsymbol{X}) = 1 - b/(3\ m_{\text{n}})$: minimum facewidth to module ratio $b \geq 3\ m_{\text{n}}$;

$g_6(\boldsymbol{X}) = b/(14\ m_{\text{n}}) - 1$: maximum facewidth to module ratio $b \leq 14\ m_{\text{n}}$;

There are also functions to ensure the minimum surface durability and tooth root bending resistance. These are established resorting to the DIN 3990:

$g_7(\boldsymbol{X}) = 1 - \mathrm{S_{H1}}$: minimum surface durability safety factor for the pinion $\mathrm{S_{H1}} \geq 1$;

$g_8(\boldsymbol{X}) = 1 - \mathrm{S_{H2}}$: minimum surface durability safety factor for the wheel $\mathrm{S_{H2}} \geq 1$;

$g_9(\boldsymbol{X}) = 1 - \mathrm{S_{F1}}/1.4$: minimum tooth root stress safety factor for the pinion $\mathrm{S_{F1}} \geq 1.4$;

$g_{10}(\boldsymbol{X}) = 1 - \mathrm{S_{F2}}/1.4$: minimum tooth root stress safety factor for the wheel $\mathrm{S_{F2}} \geq 1.4$;

In order to guarantee a minimum gear meshing efficiency, function $g_{11}(\boldsymbol{X})$ is introduced to limit the gear loss factor $\mathrm{H_V}$. The gear loss factor is computed as in [142] with a constant gear mesh coefficient of friction equal to $\mu = 0.05$.

$g_{11}(\boldsymbol{X}) = \mathrm{H_V}/0.15 - 1$: maximum gear mesh loss factor $\mathrm{H_V} \leq 0.15$.

The conversion of the optimization problem into a **penalty problem** to maximize the fitness is, considering the established primal problem, presented as:

$$\max\ fit(\boldsymbol{X}) = \begin{cases} C_\mathrm{p} - \left(\lambda_\mathrm{f} f(\boldsymbol{X}) + \lambda_\mathrm{p} \sum_{j=1}^{11} \max\left(g_j(\boldsymbol{X}), 0\right)^2 \right), & \boldsymbol{X} \in S \\ C_\mathrm{p} - 0.99 \times 10^{12}, & \boldsymbol{X} \notin S \end{cases}$$

where C_p, λ_f and λ_p are constants. C_p is employed to guarantee positive fitness values, λ_f is a proportionality factor and λ_p is the penalty parameter.

6.2.2. Gear mesh stiffness

The gear mesh stiffness model developed by Marafona et al. [196] is implemented to optimize the gear pair with regard to its mesh stiffness fluctuations. It is an approximate gear mesh stiffness model, meaning it resorts to straightforward and effortless expressions that are simplifications of high computational cost numerical procedures. Therefore, this model presents very low computational cost making it the ideal choice for optimization processes where it is necessary to run the models multiple times.

To estimate the gear mesh stiffness of both spur and helical gears, the model [196] applies the slicing method, where helical gears are interpreted as being a combination of staggered spur gears. Each slice has its stiffness determined by combining the expression for the single tooth pair slice mesh stiffness from [171] with the a parabolic contact line stiffness distribution that couples the slices. Phenomena like the extension of contact, in which contact occurs outside the path of contact due to the deflections of the gear mesh; border weakening factor, reduction of the stiffness in helical teeth due to the lack of a full supporting teeth in the normal direction; and profile modifications, changes in the gear tooth profile (micro-geometry) that are applied to obtain improved gear behavior, can all be accounted for in the model.

The gear mesh stiffness (K) for a given design variable is computed with 100 points per mesh period and a number of slices equal to 100 per unit of overlap ratio. The objective function for the gear mesh stiffness optimization is the root-mean-square of the gear mesh stiffness fluctuation

around its average value, given by equation (6.1), where T_{mesh} is the mesh period and K_{avg} is the average gear mesh stiffness.

$$f(\boldsymbol{X}) = \text{RMS}_K = \sqrt{\frac{1}{T_{\text{mesh}}} \int_0^{T_{\text{mesh}}} (K - K_{\text{avg}})^2 \; dt} \tag{6.1}$$

6.2.3. Gear dynamics

A single-stage gear-shaft-bearing dynamic model [196] is used to optimize the single-stage geared transmission towards improved dynamic behavior. A representation of the dynamic model is shown in Figure 6.2. Main characteristics of the dynamic model are:

- The gear pair is introduced as two rigid disks by their base radius with a time-varying stiffness representing their meshing. The shafts are included by Timoshenko beam elements [186; 187] with two different length of elements, 10 mm and 40 mm. In Figure 6.2, the numbered dots refer to the nodes of the Timoshenko beam elements. Lumped stiffnesses are employed for the representation of the bearing elements, see Table 6.2.

Table 6.2: Bearing data.

Bearing inputs	**Pinion's shaft**	**Wheel's shaft**
Radial stiffness / N m^{-1}	1.40×10^8	2.50×10^8
Axial stiffness / N m^{-1}	3.50×10^7	6.00×10^7
Torsional stiffness (radial direction) / N m rad^{-1}	1.00×10^{12}	1.00×10^{12}

- The equations of motion are obtained by first considering a 12 degree-of-freedom subsystem for the gear pair which is then incorporated with the other elements of the system in the global mass and stiffness matrices. The damping matrix is determined using modal damping and a damping ratio of $\zeta = 0.1$, in accordance with [178].

- The unconditionally stable Newmark integration algorithm, with corresponding constants $\delta = 0.5$ and $\alpha = 0.25$, is utilized to solve the equations of motion;

- time discretization and stiffness discretization are the same for the dynamic model, which is 50 points per period (50 slices per unit of overlap ratio). The dynamic response is regarded of being in steady-state conditions after one complete turn of the pinion. The system is tested from input speeds starting at 50 rpm (n_{start}) up to 4500 rpm (n_{end}) in steps of 50 rpm.

A full presentation of this dynamic model covering the formulation of the equations of motion as well as details about the algorithm implemented is found in [196].

For the objective function of the dynamic optimization, the average value the $A_{\text{RMS}}(\text{DTE}_{\text{osc}})$ for the analyzed speed range is considered, equation (6.2).

$$f(\boldsymbol{X}) = \text{RMS}_D = \frac{1}{n_{\text{end}} - n_{\text{start}}} \int_{n_{\text{start}}}^{n_{\text{end}}} A_{\text{RMS}}(\text{DTE}_{\text{osc}}) \; dn \tag{6.2}$$

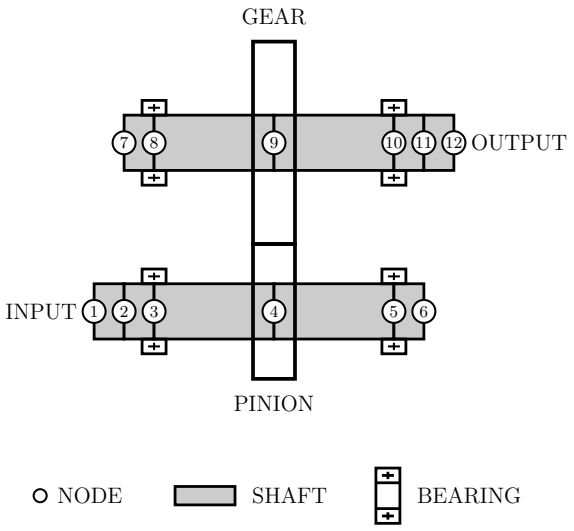

Figure 6.2: Schematic of the dynamic system.

where $A_{\mathrm{RMS}}(\mathrm{DTE_{osc}})$ is an equivalent root-mean-square of the DTE oscillating component, defined according to equation (6.3). $A_i(\mathrm{DTE_{osc}})$ is the ith harmonic amplitude of the Fast Fourier Transform of $\mathrm{DTE_{osc}}$.

$$A_{\mathrm{RMS}}(\mathrm{DTE_{osc}}) = \sqrt{A_1^2(\mathrm{DTE_{osc}}) + A_2^2(\mathrm{DTE_{osc}}) + A_3^2(\mathrm{DTE_{osc}})} \tag{6.3}$$

6.2.4. Genetic algorithm

The applied genetic algorithm has a more complex algorithmic structure than the simple genetic algorithm. It is designed so that its operators aim to achieve a good balance between exploration and exploitation. Therefore an explanation of the algorithm itself and the genetic operators used is performed. Figure 6.3, presented at the end of this section, shows the pseudo-code of the genetic algorithm.

Let $\mathbb{B}^l$ be the set of binary strings of length l. An element $s \in \mathbb{B}^l$ is called a genotype and is the binary representation of a solution in the search space, decoded via the usual binary-to-real transformation. A population $\boldsymbol{P}^t$, at generation t, is a list $(s_1, \ldots, s_{n_{\boldsymbol{P}}})$ of size $n_{\boldsymbol{P}}$, ordered in terms of fitness and allowing repetition. A list $\boldsymbol{E}^t \in \boldsymbol{P}^t$, containing the genotypes with the highest fitness, defines the elite of the population, and $\boldsymbol{B}^t$ defines the list of all offspring genotypes, generated by the crossover operator.

A set of diverse evolutionary operators is introduced, combining high selective pressure (supported by a strong elitist strategy) with highly disruptive operators. The benefits of such a polarized approach are discussed by Eshelman [209]. The set of chosen operators is based on the algorithm presented in [210], with necessary adaptations to suit the current problem.

Random initialization

The initialization process is applied at different stages of the evolution: each genotype $s \in \boldsymbol{P}^t$ is initialized uniformly at random. In the first generation, the entire population is initialized. At later stages, only selected genotypes are reinitialized.

"Elitist" parent selection

The parent selection mechanism begins by sorting $\boldsymbol{P}^t$, according to the fitness of its elements. The mechanism is responsible for the stochastic selection of $n_{\boldsymbol{B}}$ parent-lists that compose the mating pool, at each generation. Each parent-list contains two individuals chosen at random by two independent fitness-proportional selection processes: one parent selected from the elite group $\boldsymbol{E}^t$ and another from the remaining population $\boldsymbol{P}^t \setminus \{\boldsymbol{E}^t\}$.

Such a bipartite selection procedure implies that, for each pair of parents, one parent belongs necessarily to the elite group, hence being deemed as "elitist". With it, it is expected to achieve two simultaneous goals: first, an increased selective pressure (bias) towards the best fitted individuals of the population; second, an increased reproduction probability of the weakest individuals of the population.

Uniform crossover

For each parent-list, one (and only one) offspring solution is constructed and stored in the offspring population $\boldsymbol{B}^t$, hence generating a total of $n_{\boldsymbol{B}}$ solutions. The uniform crossover operator consists of selecting at random from which parent each gene comes from. The process is biased by the parameter r_{uc}, representing the probability of selecting genes from the elite parent.

In the presence of (strong) elitism, it is desirable to have an operator capable of generating productive genetic recombination, avoiding stagnation of the search process, due to the excessive preservation of genetic features. The interesting property of uniform crossover is that a genetic feature is not heritable unless it is common to both parents. As such, uniform crossover is a highly disruptive recombination operator with the ability to create new linkages among the genes of the offspring solutions, induced by the conflicting genes of the respective parents. Indeed, the greater the genetic difference between two parents the more explorative uniform crossover becomes.

Elitist survivors selection

After genetic recombination, the entire population is extended to a list $\boldsymbol{P}^t \cup \boldsymbol{B}^t$. The survivor selection mechanism is responsible for the composition of the population of the next generation. The overall selection process is performed by three elitist operators.

Similarity control In later generations, the fittest genotypes often recombine with near relatives and the explorative ability of uniform crossover degenerates. Two genotypes s_1, $s_2 \in \mathbb{B}^l$ have an equal variable if $s(X_i)_1 = s(X_i)_2$, for $i = 1, \ldots, N$. Two genotypes are similar if the number of equal variables is larger than some $\epsilon_{\text{SC}} \leq N$. The similarity control operator is introduced as an elitist and highly disruptive replacement mechanism. Similarity is evaluated variable-by-variable. After fitness-based ranking of $\boldsymbol{P}^t \cup \boldsymbol{B}^t$, each genotype is compared against all the weaker ones, one at a time. For each pair of similar genotypes, the one with smaller fitness value is removed from the population. After the comparison process, the size of $\boldsymbol{P}^t \cup \boldsymbol{B}^t$ is recovered with the random initialization of new genotypes.

Replacement mechanism In order to achieve a monotone evolution, it is adopted an elitist $(n_{\boldsymbol{P}} + n_{\boldsymbol{B}})$ replacement mechanism, where the newly created offspring and the existent population

members compete for survival: the extended population $\boldsymbol{P}^t \cup \boldsymbol{B}^t$ is ranked by fitness, after which only the top $n_{\boldsymbol{P}}$ genotypes are selected to survive. Unlike the elitist parent selection, characterized by two independent moments of stochastic selection, the adopted elitist replacement scheme imposes a deterministic selection rule, steered by fitness. This replacement scheme is robust against the quality loss in the solutions generated by the recombination operator, in the sense that both top and average genotypes are allowed to survive longer, if not outperformed by the offspring.

Implicit mutation The combination of uniform crossover and similarity control may have a positive effect delaying premature convergence. But these mechanisms cannot guarantee desirable levels of genetic diversity throughout the entire evolution. As the number of generations increases, it is expected that the algorithm manages to preserve in the population only those genotypes that are as similar as possible. In such case, the similarity control operator loses importance as it is no longer called to inject raw diversity. After restoring the original size of the population, the $n_{\text{bot}} < n_{\boldsymbol{P}}$ genotypes with smaller fitness value are eliminated from the population and initialized at random. Contrary to the similarity control operator, the main goal of implicit mutation is to inject raw diversity into the population, affecting the evolution in the long-term. Indeed, its combination with the elitist parent selection of the next generation promotes the recombination between the elite and the newly generated individuals, in future generations.

repeat

for $\boldsymbol{P}^t$ **do**
  Fitness-based ranking
  Elitist parent selection of $n_{\boldsymbol{B}}$ parent-lists
    one parent from $\boldsymbol{E}^t$ *and another from* $\boldsymbol{P}^t \setminus \{\boldsymbol{E}^t\}$
  Uniform crossover
    generate $n_{\boldsymbol{B}}$ *offspring solutions, one per parent-list*
  Allocate offspring solutions into $\boldsymbol{B}^t$
end do

for $\boldsymbol{P}^t \cup \boldsymbol{B}^t$ **do**
  Fitness-based ranking
  Similarity control
    for each pair of similar individuals, replace the worst with a random one
  Fitness-based ranking
  $(n_{\boldsymbol{P}} + n_{\boldsymbol{B}})$ replacement mechanism
    eliminate the worst $n_{\boldsymbol{B}}$ *individuals*
end do

for $\boldsymbol{P}^t$ **do**
  Implicit mutation
    replace the worst n_{bot} *individuals with* n_{bot} *random individuals*
end do

Set $t = t + 1$

until *stopping criterion*

Figure 6.3: Pseudo-code of the genetic algorithm.

Genetic algorithm parameters

Table 6.3 defines the parameters used for the gear design optimization for both optimization functions, stiffness and dynamics, which were established with a preliminary study of the optimization problem.

A stopping criterion of $t = 10000$ generations is used for convergence of the population in order to correlate the optimization results from the stiffness and dynamic objective functions. With the same purpose, a constant λ_{f} was introduced so that the evolution can be as similar as possible even with different objective function values.

Table 6.3: Genetic algorithm parameters.

Parameters	**Value**
$n_{\boldsymbol{P}}$, population size	50
$n_{\boldsymbol{E}}$, elite size (elite ratio)	17 (0.33)
$n_{\boldsymbol{B}}$, number of offsprings (cross rate)	16 (0.65)
r_{uc}, bias ratio	0.60
ϵ_{SC}, similarity control	2
n_{bot}, implicit mutation ratio	0.10
C_{p}	1×10^{12}
λ_{p}	5×10^{9}
λ_{f}, stiffness / dynamics	1 / 1×10^{12}
stopping criterion	$t = 10000$

Concerning the design variables, z_1 and m_{n}, the respective genes encode integer values representing the index/position in the set of possible values, as in equations (6.4) and (6.5). For the number of teeth, only even integer numbers are included due to the gear ratio that is imposed in the system. Both sets were adapted so that the number of possible values satisfies 2^q, where q is a predetermined number of bits. That being said, z_1 is coded with 3 bits, m_{n} with 4 and b, x_1 as well as β are encoded with 7 bits.

$$z_1 = \{36, 38, 40, 42, 44, 46, 48, 50\} \tag{6.4}$$

$$m_{\mathrm{n}} = \{0.7, 0.8, 0.9, 1, 1.125, 1.25, 1.375, 1.5, 1.75, 2, 2.25, 2.5, 2.753, 3.5, 4\} \tag{6.5}$$

6.3. Gear optimization: relaxed problem

The first gear optimization study is a less restricted problem in terms of both applied constraints and required nominal working conditions which allows for a broader design domain. In the relaxed problem there is not the gear meshing efficiency restriction ($g_{11}(\boldsymbol{X})$) and the nominal conditions are displayed in Table 6.4.

After performing the optimization for both the gear mesh stiffness (identified as RMS_K) and gear dynamics (labeled as RMS_D) objective functions, the obtained optimum design variables for each process is shown in Table 6.5 with the corresponding values for the objective functions. The number of teeth and module is the same for both functions (strong indicator of similarity between the two optimization approaches) with the remaining geometrical parameters begin

Table 6.4: Nominal working conditions for the relaxed problem.

Parameters	**Value**
$\boldsymbol{n_1}$/rpm	1000
$\boldsymbol{T_1}$/N m	100

very close to each other. Despite that, there are some differences in the values of the objective functions in relative terms. However, it must be stressed out that these objective function values are very low, meaning that they are both excellent gears in what regards gear mesh stiffness fluctuation and dynamic behavior, as it is exhibited in Figure 6.4 by their gear mesh stiffness and A_{RMS} curves.

Table 6.5: Design variables of the optimum individuals: relaxed problem.

$f(\boldsymbol{X})$	z_1/-	m_n/mm	b/mm	x_1/-	β/°	RMS_K/N m^{-1}	RMS_D/m
RMS_K	46	1.50	13.7386	-0.4646	21.0236	9.4720×10^4	1.9191×10^{-9}
RMS_D	46	1.50	14.0370	-0.4616	20.5512	1.2171×10^5	1.1298×10^{-9}

Figure 6.4, which displays the gear mesh stiffness (Figure 6.4a) and A_{RMS} (Figure 6.4b) for the optimum solutions, highlights their affinity. The limits for the y-axis in Figure 6.4a are established as 2.5% above/below of the highest/lowest average stiffness value of the two gears. This way, the almost constant characteristic of the gear designs becomes clear. As for the dynamic behavior, looking at Figure 6.4b, the order of magnitude of the equivalent root-mean-square is in the order of the 0.002 µm which is ridiculously low. Regardless, the shape of the curves are close to each other with the main difference being in the magnitude of the values.

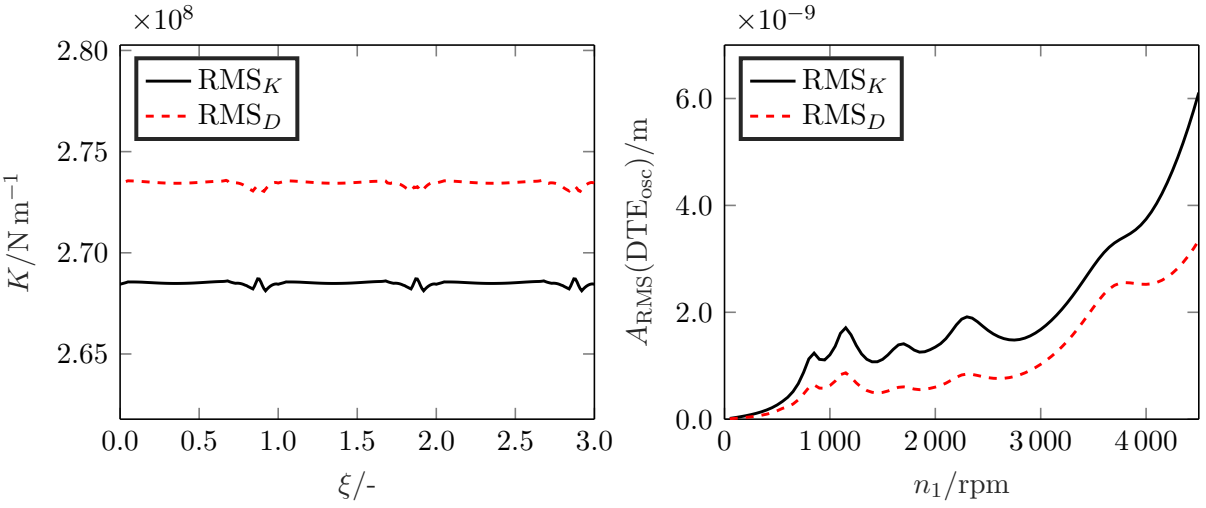

(a) Gear mesh stiffness.

(b) DTE_{osc} equivalent root-mean-square.

Figure 6.4: Comparison between the optimum solutions with stiffness and dynamic objective functions.

At this point, the high-end population from both problems is studied for possible correlations between stiffness and dynamic optimizations as well as geometrical features. High-end population is defined as the top 30 individuals that respect the problem restrictions ranked according to

their objective function values. The top 30 is selected from combining both the final population with the highest fitness individual found along the generations.

In a previous work, Marafona et al. [8] designed sets of gear pairs that had integer overlap ratio since it was shown that under those circumstances the resulting gear mesh stiffness fluctuations are minimized. Considering that in the conducted optimization process there is no imposition for integer values of either contact/overlap ratio, if the high-end population tended to those values, there is a strong indication that designing a gear for integer contact/overlap ratios is a guideline to consider for minimization of gear mesh stiffness fluctuations and low dynamic excitation. To reach a conclusion on this topic, the contact/overlap ratio maps of the high-end populations for the stiffness and dynamic objective functions is plotted in Figure 6.5 - the contact ratio is computed considering the extension of contact.

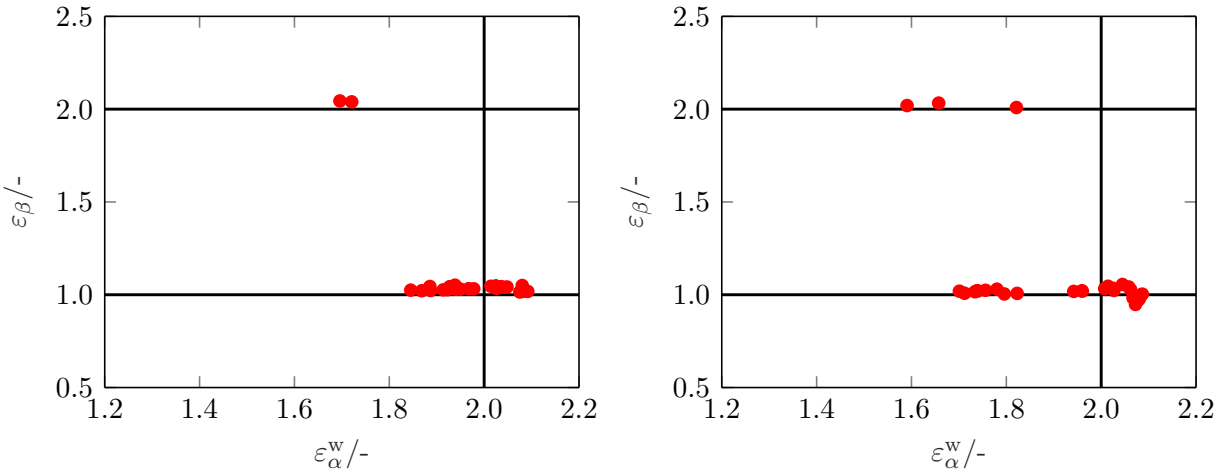

(a) Stiffness objective function.

(b) Dynamic objective function.

Figure 6.5: Comparison between the high-end individuals in a contact/overlap ratios map.

Overall, from Figure 6.5, it can be stated that there is a tendency for the gear designs to gather around integer values of the overlap ratio with a major cluster formed at the intersection of $\varepsilon_\alpha^{\mathrm{w}} = 2$ and $\varepsilon_\beta = 1$. In this particular problem, very few individuals are place close to $\varepsilon_\beta = 2$. The values of the contact and overlap ratios for the optimum are $\varepsilon_\alpha^{\mathrm{w}} = 2.0241/\varepsilon_\beta = 1.0459$ for the stiffness objective function and $\varepsilon_\alpha^{\mathrm{w}} = 2.0143/\varepsilon_\beta = 1.0457$ for the dynamic objective function. All considered, the positioning of the high-end individuals on the contact/overlap ratio maps is no coincidence. Although, the number of bits used for each variable and the similarity control applied in the genetic algorithm reduce the freedom in obtaining a wide variety of solutions with exact integer values. A separate optimization study is required to achieve more substantial evidence.

6.3.1. Stiffness *versus* Dynamics

The investigation conducted in this section is to relate the stiffness and dynamic approaches concerning their evolution along the generations. The purpose is to evaluate to what extent one evolution contradicts the other, for instance, as the best individual is improved from a dynamic perspective along the generations how is its stiffness fluctuations being affected. To do so, the best individual from the stiffness evolution and the dynamic evolution is taken. Then, the values of the fitness score, according to equation (6.6), are computed with respect to the gear mesh stiffness and dynamic objective functions, equations (6.1) and (6.2) respectively.

$$S^{\text{fit}} = \lambda_{\text{f}} f(\boldsymbol{X}) + \lambda_{\text{p}} \sum_{j=1}^{11} \max\left(g_j(\boldsymbol{X}), 0\right)^2 \tag{6.6}$$

By doing this, the values of the stiffness S^{fit} can be compared when using a stiffness and dynamic objective functions. The same procedure is also carried out for the dynamic S_{fit}. The result of this analysis for the relaxed problem creates Figure 6.6 - data is taken from 250 to 250 generations. When looking at the stiffness and dynamic evolution in both figures, it can be stated that the stiffness evolution reaches its optimum solution earlier than the dynamic evolution. Also, S^{fit} is decreasing when is of the same type as the evolution. From the stiffness parameter $S^{\text{K}}_{\text{fit}}$ in Figure 6.6a, the dynamic curve shows that for the relaxed problem reducing the gear mesh stiffness variations is part of improving the dynamic behavior since there is a consistent decrease along the generations. Although, for the dynamic analogue analysis, early stiffness evolution leads to worse dynamic score which is suddenly decreased, putting the stiffness evolution closer to the dynamic one.

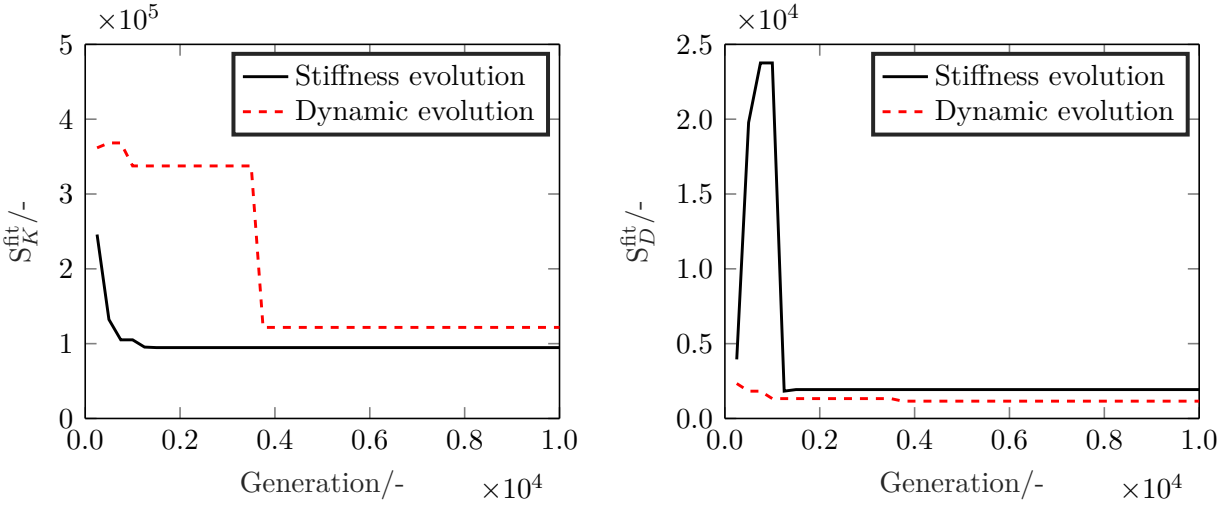

(a) Stiffness parameter.

(b) Dynamic parameter.

Figure 6.6: Evolution of the best solution along the generations: relaxed problem.

To analyze the high-end populations obtained from the different objective functions, the objective function value of the stiffness is determined for the dynamic high-end population and vice-versa. With this operation, the cross values are obtained and the same parameter can be compared for two different populations and correlations can be established. Besides comparing values of the stiffness and dynamic objective functions, the emitted noise level is also evaluated - even though there is no objective function or any kind of constraint to the problem on the emitted noise level. After computing the parameters being studied, the high-end population is reordered given the parameter being analyzed and then compared by ranking.

RMS_K is the first investigated parameter with its results graphically represented in Figure 6.7. Note that $\text{RMS}_K(K)$ means that the stiffness high-end population is used and $\text{RMS}_K(D)$ refers to the dynamic high-end population (same nomenclature is applied for every parameter). Figure 6.7 shows the individuals of the high-end populations in the sense that each dot contains the information from the equally ranked individuals. Then, points are fitted by a linear function using the linear least squares method. The same procedure is repeated for RMS_D, attend to Figure 6.8.

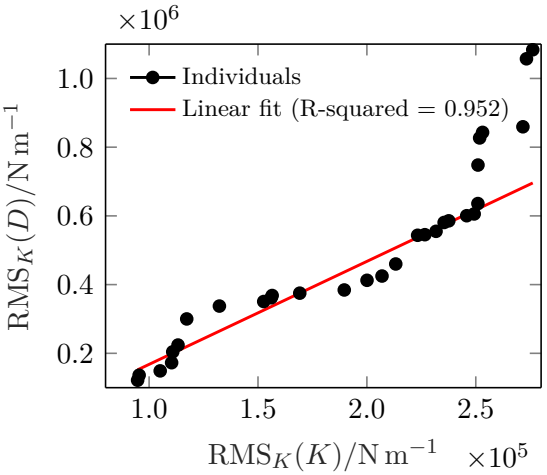

Figure 6.7: Correlation for gear mesh stiffness - relaxed problem.

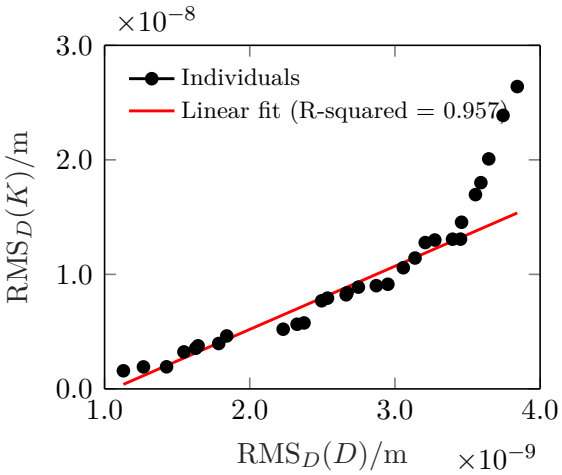

Figure 6.8: Correlation for gear dynamics - relaxed problem.

It can be seen in both Figure 6.7 and 6.8 that the bottom ranked individuals deviate from the trend that the remaining individuals are creating, which decreases the quality of the linear fit. The reason attributed to this deviation is an incomplete convergence of the high-end individuals, showing that more generations might be necessary for improved agreement. Nevertheless, high R-squared values are achieved for both situations. On the linear fits, their slope values can provide information about the connection between the optimization processes. For Figure 6.7 and 6.8 the x-axis represents the optimization parameter with the population that is optimized with it. Therefore, a higher slope points towards a higher difference in the range of values. For instance, the slopes obtained are $m_{\mathrm{K}} = 2.997$ for the stiffness and $m_{\mathrm{D}} = 5.517$ for the dynamics. This implies that the dynamic objective function is better at improving the gear mesh stiffness fluctuations than the stiffness objective function is at reducing the average $A_{\mathrm{RMS}}(\mathrm{DTE}_{\mathrm{osc}})$.

6.3.2. Noise level

When studying the noise level emitted by gear pairs with different finishing methods and under varied operating conditions, Masuda et al. [197] found that the transmitted power and relative vibration amplitude play a major role on its definition. Hence, a semi-empirical expression, presented in equation (6.7), was developed considering the retrieved experimental data.

$$L^{1\mathrm{m}} = \frac{20(1-\tan(\beta/2))u^{1/8}}{{\varepsilon_\alpha}^{1/4}}\sqrt{\frac{5.56+\sqrt{v}}{5.56}} + 20\log\left(W\right) + 20\log\left(\tilde{X}\right) + 20 \tag{6.7}$$

Equation (6.7) defines the overall emitted noise level ($(L^{1\mathrm{m}}$ [dB(A)])) 1 meter above the gearbox which can be estimated with six parameters, the helix angle (β), gear ratio (u), contact ratio (ε_α), pitch line velocity (v [m s^{-1}]), transmitted power (W [kW]) and peak-to-peak amplitude of the DTE normalized by the transmission error ($\tilde{X}$).

Masuda's noise level prediction, equation (6.7), is employed to give an estimation of the average emitted noise level of the high-end populations in the speed range assessed: used not for noise level prediction but as a parameter for relative comparison between the individuals. Figure 6.9 shows the average noise level for the dynamic and stiffness populations. Even though the correlation is not as strong as for the stiffness and dynamics objective functions, shown in Figures 6.7 and

6.8, the slope obtained from the noise level linear fit is close to 1, $m_L = 0.836$. With a slope close to 1, further analysis was conducted on the parameters that define the estimation of the noise level. Looking into equation (6.7), $\tilde{X}$ is established as the ratio between a dynamic and a quasi-static transmission error, being the latter closely related to the gear mesh stiffness. From Figure 6.10, it is shown that $\tilde{X}$ values from stiffness and dynamic populations have an almost linear relationship since the linear fit has an R-squared = 0.978. The slope of the linear fit in Figure 6.10 is $m_{\tilde{X}} = 2.059$, meaning that the dynamic objective function promotes a lower relative vibration amplitude than the stiffness one. The strong correlation found for $\tilde{X}$ explains to some extend the similarity in the values of the emitted noise level as other influential factors relate to gear geometrical parameters (design variables) as well as operating conditions, which are the same for every individual.

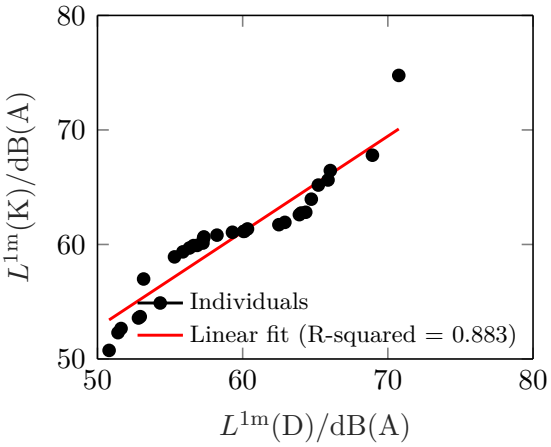

Figure 6.9: Correlation for noise level - relaxed problem.

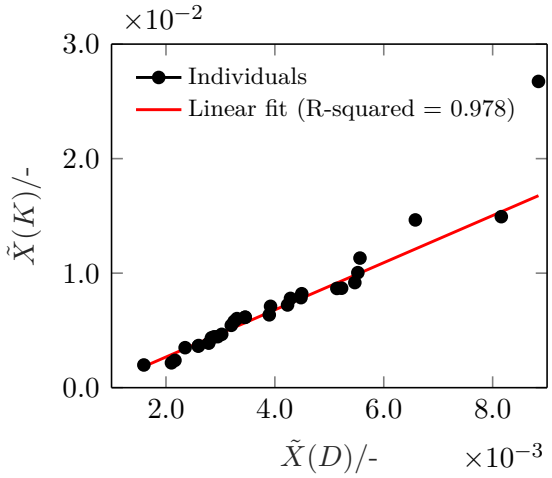

Figure 6.10: Correlation for normalized dynamic amplitude - relaxed problem.

It is noteworthy here that the very low $\tilde{X}$ values obtained for the high-end population lead to negative values its logarithm in equation (6.7). The main reason for this to occur is assigned to the dynamic model employed for the estimation of the vibration amplitude - this also shows that the semi-empirical equation was adjusted for the available experimental data. Masuda et al. [197] used a torsional model (no shafts or bearing elements included) with the single tooth pair stiffness being approximated by a half-sine wave for both spur and helical gears, where for helical gears the total contact ratio is considered. Considering this dynamic model leads to an overestimation of the relative dynamic amplitude, which, most likely, will not result in $\tilde{X} < 1$.

6.4. Gear optimization: full problem

The second optimization study is a more restricted one in the sense that all the defined restrictions are included, which accounts for the gear meshing efficiency, and more demanding nominal operating conditions are selected, attend to Table 6.6. Since the procedure taken is the same as in the analysis of the relaxed problem (section 6.3), only the necessary explanations are given.

Table 6.7 shows the optimum gear designs according to each objective function, which resulted in two gear designs that have the same number of teeth and module. However, unlike the relaxed problem, there is a slight difference in the facewidth and helix angle along with a respectable difference in the profile shift coefficient of the pinion. Objective function values have higher relative difference in comparison with the relaxed problem but are still very low in absolute terms

for both scenarios.

Table 6.6: Nominal working conditions for the full problem.

Parameters	**Value**
$\boldsymbol{n_1}$/rpm	4500
$\boldsymbol{T_1}$/N m	215.6

Table 6.7: Design variables of the optimum individuals: full problem.

$f(\boldsymbol{X})$	z_1/-	m_n/mm	b/mm	x_1/-	β/°	RMS_K/N m^{-1}	RMS_D/m
RMS_K	40	1.75	19.1102	-0.3701	17.2441	1.2426×10^5	5.1100×10^{-9}
RMS_D	40	1.75	18.2150	-0.7008	18.1890	1.9603×10^5	1.0163×10^{-9}

Looking at Figure 6.11 to analyze the optimum solutions in terms of gear mesh stiffness (Figure 6.11a) and its dynamic performance (Figure 6.11b) the two solutions are clearly more distinct then for the relaxed problem. It is visually perceptible from Figure 6.11a that the stiffness from RMS_D is not as smooth as the one from RMS_K mainly due to the peak right before $\xi = 1$. Concerning the dynamic response in Figure 6.11b, even though there is some difference for rotating speeds $n_1 < 3000$ rpm, the fact that in the spanned rotating speeds the gear design from stiffness objective function has a critical frequency makes all the difference. This is a clear example of an advantages of using a dynamic objective function for optimizing the dynamic behavior in contrast to the stiffness which without further information cannot avoid this phenomena: with the dynamic minimization the algorithm will also consider the mass of the gear pair, making the dynamic problem more complex which, in turn, gives it more flexibility in the design possibilities.

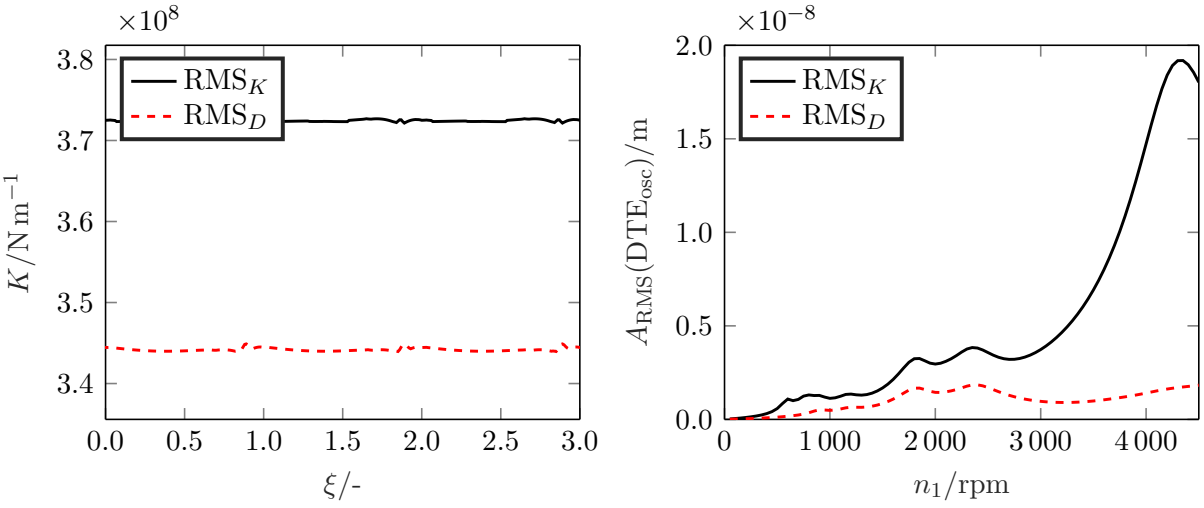

(a) Gear mesh stiffness.

(b) DTE_{osc} equivalent root-mean-square.

Figure 6.11: Comparison between the optimum solutions with stiffness and dynamic objective functions.

With a different problem at hands, the positioning of the high-end individuals in a contact/overlap ratios map gives information if the gear meshing efficiency constraint will not allow for the individuals to reach the areas of integer numbers. Figure 6.12 shows a very similar contact/overlap ratios map to the relaxed problem (Figure 6.5) with most individuals in the interception of

$\varepsilon_\alpha = 2$ with $\varepsilon_\beta = 1$. However, for the full problem, there are more individuals close to the line of $\varepsilon_\beta = 2$ for the dynamic objective function which is related to the more demanding conditions combined with the need to remove the critical frequencies from the speed range being optimized: higher total contact ratio gives rise to higher average gear mesh stiffness which, in turn, leads to higher critical frequencies. Optimum designs have $\varepsilon_\alpha^{\mathrm{w}} = 2.0096/\varepsilon_\beta = 1.0304$ and $\varepsilon_\alpha^{\mathrm{w}} = 2.0358/\varepsilon_\beta = 1.0342$ correspondingly for the stiffness and dynamic objective functions.

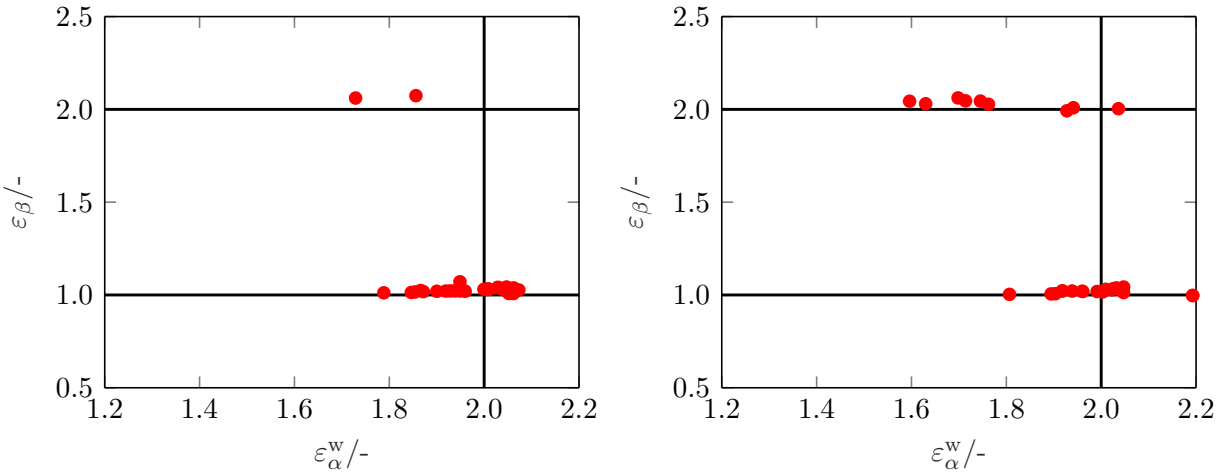

(a) Stiffness objective function.

(b) Dynamic objective function.

Figure 6.12: Comparison between the high-end individuals in a contact/overlap ratios map.

6.4.1. Stiffness *versus* Dynamics

The first tool for comparison of the stiffness and dynamic evolution for the full problem is the progression of the best individual during both the stiffness and dynamic objective functions regarding a stiffness and dynamic score according to equation (6.6). Figure 6.13 shows the evolution from the stiffness and dynamic point of views. For the stiffness evolution the best design is found before 500 generations while for the dynamic is before 5000 generations. Adding this information to the equivalent one from the relaxed problem (Figure 6.13) gives a strong indication that an optimum stiffness design is faster to find than a dynamic one. The only change that occurs in the stiffness evolution reduces the gear mesh stiffness fluctuations (as expected) but causes a worse dynamic excitation. The dynamic evolution in Figure 6.13a reveals that there is a minimization of the gear mesh stiffness fluctuations yet it was necessary to deteriorate the solution in what regards stiffness to achieve a dynamically improved design. This action relates to the adjustment of the system's critical frequencies which can imply higher gear mesh stiffness fluctuations.

Moving to the analysis of the high-end individuals in terms of their stiffness and dynamic parameters, Figures 6.14 and 6.15, it is verified that fewer individuals deviate from the linear fit when compared to the relaxed problem (Figures 6.7 and 6.8) which implies a higher R-squared value. In addition, for the full problem, the slope of the linear fits are closer to 1. In particular, for the gear mesh stiffness in Figure 6.14, the slope is $m_K = 1.195$ meaning that high-end individuals from the dynamic part have very similar gear mesh stiffness fluctuations as the ones from the stiffness part. The slope for the linear fit in Figure 6.15 is $m_D = 1.932$ which is higher than for the stiffness counterpart. Nevertheless, it is still found that the dynamic objective function is better at optimizing gear mesh stiffness fluctuations than the stiffness objective function is at minimizing dynamic oscillations.

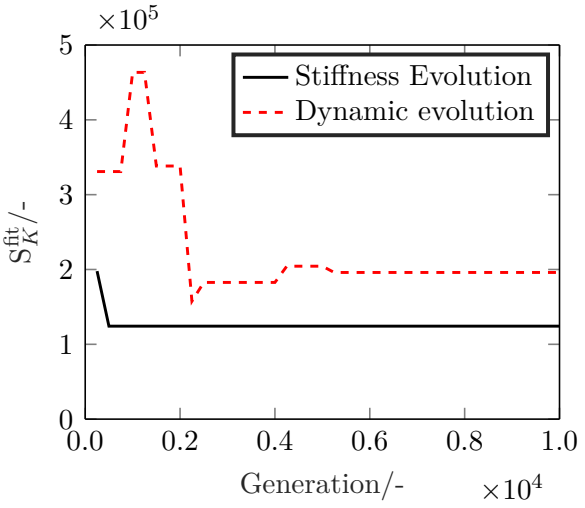

(a) Stiffness parameter.

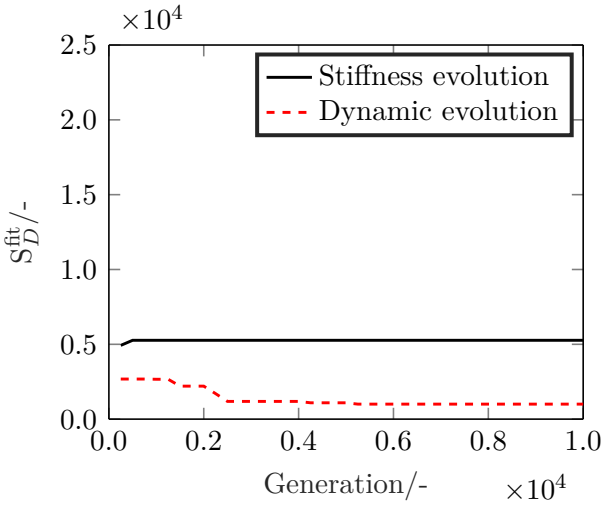

(b) Dynamic parameter.

Figure 6.13: Evolution of the best solution along the generations: full problem.

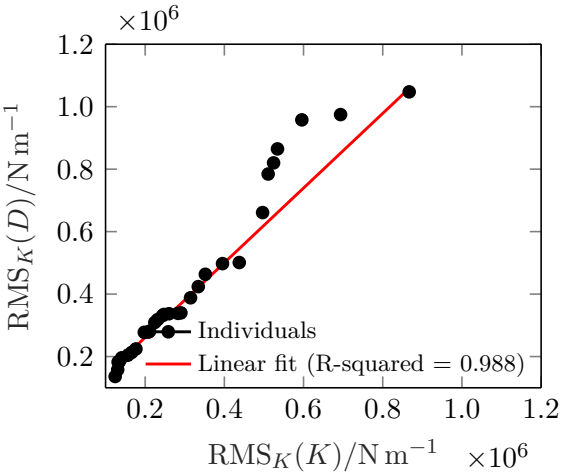

Figure 6.14: Correlation for gear mesh stiffness - full problem.

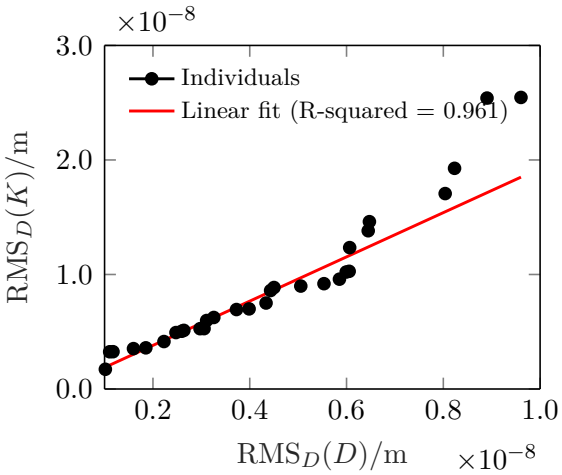

Figure 6.15: Correlation for gear dynamics - full problem.

6.4.2. Noise level

To describe the high-end populations with respect to the noise level, equation (6.7), developed by Masuda et al. [197] is utilized. This way, it is possible to relatively compare the emitted noise level os the different gear designs. Figure 6.16 shows the estimation of the emitted noise level of the different individuals from the stiffness and dynamic approaches while Figure 6.17 relates the normalized vibration amplitude. The slope of the linear fit is $m_L = 0.7629$ which similar to the slope from the relaxed problem (Figure 6.9). However, there is a significantly higher value for the R-squared which passed from R-squared = 0.883 in the relaxed problem to R-squared = 0.974 in the full problem. As for the normalized dynamic amplitude, it maintains its high R-squared value and a very similar slope, which is, for the full problem, of $m_{\tilde{X}} = 2.108$.

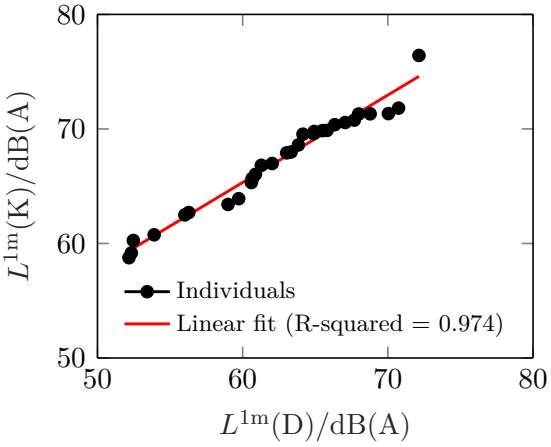

Figure 6.16: Correlation for noise level - full problem.

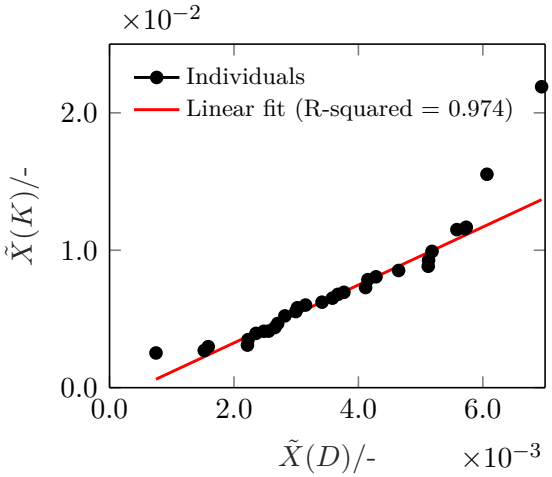

Figure 6.17: Correlation for normalized dynamic amplitude - full problem.

6.5. Closure

In order to find an expeditious manner to optimize a gear system regarding its dynamic excitation without needing to compute the gear steady-state response, an optimization towards the minimization of the gear mesh stiffness fluctuations is compared with the direct minimization of the dynamic excitation of the gear system. To reach this aim, a genetic algorithm is implemented and previously developed models [196] are used as tools to determine the objective functions. Concerning the attained results of the gear optimization problems:

- dynamic minimization takes sensibly 5 times more time, on average, than the stiffness one on each generation for the considered methodologies;
- the optimized gear designs from both objective functions are very similar, meaning that the main characteristics of the problems are captured by both instances;
- the gear mesh stiffness is almost constant and very low values of DTE_{osc} equivalent root-mean-square are obtained for all the designs, indicating that either approach can minimize the other. The major difference found is in the dynamic curve of the full problem which reveals a key flaw of the stiffness optimization: stiffness optimization does not take into account the location of the critical frequencies but this is not an impediment of reaching very low values for the dynamic parameter;
- the contact/overlap ratios maps revealed the tendency of the optimized gear designs of going for integer overlap ratios, regardless of the objective function. This topic was already discussed by Marafona et al. [8] where gear design optimization is applied to reach gears with integer overlap ratios, the concept behind this procedure is that integer values of contact or overlap ratios make the theoretical length of the contact lines constant. A dedicated optimization investigation is necessary to verify this tendency for gear mesh stiffness fluctuation/dynamic excitation minimization;
- the evolution of the best individual along the generations showed that gear mesh stiffness optimization found the optimum solution earlier than the dynamic optimization. In addition, as the design is being improved in dynamic terms there is an overall tendency for the gear

mesh stiffness fluctuations to also decrease while the inverse statement cannot be said about the optimization of the stiffness. This means that minimizing gear mesh stiffness fluctuations is necessary to reduce the dynamic excitation but not sufficient;

- the comparison of the populations for stiffness, dynamic and noise parameters imply that dynamics is better at optimizing stiffness than stiffness is at optimizing dynamics and that both objective functions give overall emitted noise levels that are in line with each considering the discrepancies in the remaining parameters.

Concluding, reducing the gear mesh stiffness fluctuation is a necessary condition for minimizing the dynamic excitation. Nonetheless, in dynamics, the gears' mass and average mesh stiffness value influence the natural frequencies of the gear system. It is almost as if optimizing gear mesh stiffness fluctuations is a particular case of gear dynamic optimization in the sense that both go for low mesh stiffness fluctuation but the stiffness optimization is "blind" to the location of critical frequencies. Hence, for dynamic optimization, it is not necessary to compute the steady-state dynamic response. Instead, for dynamic optimization, the proposed approach is to use the minimization of gear mesh stiffness fluctuations with information on the natural frequencies of the gear system, thus reducing the computational cost.

Chapter 7

Conclusion

7.1. Conclusions

Throughout this work, several gear research topics are addressed with the objective of establishing an accurate gear mesh stiffness model that has low computational cost. There are five investigation elements that represent the path taken to reach that goal and demonstrate the applicability of the developed modeling approach on several gear research topics. Thus, these elements merit a discussion and presentation of their main conclusions.

Chapter 2: Mesh stiffness models comprises a broad and in-depth literature review on the different types of gear mesh stiffness models while also providing guidelines for the selection and implementation of the type of model that best suits the reader. Considering the literature review, gear mesh stiffness has consistently been studied and it is still of great concern for gear engineers. Four types of gear mesh stiffness model were found: (i) analytical; (ii) finite element; (iii) hybrid and (iv) approximate analytical.

Analytical models express the gear mesh stiffness through the usage of analytical expressions acquired from material mechanics. The most common analytical model found in the literature is the potential energy method where the gear tooth is modeled as a cantilever beam fixed at the dedendum circle. They have low computational cost and flexibility in incorporating geometrical modifications, hence it shows applicability for teeth damaged with pitting, spalling and/or cracks. On the other hand, it requires an analytical description of the gear tooth geometry and numerical integration for every contact point which is not very computationally efficient neither for its implementation nor for multiple computations.

Finite element models can have high geometrical and contact detail and thus are considered to be the most accurate type fo gear mesh stiffness model - used as reference for validation of other models. The different softwares, gear body modeling procedure, types of elements and mesh stiffness determination are discussed. Different element meshing strategies are debated to guarantee that critical meshing regions (tooth contact and root) are properly accounted while keeping computational cost to the minimum. The biggest drawback for finite element models is their high computational cost which make them impractical for repeated gear mesh stiffness estimations.

Hybrid models were developed with the objective of reducing the computational cost of finite element models by coupling them with analytical procedures. Using this hybrid approach, the global deformations are estimated with the finite element method while the local (contact)

deformations are determined with analytical models. The implementation of this type of models requires the removal of the contact deformations from the finite element analysis and combination of these results with analytically estimated contact deflections. Hybrid models show improved computational cost when comparing to finite element models with the cost of a reduction (not significant) in the accuracy of the results.

Approximate analytical models are denoted for reducing expensive numerical calculations to an approximate and straightforward expression. Presented models resort to a parabolic/cosine function to describe the single tooth pair (slice) mesh stiffness. Their computational cost is the lowest and its implementation is the simplest from all types of models. In opposition, their accuracy is not their strength.

This chapter lead to the conclusion that the best gear mesh stiffness modeling strategy for consecutive gear mesh stiffness calculations are approximate analytical models.

Chapter 3: Single tooth pair slice mesh stiffness develops an approximate expression for the single tooth pair slice mesh stiffness in order to improve accuracy of approximate gear mesh stiffness models. Since the accuracy was the biggest flaw for this type of models, the work presented in this chapter aims to solve it. The main approximation performed in this type of models is in the single tooth pair (slice) mesh stiffness which is commonly assumed as having a symmetrical shape along the path of contact and with its value establish by the ISO 6336 [141].

The single tooth pair slice mesh stiffness is divided into three components: the tooth pair structural stiffness (includes the tooth bending, shear and axial compressive deformations), the fillet-foundation stiffness (to account for the gear hub radius) [78; 79] and the contact stiffness [77]. With the fillet-foundation and contact stiffnesses already presenting simple yet good estimations, this chapter focuses on the tooth pair structural stiffness. The work developed consists on a series of fits to the results obtained using the potential energy method and maximum stiffness values from ISO 6336 [141] for a comprehensive range of gear parameters. The tooth pair structural stiffness has a parabolic shape and requires three modeling parameters to fully define it: the relative amplitude, the asymmetry parameter and the maximum stiffness value. When investigating how each variable influences the quality of the approximation, it was found that the number of teeth of the pinion presents the best correlation - lower number of teeth of pinion implies a worse approximation.

As an output, an alternative to the potential energy method is presented with an easier implementation and without requiring numerical integration. In addition, with the formulation developed for the single tooth pair slice mesh stiffness, the accuracy of approximate gear mesh stiffness models is improved.

Chapter 4: Gear modeling is divided into three main parts, the developed gear mesh stiffness model, the implemented gear-shaft-bearing dynamic model and a parametric study on the effect of the asymmetry parameter (presented in the previous chapter).

The gear mesh stiffness model resorts to the slicing method which consists on dividing the gear body into slices along the axis of rotation and by staggering them to create the approximate gear body. This methodology is commonly applied for helical gears since this way they can be viewed as a combination of several spur gears but it can also be used for spur gears to consider changes along the facewidth. The single tooth pair slice mesh stiffness is the starting stiffness point leading to the gear mesh stiffness and is defined with the approximate expression developed in the previous chapter. To define continuity along the gear body, the slices are connected through a coupling parabolic function. The model considers the phenomena of extension of contact (contact outside the theoretical path of contact), buttressing (stiffness reduction due

to not having a full supporting tooth in the load direction) and profile modifications (tip and root relief for linear and parabolic shapes). The procedure implemented to account for profile modifications allows for any alteration in the tooth shape, meaning manufacturing errors can be as easily included in the model. Regarding the gear transmission dynamic model, gears are included as rigid disks by their base radii with a time-varying mesh stiffness representing their meshing - tooth contact loss is considered but not back-side contact. Shafts are modeled with the finite element method (Timoshenko beam elements). Bearings are introduced as lumped stiffnesses. Damping is included in the modal form with a global damping ratio. Unconditionally stable Newmark method is implemented to solve the equation of motion.

Being the single tooth pair (slice) mesh stiffness considered symmetric in most approximate gear mesh stiffness models found in the literature, a parametric study on its influence is conducted. However, the asymmetry parameter at stake is from one of the components of the single tooth pair slice mesh stiffness, the tooth pair structural stiffness. To perform this study, two batches (one for spur and other for helical) of 10000 random gear geometries representing the gear geometrical domain are created. For each batch, the gear mesh stiffness, load sharing ratio, oscillating component of both the dynamic transmission error and dynamic mesh force are computed - comprising a total of 80000 gear quasi-static and dynamic evaluations. It was concluded that even though the tooth pair structural stiffness asymmetry does not impose significant differences on the shape of quasi-static gear characteristics, pronounced deviations are found at a dynamic level due to changes in the frequency content of the gear mesh stiffness.

With this chapter, the successful development of a low computational cost gear mesh stiffness model giving accurate estimations is settled. An example of application of the newly developed model for repeated calculations is done, revealing its potential as a powerful tool for exploratory investigations. The low computational cost approach results, according to the work in this chapter, in an average gear mesh stiffness computation time (intel(R) core(TM) i7-9700 CPU with 64 GB of memory RAM at 2667 MHz - MATLAB® R2023a) of 5.1 ms for spur gears and 1.0 s for helical gears.

Chapter 5: Integer overlap ratio gears: preliminary study includes the development of integer overlap ratio gears with a previously developed methodology [8]. By varying the overlap ratio through the modification of the gear facewidth, numerical testing of the gear mesh stiffness, dynamic behavior and emitted noise level is performed.

For the gear mesh stiffness and dynamic analysis the models in chapter 4 are employed while for the estimation of the emitted noise level the semi-empirical expression by Masuda et al. [197] is utilized. Increasing the overlap ratio does not necessarily mean a decrease in the gear mesh stiffness fluctuations but minimum gear mesh stiffness fluctuations are found for integer values of the overlap ratio. Alternatively, from a dynamic point of view, increasing the overlap ratio leads to an overall decrease in the dynamic transmission error fluctuations yet minimums are still for integer values of the overlap ratio. According to the noise level evaluation, there is not a clear minimization of the noise level for integer overlap ratios as minimums can occur for $\varepsilon_\beta = 1.00$, 1.50, 2.00 and/or 2.50 depending on the speed analyzed: $\varepsilon_\beta = 1$ is the only value with consistent decrease.

Results indicate a high potential for this gear design concept (integer overlap ratio gears) in terms of reducing gear mesh stiffness fluctuations and dynamic excitation.

Chapter 6: Gear design optimization consists on the application of an implemented genetic optimization algorithm to study how a gear mesh stiffness and dynamic objective functions compare to obtain a gear design (macro-geometry) with reduced dynamic excitation. Gear mesh

stiffness has a significantly lower computational cost when compared to the dynamic evaluation so finding a way to replace the latter to obtain equivalent gear designs grants the possibility for a more exploratory and in-depth analysis.

Two different optimization problems, one more restrictive than the other, are solved simultaneously with the gear mesh stiffness and dynamic objective functions. Final gear designs are mostly concentrated around a contact ratio of $\varepsilon_\alpha = 2.00$ and spread along an overlap ratio $\varepsilon_\beta = 1.00$ - results in agreement with the study conducted in chapter 5 and excellent indicator for the integer overlap ratio gear design concept. Minimization of gear mesh stiffness fluctuations leads to a minimization of the dynamic excitation and minimization of the dynamic transmission error oscillating component originates gears with minimized mesh stiffness fluctuations. However, the gear mesh stiffness approach is insensible to the location of critical frequencies, in opposition to the dynamic approach that can adjust the mass and stiffness for improved dynamic behavior in the working speed range.

The proposed optimization approach consists in using the gear mesh stiffness fluctuations as the objective function with information on the natural frequencies of the dynamic system (modal analysis with average gear mesh stiffness value) - yielding a gear dynamic optimization process while avoiding direct computation of the dynamic response.

7.2. Future work

Future work addresses ideas that came up during the *philosophiae doctor* as well as other approaches to problems to which solutions were presented.

- research on approximate procedures for the axial gear mesh stiffness and improve the range of gear geometry applicability for the fillet-foundation stiffness considering coupling effects;
- influence of gear facewidth modifications and misalignment errors on the gear mesh stiffness, dynamic behavior and meshing efficiency - by taking advantage of the slicing method this effects can be included as modifications in the separation distance;
- dynamic modeling of gear behavior while considering the dynamic load to iterate the gear mesh stiffness at each time step and modeling of multi-mesh transmissions;
- study of the shooting method (numerical solver for nonlinear systems) as an alternative for the Newmark method to solve the equations of motion in a gear transmission system: faster computation of the dynamic response and directly output of the steady-state response.
- evaluation of gear meshing efficiency considering the dynamic response: large-scale parametric study;
- experimental testing of integer overlap ratio gears on mesh stiffness, dynamic response and noise level for the proof of concept;
- gear design optimization at macro- and micro-geometry levels - the developed gear mesh stiffness model has the capability to include micro-geometry parameters.

References

[1] Karsten Stahl. Foreword "Best of Gears 2022". *Forschung im Ingenieurwesen*, 86(3): 249–249, 2022.

[2] EARPA Foresight Group EPE. EARPA position paper: Research needs on energy, powertrains and electrification. *EARPA*, 2020.

[3] WindEurope Business Intelligence. Wind energy in europe: 2021 statistics and the outlook for 2022-2026. *WindEurope*, 2022.

[4] Kenneth Holmberg and Ali Erdemir. Influence of tribology on global energy consumption, costs and emissions. *Friction*, 5:263–284, 2017.

[5] A. Lex Brown. Effects of road traffic noise on health: From burden of disease to effectiveness of interventions. *Procedia Environmental Sciences*, 30:3–9, 2015.

[6] Andreas Seidler, Janice Hegewald, Anna Lene Seidler, Melanie Schubert, Mandy Wagner, Patrik Dröge, Eva Haufe, Jochen Schmitt, Enno Swart, and Hajo Zeeb. Association between aircraft, road and railway traffic noise and depression in a large case-control study based on secondary data. *Environmental research*, 152:263–271, 2017.

[7] Alireza Zeydabadi, Jafar Askari, Mahmood Vakili, Seyyed Jalil Mirmohammadi, Mohammad Ali Ghovveh, and Amir Houshang Mehrparvar. The effect of industrial noise exposure on attention, reaction time, and memory. *International archives of occupational and environmental health*, 92:111–116, 2019.

[8] João D.M. Marafona, Pedro M.T. Marques, Ramiro C. Martins, and Jorge H.O. Seabra. Towards constant mesh stiffness helical gears: The influence of integer overlap ratios. *Mechanism and Machine Theory*, 136:141–161, 2019.

[9] Christopher G. Cooley, Chunguang Liu, Xiang Dai, and Robert G. Parker. Gear tooth mesh stiffness: A comparison of calculation approaches. *Mechanism and Machine Theory*, 105:540–553, 2016.

[10] Monsak Pimsarn and Kazem Kazerounian. Efficient evaluation of spur gear tooth mesh load using pseudo-interference stiffness estimation method. *Mechanism and Machine Theory*, 37 (8):769–786, 2002.

[11] A. F. Rincon, Fernando Viadero, M. Iglesias, P. García, A. de Juan, and R. Sancibrian. A model for the study of meshing stiffness in spur gear transmissions. *Mechanism and Machine Theory*, 61:30–58, 2013.

[12] Lehao Chang, Geng Liu, and Liyan Wu. A robust model for determining the mesh stiffness of cylindrical gears. *Mechanism and Machine Theory*, 87:93–114, 2015.

[13] Xiaoyu Gu, Philippe Velex, Philippe Sainsot, and Jérôme Bruyère. Analytical investigations on the mesh stiffness function of solid spur and helical gears. *Journal of mechanical design*, 137(6), 2015.

[14] W. Yu and C.K. Mechefske. A new model for the single mesh stiffness calculation of helical gears using the slicing principle. *Iranian Journal of Science and Technology, Transactions of Mechanical Engineering*, 43(1):503–515, 2019.

[15] Xihui Liang, Hongsheng Zhang, Ming J. Zuo, and Yong Qin. Three new models for evaluation of standard involute spur gear mesh stiffness. *Mechanical Systems and Signal Processing*, 101:424–434, 2018.

[16] Mengjiao Feng, Hui Ma, Zhanwei Li, Qibin Wang, and Bangchun Wen. An improved analytical method for calculating time-varying mesh stiffness of helical gears. *Meccanica*, 53(4-5):1131–1145, 2018.

[17] Hui Ma, Jin Zeng, Ranjiao Feng, Xu Pang, and Bangchun Wen. An improved analytical method for mesh stiffness calculation of spur gears with tip relief. *Mechanism and Machine Theory*, 98:64–80, 2016.

[18] Yang Luo, Natalie Baddour, and Ming Liang. Effects of gear center distance variation on time varying mesh stiffness of a spur gear pair. *Engineering Failure Analysis*, 75:37–53, 2017.

[19] Miryam B. Sánchez, Miguel Pleguezuelos, and José I. Pedrero. Approximate equations for the meshing stiffness and the load sharing ratio of spur gears including hertzian effects. *Mechanism and Machine Theory*, 109:231–249, 2017.

[20] Yangshou Xiong, Kang Huang, Fengwei Xu, Yong Yi, Meng Sang, and Hua Zhai. Research on the influence of backlash on mesh stiffness and the nonlinear dynamics of spur gears. *Applied Sciences*, 9(5):1029, 2019.

[21] Giorgio Bonori, Marco Barbieri, and Francesco Pellicano. Optimum profile modifications of spur gears by means of genetic algorithms. *Journal of sound and vibration*, 313(3-5): 603–616, 2008.

[22] Marcello Faggioni, Farhad S. Samani, Gabriele Bertacchi, and Francesco Pellicano. Dynamic optimization of spur gears. *Mechanism and Machine Theory*, 46(4):544–557, 2011.

[23] Daniel Miler and Matija Hoić. Optimisation of cylindrical gear pairs: A review. *Mechanism and Machine Theory*, 156:104–156, 2021.

[24] A.Y. Attia. Deflection of spur gear teeth cut in thin rims. *Journal of Engineering for Industry*, 86(4):333–341, 1964.

[25] F. Baumgart. Stiffness-an unknown world of mechanical science? *Injury-International Journal for the Care of the Injured*, 31(2):14–23, 2000.

[26] Donald R. Houser and G. Wesley Blankenship. Methods for measuring gear transmission error under load and at operating speeds. *SAE transactions*, pages 1367–1374, 1989.

[27] D. Remond. Practical performances of high-speed measurement of gear transmission error or torsional vibrations with optical encoders. *Measurement Science and Technology*, 9(3): 347, 1998.

[28] Robert White and Vikrant Palan. Measurement of transmission error using rotational laser vibrometers. In *International Design Engineering Technical Conferences and Computers and Information in Engineering Conference*, volume 48086, pages 527–545, 2007.

[29] Nabih Feki, Jérôme Cavoret, Fabrice Ville, and Philippe Velex. Gear tooth pitting modelling and detection based on transmission error measurements. *European Journal of Computational Mechanics/Revue Européenne de Mécanique Numérique*, 22(2-4):106–119, 2013.

[30] M.A. Hotait and A. Kahraman. Experiments on the relationship between the dynamic transmission error and the dynamic stress factor of spur gear pairs. *Mechanism and Machine Theory*, 70:116–128, 2013.

[31] Antonio Palermo, Laurent Britte, Karl Janssens, Domenico Mundo, and Wim Desmet. The measurement of gear transmission error as an nvh indicator: theoretical discussion and industrial application via low-cost digital encoders to an all-electric vehicle gearbox. *Mechanical Systems and Signal Processing*, 110:368–389, 2018.

[32] Haonan Li, Siyu Chen, Jinyuan Tang, Weitao Chen, and Hongwu Ouyang. A novel approach for calculating no-load static transmission error based on measured discrete tooth surfaces. *Mechanism and Machine Theory*, 138:112–123, 2019.

[33] Xiong Chun and Chen Siyu. Experimental study of the effect of assembly error on the lightly loaded transmission error of spur gear with crown modification. *Journal of Low Frequency Noise, Vibration and Active Control*, page 1461348419854833, 2019.

[34] M. Benatar, M. Handschuh, A. Kahraman, and D. Talbot. Static and dynamic transmission error measurements of helical gear pairs with various tooth modifications. *Journal of Mechanical Design*, 141(10), 2019.

[35] R.G. Munro, D. Palmer, and L. Morrish. An experimental method to measure gear tooth stiffness throughout and beyond the path of contact. *Proceedings of the Institution of Mechanical Engineers, Part C: Journal of Mechanical Engineering Science*, 215(7):793–803, 2001.

[36] M. El Badaoui, V. Cahouet, F. Guillet, J. Danie‘re, and P. Velex. Modeling and Detection of Localized Tooth Defects in Geared Systems . *Journal of Mechanical Design*, 123(3): 422–430, 2001.

[37] Yogesh Pandya and Anand Parey. Experimental investigation of spur gear tooth mesh stiffness in the presence of crack using photoelasticity technique. *Engineering Failure Analysis*, 34:488–500, 2013.

[38] Naresh K. Raghuwanshi and Anand Parey. Experimental measurement of gear mesh stiffness of cracked spur gear by strain gauge technique. *Measurement*, 86:266–275, 2016.

[39] Naresh K. Raghuwanshi and Anand Parey. Experimental measurement of spur gear mesh stiffness using digital image correlation technique. *Measurement*, 111:93–104, 2017.

[40] Naresh K. Raghuwanshi and Anand Parey. Experimental measurement of mesh stiffness by laser displacement sensor technique. *Measurement*, 128:63–70, 2018.

[41] Fatih Karpat, Celalettin Yuce, and Oğuz Doğan. Experimental measurement and numerical validation of single tooth stiffness for involute spur gears. *Measurement*, 150:107043, 2020.

[42] S. Du and R.B. Randall. Encoder error analysis in gear transmission error measurement. *Proceedings of the Institution of Mechanical Engineers, Part C: Journal of Mechanical Engineering Science*, 212(4):277–285, 1998.

[43] Yuhua Li, Fengshou Gu, Georgina Harris, Andrew Ball, Nick Bennett, and Ken Travis. The measurement of instantaneous angular speed. *Mechanical Systems and Signal Processing*, 19(4):786–805, 2005.

[44] P.J. Sweeney and R.B. Randall. Gear transmission error measurement using phase demodulation. *Proceedings of the Institution of Mechanical Engineers, Part C: Journal of Mechanical Engineering Science*, 210(3):201–213, 1996.

[45] W. Lewis. Investigation of the strength of gear teeth. In *Proceedings of the Engineers Club (Philadelphia)*, 1892.

[46] E.J. Wellauer and A. Seireg. Bending Strength of Gear Teeth by Cantilever-Plate Theory. *Journal of Engineering for Industry*, 82(3):213–220, 1960.

[47] Robert Viktor Baud and R.E. Peterson. Load and stress cycles in gear teeth. *Mechanical Engineering*, 51(9):653–662, 1929.

[48] Harry Walker et al. Gear tooth deflection and profile modification. *Engineer*, 166:409–412, 1938.

[49] C. Weber. The deformation of loaded gears and the effect on their load carrying capacity. *British Department of Scientific and Industrial Research, Research Report 3*, 1949.

[50] C. Weber and K. Banaschek. The deformation of loaded gears and the effect on their load carrying capacity (part 5). *British Department of Scientific and Industrial Research, Research Report 6*, 1950.

[51] Stephen P. Timoshenko and J. N. Goodier. *Theory of Elasticity*. McGraw-Hill, 1951.

[52] Stephen P. Timoshenko and Sergius Woinowsky-Krieger. *Theory of plates and shells*. McGraw-Hill, 1959.

[53] Charles W. MacGregor. Deflection of a long helical gear tooth. *Mechanical Engineering*, 57:225–227, 1935.

[54] D.L. Holl. Cantilever Plate With Concentrated Edge Load. *Journal of Applied Mechanics*, 4(1):A8–A10, 1937.

[55] T.J. Jaramillo. Deflections and Moments Due to a Concentrated Load on a Cantilever Plate of Infinite Length. *Journal of Applied Mechanics*, 17(1):67–72, 1950.

[56] Kiyohiko Umezawa, Jiro Ishikawa, and Kunikazu Hayashi. Deflections due to a concentrated load on a cantilever thick plate of finite length for gears. *Bulletin of JSME*, 12(53):1204–1211, 1969.

[57] Kiyohiko Umezawa. Deflections and moments due to a concentrated load on a rack-shaped cantilever plate with finite width for gears. *Bulletin of JSME*, 15(79):116–130, 1972.

[58] D.L. Seager. Tooth loading and static behavior of helical gears. *ASLE TRANSACTIONS*, 13(1):66–77, 1970.

[59] Yoshio Terauchi and Kazuteru Nagamura. Study on deflection of spur gear teeth : 1st report, calculation of tooth deflection by two-dimensional elastic theory. *Bulletin of JSME*, 23(184):1682–1688, 1980.

[60] Yoshio Terauchi and Kazuteru Nagamura. Study on deflection of spur gear teeth : 2nd report, calculation of tooth deflection for spur gears with various tooth profiles. *Bulletin of JSME*, 24(188):447–452, 1981.

[61] A. Cardou and G.V. Tordion. Calculation of Spur Gear Tooth Flexibility by the Complex Potential Method. *Journal of Mechanisms, Transmissions, and Automation in Design*, 107 (1):38–42, 1985.

[62] Julian Holmes Steward. *Elastic analysis of load distribution in wide-faced spur gears.* PhD thesis, Newcastle University, 1989.

[63] J.H. Steward. The Compliance of Solid, Wide-Faced Spur Gears. *Journal of Mechanical Design*, 112(4):590–595, 1990.

[64] E. Yau, H.R. Busby, and D.R. Houser. A Rayleigh-Ritz approach to modeling bending and shear deflections of gear teeth. *Computers & Structures*, 50(5):705–713, 1994.

[65] M.E. Stegemiller and D.R. Houser. A Three-Dimensional Analysis of the Base Flexibility of Gear Teeth. *Journal of Mechanical Design*, 115(1):186–192, 1993.

[66] H.C. Kim, J.P. de Vaujany, M. Guingand, and D. Play. Stress Analysis of Cylindrical Webbed Spur Gears: Parametric Study. *Journal of Mechanical Design*, 120(2):349–357, 1998.

[67] F.L. Litvin, J.-S. Chen, J. Lu, and R.F. Handschuh. Application of Finite Element Analysis for Determination of Load Share, Real Contact Ratio, Precision of Motion, and Stress Analysis. *Journal of Mechanical Design*, 118(4):561–567, 1996.

[68] Raynald Guilbault, Claude Gosselin, and Louis Cloutier. Express Model for Load Sharing and Stress Analysis in Helical Gears. *Journal of Mechanical Design*, 127(6):1161–1172, 2004.

[69] J. Derek Smith. *Gear noise and vibration.* CRC Press, 2003.

[70] Heinz Linke, Jörg Börner, and Ralf Hess. *Cylindrical gears: calculation–materials–manufacturing.* Carl Hanser Verlag GmbH Co KG, 2016.

[71] Jia Lian Shi, Xiao Gang Ma, Chang Liang Xu, and Sheng Ju Zang. Meshing stiffness analysis of gear using the ishikawa method. In *Applied Mechanics and Materials*, volume 401, pages 203–206. Trans Tech Publications, 2013.

[72] R. Budynas and K. Nisbett. *Shigley's Mechanical Engineering Design 9th Edition.* McGraw-Hill, 2011.

[73] Jose I. Pedrero, Miguel Pleguezuelos, Mariano Artés, and Juan A. Antona. Load distribution model along the line of contact for involute external gears. *Mechanism and Machine Theory*, 45(5):780–794, 2010.

[74] J.I. Pedrero, M. Artés, and C. García-Masiá. Determination of the effective path of contact of undercut involute gear teeth. *Proceedings of the Institution of Mechanical Engineers, Part C: Journal of Mechanical Engineering Science*, 218(7):751–760, 2004.

[75] R.W. Cornell. Compliance and stress sensitivity of spur gear teeth. *J. Mech. Des.*, 103: 447–459, 1981.

[76] Arvid Palmgren. Ball and roller bearing engineering. *Philadelphia: SKF Industries Inc.*, 1959.

[77] Philippe Sainsot and Philippe Velex. On contact deflection and stiffness in spur and helical gears. *Mechanism and Machine Theory*, 154:104049, 2020.

[78] P. Sainsot, P. Velex, and O. Duverger. Contribution of gear body to tooth deflections – a new bidimensional analytical formula. *J. Mech. Des.*, 126(4):748–752, 2004.

[79] Chongyang Xie, Lin Hua, Xinghui Han, Jian Lan, Xiaojin Wan, and Xiaoshuang Xiong. Analytical formulas for gear body-induced tooth deflections of spur gears considering structure coupling effect. *International Journal of Mechanical Sciences*, 148:174–190, 2018.

[80] Eng. Benjamin Mahr and Dr. Ulrich Kissling. Comparison between different commercial gear tooth contact analysis software packages, 2018. KISSsoft AG.

[81] KISSsoft. *KISSsoft's User Manual*, 2019.

[82] Andreas Beinstingel, Michael Keller, Michael Heider, Burkhard Pinnekamp, and Steffen Marburg. A hybrid analytical-numerical method based on isogeometric analysis for determination of time varying gear mesh stiffness. *Mechanism and Machine Theory*, 160:104291, 2021.

[83] He Dai, Xinhua Long, Feng Chen, and Chao Xun. An improved analytical model for gear mesh stiffness calculation. *Mechanism and Machine Theory*, 159:104262, 2021.

[84] Yi Yang, Liyan Cao, Hang Li, and Yiping Dai. Nonlinear dynamic response of a spur gear pair based on the modeling of periodic mesh stiffness and static transmission error. *Applied Mathematical Modelling*, 72:444–469, 2019.

[85] Zaigang Chen and Yimin Shao. Mesh stiffness calculation of a spur gear pair with tooth profile modification and tooth root crack. *Mechanism and Machine Theory*, 62:63–74, 2013.

[86] A. Fernández, M. Iglesias, A. De-Juan, P. García, R. Sancibrián, and F. Viadero. Gear transmission dynamic: Effects of tooth profile deviations and support flexibility. *Applied Acoustics*, 77:138–149, 2014.

[87] Hui Ma, Mengjiao Feng, Zhanwei Li, Ranjiao Feng, and Bangchun Wen. Time-varying mesh characteristics of a spur gear pair considering the tip-fillet and friction. *Meccanica*, 52(7):1695–1709, 2017.

[88] Qibin Wang, Kun Xu, Tianshu Huai, Hui Ma, and Kun Wang. A mesh stiffness method using slice coupling for spur gear pairs with misalignment and lead crown relief. *Applied Mathematical Modelling*, 90:845–861, 2021.

[89] Chongyang Xie and Xuedao Shu. A new mesh stiffness model for modified spur gears with coupling tooth and body flexibility effects. *Applied Mathematical Modelling*, 91:1194–1210, 2021.

[90] Zaigang Chen, Ziwei Zhou, Wanming Zhai, and Kaiyun Wang. Improved analytical calculation model of spur gear mesh excitations with tooth profile deviations. *Mechanism and Machine Theory*, 149:103838, 2020.

[91] Herbert H. Richardson. *Static and dynamic load, stress, and deflection cycles in spur-gear systems*. PhD thesis, Massachusetts Institute of Technology, 1958.

[92] D.L. Seager. Separation of gear teeth in approach and recess, and the likelihood of corner contact. *ASLE TRANSACTIONS*, 19(2):164–170, 1976.

[93] David Tse and Hsiang Lin. Separation distance and static transmission error of involute spur gears. In *28th Joint propulsion conference and exhibit*, page 3490, 1992.

[94] Hsiang Lin, Jifeng Wang, Fred Oswald, and John Coy. Effect of extended tooth contact on the modeling of spur gear transmissions. In *29th Joint propulsion conference and exhibit*, page 2148, 1993.

[95] R.G. Munro, L. Morrish, and D. Palmer. Gear transmission error outside the normal path of contact due to corner and top contact. *Proceedings of the Institution of Mechanical Engineers, Part C: Journal of Mechanical Engineering Science*, 213(4):389–400, 1999.

[96] Woo-Jin Chung, Jung-Ho Park, Ho-Gil Yoo, Young-Jun Park, Su-chul Kim, Jong-hyeon Sohn, and Geun-ho Lee. Improved analytical model for calculating mesh stiffness and transmission error of helical gears considering trochoidal root profile. *Mechanism and Machine Theory*, 163:104386, 2021.

[97] Y. Cai. Simulation on the Rotational Vibration of Helical Gears in Consideration of the Tooth Separation Phenomenon (A New Stiffness Function of Helical Involute Tooth Pair). *Journal of Mechanical Design*, 117(3):460–469, 1995.

[98] Qibin Wang and Yimin Zhang. A model for analyzing stiffness and stress in a helical gear pair with tooth profile errors. *Journal of vibration and control*, 23(2):272–289, 2017.

[99] Yu Wang, Yimin Shao, Zaigang Chen, Minggang Du, and Huifang Xiao. Mesh stiffness calculation of helical gears with profile modification. *The Journal of Engineering*, 2019 (13):225–230, 2019.

[100] Xiaolin Tang, Liang Zou, Wei Yang, Yanjun Huang, and Hong Wang. Novel mathematical modelling methods of comprehensive mesh stiffness for spur and helical gears. *Applied Mathematical Modelling*, 64:524–540, 2018.

[101] Qibin Wang, Bo Zhao, Yang Fu, Xianguang Kong, and Hui Ma. An improved time-varying mesh stiffness model for helical gear pairs considering axial mesh force component. *Mechanical Systems and Signal Processing*, 106:413–429, 2018.

[102] Shaoshuai Hou, Jing Wei, Aiqiang Zhang, Chunpeng Zhang, Junhui Yan, and Changlu Wang. A novel comprehensive method for modeling and analysis of mesh stiffness of helical gear. *Applied Sciences*, 10(19):6695, 2020.

[103] Zong Meng, Guixia Shi, and Fulin Wang. Vibration response and fault characteristics analysis of gear based on time-varying mesh stiffness. *Mechanism and Machine Theory*, 148:103786, 2020.

[104] Siyu Wang and Rupeng Zhu. An improved mesh stiffness calculation model of spur gear pair under mixed ehl friction with spalling effect. *Vibroengineering PROCEDIA*, 33:176–181, 2020.

[105] Yinghui Liu, Zhanqun Shi, Guoji Shen, Dong Zhen, Feiyue Wang, and Fengshou Gu. Evaluation model of mesh stiffness for spur gear with tooth tip chipping fault. *Mechanism and Machine Theory*, 158:104238, 2021.

[106] Wei Chen, Yulong Lei, Yao Fu, and Liguo Hou. A study of effects of tooth surface wear on time-varying mesh stiffness of external spur gear considering wear evolution process. *Mechanism and Machine Theory*, 155:104055, 2021.

[107] Zhixian Shen, Baijie Qiao, Laihao Yang, Wei Luo, and Xuefeng Chen. Evaluating the influence of tooth surface wear on TVMS of planetary gear set. *Mechanism and Machine Theory*, 136:206–223, 2019.

[108] Zhiying Chen and Pengfei Ji. Research on the variation of mesh stiffness and transmission error for spur gear with tooth profile modification and wear fault. *Engineering Failure Analysis*, 122:105184, 2021.

[109] Bilal Yousfi, Abdenour Soualhi, Kamal Medjaher, and François Guillet. New approach for gear mesh stiffness evaluation of spur gears with surface defects. *Engineering Failure Analysis*, 116:104740, 2020.

[110] Kangkang Chen, Hui Ma, Linyang Che, Zhanwei Li, and Bangchun Wen. Comparison of meshing characteristics of helical gears with spalling fault using analytical and finite-element methods. *Mechanical Systems and Signal Processing*, 121:279–298, 2019.

[111] Zhiguo Wan, Hongrui Cao, Yanyang Zi, Wangpeng He, and Yimin Chen. Mesh stiffness calculation using an accumulated integral potential energy method and dynamic analysis of helical gears. *Mechanism and Machine Theory*, 92:447–463, 2015.

[112] Hanjun Jiang and Fuhao Liu. Mesh stiffness modelling and dynamic simulation of helical gears with tooth crack propagation. *Meccanica*, pages 1–22, 2020.

[113] E. Oñate. *Structural Analysis with the Finite Element Method. Linear Statics: Volume 1: Basis and Solids*. Lecture Notes on Numerical Methods in Engineering and Sciences. Springer Netherlands, 2009.

[114] J. Fish and T. Belytschko. *A First Course in Finite Elements*. Wiley, 2007.

[115] J.N. Reddy. *An Introduction to the Finite Element Method*. McGraw-Hill International Editions: Engineering Mechanics Series. McGraw-Hill, 1993.

[116] Rama Thirumurugan and N. Gnanasekar. Influence of finite element model, load-sharing and load distribution on crack propagation path in spur gear drive. *Engineering Failure Analysis*, page 104383, 2020.

[117] Jiaxing Zhan, Mohammad Fard, and Reza Jazar. A cad-fem-qsa integration technique for determining the time-varying meshing stiffness of gear pairs. *Measurement*, 100:139–149, 2017.

[118] Jiande Wang and Ian Howard. Finite element analysis of high contact ratio spur gears in mesh. *J. Trib.*, 127(3):469–483, 2005.

[119] S. Zouari, M. Maatar, T. Fakhfakh, and M. Haddar. Three-dimensional analyses by finite element method of a spur gear: effect of cracks in the teeth foot on the mesh stiffness. *Journal of failure analysis and prevention*, 7(6):475–481, 2007.

[120] Xihui Liang, Hongsheng Zhang, Libin Liu, and Ming J. Zuo. The influence of tooth pitting on the mesh stiffness of a pair of external spur gears. *Mechanism and Machine Theory*, 106:1–15, 2016.

[121] M.H. Arafa and M.M. Megahed. Evaluation of spur gear mesh compliance using the finite element method. *Proceedings of the Institution of Mechanical Engineers, Part C: Journal of Mechanical Engineering Science*, 213(6):569–579, 1999.

[122] Caterina Natali, Mattia Battarra, Giorgio Dalpiaz, and Emiliano Mucchi. A critical review on fe-based methods for mesh stiffness estimation in spur gears. *Mechanism and Machine Theory*, 161:104319, 2021.

[123] J. Hedlund and A. Lehtovaara. A parameterized numerical model for the evaluation of gear mesh stiffness variation of a helical gear pair. *Proceedings of the Institution of Mechanical Engineers, Part C: Journal of Mechanical Engineering Science*, 222(7):1321–1327, 2008.

[124] John J. Coy and C. Chao. A method of selecting grid size to account for hertz deformation in finite element analysis of spur gears. *J. Mech. Des.*, 104:759–764, 1982.

[125] Lars Vedmar. *On the design of external involute gears*. Division of Machine Elements, Department of Mechanical Engineering, Lund Technical University, 1981.

[126] L. Vedmar and B. Henriksson. A General Approach for Determining Dynamic Forces in Spur Gears. *Journal of Mechanical Design*, 120(4):593–598, 1998.

[127] Alberto Diez-Ibarbia, A. F. Rincon, M. Iglesias, A. de Juan, P. Garcia, and F. Viadero. Efficiency analysis of spur gears with a shifting profile. *Meccanica*, 51(3):707–723, 2016.

[128] Alberto Diez-Ibarbia, A. F. Rincon, A. de Juan, M. Iglesias, P. Garcia, and F. Viadero. Frictional power losses on spur gears with tip reliefs. The load sharing role. *Mechanism and Machine Theory*, 112:240–254, 2017.

[129] Alberto Diez-Ibarbia, A. F. Rincon, A. De-Juan, M. Iglesias, P. Garcia, and F. Viadero. Frictional power losses on spur gears with tip reliefs. The friction coefficient role. *Mechanism and Machine Theory*, 121:15–27, 2018.

[130] A. F. Rincon, M. Iglesias, A. de Juan, Alberto Diez-Ibarbia, P. García, and F. Viadero. Gear transmission dynamics: effects of index and run out errors. *Applied Acoustics*, 108: 63–83, 2016.

[131] Bing Yuan, Lehao Chang, Geng Liu, Shan Chang, Lan Liu, and Yunbo Shen. An efficient three-dimensional dynamic contact model for cylindrical gear pairs with distributed tooth flank errors. *Mechanism and Machine Theory*, 152:103930, 2020.

[132] Paul Langlois, Baydu Al, and Owen Harris. Hybrid hertzian and fe-based helical gear-loaded tooth contact analysis and comparison with fe. *Gear Technology*, 6:54–57, 2016.

[133] Kangkang Chen, Yifan Huangfu, Hui Ma, Zhitao Xu, Xu Li, and Bangchun Wen. Calculation of mesh stiffness of spur gears considering complex foundation types and crack propagation paths. *Mechanical Systems and Signal Processing*, 130:273–292, 2019.

[134] YiFan Huangfu, KangKang Chen, Hui Ma, Xu Li, Xi Yu, BaiShun Zhao, and BangChun Wen. Investigation on meshing and dynamic characteristics of spur gears with tip relief under wear fault. *Science China Technological Sciences*, 62(11):1948–1960, 2019.

[135] Pedro Marques, Ramiro Martins, and Jorge Seabra. Analytical load sharing and mesh stiffness model for spur/helical and internal/external gears–towards constant mesh stiffness gear design. *Mechanism and Machine Theory*, 113:126–140, 2017.

[136] Y. Cai and T. Hayashi. The linear approximated equation of vibration of a pair of spur gears (theory and experiment). *Journal of Mechanical Design*, 116(2):558–564, 1994.

[137] Kiyohiko Umezawa, Toshio Suzuki, and Taichi Sato. Vibration of power transmission helical gears : Approximate equation of tooth stiffness. *Bulletin of JSME*, 29(251):1605–1611, 1986.

[138] Miryam B. Sánchez, Miguel Pleguezuelos, and José I. Pedrero. Influence of profile modifications on meshing stiffness, load sharing, and trasnsmission error of involute spur gears. *Mechanism and Machine Theory*, 139:506–525, 2019.

[139] Miguel Pleguezuelos, Miryam B. Sánchez, and José I. Pedrero. Control of transmission error of high contact ratio spur gears with symmetric profile modifications. *Mechanism and Machine Theory*, 149:103839, 2020.

[140] Miguel Pleguezuelos, Miryam B. Sánchez, and José I. Pedrero. Analytical model for meshing stiffness, load sharing, and transmission error for spur gears with profile modification under non-nominal load conditions. *Applied Mathematical Modelling*, 97:344–365, 2021.

[141] ISO 6336. Calculation of load capacity of spur and helical gears. *ISO Standard*, 2006.

[142] Pedro Miguel Teixeira Marques. *Power Loss in Planetary Gearboxes Including the Influence of Gear Elastic and Dynamic Effects*. PhD thesis, Faculdade de Engenharia da Universidade do Porto, 2017.

[143] Pedro M.T. Marques, João D.M. Marafona, Ramiro C. Martins, and Jorge H.O. Seabra. A continuous analytical solution for the load sharing and friction torque of involute spur and helical gears considering a non-uniform line stiffness and line load. *Mechanism and Machine Theory*, 161:104320, 2021.

[144] American Gears Manufacturers Association. AGMA 925-A03, Effect of lubrication on gear surface distress. *American Gears Manufacturers Association*, 2003.

[145] Ming-Haung Tsai and Ying-Chien Tsai. A method for calculating static transmission errors of plastic spur gears using fem evaluation. *Finite Elements in Analysis and Design*, 27(4): 345–357, 1997.

[146] Ah-Der Lin and Jao-Hwa Kuang. Dynamic interaction between contact loads and tooth wear of engaged plastic gear pairs. *International Journal of Mechanical Sciences*, 50(2): 205–213, 2008.

[147] M. Karimpour, K.D. Dearn, and Douglas Walton. A kinematic analysis of meshing polymer gear teeth. *Proceedings of the Institution of Mechanical Engineers, Part L: Journal of Materials: Design and Applications*, 224(3):101–115, 2010.

[148] E. Letzelter, J. P. Vaujany, and M. Guingand. Load-sharing model for polymer cylindrical gears. *Gear Technology*, 28:28–34, 2011.

[149] Julien Cathelin, Eric Letzelter, Michele Guingand, Jean-Pierre de Vaujany, and Laurent Chazeau. Experimental and numerical study of a loaded cylindrical pa66 gear. *Journal of Mechanical design*, 135(4), 2013.

[150] M. Kodeeswaran, R. Suresh, and S. Senthilvelan. Transmission characteristics of injection moulded polymer spur gears: experimental and numerical evaluation. *International Journal of Powertrains*, 5(3):246–263, 2016.

[151] *A Fast Finite Element Based Methodology to Predict the Temperature Field in a Thermoplastic Spur Gear Drive*, volume 10: 2017 ASME International Power Transmission and Gearing Conference of *International Design Engineering Technical Conferences and Computers and Information in Engineering Conference*, 2017.

[152] Wafiuddin Ghazali, Daing Idris, Azizul Sofian, Januar Siregar, and Abdul Aziz. A review on failure characteristics of polymer gear. In *MATEC Web of Conferences*, volume 90, page 01029. EDP Sciences, 2017.

[153] X.D. Xue, K.W.E. Cheng, and N.C. Cheung. Selection of electric motor drives for electric vehicles. In *2008 Australasian Universities Power Engineering Conference*, pages 1–6. IEEE, 2008.

[154] Andrea Credo, Giuseppe Fabri, Marco Villani, and Mircea Popescu. High speed synchronous reluctance motors for electric vehicles: a focus on rotor mechanical design. In *2019 IEEE International Electric Machines & Drives Conference (IEMDC)*, pages 165–171. IEEE, 2019.

[155] Monica Beyer, Gareth Brown, Michael Gahagan, Tomoya Higuchi, Gregory Hunt, Michael Huston, Doug Jayne, Chris McFadden, Timothy Newcomb, Suzanne Patterson, et al. Lubricant concepts for electrified vehicle transmissions and axles. *Tribology Online*, 14(5): 428–437, 2019.

[156] Toni Jabbour and Ghazi Asmar. Stress calculation for plastic helical gears under a real transverse contact ratio. *Mechanism and Machine theory*, 44(12):2236–2247, 2009.

[157] Christian Hasl, Hua Liu, Peter Oster, Thomas Tobie, Karsten Stahl, et al. Method for calculating the tooth root stress of plastic spur gears meshing with steel gears under consideration of deflection-induced load sharing. *Mechanism and Machine Theory*, 111: 152–163, 2017.

[158] S. Du, R.B. Randall, and D.W. Kelly. Modelling of spur gear mesh stiffness and static transmission error. *Proceedings of the Institution of Mechanical Engineers, Part C: Journal of Mechanical Engineering Science*, 212(4):287–297, 1998.

[159] Carlos M.C.G. Fernandes, Diogo M.P. Rocha, Ramiro C. Martins, Luis Magalhães, and Jorge H.O. Seabra. Finite element method model to predict bulk and flash temperatures on polymer gears. *Tribology International*, 120:255–268, 2018.

[160] Victor Roda-Casanova and Francisco Sanchez-Marin. A 2D finite element based approach to predict the temperature field in polymer spur gear transmissions. *Mechanism and Machine Theory*, 133:195–210, 2019.

[161] Carlos M.C.G. Fernandes, Diogo M.P. Rocha, Ramiro C. Martins, Luís Magalhães, and Jorge H.O. Seabra. Hybrid polymer gear concepts to improve thermal behavior. *Journal of Tribology*, 141(3), 2019.

[162] Stefan Reitschuster, Enzo Maier, Thomas Lohner, and Karsten Stahl. Friction and temperature behavior of lubricated thermoplastic polymer contacts. *Lubricants*, 8(6):67, 2020.

[163] B. Černe, M. Petkovšek, Joze Duhovnik, and J. Tavčar. Thermo-mechanical modeling of polymer spur gears with experimental validation using high-speed infrared thermography. *Mechanism and Machine Theory*, 146:103734, 2020.

[164] Sumanth Kashyap, Donald R. Houser, Zan Smith, Senthilvelan Selvaraj, James M. Casella, and Jeffrey John Bradway. Methods of describing plastic gear geometry after a temperature change with application to the prediction of gear load distribution. In *International Design Engineering Technical Conferences and Computers and Information in Engineering Conference*, volume 54853, pages 497–505, 2011.

[165] P. Klein Meuleman, D. Walton, K.D. Dearn, D.J. Weale, and I. Driessen. Minimization of transmission errors in highly loaded plastic gear trains. *Proceedings of the Institution of Mechanical Engineers, Part C: Journal of Mechanical Engineering Science*, 221(9): 1117–1129, 2007.

[166] João D.M. Marafona, Pedro M.T. Marques, Ramiro C. Martins, and Jorge H.O. Seabra. Mesh stiffness models for cylindrical gears: A detailed review. *Mechanism and Machine Theory*, 166:104472, 2021.

[167] M.B. Sánchez, M. Pleguezuelos, and J.I. Pedrero. Enhanced model of load distribution along the line of contact for non-standard involute external gears. *Meccanica*, 48(3):527–543, 2013.

[168] José I. Pedrero, Miryam B. Sánchez, and Miguel Pleguezuelos. Load sharing and quasi-static transmission error of non-standard tooth height spur gears. In *European Conference on Mechanism Science*, pages 231–238. Springer, 2020.

[169] ISO 53. Cylindrical gears for general and heavy engineering - standard basic rack tooth profile. *ISO Standard*, 1998.

[170] MAAG Gear Company Ltd. *Maag Gear Book: Calculation and Practice of Gears, Gear Drives, Toothed Couplings and Synchronous Clutch Couplings*. Maag Gear Company Limited, 1990.

[171] João D.M. Marafona, Pedro M.T. Marques, Ramiro C. Martins, and Jorge H.O. Seabra. Approximate expression for the single tooth pair slice mesh stiffness. *Mechanism and Machine Theory*, 187:105367, 2023.

[172] J. Bruyère, P. Velex, B. Guilbert, and D.R. Houser. An analytical study on the combination of profile relief and lead crown minimizing transmission error in narrow-faced helical gears. *Mechanism and Machine Theory*, 136:224–243, 2019.

[173] J. Bruyère and Ph. Velex. Towards general performance diagrams to define optimum profile and lead modifications with regard to transmission error in spur and helical gears. *Mechanism and Machine Theory*, 176:105021, 2022.

[174] José I. Pedrero, Miguel Pleguezuelos, and Miryam B. Sánchez. Analytical model for meshing stiffness, load sharing, and transmission error for helical gears with profile modification. *Mechanism and Machine Theory*, 185:105340, 2023.

[175] G. Wesley Blankenship and Rajendra Singh. A new gear mesh interface dynamic model to predict multi-dimensional force coupling and excitation. *Mechanism and Machine Theory*, 30(1):43–57, 1995.

[176] G.W. Blankenship and A. Kahraman. Steady state forced response of a mechanical oscillator with combined parametric excitation and clearance type non-linearity. *Journal of Sound and Vibration*, 185(5):743–765, 1995.

[177] P. Velex and M. Maatar. A mathematical model for analyzing the influence of shape deviations and mounting errors on gear dynamic behaviour. *Journal of Sound and Vibration*, 191(5):629–660, 1996.

[178] J.P. Raclot and P. Velex. Simulation of the dynamic behaviour of single and multi-stage geared systems with shape deviations and mounting errors by using a spectral method. *Journal of Sound and Vibration*, 220(5):861–903, 1999.

[179] M. Kubur, A. Kahraman, D.M. Zini, and K. Kienzle. Dynamic analysis of a multi-shaft helical gear transmission by finite elements: model and experiment. *J. Vib. Acoust.*, 126 (3):398–406, 2004.

[180] Y. Zhang, Q. Wang, H. Ma, J. Huang, and C. Zhao. Dynamic analysis of three-dimensional helical geared rotor system with geometric eccentricity. *Journal of Mechanical Science and Technology*, 27(11):3231–3242, 2013.

[181] M.R. Kang and A. Kahraman. An experimental and theoretical study of the dynamic behavior of double-helical gear sets. *Journal of Sound and Vibration*, 350:11–29, 2015.

[182] Q. Wang, Z. Li, H. Ma, and B. Wen. Effects of different coupling models of a helical gear system on vibration characteristics. *Journal of Mechanical Science and Technology*, 31(5): 2143–2154, 2017.

[183] M. Ajmi and P. Velex. A model for simulating the quasi-static and dynamic behaviour of solid wide-faced spur and helical gears. *Mechanism and Machine Theory*, 40(2):173–190, 2005.

[184] A. Kahraman, J. Lim, and H. Ding. A dynamic model of a spur gear pair with friction. In *12th IFToMM World Congress*, pages 18–21, 2007.

[185] S. Li and A. Kahraman. A tribo-dynamic model of a spur gear pair. *Journal of Sound and Vibration*, 332(20):4963–4978, 2013.

[186] J.M. Proix, P. Mialon, and M.T. Bourdeix. Eléments exacts de poutres droites et courbes. *Documentation de référence du Code_Aster*, 3, 2012.

[187] J.M. Proix and J.M. Proix. Calcul des caractéristiques d'une poutre de section transversale quelconque. *Mechanics*, pages 335–340, 1966.

[188] Jaques Dufailly. Calcul de la capacité de charge des engrenages cylindriques de transmission de puissance: présentation et analyse des méthodes iso 6336. *Edition Ellipses, Paris*, 1998.

[189] Carlos M.C.G. Fernandes, Pedro M.T. Marques, Ramiro C. Martins, and Jorge H.O. Seabra. Gearbox power loss. part ii: Friction losses in gears. *Tribology International*, 88:309–316, 2015.

[190] K. Inoue, D. P. Townsend, and J.J. Coy. Optimum Design of a Gearbox for Low Vibration. *Journal of Mechanical Design*, 115(4):1002–1007, 1993.

[191] Venkata Krishna Tamminana, A. Kahraman, and S. Vijayakar. A study of the relationship between the dynamic factors and the dynamic transmission error of spur gear pairs. *Journal of Mechanical Design*, 129(1):75–84, 2007.

[192] Eiichirou Tanaka, Haruo Houjoh, Daisuke Mutoh, Hirofumi Motoshiromizu, Kousaku Ohno, and Naoyuki Tanaka. Vibration and sound-radiation analysis for designing a low-noise gearbox with a multi-stage helical gear system. *JSME International Journal Series C Mechanical Systems, Machine Elements and Manufacturing*, 46(3):1178–1185, 2003.

[193] M. Maatar and P. Velex. An analytical expression for the time-varying contact length in perfect cylindrical gears: some possible applications in gear dynamics. *Journal of mechanical design*, 118(4):586–589, 1996.

[194] Velex Philippe. On the modelling of spur and helical gear dynamic behaviour. *Mechanical engineering*, page 75, 2012.

[195] Tong-Chol Choe, Chol-Nam Ri, Myong-Jin Jo, and Myong-Chol Ri. Research on the engagement process and contact line of involute helical gears. *Mechanism and Machine Theory*, 171:104778, 2022.

[196] João D.M. Marafona, Pedro M.T. Marques, Stéphane Portron, Ramiro C. Martins, and Jorge H.O. Seabra. Gear mesh stiffness and dynamics: Influence of tooth pair structural stiffness asymmetry. *Mechanism and Machine Theory*, 190:105447, 2023.

[197] Teruo Masuda, Toru Abe, and Kanji Hattori. Prediction Method of Gear Noise Considering the Influence of the Tooth Flank Finishing Method. *Journal of Vibration, Acoustics, Stress, and Reliability in Design*, 108(1):95–100, 1986. ISSN 0739-3717.

[198] Takao Yokota, Takeaki Taguchi, and Mitsuo Gen. A solution method for optimal weight design problem of the gear using genetic algorithms. *Computers & industrial engineering*, 35(3-4):523–526, 1998.

[199] V. Savsani, R.V. Rao, and D.P. Vakharia. Optimal weight design of a gear train using particle swarm optimization and simulated annealing algorithms. *Mechanism and machine theory*, 45(3):531–541, 2010.

[200] Daniel Miler, Antonio Lončar, Dragan Žeželj, and Zoran Domitran. Influence of profile shift on the spur gear pair optimization. *Mechanism and Machine Theory*, 117:189–197, 2017.

[201] Daniel Miler, Dragan Žeželj, Antonio Lončar, and Krešimir Vučković. Multi-objective spur gear pair optimization focused on volume and efficiency. *Mechanism and Machine Theory*, 125:185–195, 2018.

[202] Shaul Salomon, Gideon Avigad, Robin C. Purshouse, and Peter J. Fleming. Gearbox design for uncertain load requirements using active robust optimization. *Engineering Optimization*, 48(4):652–671, 2016.

[203] Emna Ben Younes, Christophe Changenet, Jérôme Bruyère, Emmanuel Rigaud, and Joël Perret-Liaudet. Multi-objective optimization of gear unit design to improve efficiency and transmission error. *Mechanism and Machine Theory*, 167:104499, 2022.

[204] Ph. Velex, M. Chapron, H. Fakhfakh, Jérôme Bruyère, and S. Becquerelle. On transmission errors and profile modifications minimising dynamic tooth loads in multi-mesh gears. *Journal of Sound and Vibration*, 379:28–52, 2016.

[205] Jérôme Bruyère, Xiaoyu Gu, and Ph. Velex. On the analytical definition of profile modifications minimising transmission error variations in narrow-faced spur helical gears. *Mechanism and Machine theory*, 92:257–272, 2015.

[206] C. Lagresle, M. Guingand, J.P. Vaujany, and B. Fulleringer. Optimization of tooth modifications for spur and helical gears using an adaptive multi-objective swarm algorithm. *Proceedings of the Institution of Mechanical Engineers, Part C: Journal of Mechanical Engineering Science*, 233(21-22):7292–7308, 2019.

[207] Yulong Lei, Liguo Hou, Yao Fu, Jianlong Hu, and Wei Chen. Research on vibration and noise reduction of electric bus gearbox based on multi-objective optimization. *Applied Acoustics*, 158:107037, 2020.

[208] Mehmet Bozca and Peter Fietkau. Empirical model based optimization of gearbox geometric design parameters to reduce rattle noise in an automotive transmission. *Mechanism and Machine Theory*, 45(11):1599–1612, 2010.

[209] Larry J. Eshelman. The CHC adaptive search algorithm: How to have safe search when engaging in nontraditional genetic recombination. In *Foundations of genetic algorithms*, volume 1, pages 265–283. Elsevier, 1991.

[210] Carlos C. António, Catarina F. Castro, and Luísa C. Sousa. Optimization of metal forming processes. *Computers & structures*, 82(17-19):1425–1433, 2004.